Spin and Lattice Structures in Materials with Competing Interactions Investigated by Neutron Scattering Techniques

by

Lingjia Shen

A thesis submitted to
The University of Birmingham
for the degree of
DOCTOR OF PHILOSOPHY

Condensed Matter Group
School of Physics and Astronomy
College of Engineering and Physical Sciences
The University of Birmingham

October 2016

Abstract

Neutron diffraction and small angle neutron scattering have been used to explore three different materials, including γ-CoV_2O_6, $Pr_{0.5}Ca_{0.5}Mn_{0.97}Ga_{0.03}O_3$, and $Y_2(Cr_{1-x}Ga_{x-0.5}Sb_{0.5})_2O_7$, in which the magnetic or crystallographic properties are closely related to the comepting interactions.

In the quasi-one-dimensional magnet γ-CoV_2O_6, we demonstrate that the magnetic ground state below 6.6 K (T_N) is composed of two single-k phases in a volume ratio of 65(1) : 35(1). The minority phase modulated by k_2 = (-0.25, 0, 0.25) undergoes an incommensurate short range order to commensurate long range order transition while cooled through 5.6 K (T^*). On the other hand, the majority phase modulated by k_1 = (0.5, 0, 0) remains commensurate and long range ordered down to the lowest temperature probed (1.5 K). We propose that this magnetic phase separation is linked to the competition between the single-ion anisotropy and frustrated spin exchange interactions in γ-CoV_2O_6.

In the strained manganese perovskite $Pr_{0.5}Ca_{0.5}Mn_{0.97}Ga_{0.03}O_3$, the electronic phase separation (e.g. orbital order, polaron) is linked to the competition between the Jahn-Teller distortion which tends to localize the carriers and the ferromagnetic double-exchange. By varying the magnetic field at 150 K where the system is a paramagnet, we have found a novel carrier delocalization transition, which enhances the local Jahn-Teller distortion, at B_{c1} = 5.1 T. Surprisingly, most of the spins ($\sim$ 97.5 %) remain paramagnetic at B_{c1}, and only become ferromagnetic at B_{c2} = 7.9 T, where the strong anisotropic strains are softened, accompanied by a giant magnetostriction effect. Most of all, the magnetoresistance of $Pr_{0.5}Ca_{0.5}Mn_{0.97}Ga_{0.03}O_3$ remains detectable up to B_{c2}. Our results strongly suggest that colossal magnetoresistance is governed by two mechanisms: (I) carrier delocalization, and (II) ferromagnetic double-exchange.

In the diluted pyrochlores $Y_2(Cr_{1-x}Ga_{x-0.5}Sb_{0.5})_2O_7$, the nonmagnetic sites does not percolate until x_c = 0.61. However, we cannot detect any magnetic long range order in Y_2CrSbO_7 (x = 0.5) down to 2 K. We propose that bond disorder caused by the weak ionic size mismatch between Cr^{3+} (0.615 Å) and Ga^{5+} (0.600 Å) has a nonnegligible role in Y_2CrSbO_7. This is confirmed by our simulations in which the bond disorder has a much lower percolation threshold at x_c' = 0.23, which means that Y_2CrSbO_7 is dominated by the percolative bond disorder. As a result, we argue that Y_2CrSbO_7 is a potential spin glass candidate which is caused by bond disorder. In this class of spin glasses, the spin freezing temperature scales with the bond disorder strength in the absence of spin-lattice coupling. This is consistent with the very weak bond disorder and the lack of any transition above 2 K in Y_2CrSbO_7.

for my great grandmother Lindi Sheng

ACKNOWLEDGEMENTS

First and foremost, I would like to say uncountable 'Thanks' to my parents, Dakai Shen and Jingxiao Tao, for their invaluable support since my birth. By 'measuring' their granddaughter, Jessica Shen, I can feel the hard work her grandparents have done to her father!

As a PhD student, I have had a fantastic time in the Birmingham condensed matter group. I acknowledge my doctoral supervisor Elizabeth Blackburn for offering me a position and her invaluable support in this period. I am especially grateful that I was allowed to focus on my personal research interests in my PhD program. I also would like to thank Ted Forgan. It seems to us that he knows everything. And as a man in his 70s, he definitely runs faster than the average. I thank both Elizabeth and Ted for getting me involved in the 17-Tesla magnet project, in which I have learnt the very great importance of being patient and careful.

This PhD program is based on a wide range of collaboration. I would like to thank the scientists at the large facilities I have used. These include Sebastian MühlBauer, André Heinemann, Astrid Schneidewind, Petr Čermák, Júrg Schefer, Oksana Zaharko, Jonas Okkels Birk, Urs Gasser, Jorge Gavilano, Emmanuel Canévet, Thomas Prokscha, Thomas Hansen, Charles Dewhurst, Eric Ressouche, Marek Bartkowiak, Markus Zolliker, Pascal Manuel, Dmitry Khalyavin, Peter Baker, Gavin Stenning, etc. I also thank Zhangzhen He and Mitsuru Itoh for kindly providing me their crystals. I would particularly like to thank Mark Laver, who not only taught me how to write a scientific paper, but also offered me many inspiring career suggestions.

I would like to thank other members of the Birmingham condensed matter group I have worked with: Alex Holmes, Josh Lim, Alistair Cameron, Bindu Malini Gunupudi, Louis Lemberger, Randeep Riyat, Erik Jellyman, Michael Parkes, and Jonathan Perrins. Alex Holmes always told me 'Think twice before you do it!'. Josh Lim was a very good tutor during my first year. Alistair Cameron gave me the first lesson of how to lead an experiment. Bindu Malini Gunupudi was a good listener. Louis Lemberger proposed a curry tour everytime when he went back from Institut Laue-Langevin (ILL). Randeep Riyat was always happy to offer me a ride when there was a heavy rain after work. Erik Jellyman offered me some pills to kill my fever during a very stressful beamtime. Michael Parkes was always able to provide the liquid helium in time. Jonathan

Perrins made some very useful sample holders for me.

Last but not the least, I thank my wife, Yunqing Zhang, for her effort of supporting and expanding the family in Birmingham. We came to Birmingham on 13th September, 2012 as a 'duo'. Four years later, we are almost ready to be a 'quartet'!

22 : 39, 13th September, 2016.

CONTENTS

LIST OF FIGURES

LIST OF TABLES

CHAPTER 1

INTRODUCTION

Competing interactions in strongly correlated electron systems often lead to many phases which are close, or even identical, in free energy at low temperatures. As a result, the physical properties are very sensitive to external perturbations such as doping, magnetic field, pressure, *etc* [1, 2]. In the first part of this chapter, we will briefly recall some key concepts in quantum mechanics. With this knowledge, we will demonstrate several particle-particle interacting 'forces', including the Coulomb interaction, spin exchange interactions, spin-orbit coupling, and so forth. These terms are of particular importance in understanding the physics discussed in this thesis. Finally, we will show how the competition of these interactions can lead to exotic particle condensation using several example materials. Following this chapter, there will be a chapter introducing the various experimental techniques referred to in this thesis. We will then present work illustrating new potential effects of these competing interactions. Chapter 3 looks at magnetic phase separation in γ-CoV_2O_6, a frustrated quasi-one-dimensional magnet. Chapter 4 is mainly about the decoupling of carrier delocalization and ferromagnetism in the strained manganese perovskite $Pr_{0.5}Ca_{0.5}Mn_{0.97}Ga_{0.03}O_3$. In the final chapter, we will illustrate the absence of magnetic long range order in the diluted pyrochlore compound Y_2CrSbO_7.

1.1 Fundamental concepts

1.1.1 Orbital angular momentum

In classical mechanics, the angular momentum ($\vec{L}$) of a macroscopic object is defined as $\vec{L} = \vec{r} \times \vec{p}$, where $\vec{p}$ is the linear momentum and $\vec{r}$ is the spatial position of this object. However, it is necessary to adjust this formula in order to correctly describe the 'orbit' of a microscopic quantum mechanical particle (*e.g.* atom, electron). The vector $\vec{L}$ therefore becomes an operator ($\hat{L}$) instead: $\hat{L} = \mathrm{i}\hbar\hat{r} \times \nabla$. Assuming L_i ($i = x, y, z$)

is the projection of the orbital momentum along a particular axis so that $\hat{L}^2 = \hat{L}_x^2 + \hat{L}_y^2 + \hat{L}_z^2$, the following commutation relations are obtained

$$[\hat{L}_i, \hat{L}^2] = 0, \quad [\hat{L}_i, \hat{L}_j] = i\epsilon_{ijk}\hbar\hat{L}_k \, (i \neq j \neq k), \tag{1.1}$$

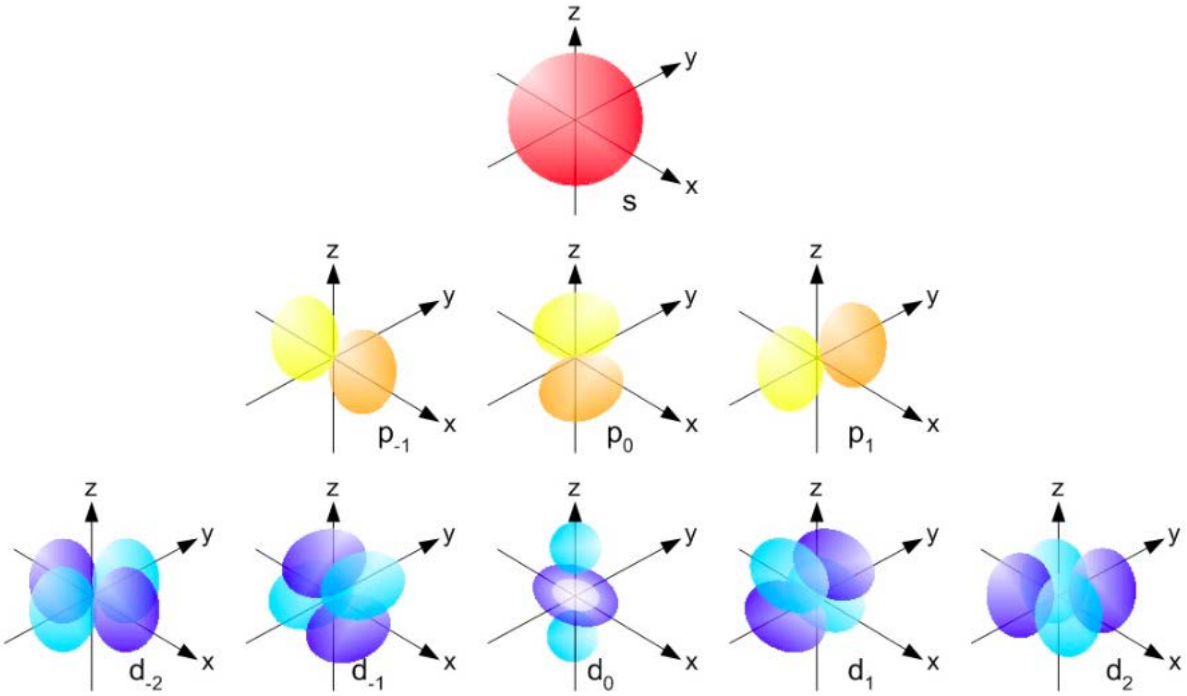

Figure 1.1: Angular distribution of s, p, d orbitals, from Ref. [3].

This means that the two operators, $\hat{L}_i$ and $\hat{L}^2$, share the same set of eigenfunctions

$$|\, l,\, m_l >= Y_{lm_l}(\theta,\, \phi) \propto P_l^{m_l}(cos\theta)e^{im_l\phi}, \tag{1.2}$$

where l ($l = 0, 1, 2, ...$), m_l ($m_l = -l, -l+1, ..., 0, ..., l-1, l$), $P_l^{m_l}(cos\theta)$ and ϵ_{ijk} are angular, magnetic momentum quantum numbers, Legendre polynomials and Levi-Civita symbol, respectively [4, 5]. As we shall focus on the $3d$ ($l=2$) transition metal (TM) oxides in this thesis, we plot out the angular dependence of eigenfunctions belonging to s ($l=0$), p ($l=1$) and d orbitals in Fig. 1.1. Linear combinations of the eigenfunctions at a fixed l value are used in this figure. For the p orbitals, we have

$$Y_x = \frac{1}{\sqrt{2}}(Y_{11} + Y_{1-1}), \tag{1.3}$$

$$Y_y = \frac{1}{i\sqrt{2}}(Y_{11} - Y_{1-1}), \tag{1.4}$$

$$Y_z = Y_{10}. \tag{1.5}$$

For the d orbitals, we have

$$Y_{xy} = \frac{1}{i\sqrt{2}}(Y_{22} - Y_{2-2}), \tag{1.6}$$

$$Y_{x^2-y^2} = \frac{1}{\sqrt{2}}(Y_{22} + Y_{2-2}), \tag{1.7}$$

$$Y_{yz} = \frac{1}{i\sqrt{2}}(-Y_{21} - Y_{2-1}), \tag{1.8}$$

$$Y_{zx} = \frac{1}{\sqrt{2}}(-Y_{21} + Y_{2-1}), \tag{1.9}$$

$$Y_{z^2} = Y_{20}. \tag{1.10}$$

However, one can never measure the three components of $\hat{L}$, as per eq. 1.1. In the following treatments, we will always use the z-component ($\hat{L}_z$) as the commutative operator of $\hat{L}^2$ and m as the magnetic momentum angular number instead of m_l. Moreover, we can obtain the eigenvalues of $\hat{L}^2$ and $\hat{L}_z$ which are $L^2 = l(l-1)\hbar$, $L_z = m\hbar$, respectively.

In classical systems, if a magnetic field $\vec{B}$ is applied to a particle with charge e, its Zeeman energy will be

$$E = -\vec{\mu} \cdot \vec{B}, \tag{1.11}$$

where $\vec{\mu} = \frac{e}{2m_e}\vec{L}$ is the magnetic moment of this charged particle [5]. As mentioned above, these vectors are replaced by operators in quantum mechanics. As a result, the eigenstate of an electron can be described by the following equations:

$$\hat{\mu} = \frac{e}{2m_e}\hat{L}, \quad \hat{\mu}_z = \frac{e}{2m_e}\hat{L}_z. \tag{1.12}$$

If we further assume the magnetic field is along the z-direction and the electron is in an eigenstate with eigenvalues l and m, the resulting energy change, which can be meausured, is

$$\Delta E = \frac{eBm\hbar}{2m_e} = m\mu_B B, \tag{1.13}$$

where $\mu_B = \frac{e\hbar}{2m_e}$ is the Bohr magneton and takes the value $9.274 \times 10^{-24}\,\mathrm{Am}^2$ [5].

1.1.2 Spin angular momentum

The electron not only has an orbital angular momentum ($\hat{L}$), but also possesses an intrinsic spin angular momentum ($\hat{S}$). As shown by Dirac, it is purely quantum mechanical in origin [6]. Three 2×2 matrices, named the Pauli spin matrices, are useful for describing the spin operator $\hat{S}$

$$\sigma_x = \begin{pmatrix} 0 & 1 \\ 1 & 0 \end{pmatrix}, \quad \sigma_y = \begin{pmatrix} 0 & -i \\ i & 0 \end{pmatrix}, \quad \sigma_z = \begin{pmatrix} 1 & 0 \\ 0 & -1 \end{pmatrix}. \tag{1.14}$$

We then define $\hat{S}$ as

$$\hat{S} = \frac{1}{2}\hat{\sigma} = \frac{1}{2}(\sigma_x, \sigma_y, \sigma_z). \tag{1.15}$$

We have adopted the convention that the angular momentum is measured in units of $\hbar$. Then commutation relations can be obtained for the spin operators

$$[\hat{S}_i, \hat{S}^2] = 0, \quad [\hat{S}_i, \hat{S}_j] = i\hat{S}_k \, (i \neq j \neq k). \tag{1.16}$$

The spin quantum number, S, is $\frac{s}{2}$ (s = 0, 1, 2...) and its z-component S_z can take $2s+1$ possible values between -S and S.

1.1.3 Total angular momentum

With the knowledge of both orbital and spin angular momenta, we can define the total momentum ($\hat{J}$) of a system

$$\hat{J} = \hat{L} + \hat{S}. \tag{1.17}$$

At this point it is helpful to introduce the Landé g-factor (g). For the orbital angular momentum, $\hat{\mu}_L = \frac{e}{2m_e}\hat{L}$, which we can write as $\hat{\mu}_L = g_L \mu_B \hat{L}$, where $g_L = 1$. It is nontrivial to calculate the Landé factor for the spin angular momentum (g_s) [5]; it is $g_S \approx 2$ [4, 5]. Bear in mind that our angular momentum is in units of $\hbar$.

For the total magnetic moment

$$\hat{\mu}_J = \mu_B(g_L\hat{L} + g_S\hat{S}) = g_J \mu_B \hat{J}, \tag{1.18}$$

where g_J is the Landé g-factor of the total angular momentum. In order to obtain an expression for g_J using

g_L, g_S, J, L and S (J, L and S are eigenvalues of $\hat{J}$, $\hat{L}$ and $\hat{S}$), we mutiply both sides of eq. 1.18 by $\hat{J}$

$$\mu_B(g_L\hat{L}\cdot\hat{J} + g_S\hat{S}\cdot\hat{J}) = g_J\mu_B\hat{J}^2. \tag{1.19}$$

And by inserting the following known expressions into eq. 1.19,

$$\hat{J}^2 = J(J+1), \quad \hat{L}^2 = L(L+1), \quad \hat{S}^2 = S(S+1), \tag{1.20}$$

$$\hat{L}\cdot\hat{J} = \frac{1}{2}(\hat{J}^2 + \hat{L}^2 - \hat{S}^2), \tag{1.21}$$

$$\hat{S}\cdot\hat{J} = \frac{1}{2}(\hat{J}^2 - \hat{L}^2 + \hat{S}^2), \tag{1.22}$$

we obtain the Landé g-factor for the total angular momentum

$$g_J = g_L\frac{J(J+1) + L(L+1) - S(S+1)}{2J(J+1)} + g_S\frac{J(J+1) - L(L+1) + S(S+1)}{2J(J+1)}. \tag{1.23}$$

Experimentally, we always measure the eigenvalues of $\hat{J}^2$ and $\hat{J}_z$. As a result, we define two very important parameters: the effective magnetic moment (M_{eff}) and the saturation moment along the field direction (M_s)

$$M_{eff} = g_J\mu_B\sqrt{J(J+1)}, \qquad M_s = g_J J\mu_B. \tag{1.24}$$

1.1.4 Paramagnetism

A material is expected to be paramagnetic in one of two conditions:

(i) the spins are well isolated in space so that the interaction energy between each pair (E_i) of spins is negligible;

(ii) the thermal fluctuation energy ($k_{\mathrm{B}}\mathrm{T}, k_B \approx 8.617 \times 10^{-5}\, eVK^{-1}$ is the Boltzmann constant) overwhelms E_i.

In both cases, E_i is insignificant to the spin orientations. However, a non-zero magnetic moment will be induced by applying a magnetic field. The energy of the electron with total angular momentum $\hat{J}$ is $g_J m\mu_B B$ ($m = -J, -J+1, ..., J-1, J$). As a result, the partition function is

$$Z = \sum_{m=-J}^{J}\exp(g_J m\mu_B B/k_B T). \tag{1.25}$$

So the mean value of the total magnetic angular momentum m is

$$< m >= \frac{\sum_{m=-J}^{J} m \times \exp(g_J m \mu_B B/k_B T)}{\sum_{m=-J}^{J} \exp(g_J m \mu_B B/k_B T)}. \tag{1.26}$$

The magnetization of a system with n free spins can be determined by

$$M = n g_J \mu_B < m > . \tag{1.27}$$

By writing $y = g_J \mu_B J B/k_B T$ and $M_s = n g_J J \mu_B$, we finally obtain

$$M = M_s \frac{2J+1}{2J} coth(\frac{2J+1}{2J} y) - \frac{1}{2J} coth(\frac{y}{2J}), \tag{1.28}$$

where the $B_J(y) = \frac{2J+1}{2J} coth(\frac{2J+1}{2J} y) - \frac{1}{2J} coth(\frac{y}{2J})$ is the Brillouin function [4].

In the small y region ($y \ll 1$, often corresponding to low magnetic field and not very low temperatures), the susceptibility is expressed by

$$\chi = \frac{M}{H} \approx \frac{\mu_0 M}{B} = \frac{n \mu_0 M_{eff}^2}{3 k_B T}, \tag{1.29}$$

using the Maclaurin expansion of $\coth(y)$. As a result, $\chi \propto 1/T$ and one can extract M_{eff} (eq. 1.24) by measuring χ in the paramagnetic region.

1.1.5 Crystal fields

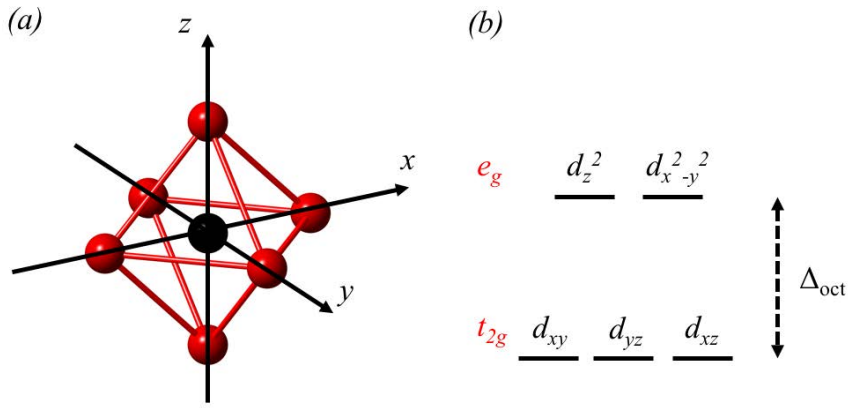

Figure 1.2: (a) MO_6-octahedron. M = TM ion (black solid). Oxygens are red solids. The orthogonal axes are also labelled. (b) Crystal field splitting of the d orbitals.

For the $3d$ TM ion oxides, another important feature to consider is the local crystal environment due to the exposed d orbitals. This effect is much weaker for $4f$ rare earth ions in which the $4f$ orbitals are well shielded by the $5s$ and $5p$ outer shells. In the compounds investigated in this thesis, such crystal fields originate from the overlap between the d orbitals of TM ions (e.g. $Mn^{3+}, Mn^{4+}, Cr^{3+}, Co^{2+}$) and the p oxygen orbitals. For example, when an $3d$ TM ion is placed on the center of an octahedron where oxygens occupy the vertices (Fig. 1.2a), the degeneracy of the d orbital will be lifted (Fig. 1.2b).

As shown in Fig. 1.1, the lobes of the d_{xy}, d_{xz} and d_{yz} orbitals (called t_{2g} orbitals) all point along the diagonal directions between the x, y and z axes. However, the d_{z^2} and $d_{x^2-y^2}$ orbitals (called e_g orbitals) have their lobes lying along the main axes. Since the neighbouring $2p$ oxygen orbitals are also pointing along the three main axes (Fig. 1.1), the e_g orbitals will have a stronger electrostatic energy produced by the electrons in the $2p$ oxygen orbitals. As a result, the five level d orbitals split into two groups, with the three-fold t_{2g} orbitals lying underneath the two-fold e_g orbitals (Fig. 1.2b). The calculation of the energy gap (Δ_{oct}) between the two levels can be found in Ref. [7]

It is also worth mentioning the empirical Hund's rules which are used to predict the electron filling sequence in the d orbitals if they are not fully occupied [4]. They are arranged in decreasing importance:

1. The configuration with lowest energy is also the configuration with maximum S.
2. When (1) is fullfilled, the next step to lower the energy is to maximize L.

3. J = |L - S| if the shell is less than half filled, otherwise J = |L + S|.

These rules work very well for predicting the electronic configuration of $4f$ ions. In contrast, big discrepancies may occur for $3d$ TM ions due to the presence of the crystal field [4]. Indeed, even the first of Hund's rules may be ignored if the crystal field is strong enough [8]. Moreover, Hund's rules match the experiment much better if one assumes that the orbital quantum number $L = 0$ [4]. This effect is called orbital quenching and prevails in many TM oxides. However, non-zero angular momentum states can be introduced in systems where the spin-orbit coupling is nonnegligible, e.g, α-CoV_2O_6 [9].

1.1.6 Jahn-Teller distortion

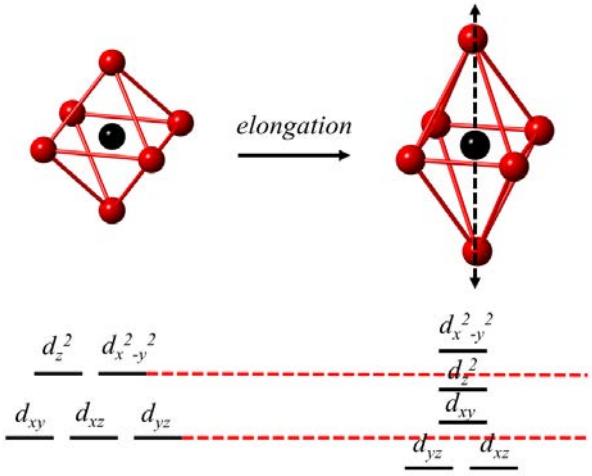

Figure 1.3: (upper) A Jahn-Teller distortion (elongation) for the MO_6-octahedron. (bottom) The degeneracy lifting after the distortion. The energy is lowered because the d_{z^2} level is lowered. The energy saving for lowering the d_{xz} and d_{yz} levels is balanced by the energy raising of the d_{xy} level [4].

In a TMO_6-octahedral environment, deviation of oxygen ions from their equilibrium positions is usually not favoured. An increase in the energy, proportional to the square of the distortion, will be introduced [4, 2]. However, this motion may also lower the energy by lifting the orbital degeneracy of the central TM ion. The resulting lattice change is called a Jahn-Teller (JT) distortion. As discussed in the last section, the five-fold degeneracy of the $3d$ orbitals can be lifted by the crystal field effect to form e_g (two-fold) and t_{2g} (three-fold) levels. When a JT effect happens, these levels may be further split [4]. This is achieved by changing the overlap between the $3d$ TM orbitals and the $2p$ oxygen orbitals. Consequently, the energy of certain orbitals is raised, while for the others' it is lowered. Fig. 1.3 corresponds to the case of 'elongation'

along the z-axis. For the Mn^{3+} ion ($3d^4$), the four electrons singly occupy the d_{yz}, d_{xz}, d_{xy} and d_{z^2} orbitals, respectively. The JT distortion thus lowers the total energy related to these occupied d orbitals. When placed into a lattice arrangement, such TMO_6-octahedral distortion may become cooperative [2, 10]. As will be demonstrated in this thesis, the cooperative JT distortion is crucial to understand various emergent properties in mixed-valence perovskite manganites.

1.2 Interactions

1.2.1 Coulomb interactions

In a multiple orbital system, we can write the kinetic energy of the electrons as

$$\hat{H}_{kin} = \sum_{\vec{j},\vec{j}',\gamma,\gamma',\sigma} t^{\gamma\gamma'}_{\vec{j}\vec{j}'} c^{\dagger}_{\vec{j}\gamma\sigma} c_{\vec{j}'\gamma'\sigma}, \tag{1.30}$$

where $\vec{j}$ is the site occupied by magnetic ions, γ and σ label the orbital and spin states, respectively [2]. The Coulomb potential is

$$\hat{H}_C = \frac{1}{2}\sum_{\vec{j}} \sum_{\gamma_1\gamma_2\gamma_1'\gamma_2'} \sum_{\sigma_1\sigma_2\sigma_1'\sigma_2'} < \gamma_1\sigma_1,\, \gamma_2\sigma_2 \,||\, \gamma_1'\sigma_1',\, \gamma_2'\sigma_2' > c^{\dagger}_{\vec{j}\gamma_1\sigma_1} c^{\dagger}_{\vec{j}\gamma_2\sigma_2} c_{\vec{j}\gamma_2'\sigma_2'} c_{\vec{j}\gamma_1'\sigma_1'}. \tag{1.31}$$

In solid-state physics, an electron's state $(\sigma, \gamma, \vec{j})$ can be described by the Wannier function, $\phi_{\gamma\,\sigma}(\vec{j})$, which is composed of a complete set of orthogonal functions [11]. Following this approach, the matrix element in eq. 1.31 can be given by [10]

$$< \gamma_1\sigma_1,\, \gamma_2\sigma_2 \,||\, \gamma_1'\sigma_1',\, \gamma_2'\sigma_2' >= \int\int d\vec{j} d\vec{j}' \phi^{*}_{\gamma_1\sigma_1}(\vec{j}) \phi^{*}_{\gamma_2\sigma_2}(\vec{j}') g_{\vec{j}-\vec{j}'} \phi_{\gamma_1'\sigma_1'}(\vec{j}) \phi_{\gamma_2'\sigma_2'}(\vec{j}'). \tag{1.32}$$

As a result, the Hamiltonian for a general problem is $\hat{H} = \hat{H}_{kin} + \hat{H}_C$. However, it is very difficult to exactly solve these complicated interactions. Alternatively, eq. 1.31 can be replaced by an effective Hamiltonian consisting of several parts as long as they can capture the essential underlying physics. For the $3d$ TM ions investigated in this thesis, we have already shown that the five-fold orbitals split into e_g and t_{2g} levels due to the crystal field effect. In many systems, e.g. manganese oxides, the t_{2g} spins are very localized and less affected by external perturbations. They can be treated as a 'core-spin' $\hat{S}_{\vec{j}}$ so that the Coulomb coupling between electron(s) in the e_g ($\hat{s}_i$) and t_{2g} orbitals in one TM ion may be described by a Hund's coupling

term

$$\hat{H}_{Hund} = -J_H \sum_i \hat{s}_i \hat{S}_{\vec{j}}. \tag{1.33}$$

Another term H_{el-el} is required to account for the remaining Coulomb interactions between e_g electrons [2, 10].

1.2.2 Exchange interactions

In the non-interacting limit, two indistinguishable electrons can be separately described by a spatial wave function $\psi_i(r)$ $(i = \mathrm{a}, \mathrm{b})$ [5]. One can use these functions to construct the spatial wave functions (Φ) of an interacting two-electron system. Considering the exchange symmetry of Fermions as well as the spin part of the wave function [5], there are two possible forms for Φ

$$\Phi_1 = \frac{1}{\sqrt{2}}[\psi_a(r_1)\psi_b(r_2) + \psi_a(r_2)\psi_b(r_1)]\chi_s, \tag{1.34}$$

$$\Phi_2 = \frac{1}{\sqrt{2}}[\psi_a(r_1)\psi_b(r_2) - \psi_a(r_2)\psi_b(r_1)]\chi_t, \tag{1.35}$$

where χ_s (χ_t) represents the singlet $\mathrm{S} = 0$ (triplet $\mathrm{S} = 1$) spin state [5]. Given the Hamiltonian ($\hat{H}$) of the system, one can also calculate the energy difference of the two possible states

$$\Delta E = E_1 - E_2 = 2 \int \phi_a^*(r_1)\phi_b^*(r_2)\hat{H}\phi_a^*(r_2)\phi_b^*(r_1)dr_1dr_2. \tag{1.36}$$

If Δ E is negative (positive), a singlet (triplet) state is favoured, corresponding to two spins antiparallel (parallel) to each other. We can also construct an effective Hamiltonian (H_{eff}) using the following procedures

$$S_{tot}^2 = (\hat{S}_1 + \hat{S}_2)^2 = \hat{S}_1^2 + \hat{S}_2^2 + 2\hat{S}_1\hat{S}_2. \tag{1.37}$$

Since $S_{tot} = 0, 1$ and $S_1, S_2 = 1/2$, we obtain

$$\hat{S}_1\hat{S}_2 = \frac{1}{4}\,(triplet) \quad or \quad -\frac{3}{4}\,(singlet). \tag{1.38}$$

Finally, H_{eff} can be written as

$$H_{eff} = \frac{1}{4}(E_1 + 3E_2) - (E_1 - E_2)\hat{S}_1\hat{S}_2. \tag{1.39}$$

The spin part of H_{eff} is called the exchange interaction

$$\hat{H}_{ex} = -2J\hat{S}_1\hat{S}_2, \tag{1.40}$$

where $J = \dfrac{E_1 - E_2}{2}$ is the exchange constant. The main origin of such exchange interactions in solids is the electron-electron Coulomb repulsions [4, 5].

For the many-body systems, there is an interaction between each pair of spins. It is very useful to introduce the isotropic Heisenberg model

$$\hat{H} = -\sum_{ij} J_{ij}\hat{S}_i\hat{S}_j, \tag{1.41}$$

where J_{ij} is the exchange constant between each pair of spins. This model can be reduced to a XY-model if the exchange is two-dimensional and an Ising-model if the exchange is one-dimensional [1]. Considering only the nearest neighbour exchange, the relative alignment of the two neighbouring spins is determined by the sign of the exchange constant.

If the wavefunctions of two neighbouring magnetic ions are sufficiently overlapping, a direct exchange interaction is expected to set in. However, this term is usually less important in determining the magnetic ground state in oxides because the corresponding magnetic ions are well separated in space. Thus indirect exchange interactions must be taken into account.

Superexchange interaction

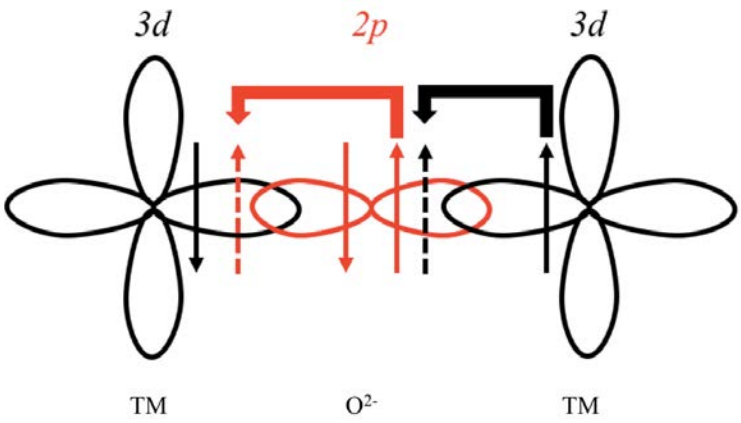

Figure 1.4: Superexchange process. The electron hopping is marked by dashed arrows. Antiferromagnetic spin alignment is achieved in this one-orbital model.

Superexchange is one type of indirect exchange which prevails in magnetic oxides. The nonmagnetic ion O^{2-} acts as an intermediary between the two magnetic ions. To simplify the physical process of superexchange, we assume the $2p$ oxygen orbital overlaps with the same d orbital on each side of it (Fig. 1.4), and that there is only one unpaired electron on the magnetic ion. To lower the kinetic energy of the system, this electron tends to hop to the oxygen site. To accommodate this change, the $2p$ electron with the same spin direction will hop into the d orbital of the other magnetic ion. Since this orbital is already singly occupied, the new electron has to adopt the opposite spin direction due to the Pauli exclusion principle, resulting in an antiferromagnetic alignment between the neighbouring spins (Fig. 1.4).

In practice, the overlap of orbitals (p, d) is much more complicated. Depending on the TM-O bond length and the TM-O-TM bond angle, the magnetic exchange can even vary from antiferromagnetic to ferromagnetic. A set of empirical rules, called the Goodenough-Kanamori rules, are helpful for determining the correct magnetic order in many oxides [12]. For example, the superexchange between two magnetic ions with partially filled d shells is strongly antiferromagnetic if the TM-O-TM bond angle is 180°, whereas a 90° superexchange interaction is ferromagnetic and much weaker. Further information can be found in Ref. [12].

Double exchange interaction

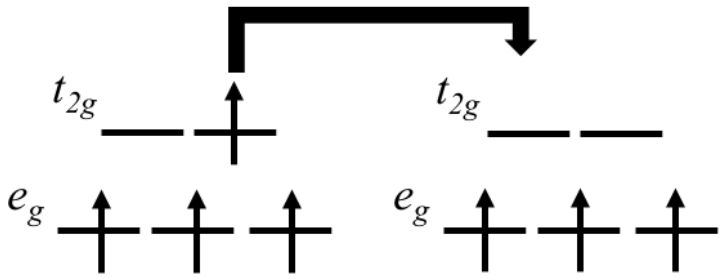

Figure 1.5: Double exchange mechanism in mixed-valence oxides.

In the superexchange framework, the unpaired electrons are only allowed to hop within the TM-O-TM bond, meaning the system is an insulator. A ferromagnetic metallic state can also occur in some mixed-valence magnetic oxides. This state is tuned by the double exchange mechanism. As shown in Fig. 1.5, mixed-valence is required to host double exchange in order to make sure the hopping range is extended (empty

orbitals), otherwise the superexchange mechanism will be recovered. Secondly, ferromagnetic alignment of the neighbouring spins is favoured since the strong Hund's couping from the core spins in the t_{2g} orbitals will try to align the e_g spin along them. The double exchange mechanism can qualitatively explain the charge transport properties in mixed-valence systems such as Fe_3O_4 and $La_{1-x}Sr_xMnO_3$, though not in a comprehensive way [10, 13].

1.2.3 Dzyaloshinsky-Moriya interaction

If the centre of the bond connecting two spins does not contain inversion symmetry, the anisotropic exchange interaction Dzyaloshinsky-Moria (DM) interaction is allowed [14]. It is the higher order correction of the Dirac equation and couples the exicted state of one ion and the ground state of the other [4]. It takes the form

$$\hat{H}_{DM} = D_{ij} \cdot \hat{S}_i \times \hat{S}_j, \tag{1.42}$$

where $\vec{D}_{ij}$ is a vector and its direction depends on the symmetry [14]. The DM interaction can play a significant role in pyrochlore lattices [15], as the geometry permits a non-zero DM term.

1.2.4 Magnetic dipolar interaction

The long range interaction between two magnetic dipoles with magnetc moments $\vec{J}_1$, $\vec{J}_2$ separated by $\vec{r}$ can be expressed by

$$H_{dip} = \frac{\mu_0}{4\pi r^3} [\vec{J}_1 \cdot \vec{J}_2 - \frac{3}{r^2}(\vec{J}_1 \cdot \vec{r})(\vec{J}_2 \cdot \vec{r})]. \tag{1.43}$$

This term is small (a few Kelvin) and therefore not important at high temperatures. However, for those oxides where the magnetism comes from rare earth ions with very large magnetic moments, the dipolar interaction still needs to be considered [4, 15].

1.2.5 Spin-orbit coupling

Although spin-orbit coupling is a relativistic effect in origin, it can be phenomenologically understood using a classical model [4]. In the electron reference frame, the motion of the electron orbiting can be alternatively viewed as the motion of nucleus. As a result, an additional magnetic field term exists,

$$\vec{B} = \frac{\vec{\epsilon} \times \vec{v}}{c^2}, \tag{1.44}$$

where $\vec{\epsilon} = -\vec{\delta}\vec{V}(\vec{r})$, v is the orbiting velocity and $\vec{V}(\vec{r})$ is the potential energy of the electron. As mentioned above, this magnetic field will interact with the electron spin ($\hat{m}$) in the form of

$$\hat{H}_{SO} = -\frac{1}{2}m \cdot B = \frac{e\hbar^2}{2m_e c^2 r}\frac{dV(r)}{dr}\hat{S} \cdot \hat{L}, \tag{1.45}$$

where $\hbar\hat{L} = m_e\vec{r} \times \vec{v}$ and $\hat{e} = (ge\hbar/2m)\hat{S}$ [4]. Since most orbital wave functions (e.g. p, d) have aspherical distributions (Fig. 1.1), the spin-orbit coupling is responsible for the magnetocrystalline (single-ion) anisotropy ($\hat{H}_{an}$) in materials.

1.2.6 Electron-phonon coupling

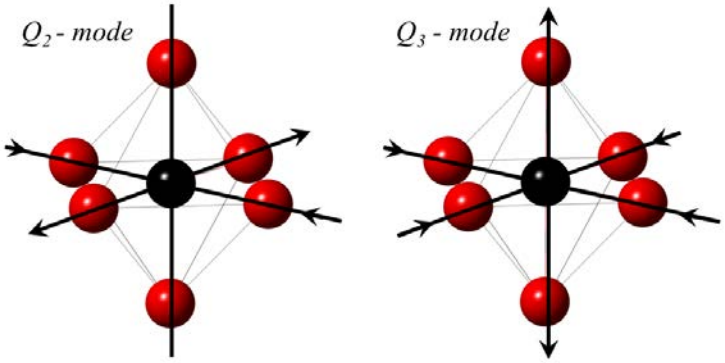

Figure 1.6: Two e_g-active JT modes.

For a TMO_6-octahedron, there are 7 (number of ions) $\times$ 3 (three dimensional motion) = 21 JT modes in total to consider. Since we shall focus on mixed-valence manganese oxides in this thesis, only 2 modes, usually written as Q_2 and Q_3, are important to the e_g orbital splitting of Mn^{3+} [2]. These two modes are depicted in Fig. 1.6. The potential change of an electron related to the JT distortion, assuming the presence of both modes is

$$\Delta V_{JT} = \frac{2\sqrt{6}}{21}\frac{9}{a^4} < r^2 > \left[Q_2 \begin{pmatrix} 0 & 1 \\ 1 & 0 \end{pmatrix} + Q_3 \begin{pmatrix} 1 & 0 \\ 0 & -1 \end{pmatrix} \right], \tag{1.46}$$

where r and a are the electron - Mn^{3+} and oxygen - Mn^{3+} distance, respectively [2]. We replace the matrices in this equation by the Pauli symbols in eq. 1.14. Then we can express the total energy by including the

energy penalization caused by distortion itself

$$\hat{H} = -g(Q_2\sigma_x + Q_3\sigma_z) + \frac{1}{2}M\omega^2[Q_2^2 + Q_3^2], \tag{1.47}$$

where g = -$(2\sqrt{6}/21)\frac{9}{a^4} < r^2 >$. Finally, by applying the second-quantization process and summing over all sites ($i = 1, 2, 3...$), the electron-phonon coupling term of the system is

$$\hat{H}_{el-ph} = \sum_i -\left[2g(Q_{2i}T_i^x + Q_{3i}T_i^z) + (k_{JT}/2)(Q_{2i}^2 + Q_{3i}^2)\right], \tag{1.48}$$

where $k_{JT} = M\omega^2$ and $T_i^{x,y,z}$ are pseudospin operators [2]. In theoretical calculations, the dimensionless parameter $\lambda = g/\sqrt{k_{JT}t}$ (t is the hopping amplitude in eq. 1.30) is used to characterize the electron-phonon coupling strength [10].

1.2.7 Ruderman-Kittel-Kasuya-Yosida interaction

The exchange between localized magnetic ions in metals is mediated by the conducting electrons. This type of indirect exchange is known as the Ruderman-Kittel-Kasuya-Yosida (RKKY) interaction [4, 16, 17, 18]. Its Hamiltonian takes the form of

$$H_{RKKY}(r) \propto \frac{\cos(2k_F r)}{r^3}, \tag{1.49}$$

where r is the distance between two localized magnetic ions, and k_F is the radius of the Fermi surface which is assumed to be spherical [4]. The key feature revealed by eq. 1.49 is that the RKKY interaction is long range in nature with its sign oscillating as a function of r.

1.3 Frustrated magnetism

1.3.1 Geometric frustration

In addition to the competing interactions, sometimes referred as 'random frustration' in the literature [15], 'geometric frustration' also plays an important role on determining the magnetic structure in relevant systems. As shown in Fig. 1.7a, when the antiferromagnetically coupled spins are assigned to occupy the corners of the triangular (tetrahedral) lattice, the antiparallel configuration between each pair of spins cannot be achieved simultaneously. This effect is called 'geometric frustration'. A pyrochlore lattice ($A_2B_2O_7$) has a cubic crystallographic structure (space group *Fd-3m*) and consists of two sets of corner-sharing tetrahedral

sublattices occupied by A and B ions, respectively 1.7b & 1.7c. Geometric frustration is allowed in this lattice, and can give rise to exotic states (e.g. spin ice, spin glass and spin liquid) in magnetic compounds with this structure.

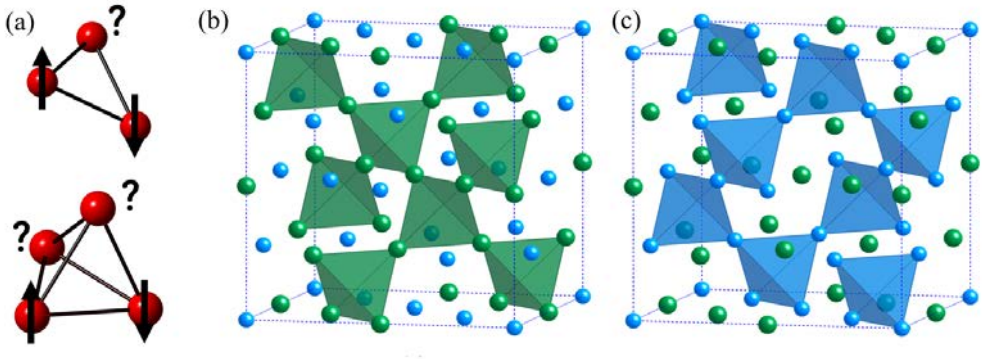

Figure 1.7: (a) Antiferromagnetically coupled spins on a triangular (upper) or tetrahedral (bottom) lattice unit. Corner-sharing tetrahedral sublattices in a pyrochlore structure (shaded) formed by (b) A (green solids), and (c) B (blue solids) ions [19]. Oxygen ions are omitted.

We will now look at several detailed examples drawing on the fundamentals discussed above, that provide the spur for the main work presented in this thesis. We will first discuss the glassy pyrochlore $Y_2Mo_2O_7$. This compound is supposed to enter an ordered state at low temperatures without the presence of bond disorder. We will then carry on to the pyrochlore $Y_2Mn_2O_7$ to show how the sample quality (disorder) can affect the magnetic long range order in this compound. These two systems are very important to understand the diluted pyrochlore Y_2CrSbO_7 studied in Chapter 5 of this thesis. We have attributed the lack of magnetic long range order in this compound down to 1.8 K to the percolative bond disorder caused by the ionic radius mismatch between Cr^{3+} and Sb^{5+} on the B-sites.

1.3.2 Spin glass in $Y_2Mo_2O_7$

When magnetic frustration is combined with some sort of disorder (e.g. site disorder, bond disorder), a spin glass (SG) state may appear. Experimentally, a SG material exhibits the following properties [20]:

1. At low field, the ac susceptibility has a cusp at a temperature T_f, the SG transition, and this temperature is frequency dependent.

2. No sharp anomaly is observed in the heat capacity data.

3. The susceptibility is history dependent below $T_{\rm f}$, i.e. the zero-field-cooled (ZFC) and field-cooled (FC) data diverge below $T_{\rm f}$.

4. Magnetization decays with time below $T_{\rm f}$

5. Absence of long range order below $T_{\rm f}$ [15]. As an example, the magnetic properties of the classic SG compound $Cu_{1-x}Mn_x$ are displayed in Fig. 1.8.

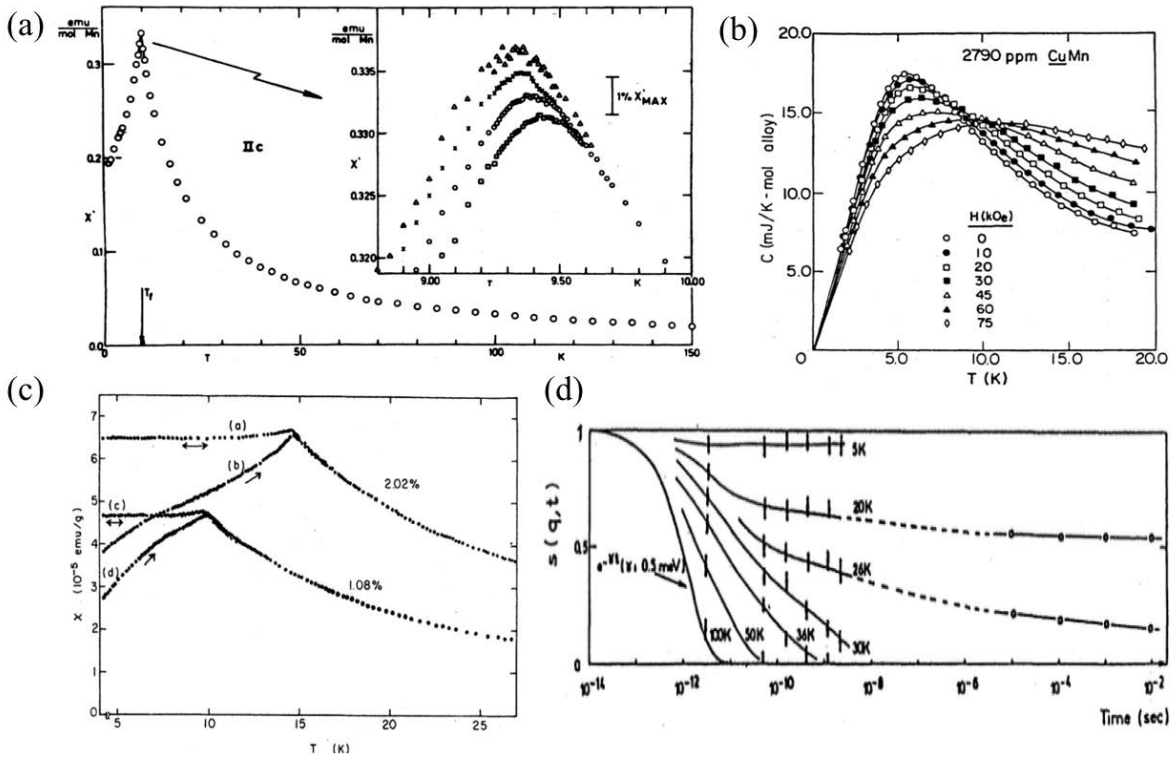

Figure 1.8: SG behaviour in a $Cu_{1-x}Mn_x$ alloy [20]. Temperature dependences of (a) ac susceptibility, (b) heat capacity, and (c) ZFC (branch b and d) and FC (branch a and c) dc susceptibility curves. (d) Spin relaxation at various temperatures, where $\vec{S}(\vec{q},\,t)\;\propto<\vec{S}_i(t)\cdot\vec{S}_j(0)>_T exp[i\vec{q}\cdot(\vec{r}_i\,-\,\vec{r}_j)]$ and $q = 0.093\,\text{Å}^{-1}$.

The pyrochlore compound $Y_2Mo_2O_7$ has magnetic Mo^{4+} ions occupying the B-sites. By fitting the susceptibility at high temperatures, a large/negative Curie-Weiss temperature $\Theta_{\rm CW} \simeq$ -200 K is obtained. On the other hand, the Mo^{4+} ions have an effective moment of 2.55 μ_B/Mo, indicating that the orbital moment is probably quenched in $Y_2Mo_2O_7$ [21] (Fig. 1.9). As shown in Fig. 1.9, clear divergence between ZFC and FC susceptibility curves are observed at $T_{\rm f} = 22$ K, suggestive of a SG transition. This feature is further studied by nonlinear susceptibility as well as neutron scattering techniques [22, 23]. Typical scaling behavour of a

SG is observed near to $T_{\rm f}$ (Fig. 1.9). Moreover, quasielastic spin excitations are detected above $T_{\rm f}$. At low temperatures, these fluctuations are replaced by a static short range order with correlation length less than 5 Å (Fig. 1.10).

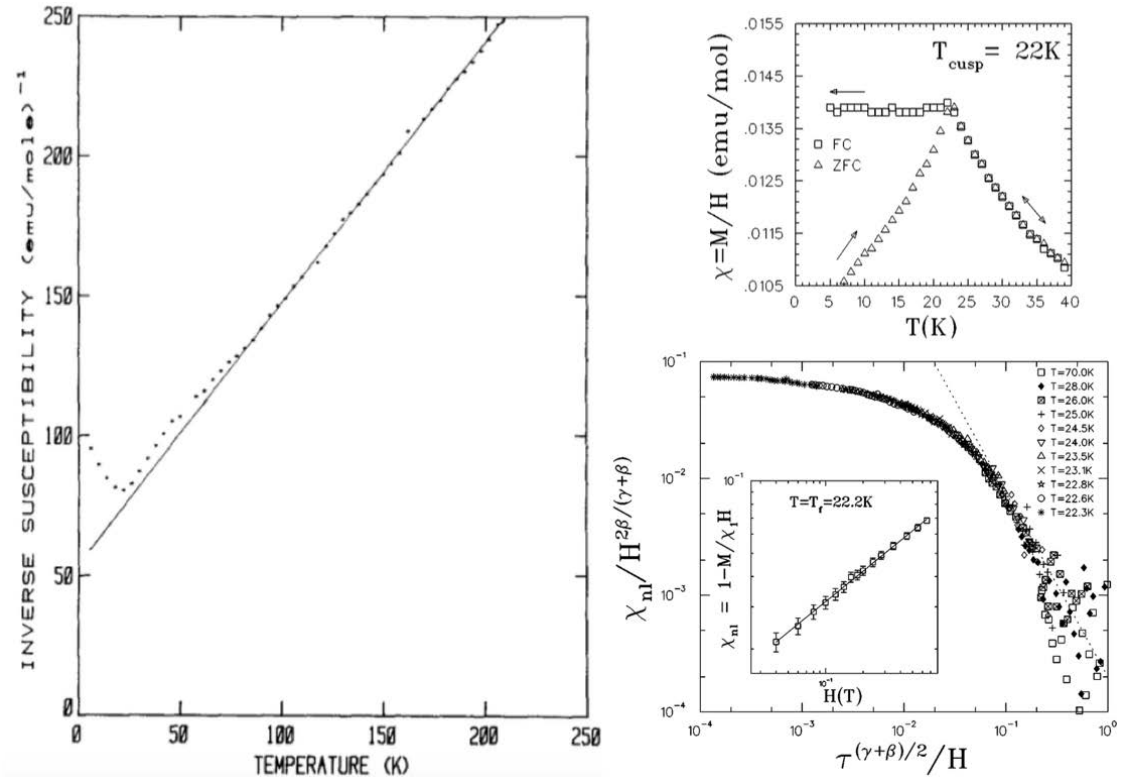

Figure 1.9: (Left) Inverse susceptibililty versus temperature (solids) curve of $Y_2Mo_2O_7$. The black line is a linear fit to its high temperature part [21]. (Top right) ZFC and FC curves when B = 0.01 T [23]. (Bottom right) Nonlinear susceptibility χ_{nl} analyzed according to the critical scaling model in Ref. [23]

Based on the experimental evidence provided above, the SG state in $Y_2Mo_2O_7$ is well established. However, the driving mechanism of this state has still not been fully understood yet. In general, magnetic frustration and disorder are the building blocks for a SG state. For example, the spin exchange in the $Cu_{1-x}Mn_x$ alloy is of the RKKY type, the sign of which is very sensitive to the distance between the two magnetic sites (eq. 1.49) [20]. The SG state in this compound is caused by the site disorder of Mn. Several investigations, including extended X-ray-absorption fine structure (EXAFS) and nuclear magnetic resonance (NMR) and neutron pair distribution function (PDF), have been carried out to characterize the local disorder level in $Y_2Mo_2O_7$ [24, 25, 26]. These results reveal: (i) discrete lattice distortions which may suppress the magnetic frustration [26], and (ii) very weak bond length fluctuations ($\leqslant 5\,\%$ for Mo-Mo bond)[24]. Never-

theless, such a disorder level is too low to induce a SG state according to the conventional mean field theory predictions [27].

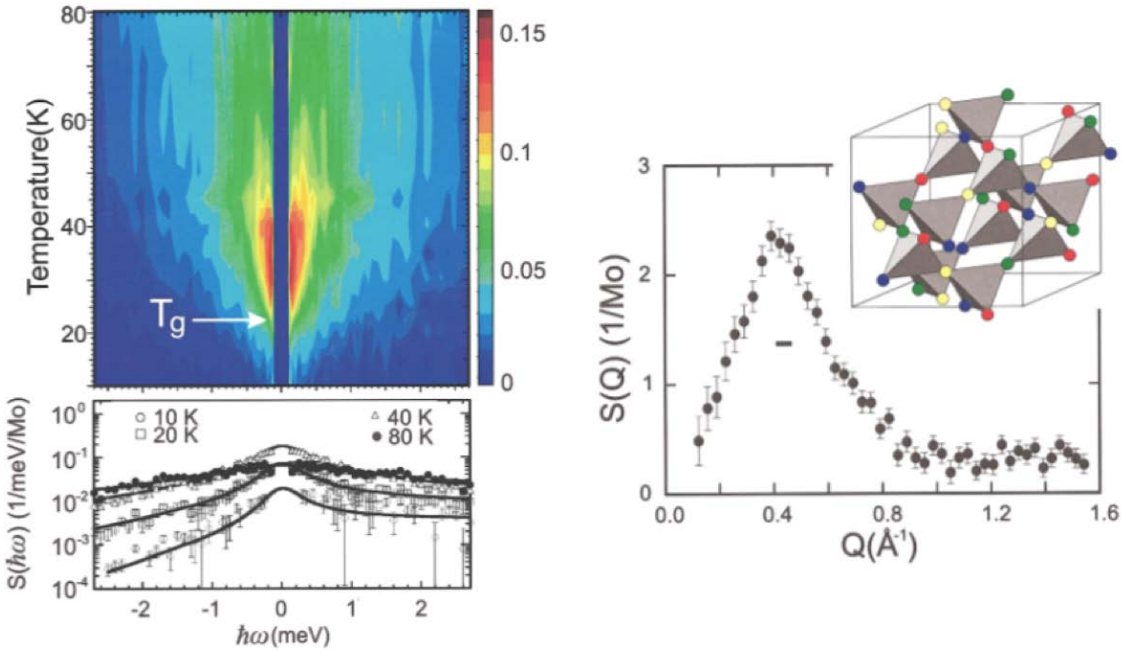

Figure 1.10: (Left) Low energy inelastic neutron spectrum of $Y_2Mo_2O_7$ at different temperatures [22]. (Right) Elastic magnetic structure factor *S(Q)* versus scattering vector (Q) plot at 1.4 K [22].

An alternative approach of modelling a pyrochlore spin lattice with bond disorder is to start from the classical Heisenberg antiferromagnet in eq. 1.41, where the ground state is highly degenerate [15, 28]. Bond disorder produces exchange fluctuations $\vec{\Delta}$ to the original average exchange constant $\vec{J}$. Saunders *et al* treat $\vec{\Delta}$ as a perturbation to the ground state degeneracy in the weak disorder limit ($|\vec{\Delta}| \ll |\vec{J}|$) [29]. By parametrizing the ground states in terms of a gauge field, they project $\vec{\Delta}$ into the nearest neighbour exchange interactions so that effective long range interactions are generated [29]. Using Monte Carlo simulations, a SG transition at a finite temperature T_f is found. However, the predicted T_f only scales with $|\vec{\Delta}|$ and is much smaller than the experimentally determined value in $Y_2Mo_2O_7$ (~ 22 K) [29, 23]. In order to correctly reproduce T_f, an additional spin-lattice coupling term is required, as revealed in Ref. [30]. Finally, we note the origin of spin-lattice coupling in $Y_2Mo_2O_7$ may be related to the orbital frustration according to the latest X-ray and neutron PDF investigations as well as density functional theory (DFT) calculations [31, 32].

1.3.3 Long range order in $Y_2Mn_2O_7$

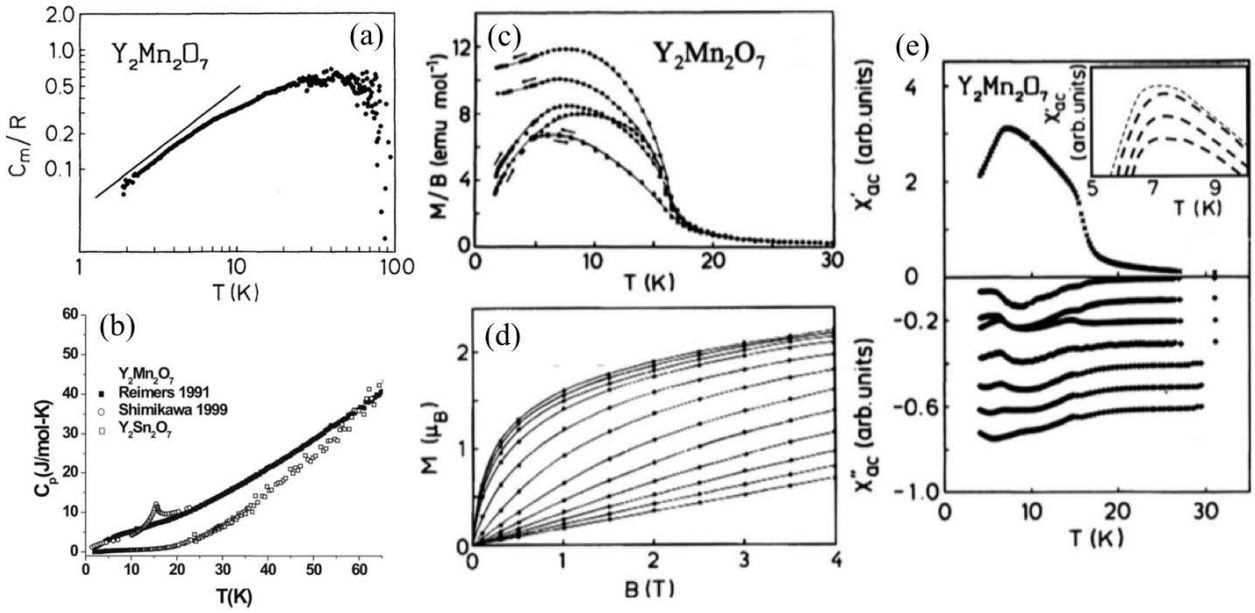

Figure 1.11: Heat capacity data measured by Reimers *et al* [33] (a) and Shimakwa *et al* [34] (b). (c) ZFC and FC magnetization versus temperature curves at B = 0.15 mT (circle), 0.56 mT(square) and 10 mT (triangle) [33]. (d) Magnetization versus magnetic field curves at various temperaures. From top to bottom: 1.8 K, 5 K, 7.5 K, 10 K, 15 K, 20 K, 25 K, 30 K, 35 K, 40 K, 45 K, 50 K [33]. (e) Real and imaginary parts of the ac susceptibility. The inset shows the frequency dependence at low temperatures [33].

To the best of our knowledge, the magnetic structure of $Y_2Mn_2O_7$ is still a mystery. Earlier studies by Reimer *et al* [33] did not show any transition in the heat capacity data. Instead, typical magnetic properties belonging to a SG, e.g. frequency dependence of ac susceptibility, divergence between ZFC and FC curves, were observed (Fig. 1.11). The SG scenario is further supported by small angle neutron scattering measurements (Fig. 1.12) [35]. In addition to the Lorentzian term which describes the conventional ferromagnetic spin-spin correlations, a Lorentzian-squared term is required to fit the neutron intensity as a function of scattering vector Q

$$I(Q) = \frac{A}{(Q^2 + 1/\xi_1^2)} + \frac{B}{(Q^2 + 1/\xi_2^2)^2}, \tag{1.50}$$

where the second term is used to characterize the random field in the sample [35]. From the temperature dependence of ξ_1 in Fig. 1.12, it is clear that true long range ferromagnetic order is never reached [35].

Since rare earth manganese pyrochlores cannot be grown at ambient pressure, these compounds must be synthesized using high pressure methods [15]. Another explanation for the earlier observations is poor sample quality. This would also explain the low saturation moment measured in high magnetic field on those samples. Although it should be $3\,\mu_B$/Mn assuming the orbital moment is quenched, only $2\,\mu_B$/Mn was reached at $B = 4\,\mathrm{T}$. In fact, weak ferromagnetism was observed in the neutron powder diffraction patterns at 7 K, which apparently contradicts the SG scenario [33]. Much better samples were produced by Shimakawa *et al* [34], who have observed a λ-shape peak in the heat capacity measurements as well as $3\,\mu_B$/Mn saturation moment at much lower field $B = 2\,\mathrm{T}$ (Fig. 1.11b). Unfortunately, there has been no subsequent work on these improved samples since then.

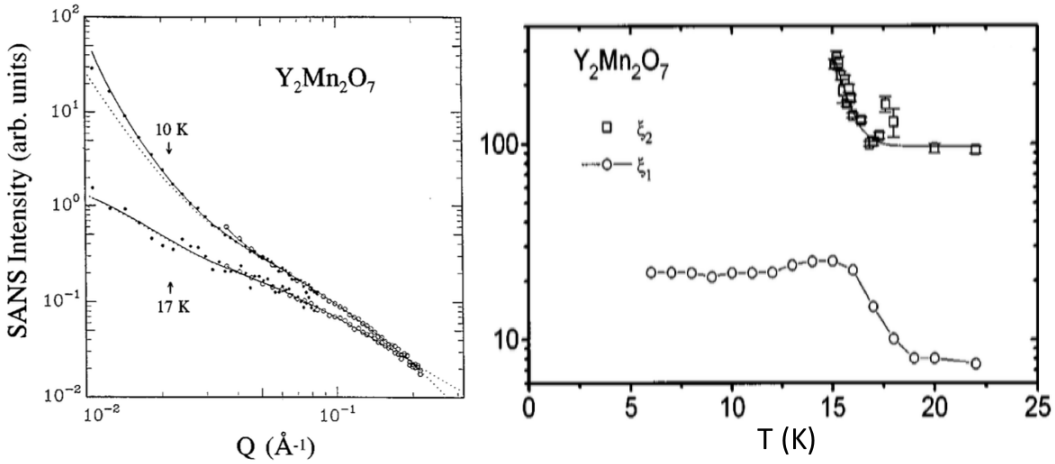

Figure 1.12: Small angle neutron scattering measurements on $Y_2Mn_2O_7$ [35]. (Left) Neutron intensity versus scattering vector Q at different temperatures (solids). The solid and dotted lines are the numerical fits using eq. 1.50 with and without the instrumental resolution function. (Right) Temperature dependences of the two types of magnetic correlation length, ξ_1 and ξ_2.

1.4 Phase separation

The ground states of some systems tend to be intrinsically inhomogeneous due to the competition of multiple interactions. This phenomenon is commonly described as 'phase separation'. In this section, we will introduce two types of phase separation compounds: (I) $Ca_3Co_2O_6$ in which the phase separation is related to the competing magnetic interactions, and (II) manganese perovskites in which the phase separation involves nonmagnetic interactions, and spans from atomic to micrometre scales. In Chapter 3, we will present another

compound, γ-CoV_2O_6, in which the phase separation is also of magnetic origin. Unlike $Ca_3Co_2O_6$ which shows a dynamic phase separation effect, the phase separation of γ-CoV_2O_6 is static. In Chapter 4, we will demonstrate how the phase separation in a strained manganese perovskite is coupled with the carrier transport and magnetic order by varying the magnetic field.

1.4.1 Dynamic phase separation in $Ca_3Co_2O_6$

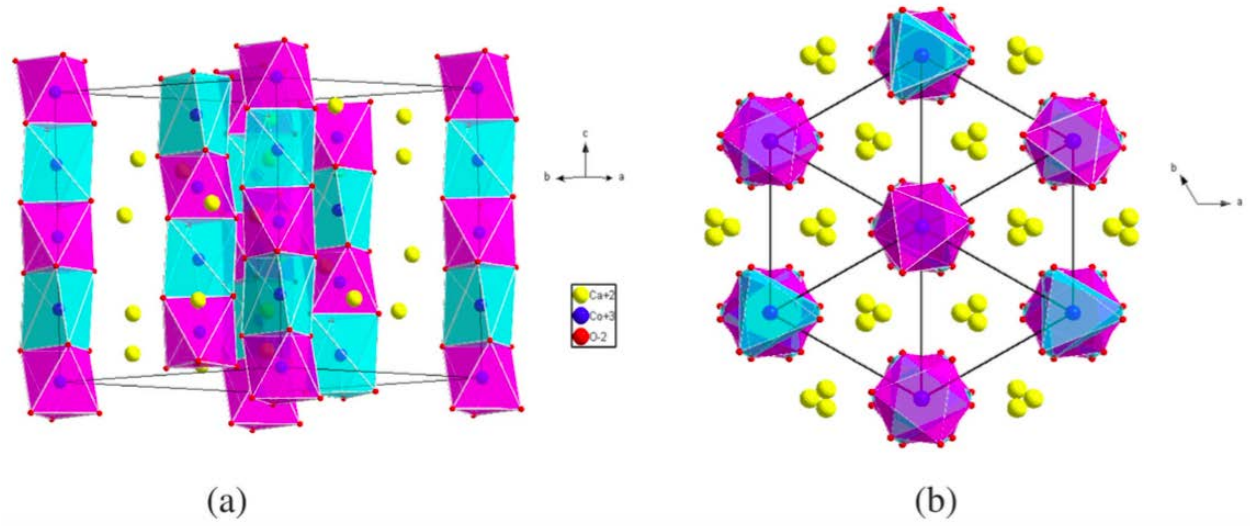

Figure 1.13: (a) Crystallographic structure of $Ca_3Co_2O_6$ [36]. (b) The triangular Co sublattice in the *ab*-plane [36].

$Ca_3Co_2O_6$ consists of face-sharing Co(I)O_6 octahedra and Co(II)O_6 trigonal prisms alternately running along the crystallographic *c*-axis (Fig. 1.13a). In the *ab*-plane, the Co ions form triangular units, allowing geometric frustration (Fig. 1.13b). Since the nearest neighbour (NN) interchain Co-Co distance (5.2 Å) is much larger than the NN intrachain Co-Co distance (2.6 Å) [37], the dominant spin exchange interaction is within the Co chain. At low temperatures, earlier neutron powder diffraction measurements carried out by Aasland *et al* revealed a ferrimagnetic state formed by the low spin ($S=0$) Co(1) sites and the high spin ($S=2$) Co(II) sites [37]. The Ising anisotropy along the *c*-axis is related to the strong crystal field effect [38].

More interest was triggered in this material on the recent discovery of the long wavelength intrachain spin density wave (SDW) phase below $T_c \simeq 25$ K [39]. In an intermediate temperature region, a slow order-order transition to a commensurate antiferromagnetic (CAFM) phase is observed [40] (Fig. 1.14a-b). Since the

thermal equilibrium is never realized within the measuring time [40, 41], it is essentially a dynamic phase separation effect in $Ca_3Co_2O_6$. The magnetic structure in this intermediate region is further complicated by the observation of ferrimagnetic microphases using the small angle neutron scattering technique [42] (Fig. 1.14c).

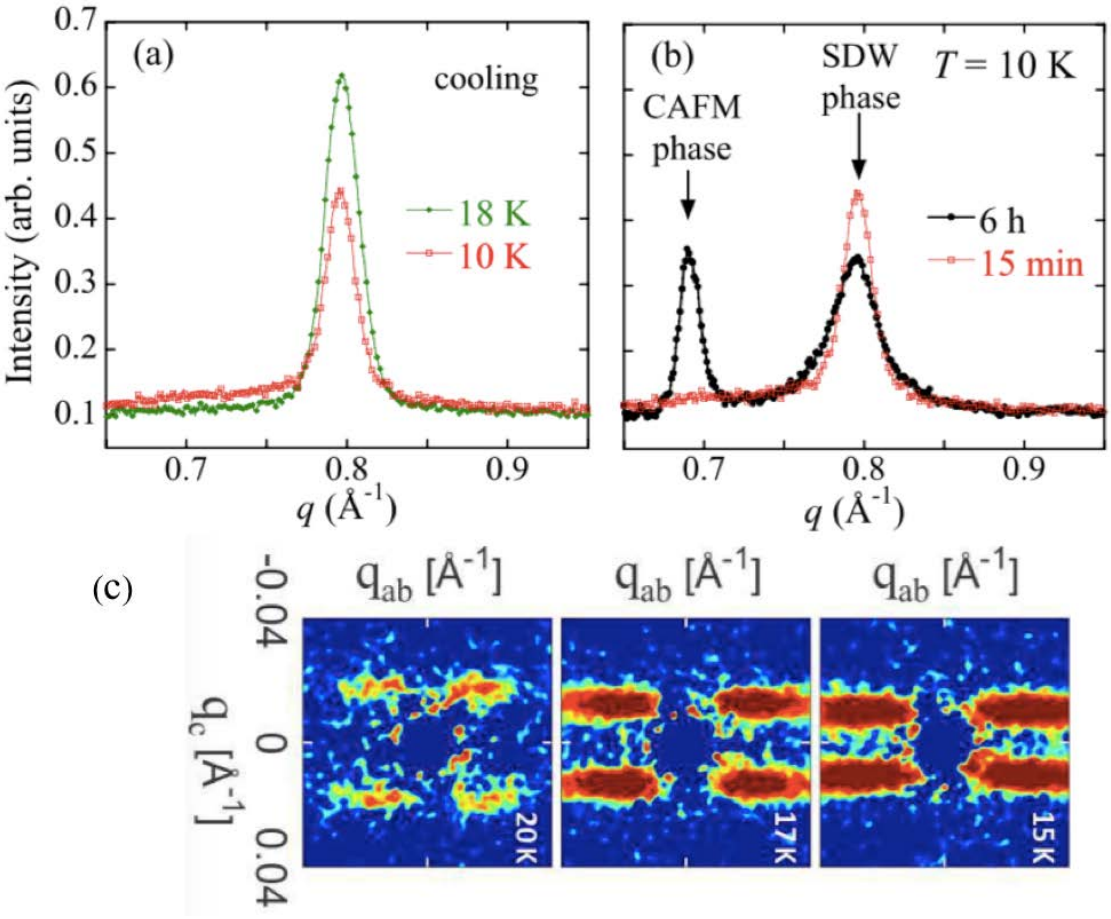

Figure 1.14: (a) -(b) Dynamic phase separation in $Ca_3Co_2O_6$ measured by neutron powder diffraction. An new peak belong to the CAFM phase gradually develops in 6 h of counting time at 10 K [40]. (c) Small angle neutron scattering patterns at different temperatures. The instrumental resolution limited peaks along the q_c are the first reflections of the SDW phase [39]. The broad steaks along q_{ab} are linked to the ferrimagnetic microphase [42].

Most of the measured magnetic properties in $Ca_3Co_2O_6$ have been quantitatively understood by the model proposed in Ref. [43]

$$\mathcal{H} = \sum_{i,j} J_{ij}\sigma_i^z\sigma_j^z - H\sum_i \sigma_i^z - \Gamma\sum_i \sigma_i^x, \tag{1.51}$$

where $J_{ij} = J_1, J_2$ and J_3 stand for the NN intrachain exchange, NN interchain exchange and next NN

interchain exchange constants, respectively. This model was solved by quantum Monte Carlo simulations [43]. A mean field approach has also been adopted to find the spin modulation. The result is an up-up-down ferrimagnetic state in the *ab*-plane triangular lattice at the lowest temperatures. However, they also locate an incommensurate SDW phase in an internediate region. Since the propagation vector of this SDW is temperature dependent, they argue the very slow dynamics in $Ca_3Co_2O_6$ is related to these metastable phases. By adding weak long range exchange coupling which is not included in that model, the SDW phase may be further stablized, as observed in $Ca_3Co_2O_6$ [43, 39].

1.4.2 Mixed-valence perovskite manganites

Structure

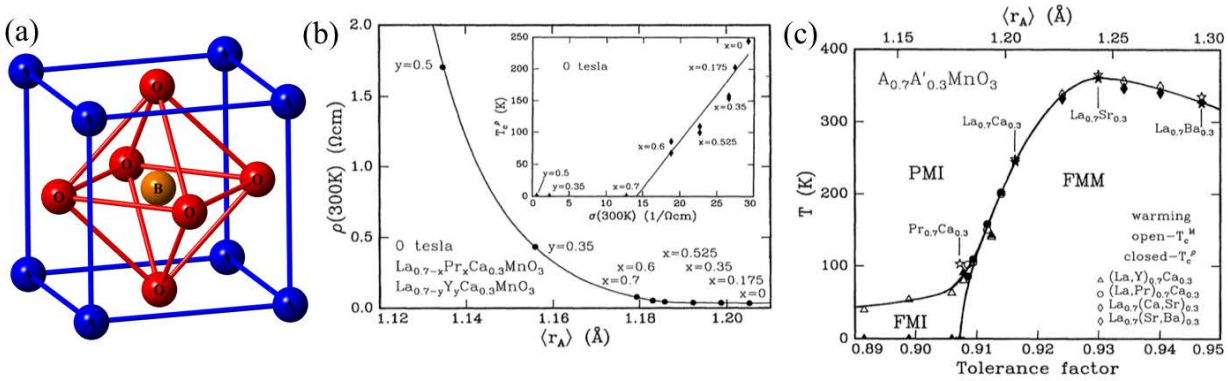

Figure 1.15: (a) Basic structure of a cubic perovskite with chemical fomula ABO_3. (b) Resistance at 300 K ($\rho(300K)$) as a function of $\bar{r}_A$ (inset) Curie temperature obtained from ρ versus temperature curve as a function of $\rho(300K)$ [44]. (c) The 'universal' phase diagram defined by the tolerence factor [44].

The basic cubic perovskite (ABO_3) structure is displayed in Fig. 1.15a. In the mixed-valence manganites discussed below, e.g. $La_{1-x}Ca_xMnO_3$ and $Pr_{1-x}Ca_xMnO_3$, this cubic symmetry is broken so that an orthorhombic lattice with space group *Pnma* ($a \sim c \sim \sqrt{2}b$) is formed. As a result, the 6 equivalent oxygen positions in the MnO_6-octahedron split into two groups: $2 \times O(1)$ and $4 \times O(2)$ [45]. In the *Pnma* setup, MnO(2) bonds are mostly in the *ac*-plane, while the two MnO(1) bonds are mainly along the *b*-axis.

The Mn^{4+}/Mn^{3+} charge separation in perovskite manganites are often realized by substituting rare earth ions (RE^{3+}) on the A-sites with alkali metal ions (A^{2+}) [10]. Due to the ionic size mismatch between RE^{3+}

and A^{2+}, different levels of substitution will apply different internal stresses to the Mn-O-Mn bonds. Since the effective electron hopping amplitude is very sensitive to the Mn-O-Mn bonds, the average ionic radius of the A site ($\bar{r}_A$) plays an important role on the carrier transport properties in $RE_{1-x}A_xO_3$ (Fig. 1.15b) [44]. Most of all, it is found that a 'universal' phase diagram, which does not rely on the type(s) of ions occupying the A-sites, can be produced by defining a 'tolerance factor', $t = d_{A-O}/\sqrt{2}d_{Mn-O}$ (Fig. 1.15c) [44].

Besides the static distortion caused by A-site substitution, the other type of structural distortion in perovskite manganites is the dynamic Jahn-Teller distortion which couples the lattice and electron together as discussed in Sec. 1.2.6 [10, 46]. As to be discussed later, this effect is the key to understand the insulator state in relevant systems [46, 47].

Colossal magnetoresistance effect

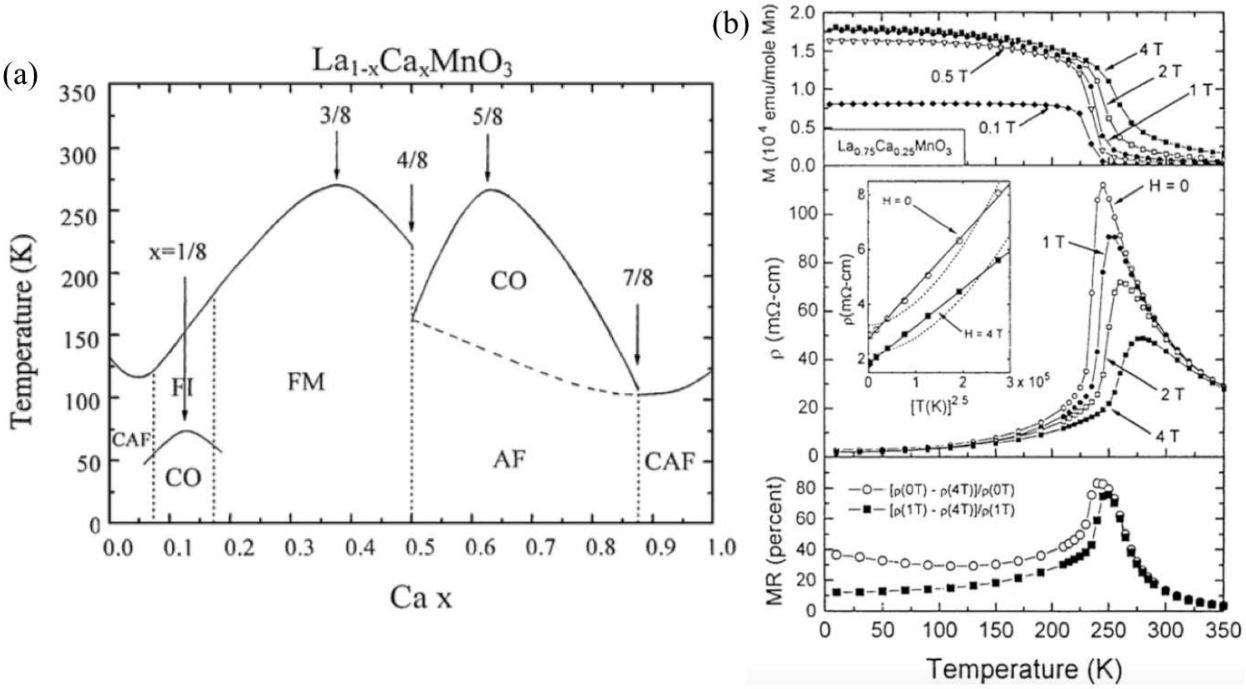

Figure 1.16: (a) Phase diagram of $La_{1-x}Ca_xMnO_3$ [2], with CAF = canted antiferromagnetism, CO = charge order, FI = ferromagnetic insulator, FM = ferromagnetic metal and AF = antiferromagnetism. (b) Magnetization, resistance and magnetoresistance as a function of temperature when x = 0.25 [2].

The colossal magnetoresistance (CMR) effect, a drastic drop in resistance by applying a magnetic field, is one of the most spectacular discoveries in mixed-valence manganese oxides [48]. The CMR effect exist in a wide range of materials possessing strong electron-phonon coupling [10]. For example, $La_{1-x}Ca_xMnO_3$ ($0.2 \leqslant x \leqslant 0.5$) shows a metal-like state below the ferromagnetic Curie temperature (T_C) due to the prevailing double exchange interactions between spins (Fig. 1.16a). By varying the temperature, a metal-insulator transition is observed concomitant with the ferromagnetic-paramagnetic transition at T_C. Surprisingly, the CMR effect also occurs in a narrow region around T_C (Fig. 1.16b).

Another interesting family of CMR compounds, e.g. $Pr_{1-x}Ca_xMnO_3$ ($0.3 \leqslant x \leqslant 0.5$), does not develop ferromagnetism at low temperatures (Fig. 1.17a) [49]. Instead, these systems are insulators in the entire temperature region and have an antiferromagnetic ground state [50]. Unlike $La_{1-x}Ca_xMnO_3$ ($0.2 \leqslant x \leqslant 0.5$) where CMR only exists in a narrow region close to T_C, CMR can be observed from the lowest temperature probed (4.2 K) and persists deeply into the paramagnetic region (Fig. 1.17b) [51]. Interestingly, the insulating state cannot be recovered after removing the magnetic field at low temperatures.

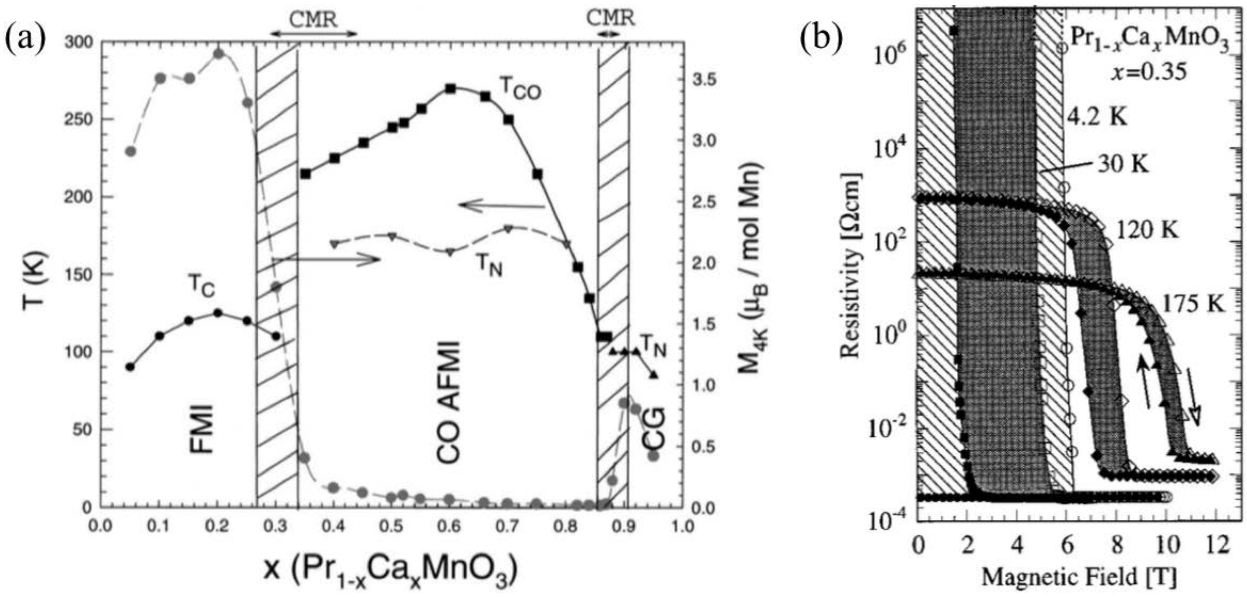

Figure 1.17: (a) Phase diagram of $Pr_{1-x}Ca_xMnO_3$, with FMI = ferromagnetic insulator, CO = charge order, AFMI = antiferromagnetic insulator and CG = cluster glass [49]. (b) Resistivity as a function of magnetic field at various temperatures when x = 0.35 [51].

Spin, charge and orbital order

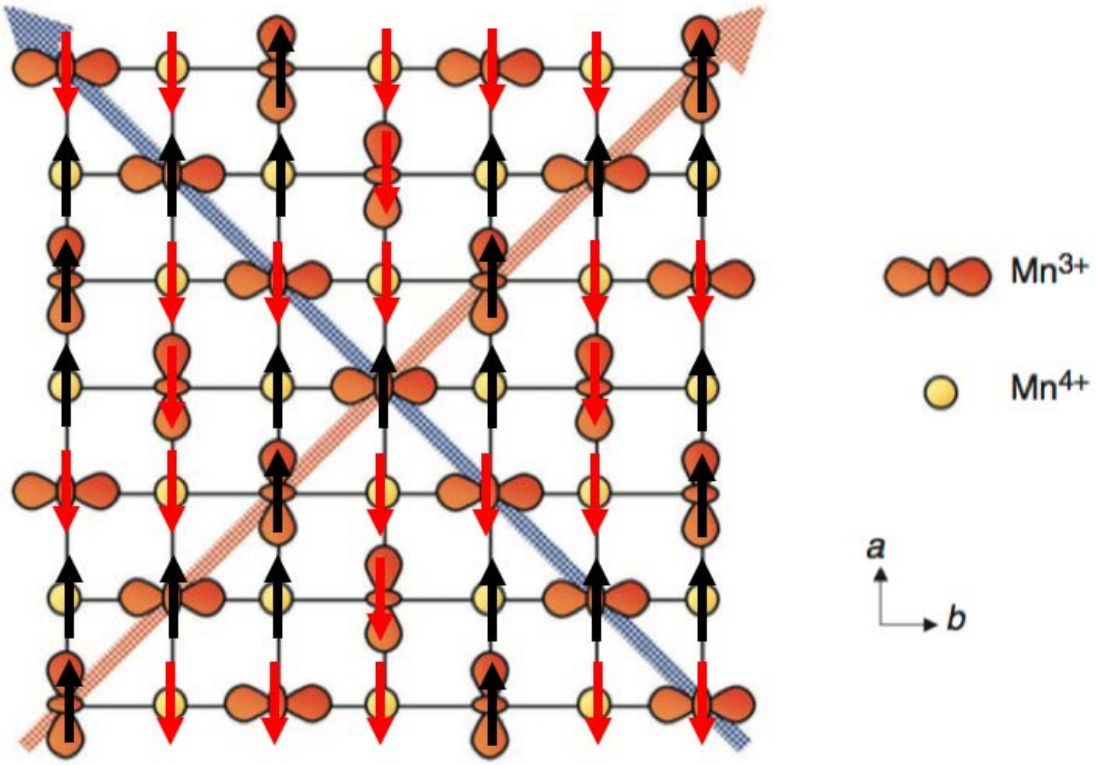

Figure 1.18: $d_{3x^2-r^2}/d_{3y^2-r^2}$ orbital order under *Pbcm* space group ($a \simeq b \simeq \sqrt{2}c$) setup [52]. The orbital orientations of the Mn^{3+} ions are marked by the lobes. The black and red arrows show the spin arrangement in the $z = 0$ plane. The spins in the $z = 1/2$ plane are reversed (unchanged) for the CE (pseudo-CE) type antiferromagnetic order [50].

The magnetic order in CMR manganites couples tightly to the charge and orbital degrees of freedom [2]. Fig. 1.18 shows the $d_{3x^2-r^2}/d_{3y^2-r^2}$ orbital order which is commonly observed in $Pr_{1-x}Ca_xMnO_3$ ($x \geqslant 0.3$) [52]. Since only Mn^{3+} has an occupied e_g orbital, orbital order is often accompanied by some sort of charge order. The antiferromagnetic spin arrangement of $Pr_{1-x}Ca_xMnO_3$ in the *ab*-plane (space group *Pbcm*, $a \simeq b \simeq \sqrt{2}c$) has also been shown in Fig. 1.18. And it is called charge-exchange (CE) or pseudo-CE type antiferromagnetism, in which the spins in the *ab*-plane couple antiferromagnetically or ferromagnetically along the *c*-axis [50].

Electronic phase separation and colossal magnetoresistance

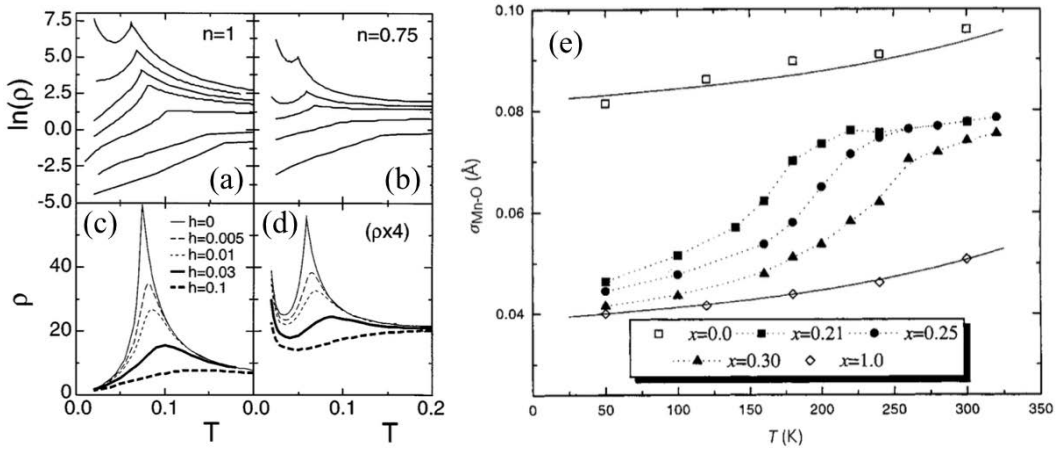

Figure 1.19: (a)-(b) Resistivity versus temperature curves under different electron-phonon coupling strengths λ with fixed n. Details of the density parameter n can be found in Ref. [47]. (c)-(d) Resistivity versus temperature curves at various magnetic fields with fixed n [47]. (e) Temperature dependence of the standard deviation of Mn-O bond lengths in $La_{1-x}Ca_xMnO_3$ measured by Booth *et al.* [53]. Clear softening of the distortion is observed below T_C.

Various models have been proposed to explain the electronic phase separation (e.g. polarons, charge order) in mixed-valence manganese oxides [10, 54]. Here we will follow the treatments carried out by Millis *et al* where the electron-phonon coupling is through the dynamic Jahn-Teller distortion [47]. First of all, we define an effective Hamiltonian

$$\hat{H}_{eff} = \hat{H}_{kin} + \hat{H}_{Hund} + \hat{H}_{el-ph} + \hat{H}_{Zeeman}. \tag{1.52}$$

These terms represent the kinetic energy (eq. 1.30), Hund's intraband coupling (eq. 1.33), electron-phonon coupling (eq. 1.48), and Zeeman energy (eq. 1.11), respectively. They have solved $\hat{H}_{eff}$ by assuming $\hat{H}_{Hund} \to \infty$. When the electron-phonon coupling strength (characterized by $\lambda = g/\sqrt{k_{JT}t}$ (t in eq. 1.48) is strong enough, a gap in the electron spectral function, corresponding to the formation of polarons, only opens above T_C (Fig. 1.19a & 1.19b). Most of all, the CMR effect can be reproduced by tuning the magnetic field in $\hat{H}_{Zeeman}$ (Fig. 1.19c & 1.19d). The existence of a Jahn-Teller distortion in the CMR temperature region, e.g. above T_C in $La_{1-x}Ca_xMnO_3$ ($0.2 \leqslant x \leqslant 0.5$), has been confirmed using local probe techniques such as PDF and EXAFS [53, 55, 46](Fig. 1.19e). Since not all of the Mn ions are Jahn-Teller active, the dynamic Jahn-Teller distortion will lead to inhomogeneities on the atomic scales, i.e. electronic phase separation [10]. The

collapse of electronic phase separation has been proposed as the driving mechanism of CMR and received overwhelming evidence experimentally [56, 57, 58].

Micrometre phase separation and colossal magnetoresistance

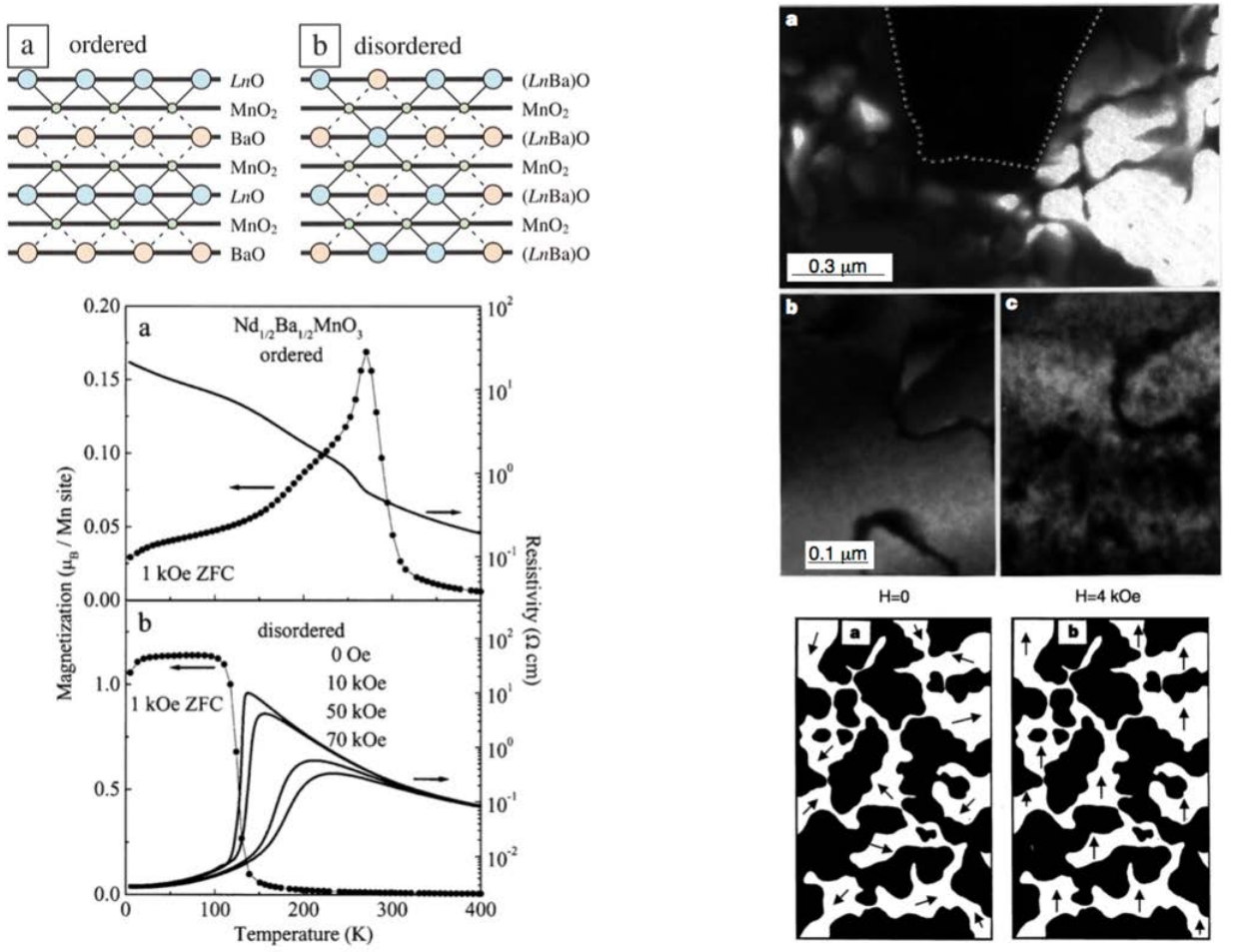

Figure 1.20: (Top-left) Schematic view of the $Ln_{0.5}Ba_{0.5}MnO_3$ lattice in the *ac*-plane, where the *a*-axis is horizontal [59]. (Bottom-left) Magnetization and resisitivity of the two end compounds as a function of temperature [59]. (Top-right) Dark field images of $La_{5/8-y}Pr_yCa_{3/8}MnO_3$ [60]. The charge disordered ferromagnetic area is dark. (a) y = 0.375 and T = 20 K (ferromagnetic). (b) y = 0.4 and T = 17 K (ferromagnetic). (c) y = 0.4 and T = 120 K (Paramagnetic). (Bottom-right) Schematic show of the percolation process as a function of magnetic field [60].

The other type of phase separation, namely micrometre phase separation, comes from quenched disorder in manganese oxides. The two end configurations of the *bc*-plane lattice structure of $Ln_{0.5}Ba_{0.5}MnO_3$ are shown in Fig. 1.20. While the most ordered state corresponds to the A-site chain along the *b*-axis alternatively occupied by Ln and Ba ions, the least ordered state is made of both ions randomly distributing on these sites. Distinct magnetic and electric transport properties are observed in these two configurations with identical bulk chemical formulae, stressing the role of disorder [59]. Since quenched disorder is often inevitable in these systems, it is necessary to include it to explain some experimental observations. Beside the electronic phase separation on the atomic scales, a second phase separation phenomenon on much larger scales has been observed (Fig. 1.20) [60, 61]. In relevant systems dominated by disorder, CMR is also associated with the percolation of the ferromagnetic conducting paths (Fig. 1.20) [60, 61, 2].

CHAPTER 2

EXPERIMENTAL TECHNIQUES

2.1 Sample synthesis

Several polycrystalline samples were prepared for this thesis using the ceramic method [62]. The detailed synthesis procedures are provided in the corresponding chapters. In general, this method contains the following steps:

1. High purity raw metal oxides in the correct stoichiometric proportions are ground together using an agate pestle and mortar.

2. The resulting homogeneous mixture is then pressed into a pellet by applying hydrostatic pressure in order to reduce the empty space between particles.

3. The pellet is heated in a furnace to trigger the solid state reaction.

A solid state reaction is realized by the diffusion of ions in the raw mixture. Since these ions need sufficient energy to break and reform chemical bonds as well as migrate over long atomic distances, these reactions are slow and require high temperatures [62].

2.2 Scattering techniques

The majority of the experimental work discussed in this thesis was done using a variety of scattering techniques, described below. First, however, we look at some basic concepts in scattering theory.

2.2.1 Basic scattering theory

As a beam of particles characterized by the wavevector $\vec{k}_i$ hits a target, those particles will be scattered to form a certain distribution in space and time (Fig. 2.1). Such a distribution can be described in terms of a quantity known as the cross-section (σ). We can set up a detector a distance D from the target to measure the number of particles scattered in a given direction (θ, ϕ) and energy (E). If $D \gg$ the dimensions of the detector and the target, we can define the partial differential cross-section $\frac{d^2\sigma}{d\Omega\, dE}$, where the solid angle $\mathrm{d}\Omega = \sin\theta \mathrm{d}\theta \mathrm{d}\phi$ [63]. If the scattering process is elastic ($|\vec{k}_i| = |\vec{k}_f|$ in Fig. 2.1), we will be only measuring the differential cross-section $\frac{d\sigma}{d\Omega}$; this quantity is the focus in this thesis.

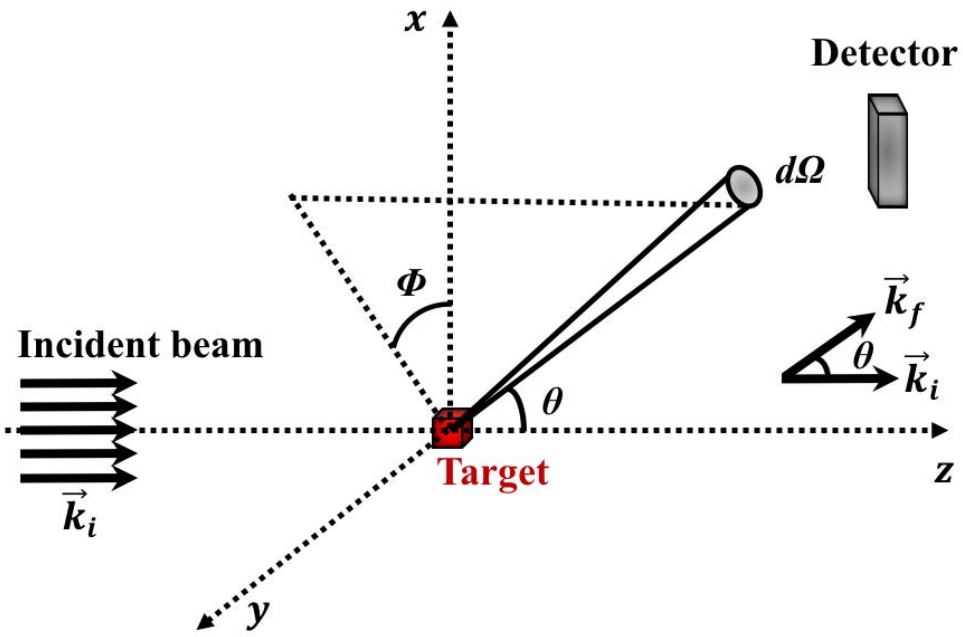

Figure 2.1: Geometry for a scattering process.

In a typical neutron (X-ray) scattering process, the wavelength ($\sim 10^{-10}$ m) of the incident particles is much larger than the effective range ($\sim 10^{-14}$ m) of the interaction between the particle and target. As a result, the scattered wave is independent of ϕ [63]. If the scattering process only involves a single target with fixed position, the scattered wavefunction at the point of r may be written as

$$\psi_f = \frac{f(\theta, \lambda)}{r} exp(ikr). \tag{2.1}$$

In reality, we are measuring a crystal consisting of a large number of atoms occupying crystallographic sites

labelled as R_j (j = 1, 2...). Eq. 2.1 therefore needs to be modified to

$$\psi_f = exp(i\vec{k}_f \cdot \vec{r}) \sum_j f_j(\theta, \lambda) \frac{exp(i\vec{Q} \cdot \vec{R}_j)}{|\vec{r} - \vec{R}_j|}, \tag{2.2}$$

where $\vec{Q} = \vec{k}_i - \vec{k}_f$. When counting the number of of neutrons $N(\theta, \lambda)$ with wavelength λ scattered in the direction of θ, the distance between the detector and target (r) is always much larger than the size of the sample. This means we can use the approximation $|\vec{r} - \vec{R}_j| = r$. $N(\theta, \lambda)$ deflected into a small area δS of the detector is then related to $|\psi_f|^2$ by

$$N(\theta, \lambda) \propto \delta S \Big| \sum_j f_j(\theta, \lambda) \frac{exp(i\vec{Q} \cdot \vec{R}_j)}{r} \Big|^2 = \delta\Omega |F_{hkl}|^2, \tag{2.3}$$

where *hkl* are the Miller indices and F_{hkl} is the structure factor. If the system contains a large number of crystals with random orientations, i.e. in a powder form, the measured intensity can be expressed as [64, 63, 65]

$$I = I_0 r_e^2 \frac{1 + cos^2 2\theta}{2} \frac{1}{16\pi\, rL} \lambda^3 |F_{hkl}|^2 n \frac{1}{V_c^2} D V_p, \tag{2.4}$$

where I_0 is the intensity per unit area of the incident beam, $r_e^2 = 7.9 \times 10^{-26}\,\mathrm{cm}^2$ (r_e is called the *Thomson* scattering length), $\frac{1 + cos^2 2\theta}{2}$ is the polarization factor, L is the Lorentz factor which depends on the experimental configuration, n is the multiplicity of the *hkl*-lattice plane, V_c is the volume of a unit cell, D is the temperature (Debye-Waller) factor and V_p is the total volume of the powder. A detailed discussion on these parameters can be found in Ref. [64, 63, 65]

2.2.2 X-ray powder diffraction

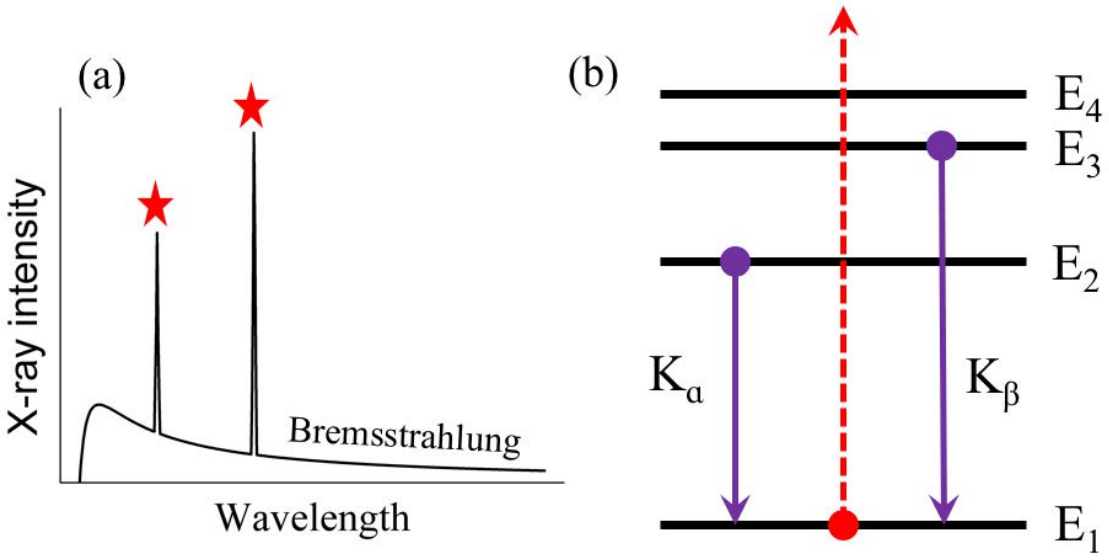

Figure 2.2: (a) Distribution of X-ray emission intensity as a function of wavelength. The broad background with a lower limit is Bremsstrahlung. The sharp peaks are from the relaxation process. (b) Typical relaxation processes (purple solid line) after the electron in the K-shell (E_1) is emitted (red dotted line).

The X-ray powder diffraction (XRPD) technique was used to characterize the crystallographic structure of our sample in a Bruker D8 Advance diffractometer. Lab-based X-rays are generated by bombarding a metal target with electron beams accelerated in an electric field. We can estimate the wavelength (λ) of the generated X-rays by combining the energy conservation rule, Planck's energy−frequency relation and de Broglie wavelength equation:

$$\lambda \geqslant \frac{hc}{eU} \approx \frac{1.24 \times 10^4}{U} \text{Å}, \tag{2.5}$$

where h, c, e, U are the Planck constant, speed of light, charge of electron and voltage, respectively. As a result, X-rays with wavelength on atomic scales ($\sim$ a few Å) can be generated by applying an appropriate voltage of around 10 kV [64].

A copper (Cu) target was used in our experiments. A more accurate description of the radiation process after the target is struck by electrons consists of two parts (Fig. 2.2a). The first part is called Bremsstrahlung which is responsible for a broad distribution of wavelength with a lower limit determined by eq. 2.1. The second part generates the particular wavelengths used in a typical diffraction measurement. When the incoming electrons strike the Cu target, an electron in a specific shell ($n = i$) is excited to a higher and

unoccupied state, leaving this shell empty. This is followed by the relaxation of another electron from a higher energy shell ($n = j,\ j > i$) to this low energy and empty shell ($n = i$), as well as the emission of a photon with a wavelength

$$\lambda_{ij} = \frac{hc}{E_j - E_i}, \tag{2.6}$$

where E_i and E_j are the energies of the denoted shells (Fig. 2.2b). The strongest emission is K_α, corresponding to $i = 1$ and $j = 2$. In practice, a filter or a crystal monochromator is used to remove the unwanted wavelengths. We have used a curved germanium crystal monochromator to select only the Cu $K_{\alpha 1}$ line ($\lambda = 1.5406$ Å).

For the crystallographic structure determination, it is very important to understand the term $f(\theta,\ \lambda)$ which is called the atomic form factor (eq. 2.1 - eq. 2.4). In a X-ray scattering case, this term can be writen as

$$f\,(\theta, \lambda) = Zg(Q)r_e, \tag{2.7}$$

where Z is the atomic number and $Q = \dfrac{4\pi\ sin\theta}{\lambda}$ is the wavevector transfer in eq. 2.2. Analytical approximations to $g(Q)$ can be found in Ref. [66].

2.2.3 Neutron powder diffraction

Neutron production

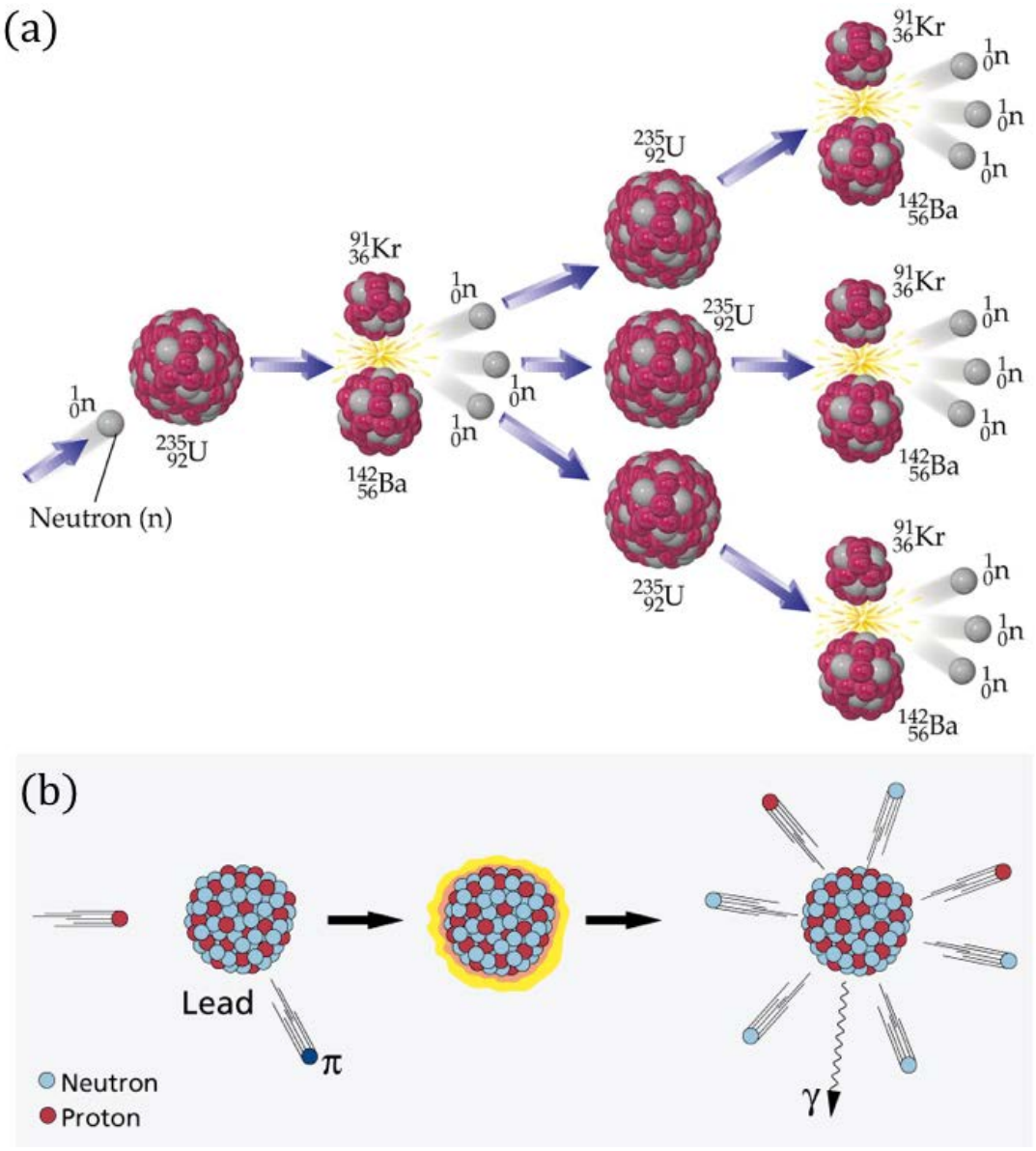

Figure 2.3: Schematic demonstrations of (a) fission [67], and (b) spallation processes [68].

A neutron is composed of one up and two down quarks with charges of 2/3 and -1/3, respectively. Similarly to the X-rays, neutrons can be used for structure determination since the de Broglie wavelength of thermal neutrons is of the same order as the atomic distances in solids. An important advantage of using neutron diffraction is that neutrons are very sensitive to light elements such as hydrogen, whereas these elements

are almost 'transparent' to X-rays (eq. 2.7) [63]. Moreover, the neutron carries a magnetic moment so that they can also interact with unpaired electrons. This makes the neutron diffraction a powerful tool to probe magnetic structure. Neutrons used for scientific purpose in large facilities can be produced by fission and spallation [69].

Typically, a nuclear fission reaction is triggered when a neutron is absorbed by a ^{235}U nucleus. This is followed by a chain of reactions where medium-heavy elements and more neutrons are generated. While some of those neutrons, 1.5 out of 2.5 for each fission in average, are still needed to maintain the chain reaction, other neutrons will leave the fuel with a kinetic energy around 2 MeV (Fig. 2.3a). On the other hand, neutrons can also be produced in a spallation process where a heavy target (e.g. tungsten) is bombarded by high energy protons ($\sim$ 1 GeV). The products include neutrons, pions, muons, neutrinos and so forth (Fig. 2.3b).

The spallation process can be either pulsed or continuous. For example, the ISIS pulsed neutron and muon source at the Rutherford Appleton Laboratory in Oxfordshire of the United Kingdom operates at 50 Hz and produces a pulse of polychromatic neutrons every 20 milliseconds. The Swiss Spallation Neutron Source (SINQ) at Paul Scherrer Institute of Switzerland produces continuous neutrons [69]. The kinetic energy of the neutrons produced by these reactions is on the order of MeV. The corresponding de Broglie wavelength (λ) is estimated to be around 2.86×10^{-4} Å [63]. As a result, additional treatment is required to slow these fast neutrons down. This is realized by injecting them into a moderator filled with light atoms (e.g. H, D, Be). These injected neutrons are scattered inelastically by these light atoms in the moderator and eventually brought into thermal equilibrium described by the Maxwellian distribution

$$\phi(v) \propto v^3 \exp(\frac{1}{2}mv^2/k_BT), \tag{2.8}$$

where v is the velocity of the output neutrons, $\phi(v)\mathrm{d}v$ is the output neutron flux density between v and $v + \mathrm{d}v$, m is the neutron mass, T is the temperature of the moderator and k_B is the Boltzmann constant [63].

Diffractometers

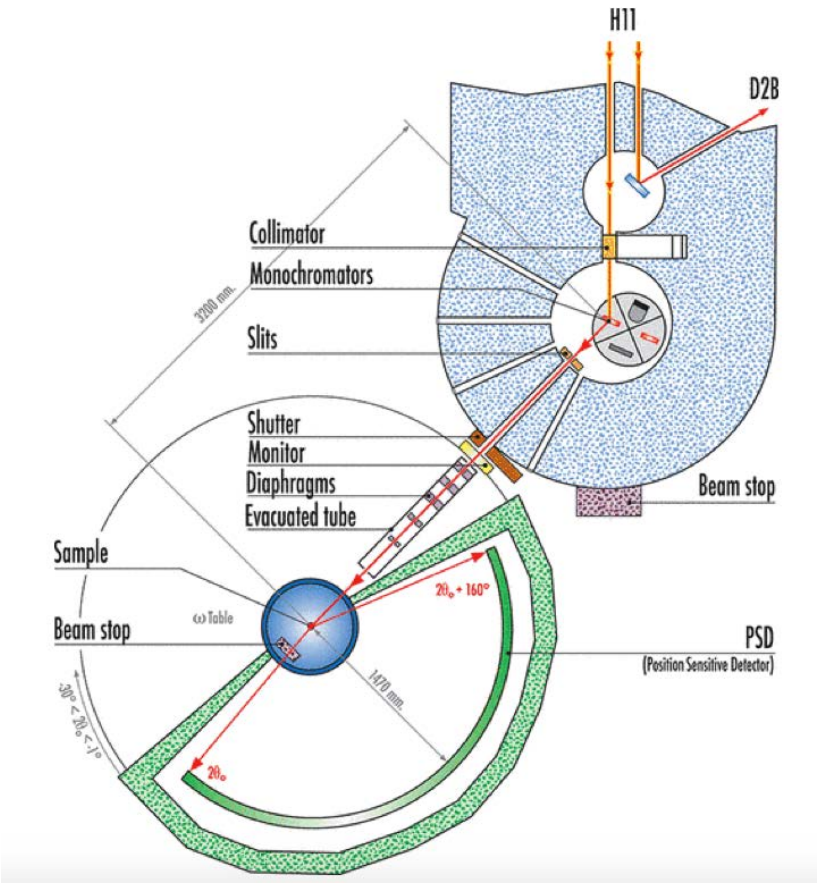

Figure 2.4: Experimental setup of the D20 2-axis diffractometer at ILL, France [70].

The Bragg's law, $2d_{hkl}\sin\theta = \lambda$, can be rewriten as $d_{hkl} = \dfrac{\lambda}{2sin\theta}$. As a result, in order to measure the lattice spacing d_{hkl}, one can scan either the scattering angle θ or the incident wavelength λ. In the first case, a monochromator single-crystal is used to create a beam of neutrons with a constant wavelength. The experimental setup of the D20 diffractormeter in the Institut Laue-Langevin (ILL) is illustrated in Fig. 2.4. The second method of measuring d_{hkl}, i.e. scanning λ, is called the time-of-flight (TOF) technique. Typical TOF neutron diffractometers include WISH and HRPD at ISIS, UK. λ is determined by measuring the flying time (t in second) of the neutrons. For example, the 'departure time' of a neutron flight can be controlled by the pulse rate in a spallation neutron source. Then the flying time can be obtained by counting the 'arrival time' on the detectors. Since the total flight path (L in kilometre) is a known parameter, λ in Å can be

obtained by [63]

$$\lambda = 3.956\frac{t}{L}. \tag{2.9}$$

Nuclear scattering length *b*

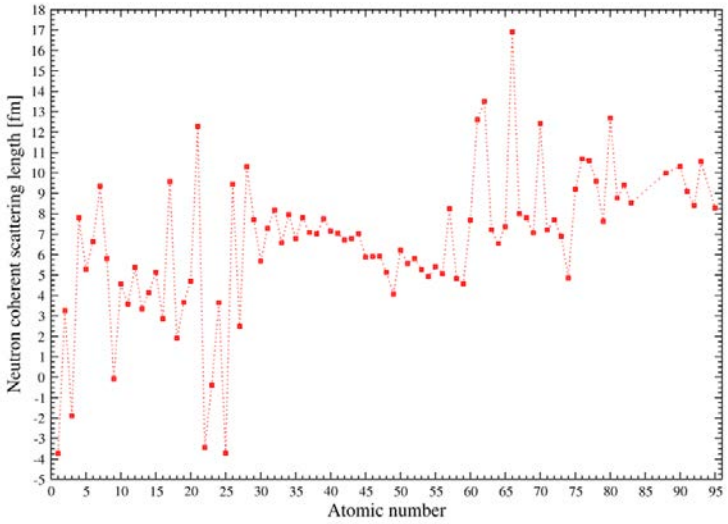

Figure 2.5: Coherent nuclear scattering length b as a function of atomic number Z [71].

In most neutron scattering processes which do not involve magnetic interactions, $f(\theta, \lambda)$ in eq. 2.1 - eq. 2.4 can be replaced by a simple constant -b called 'scattering length' (Fig. 2.5). Compared with the atomic form factor in the X-ray scattering case, the scattering length -b [64]

1. is invariant with respect to θ and λ.
2. is isotope sensitive.
3. has two different values for nuclei with a non-zero spin.
4. does not vary with atomic number Z in a trivial or monotonic way.

Magnetic form factor

As mentioned above, neutrons also carry a magnetic dipole moment which can interact with the magnetic field produced by the unpaired electrons. When a neutron is scattered with a wavevector $\vec{Q} = \vec{k}_i - \vec{k}_f$, it is only sensitive to the magnetic moment ($\vec{M}$) perpendicular to $\vec{Q}$: $M_\perp = \vec{M} - (\vec{M} \cdot \vec{Q})\vec{Q}$ [63, 64]. The magnetic

differential cross-section can be writen as

$$\left(\frac{d\sigma}{d\Omega}\right)_m \propto |F_m(Q)|^2 \sum_{\alpha,\,\beta}(\delta_{\alpha\beta} - \vec{Q}_\alpha \vec{Q}_\beta) \times \sum_R \exp(-i\vec{Q}\cdot\vec{R}) < M_0^\alpha >< M_R^\beta >, \tag{2.10}$$

where $\mathrm{F}_m(Q)$ is the magnetic form factor, $\delta_{\alpha\beta}$ is the Kronecker delta, the subscripts α and β denote the projection on the x, y and z axes, and R is the position of the unpaired electron [63].

Considering a magnetic ion has both spin and angular momentum, its magnetic form factor $\mathrm{F}_m(Q)$ can be expressed as

$$g_J F_m(Q) = g_L \frac{J(J+1)+L(L+1)-S(S+1)}{2J(J+1)}\mathcal{F}_0 + g_S \frac{J(J+1)-L(L+1)+S(S+1)}{2J(J+1)}(\mathcal{F}_0+\mathcal{F}_2), \tag{2.11}$$

where the physical meaning of the Landé g-factors can be found in Chapter 1.1.3. The term $\mathcal{F}_n$ is related to the n^{th} order spherical Bessel function $j_n(\vec{Q}\cdot\vec{r})$ and the normalised density of the unpaired electrons $\rho(\vec{r})$ [63]

$$\mathcal{F}_n = 4\pi \int_0^\infty j_n(\vec{Q}\cdot\vec{r})\rho(\vec{r})r^2 \mathrm{d}r. \tag{2.12}$$

It is worth noting that the magnetic form factors are ion-dependent. In practise, $\mathrm{F}_m(Q)$ can be parametrized using an analytical approximation [66].

2.2.4 Small angle neutron scattering

As described by Bragg's law, $d = \dfrac{\lambda}{2sin\theta}$, a structure with reflections at very small angles θ has a very long lattice spacing d, e.g. vortex lattices in superconductors [72]. In general, the small angle neutron scattering (SANS) technique is used to measure the incoherent and coherent structure on large scales, typically between 10 Å and 1000 Å[69, 64, 73]. Fig. 2.6 shows configuration of the state-of-the-art SANS-1 instrument located at the Forschungsreaktor München II (FRM-II), Germany [74]. Before reaching the velocity selector, neutrons have a broad distribution of wavelength (λ)e.g. between 4.5 Å and 30 Å for SANS-1, FRM-II. By rotating the turbine in the velocity selector at a given frequency, only neutrons with the selected wavelength are able to pass. In reality, these selected neutrons still have a distribution of wavelengths ($\Delta\lambda/\lambda \sim 10\,\%$). To control the angular divergence of the neutron beam that comes out from the velocity selector, these neutrons are sent through a collimation chamber, the inner walls of which are made of strong neutron absorbers. The collimated neutrons are then scattered by the sample and measured on the large 2-dimensional detector in the high vacuum detector tank. Since the detector unit has a fixed size, the scattering angle (θ in eq. 2.1)

being measured only depends on the distance between the detector and the sample. Besides these common features, a SANS instrument in a reactor source can also perform TOF type measurements by using a chopper disk setup (Fig. 2.6).

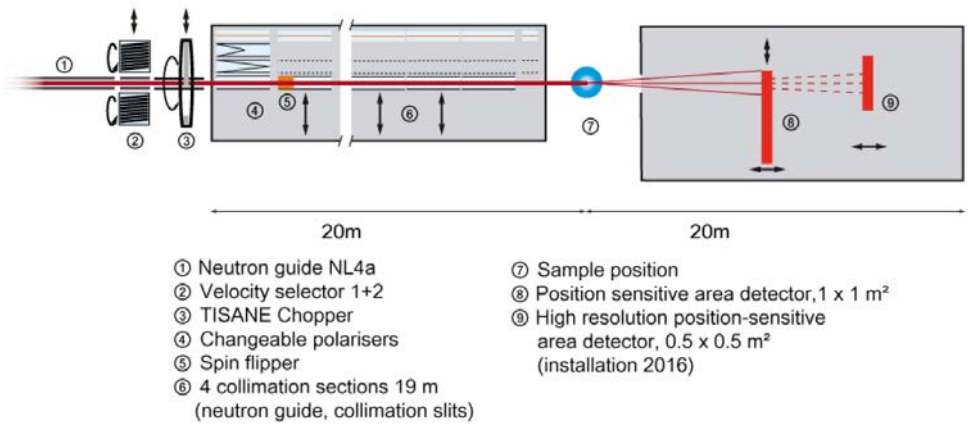

Figure 2.6: The SANS-1 instrument at FRM-II, Germany [75].

The SANS process can be described by the general scattering theory discussed in Chapter 2.2. As a result, the scattering intensity I(Q), where Q is the amplitude of the wavevector transfer $Q = \frac{4\pi sin\theta}{\lambda}$ is proportional to the square of the structure factor $|F_Q|^2$. According to Ref. [73], the term f(θ, λ) in F(Q) (eq. 2.3) can be replaced by a density function $\rho(R_j)$, where j labels the position of an individual scatterer, and the summation is replaced by an integral:

$$I(Q) = \int_{V_1}\int_{V_2} \rho(R_1)\rho(R_2)e^{-iQ(R_1 - R_2)}\mathrm{d}V_1\mathrm{d}V_2. \tag{2.13}$$

The integration can be carried out in two steps: (1) over all pairs with equal distance $|r| = |\vec{R}_1 - \vec{R}_2|$, (2) over all relative distances:

$$I(Q) = \int_V \bar{\rho}^2(r)e^{-iQr}\mathrm{d}V, \tag{2.14}$$

where $\bar{\rho}^2(r) = \int_{V_1} \rho(R_1)\rho(R_2)\mathrm{d}V_1$ can be regarded as the density function of a point in a fictious C-space which represents the pair with relative distance r in the ordinary space [73].

Now we discuss the specific SANS problem which meets the following two restrictions: (a) the scattering target is isotropic, and (b) there is no long range correlation. The first restriction means that the phase term e^{-iQr} in eq. 2.14 can be replaced by its average $< e^{-iQr} > = \frac{sinQr}{Qr}$ [73]. The second restriction indicates

that the density functions of the pair separated widely enough in ordinary space should be independent so that $\bar{\rho}^2(r) \rightarrow$ a constant $V\bar{\rho}^2$ when $r \rightarrow \infty$ [73]. Since this constant term (background) does not contribute to the intensity $I(Q)$ based on eq. 2.14, it is the density fluctuation $\Delta\rho$, also refered as the contrast term, in the finite region that matters in a SANS process [73]. In other words, if the system is homogeneous on the scales investigated by SANS, no relevant information can be probed. This makes the SANS technique an ideal tool to study the phase separation phenomenon discussed in Chapter 1.4 [10].

2.3 Magnetometry

2.3.1 Magnetic Property Measurement System (MPMS)

The MPMS, manufactured by Quantum Design, can be used to measure the magnetization of a material. It includes five principal components [76]:

1), Temperature control system.

2), Magnet control system.

3), Superconducting quantum interference device (SQUID).

4), Sample handling system.

5), Computer operating system.

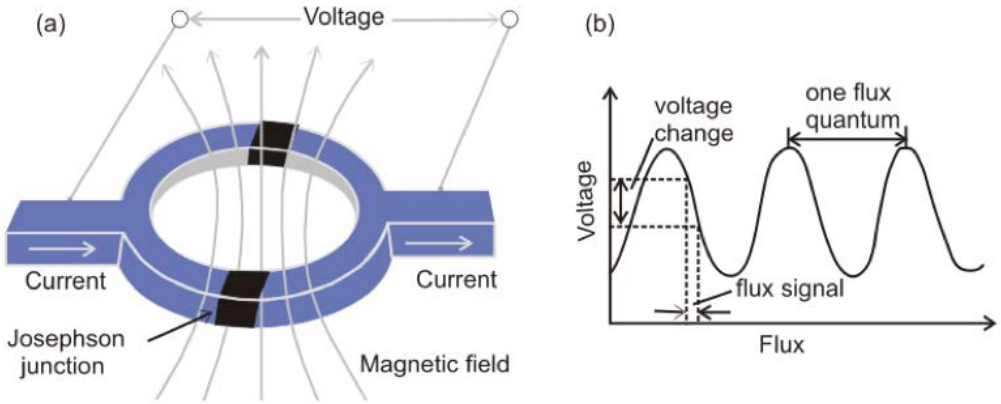

Figure 2.7: (a) A SQUID is formed by two parallel *Josephson* junctions [77]. (b) Working mechanism of the SQUID. Any weak change in the flux signal will be detected in the output voltage channel as well [77].

A SQUID is formed by two superconductors separated by thin insulating layers (Fig. 2.7a). This structure has two parallel Josephson junctions which allow the tunelling of Cooper pairs [78]. Since the SQUID is

able to measure the change of a magnetic field associated with one flux quantum ($< 10^{-14}$ T), it is very sensitive to weak magnetic signals [78]. Compared with other techniques, the SQUID-based magnetometer has particularly high resolution (between 10^{-7} and $^{-8}$ emu) in magnetization measurements [76].

The most important unit in the MPMS is the closed superconducting loop composed of the detection coils, the SQUID and the connecting wires. When a measurement is performed, the sample is moved through the superconducting detection coils located at the center of the magnet. The movement will induce an electric current in the detection coils. Due to the coupling between the SQUID and the detection coils, the induced electric current will lead to a change of the output voltage in the SQUID, which is proportional to the magnetization of the sample (Fig. 2.7b) [76, 78].

Most of our magnetization data were collected using a MPMS-XL with magnetic field range -5.0 T to 5.0 T and temperature range 1.8 K - 350 K, respectively [76].

2.3.2 Vibrating Sample Magnetometer (VSM)

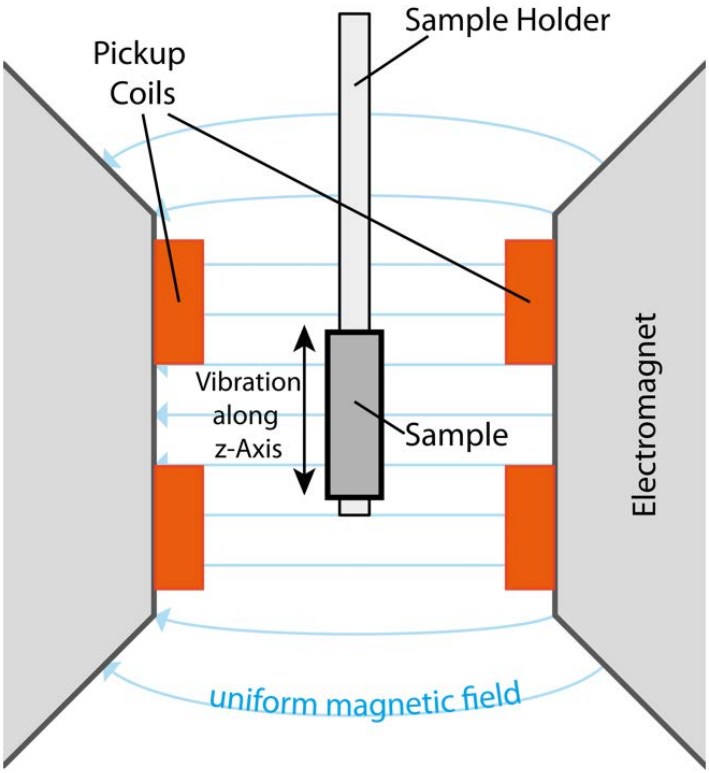

Figure 2.8: Schematic construction of a VSM [79].

VSM is based on Faraday's law: an electromagnetic force is generated in a coil where the flux through the coil is changed [79]. As shown in Fig. 2.8, the sample holder is usually controlled by an oscillator which produces sinusoidal signal. During the vertical vibration, the magnetic sample attached on the bottom of the holder will induced a voltage U_m in the pickup coils: $U_m(t) = -\frac{\partial \phi}{\partial t}$, where ϕ is the magnetic flux and t is the time. Consider the pickup coils with n windings and a surface area S, we will have the following expression if the applied magnetic field H is a constant:

$$U_m = -nS\frac{\partial B}{\partial t} \propto -nSM\cos(\omega t), \tag{2.15}$$

where M is the magnetization of the sample, and ω is the frequency of the vertical sinusoidal movement of the sample [79].

Magnetization measurements based on VSM are normally much quicker than those using a SQUID. However, the experimental resolution of a VSM is lower ($\sim 10^{-6}$ emu) than the SQUID's ($<10^{-7}$ emu), making them more suitable to measure materials with strong magnetic signals [79]. In this thesis, an Oxford Instruments MagLab VSM was used to collect the magnetization up to 12 T between 2 K and 200 K.

2.4 Physical Property Measurement System (PPMS)

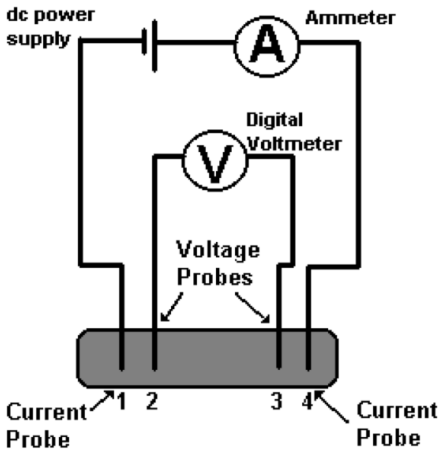

Figure 2.9: Schematic representation of a four-point probe array [80].

We have carried out resistance measurements in a PPMS-9 (Quantum Design) using the four-point probe technique [80, 81]. Unlike the two-point probe technique which measures the contact resistance as well as the

intrinsic resistance of the sample, the four-point probe technique significantly reduces the contributions of the contact resistance by separating the current injection from the voltage reading (Fig. 2.9).

CHAPTER 3

A QUASI-ONE-DIMENSIONAL MAGNET, γ-COV_2O_6

3.1 Background

3.1.1 Magnetic structure of α-CoV_2O_6

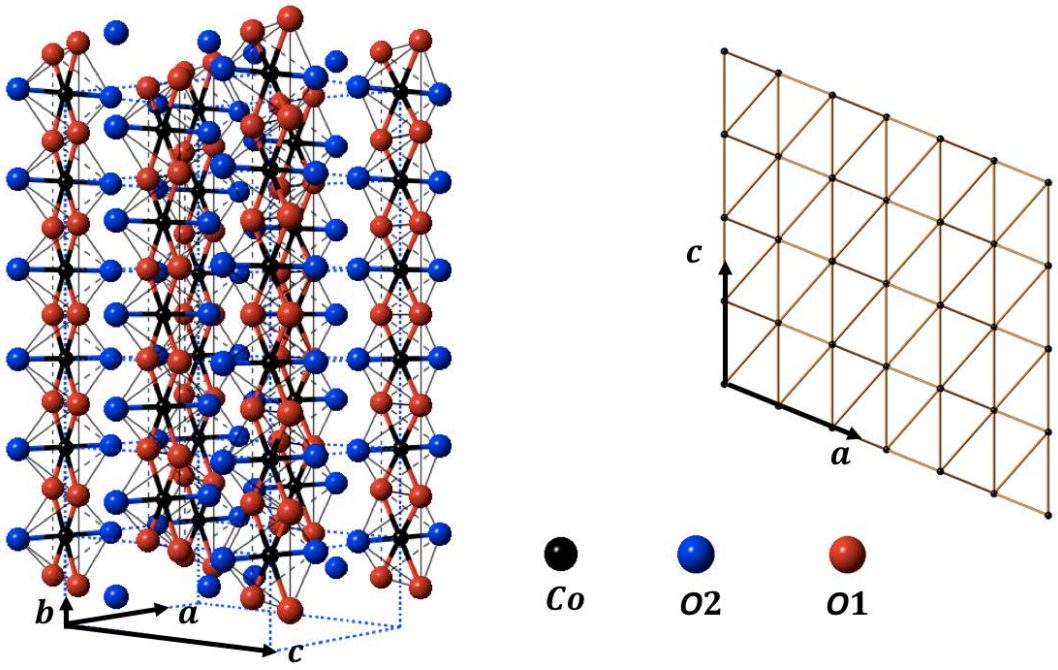

Figure 3.1: (Left) Crystallographic structure of αCVO. Edge-sharing CoO_6 octahedral chains run along the b-axis. V and O(3) cites are omitted for clarity. (Right) Projection of the Co-sites in the ac-plane. The triangular arrangement allows geometric frustration.

CoV_2O_6 crystallizes in two polymorphs, the monoclinic α-CoV_2O_6 (αCVO) and the triclinic γ-CoV_2O_6 (γCVO) [82, 83]. In both structures, the magnetic Co^{2+} has 6 nearest neighbour O^{2-}, forming an octahedral crystal field environment. The space group of αCVO is *C2/m*. The CoO_6 octahedra form edge-sharing chains along the crystallographic *b*-axis (Fig. 3.1), which are spatially separated by the VO_6 chains. As a result, the spin lattice of αCVO is quasi-one-dimensional. On the other hand, the space group of γCVO is $P\bar{1}$. In contrast with the single crystallographic site for Co in αCVO, there are two inequivalent Co sites in γCVO. Similar to the αCVO case, the γCVO structure also forms edge-sharing CoO_6 chains along the *b*-axis, whereas these chains are separated by a complex VO_4-VO_6 network between them (see next section). In this section, we will discuss the magnetic properties of αCVO, which have been studied comprehensively by both experiments and theories. The other polymorph γCVO, which is the focus of this chapter, has not been as studied in the past. We present these studies in the next section.

$T = 300\,\mathrm{K}$	$a = 9.2531(2)$ Å	$b = 3.5040(1)$ Å	$c = 6.6201(1)$ Å	$\beta = 111.617°$
Atom	x	y	z	U_{iso} (Å^2)
Co	0	0	0	0.0090(10)
V	0.3055(19)	0.5	0.3388(26)	0.0090(10)
O(1)	0.1536(2)	0.5	0.1131(3)	0.0110(6)
O(2)	0.4640(2)	0.5	0.2744(4)	0.0110(6)
O(3)	0.1916(2)	0.5	0.5622(4)	0.0110(6)

Table 3.1: Refined lattice parameters, atomic positions and isotropic displacement parameters (U_{iso}) of αCVO at 300 K [84].

The refined structural parameters of αCVO at 300 K can be found in Table. 3.1 [84]. Since the Co-O bonds ($\sim$2 Å) in the CoO_6 octahedron are much shorter than the others (>3.2 Å), the nearest neighbour (NN) intrachain spin exchange is very strong [85]. Moreover, interchain Co-O-Co superexchange paths are also found in αCVO. By projecting these paths into the *ac*-plane, the Co exchange network can be treated as a quasi-triangular lattice which permits the geometric frustration (Fig. 3.1), as discussed in Chapter 1.3 [84, 15]. Previous susceptibility measurements have revealed that αCVO shows strong Ising anisotropy along the *c*-axis (Fig. 3.2a) [86]. Since the saturation magnetic moment along the easy *c*-axis (4.4 μ_B/Co) greatly exceeds the spin-only value for Co^{2+} (3.0 μ_B/Co) (Fig. 3.2b), there must be a strong orbital contribution. Local structure analysis suggests that Co ions reside in a strongly distorted oxygen-octahedral environment [9, 87].

This may lift the orbital moment quenching in αCVO, as verified by the X-ray magnetic circular dichroism (XMCD) spectroscopy measurements [9]. The resulting complex crystal field (Fig. 3.3a), combined with the spin-orbit coupling, is responsible for the *strong Ising anisotropy* seen in αCVO[9, 87, 88].

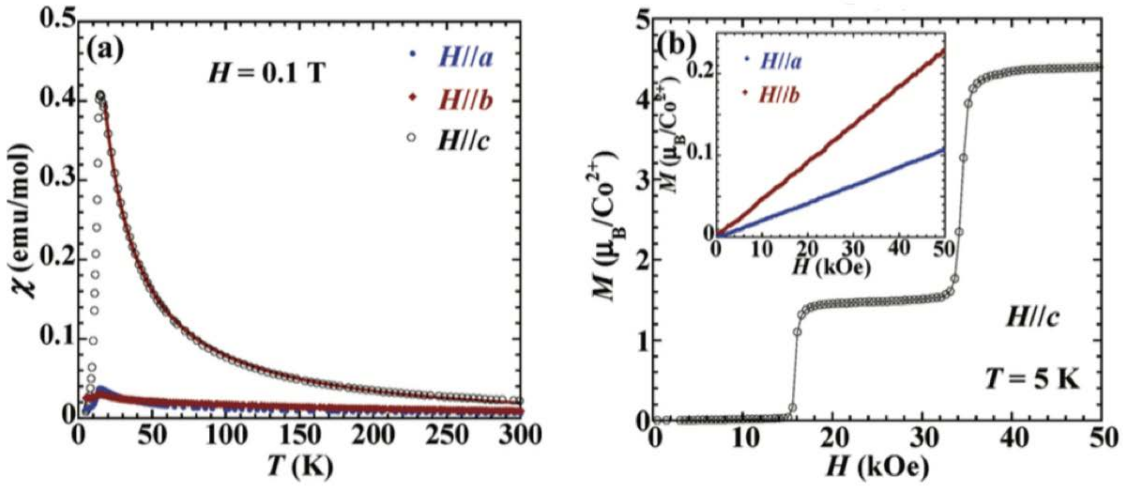

Figure 3.2: (a) Temperature dependence of the magnetic susceptibilities of αCVO. The solid line is a fit using the Ising chain model described in Ref. [86]. (b) Magnetization versus magnetic field curves taken at 5 K.

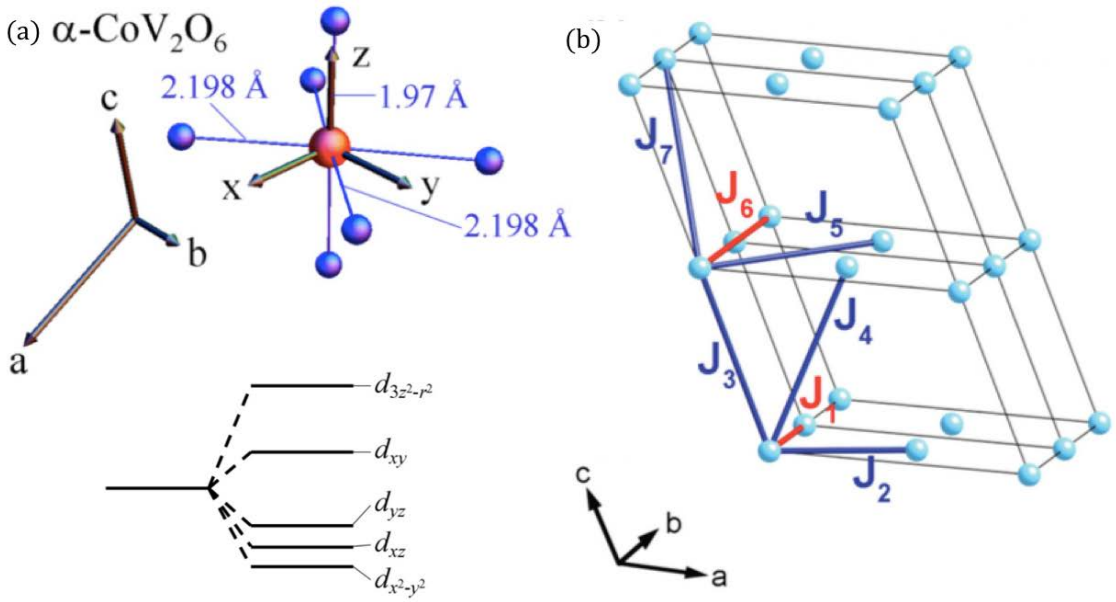

Figure 3.3: (a) The CoO_6-octahedron distortion in αCVO and the schematic crystal field levels [9]. (b) Spin exchange paths between Co ions [85]. Interchain and intrachain couplings are in blue and red, respectively.

Besides the strong Ising anisotropy, the *competing spin exchange interactions* are also crucial to fully understand the magnetic structure of αCVO (Fig. 3.3b) [85]. For example, a 1/3-plateau in magnetization can be stablized between 1.6 T and 3.3 T at 5 K by applying a magnetic field along the c-axis (Fig. 3.2b). This type of metamagnetic transition is a typical manifestation of magnetic frustration [43] and has been observed in other systems such as $Ca_3Co_2O_6$ and $SrCo_6O_{11}$ [89, 90]. By taking the longitudinal components of J_1, J_2, J_3 and J_4 (Fig. 3.3b) into an effective Hamiltonian:

$$\hat{H} = \sum_{i>j} J_{ij}\sigma_i\sigma_j - h\sum_i \sigma_i, \tag{3.1}$$

where σ_i is the pseudo-spin variable along the magnetic easy axis at i-site, Saúl *et al* have successfully reproduced this intermediate 1/3-plateau state (Fig. 3.4a) [85].

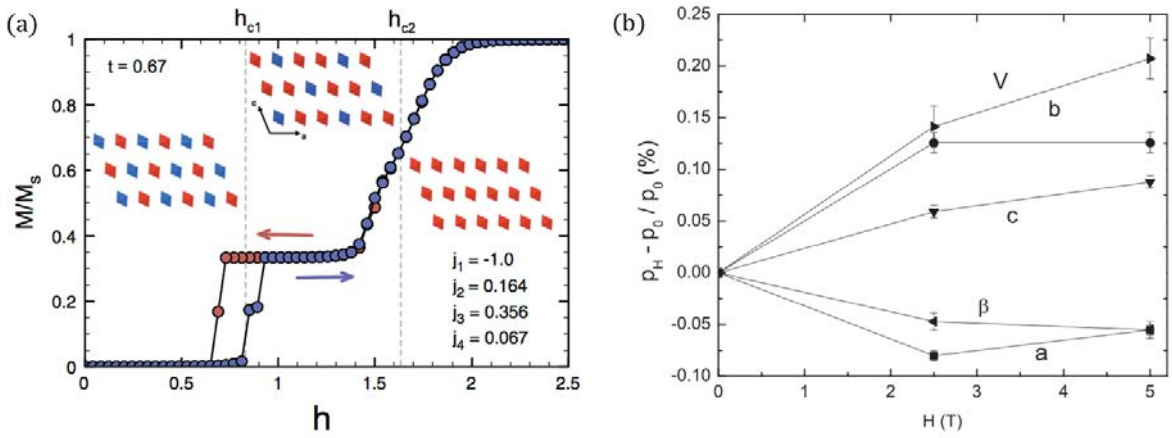

Figure 3.4: (a) Simulated magnetization versus magnetic field curve [85]. Inset: the corresponding magnetic structures in the ac-plane. (b) Magnetic field dependence of lattice parameters (p =a, b, c, β and *Volume*) [91].

Neutron powder diffraction measurements have also been performed to investigate the magnetic structure of αCVO [84, 92, 91]. The results are consistent with the theoretical predictions in Ref. [85] (Fig. 3.4a) as well as the bulk susceptibility data [86, 92]. For the zero field magnetic structure, ferromagnetic Co-chains along the b-axis are antiferromagnetically coupled to their NN chains in the ac-plane. The spins form a *collinear* arrangement in the ac-plane with a tiny tilting angle $\sim 9.3^\circ$ with respect to the c-axis [92]. For the 1/3-plateau state, the intrachain spin arrangement is still ferromagnetic. However, there are two spin-up chains for every one spin-down chain in the ac-plane (Fig. 3.4a). Alternatively, it can be viewed as an 'up-up-down' pattern in the ac-plane. At the highest field, where the full saturation is reached, all the interchain

spin arrangements become ferromagnetic. In all investigations, the spin orientations have been found to be insensitive to the magnetic field [84, 92, 91]. In addition, a magnetostructural coupling effect is also observed in αCVO [84, 92]. The unit cell volume (V) and b-axis are considerably increased between 0 T and 2.5 T when the antiferromagnetic order is suppressed, as depicted in Fig. 3.4b.

To conclude this part, we now write down a more accurate Hamiltonian to describe the interactions in αCVO [85]

$$\hat{H} = H_0 - D\sum_i \hat{S}_{iz}^2 + \sum_{i>j} J_{ij}^{\parallel}\hat{S}_{iz}\hat{S}_{jz} + \sum_{i>j} J_{ij}^{\perp}(\hat{S}_{ix}\hat{S}_{jx} + \hat{S}_{iy}\hat{S}_{jy}), \tag{3.2}$$

where H_0 is the spin independent term, D is the single-ion anisotropy constant, x, y, z are the axes in a *Cartesian* coordinate system and z is the magnetic easy axis. αCVO can be viewed as a magnet with strong anisotropy and competing spin interactions. At the limit of $D \gg \|\vec{J_{ij}}|$, it is clear that a collinear spin structure is favored since having every spin lying along the z-axis will produce the lowest energy [93, 94, 95]. Oppositely, a noncollinear spin structure may be formed if the competing spin exchange terms ($\vec{J_{ij}}$) dominate [93, 94, 95, 96]. It is worth noting that the 1/3-plateau in magnetization can still occur in the absence of any single-ion anisotropy or geometric frustration [96]. From this point of view, the collinear spin structure of αCVO is strongly related to the overwhelming single-ion anisotropy in this structure [9, 87].

3.1.2 Previous investigations on γ-CoV_2O_6: a 2-k Ising magnet?

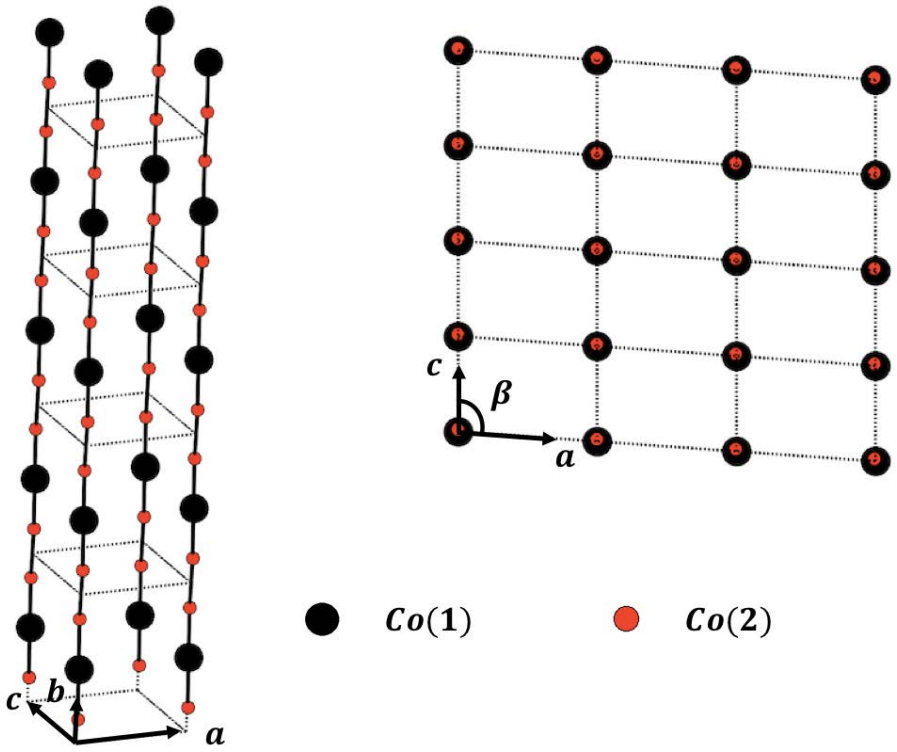

Figure 3.5: Left: Co-chains along the b-axis in γCVO. Right: Projection of the Co-sites in the ac-plane.

Compared with the monoclinic αCVO, the triclinic γ-CoV_2O_6 (γCVO) with space group $P\bar{1}$ is less understood. The room temperature structural parameters of γCVO are summarized in Table. 3.2 [82]. Except Co(1) which is an inversion center, e.g. of two adjacent Co(2) ions (Fig 3.5), most of the atoms occupy a low symmetry position. Similarly, γCVO also has Co-chains running along the b-axis composed of alternate Co(1)-Co(2) ions in a ratio of 1:2. Since the xz-coordinates of Co(2) are small, the projections of Co ions belonging to the same chain in the ac-plane are very close to each other (Fig. 3.5). As to be demonstrated in the next section, the intrachain spin exchange in γCVO is much stronger than any interchain coupling. This means the *in-plane* arrangement of Co ions in Fig. 3.5 can be approximately described as weakly coupled Co-clusters. Unlike αCVO where β is close to 120° (Table 3.1), β of γCVO is close to 90°. The corresponding Co-cluster lattice is more rectangular than triangular, meaning the geometric frustration not as significant in γCVO.

We will briefly discuss the spin exchange paths of γCVO here, although more details will be introduced in the following section. Due to the presence of two inequivalent Co-sites, one needs at least two exchange

constants, J_1 and J_2, to describe the intrachain Co(1)-Co(2) and Co(2)-Co(2) spin exchanges. On the other hand, a Co-O-Co interchain exchange path does not exist in γCVO. This means the V-sites need to be involved in the Co spin exchange process. As to be demonstrated later, at least *five* such interchain exchange paths (J_3, J_4, J_5, J_6, J_7) need to be considered.

$a = 7.164(5)$ Å	$b = 8.872(14)$ Å	$c = 4.806(4)$ Å	$\alpha = 90.29(9)^\circ$	$\beta = 93.66(4)^\circ$	$\gamma = 102.05(9)^\circ$
Atom	Multiplicity	x	y	z	B_{iso} (Å^2)
Co(1)	1	0	0.5	0	0.63(2)
Co(2)	2	0.0199(1)	0.1685(1)	0.0203(2)	0.60(1)
V(1)	2	0.7121(1)	0.9699(1)	0.4593(2)	0.51(2)
V(2)	2	0.7115(1)	0.6067(1)	0.4550(2)	0.53(1)
V(3)	2	0.5806(1)	0.2628(1)	0.1206(2)	0.48(1)
O(1)	2	0.1657(7)	0.4885(5)	0.3469(10)	0.89(6)
O(2)	2	0.8442(6)	0.6387(5)	0.1701(9)	0.74(6)
O(3)	2	0.1798(6)	0.6989(5)	0.8905(9)	0.78(6)
O(4)	2	0.1548(6)	0.0192(5)	0.8255(9)	0.70(6)
O(5)	2	0.1671(7)	0.8931(5)	0.3415(10)	0.95(6)
O(6)	2	0.7850(6)	0.7992(5)	0.6368(9)	0.70(6)
O(7)	2	0.4762(6)	0.9143(5)	0.7011(9)	0.71(6)
O(8)	2	0.4746(6)	0.5780(5)	0.7011(9)	0.70(6)
O(9)	2	0.5236(7)	0.7534(5)	0.2015(10)	0.86(6)

Table 3.2: Room temperature lattice parameters, atomic positions and isotropic displacement parameters (B_{iso}) of γCVO [82].

Bulk magnetization and heat capacity measurements have been performed on γCVO [97, 98, 99, 100, 101]. The antiferromagnetic ordering (T_N) is between 6 K and 7 K (Fig. 3.6a & b). This value is much lower than $T_N = 14\,K \sim 15\,K$ in αCVO [86], indicating a weaker interchain coupling in γCVO. On the other hand, strong Ising-like anisotropy is also observed in this compound, and the magnetization along the b-axis is much larger than those of other directions (Fig. 3.6b & c). The 1/3-plateau state can only be triggered when the magnetic field is applied to the b-axis (Fig. 3.6b). Based on these results, it has been suggested that the Ising anisotropy is still maintained in γCVO.

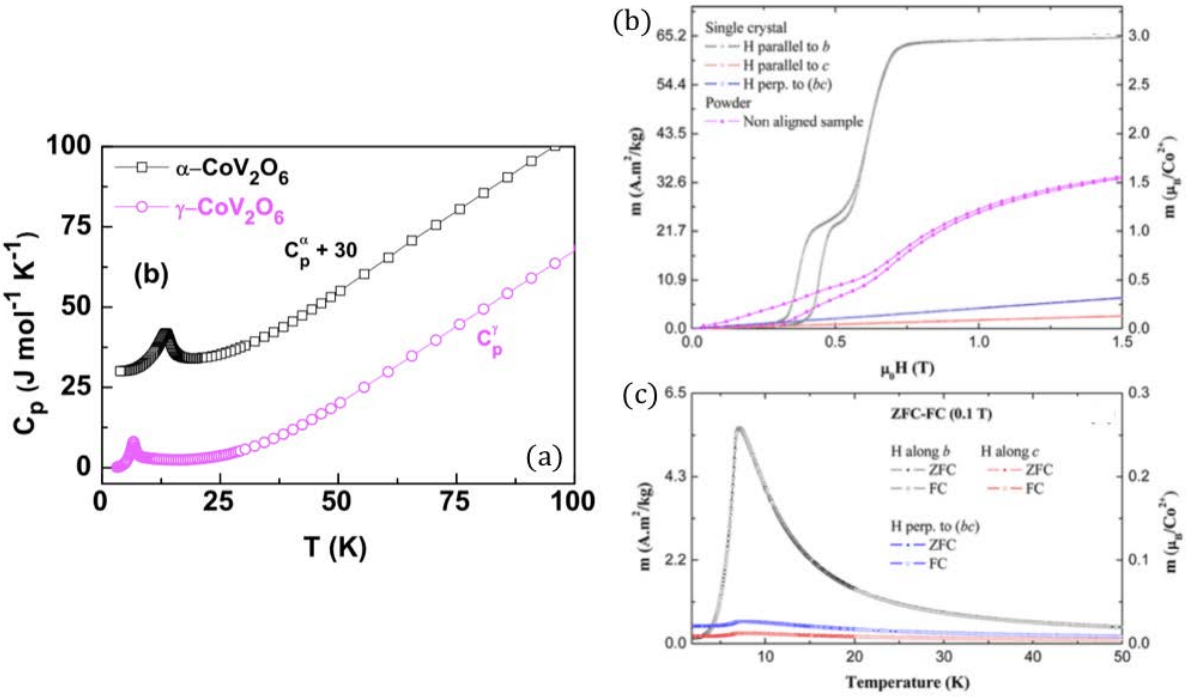

Figure 3.6: (a) Heat capacity data of αCVO and γCVO [101]. (b) and (c) Magnetization curves of γCVO single-crystal and powder [99]. The (b) magnetic field, and (c) temperature scans were taken at $T = 1.8\,\mathrm{K}$ and $B = 0.1\,\mathrm{T}$, respectively.

Although neutron diffraction has been used to investigate γCVO, the corresponding magnetic structure has not been fully established to date [98, 99, 100]. Kimber *et al* observed the magnetic reflections at low temperatures and could not assign all of the reflections with one propagation vector [98]. However, they were only able to partially solve the spin structure using a propagation vector $k_1 = (0.5, 0, 0)$ (Fig. 3.7a). The second propagation vector k_2, as they pointed out, is perhaps related to the competition between superexchange interactions and single-ion anisotropy in γCVO (eq. 3.2) [98]. A later investigation carried out by Lenertz *et al* confirms $k_1 = (0.5, 0, 0)$ and proposes $k_2 = (0.25, 0.5, 0)$ [99]. As shown in Fig. 3.7c, the full diffraction pattern can be refined using these two modulations. However, they have applied a large number of hypothetical constraints in the refinement procedure. Most importantly, the peak profile around $2\theta = 26°$ in Fig. 3.7a cannot be fully fitted by the crystallographic structure refinement in Ref. [98], indicating that it has a magnetic component. Unfortunately, both $k_1 = (0.5, 0, 0)$ or $k_2 = (0.25, 0.5, 0)$ fail to produce a magnetic reflection at this position (corresponding to $2\theta = 23° \sim 24°$ in Fig. 3.7c measured by Lenertz *et al*). As a result, the complex magnetic structure in γCVO remains to be unveiled.

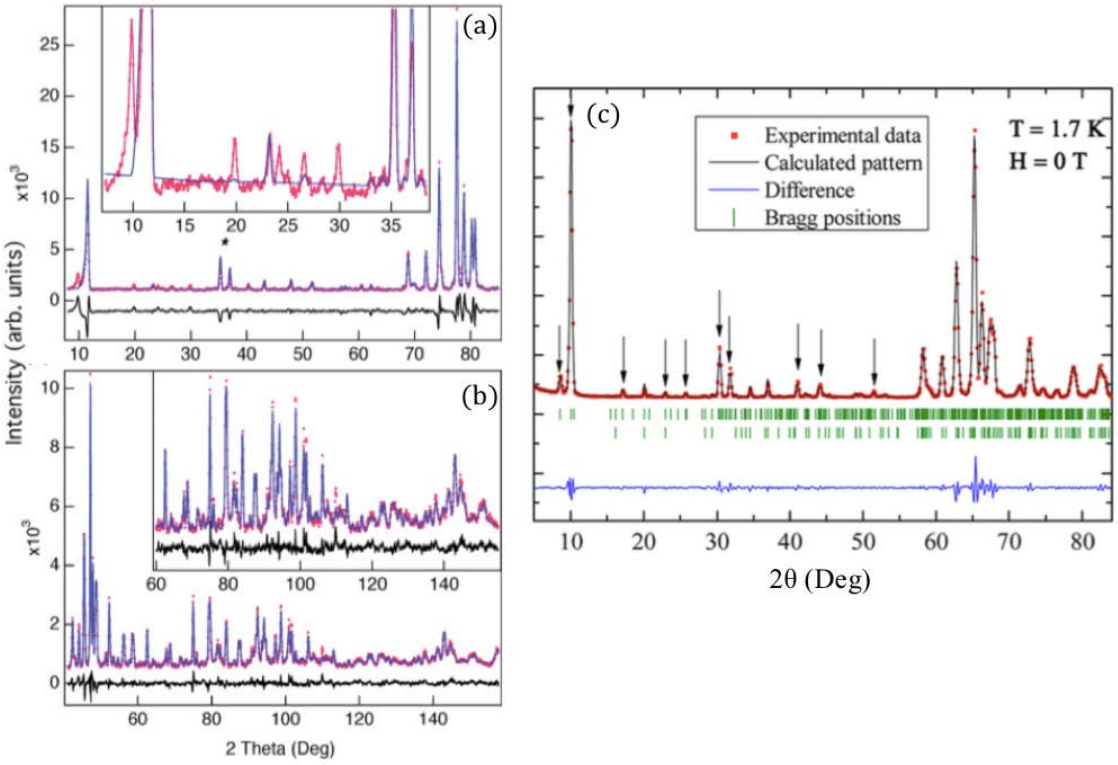

Figure 3.7: Neutron powder diffraction patterns collected by Kimber *et al* [98] at (a) $\lambda = 2.8$ Å, $T = 2$ K and (b) $\lambda = 1.79$ Å, $T = 2$ K and Lenertz *et al* [99] at (c) $\lambda = 2.423$ Å, $T = 1.7$ K.

Compared with αCVO, the CoO_6-octahedra in γCVO is much less distorted. This can be characterized by the following distortion parameter

$$\delta = \frac{1}{N}\sum_i \left(\frac{d_i - < d >}{< d >}\right)^2 \times 10^4, \tag{3.3}$$

where d_i are the Co-O bond lengths, $N = 6$ for an octahedron and $<d>$ is the average bond length [87]. It gives $\delta = 55$ in αCVO and $\delta = 2.1, 4.8$ for the two inequivalent Co-sites in γCVO [87]. Correspondingly, the crystal field splitting should be weak and therefore the orbital quenching stronger in γCVO (Fig. 3.8a), as confirmed in both experimental and theoretical investigations [88, 99, 9, 97, 100]. This also means the single-ion anisotropy in this compound is weaker compared with the αCVO case. As discussed in eq. 3.2, a noncollinear structure is favored when the exchange frustration is dominant in the system. A recent time-of-flight inelastic neutron spectroscopy study on the powder sample suggests that one-dimensional magnetism is not able to fully justify their observations [87].

To finish this part, we summarize the important points based on previous investigations:

1), γCVO cannot be treated as a geometrically frustrated magnet.

2), Exchange frustration coexists with single-ion anisotropy, whereas the latter is weaker compared with the αCVO case.

3), Bulk magnetization measurements tend to support the Ising anisotropy and orbital quenching in γCVO.

4), The Ising anisotropy cannot fully account for the inelastic neutron spectroscopy results.

5), Preliminary neutron diffraction measurements indicate a 2-k magnetic structure.

6), The field-induced 1/3-plateau ferrimagnetic (FI) state does not exist in the entire region below T_{N} (3.8b).

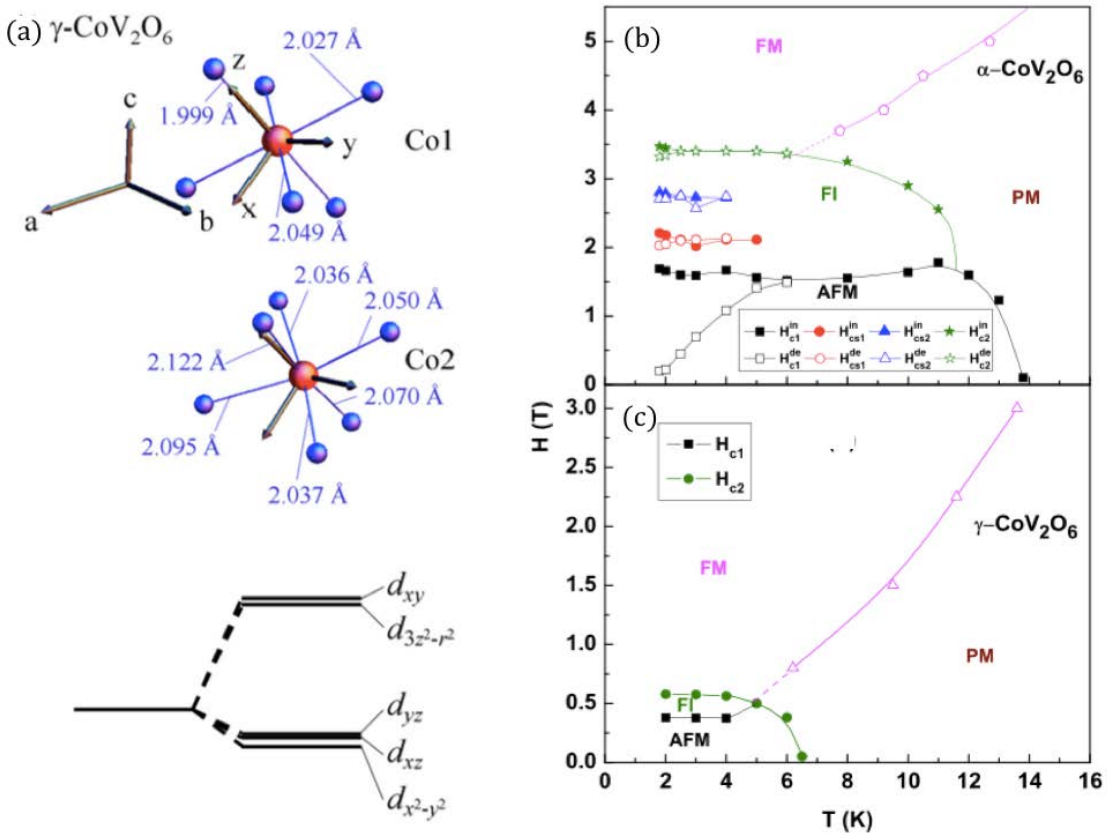

Figure 3.8: (a) Local CoO_6 enviroments of γCVO and the schematic crystal field level splitting [9]. Magnetic phase diagram of (b) αCVO and (c) γCVO [101].

3.2 Results

3.2.1 Research motivations

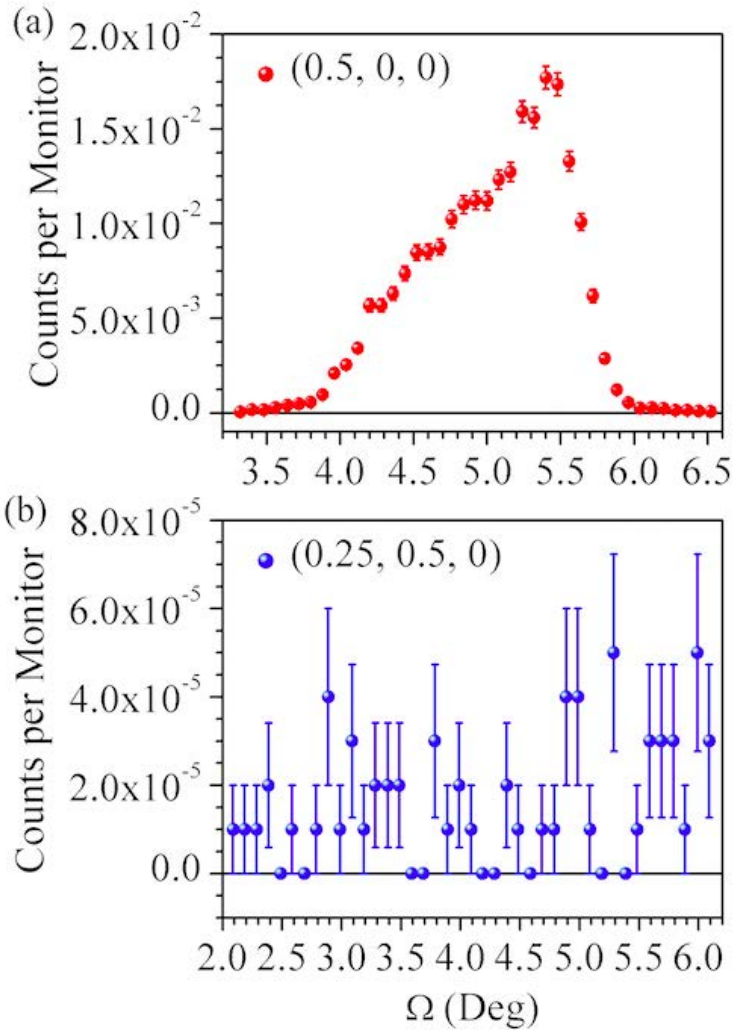

Figure 3.9: Single-crystal diffraction patterns of γCVO collected at $\lambda = 2.31$ Å, $T = 1.5$ K.

As mentioned above, one of the spin modulations $k_1 = (0.5, 0, 0)$ in γCVO has been confirmed by both Kimber *et al* [98] and Lenertz *et al* [99]. The second wavevector $k_2 = (0.25, 0.5, 0)$ proposed by Lenertz *et al* [99] cannot index all of the remaining peaks, e.g. the magnetic reflection $\sim \frac{4\pi sin\theta}{\lambda} = Q = 1.026$ Å in Fig. 3.7. We have performed single crystal neutron diffraction measurements on the TriCS instrument at PSI and have verified k_1, but could not find any reflection with a wavevector transfer $k_2 = (0.25, 0.5, 0)$ (Fig. 3.9). Under the angular resolution of the previous investigations, the magnetic reflections belonging to different

modulations are highly overlapped. For example, there are only *3* visible reflections not indexed by k_1 in Fig. 3.7a, which makes it very hard to exactly determine k_2. Moreover, the Ising anisotropy revealed by the bulk magnetization measurements does not coincide with the inelastic neutron scattering data carried out by Wallington *et al* [87]. Apparently, the magnetic structure of γCVO is the key to answer this question. As a result, further neutron diffraction investigations on γCVO with a better resolution are highly demanded. We therefore carried out a new neutron powder diffraction study.

3.2.2 Data collection and analysis

Both single crystals and powders of γCVO were investigated. Powder samples have were synthesized using the ceramic method. A homogeneous mixture of $CoC_2O_4 \cdot H_2O$ and V_2O_5 in a molar ratio of 1 : 1 were sintered at 873 K in air for 80 hours. The single crystals of γCVO were grown by the flux method; details of the procedure are given in Ref. [97]. Magnetic susceptibility data were collected using a Magnetic Property Measurement System (MPMS, Quantum Design). The existence of magnetic frustration in γCVO is experimentally supported by the commonly used frustration index $f = |\theta_{\mathrm{CW}}/T_{\mathrm{N}}| = 1.66(3)$ (θ_{CW}: Curie-Weiss temperature, T_{N}: Néel temperature). We carried out diffraction measurements on powder samples using the cold neutron powder diffractometer DMC at the Swiss Spallation Neutron Source (SINQ). Two neutron wavelengths, 2.4586 Å and 4.5 Å, were used. The longer wavelength provided the necessary angular resolution to distinguish the magnetic Bragg peaks. 6 g of powder was loaded into a thin Al cylinder (6 mm in diameter) and then into a cryostat to probe temperatures down to 1.5 K. Single crystal neutron diffraction measurements were performed on the TriCS instrument at SINQ. These data (not shown here) confirm the propagation vector $k_1 = (0.5, 0, 0)$ of the magnetic structure found by Kimber *et al.* [98] and Lenertz *et al.* [99], but we did not find peaks corresponding to the second propagation vector $(0.25, 0.5, 0)$ proposed in Ref. [99]. Furthermore, we find a magnetic Bragg peak at $Q \simeq 1.03\,\text{Å}^{-1}$ in our powder diffraction profiles (Fig. 3.13) that cannot be indexed using either of the previously found propagation vectors.

The neutron powder diffraction patterns have been analyzed using the FullProf package [102]. This software is based on a least-squares method called 'Rietveld refinement' [103]. The basic principles of Rietveld refinement are discussed in Appendix A. In order to solve the magnetic and crystallographic structure of γCVO at low temperatures, we have chosen to simultaneously refine two patterns collected under different wavelengths (4.5 Å and 2.4586 Å). The shorter wavelength enables us to determine the crystallographic structure, whereas the longer wavelength offers necessary angular resolution to determine the correct k_2 and then to solve the magnetic structure. Here we have chosen to demonstrate the refinement procedure under the *two*

single-k phases (phase separation) scenario. We note a second scenario, corresponding to the *one* double-k phase as proposed by Kimber *et al* and Lenertz *et al* [99], along with a comparison between the two will also be discussed in the next Section 3.2.3.

Propagation vector	$k_1 = (0.5, 0, 0)$	$k_1 = (0.5, 0, 0)$	$k_2 = (\text{-}0.25, 0, 0.25)$
Symmetry operator	Γ_1^1	Γ_2^1	Γ_1^1
{1|000}	1	1	1
{-1|000}	1	-1	——

Table 3.3: Irreducible representations of the magnetic little group G_k of the propagation vector $k_1 = (0.5, 0, 0)$ and $k_2 = (\text{-}0.25, 0, 0.25)$ for γCVO.

We have first carried out a representation analysis to investigate the symmetry constraints of the magnetic structure by using the BasIreps option in the FullProf package. [104]. This requires the crystallographic symmetry as well as the propagation vector of the magnetic ordering to determine the magnetic little group G_k in which the elements leave the propagation vector invariant. The magnetic representation (Γ_{mag}) of a crystallographic site can then be decomposed into a series of irreducible representations (IRs)

$$\Gamma_{\text{mag}} = \sum_v n_v \Gamma_{\text{v}}^{\mu}, \tag{3.4}$$

where n_v is the number of times that the IR Γ_{v} of order μ appears in Γ_{mag} [105].

For the $P\bar{1}$ space group of γCVO, there are only two elements in G_k (Table. 3.3). Under the $k_1 = (0.5, 0, 0)$ modulation, the magnetic representations of Co(1) and Co(2) are

$$\Gamma_{\text{mag}}^{\text{k}_1}(1) = 3\Gamma_2^1 \text{ and } \Gamma_{\text{mag}}^{\text{k}_1}(2) = 3\Gamma_1^1 + 3\Gamma_2^1, \tag{3.5}$$

respectively. Since only one IR can be involved in a second-order transition, very useful information can be obtained by such representation analysis. For example, Γ_2^1 indicates that the Co(2) spin should be either parallel (Γ_2^1) or antiparallel (Γ_1^1) with its central inversion replica $\overline{\text{Co(2)}}$. On the other hand, there is only one element in G_k under the second modulation (Table. 3.3), which has been identified as $k_2 = (\text{-}0.25, 0, 0.25)$ in our investigations. We shall extend the relevant discussion in the next subsection. The key message here is that the inversion symmetry of Co(2) is broken for the spin lattice modulated by this k_2. As a result, one should refine Co(2)- and $\overline{\text{Co(2)}}$- sites independently.

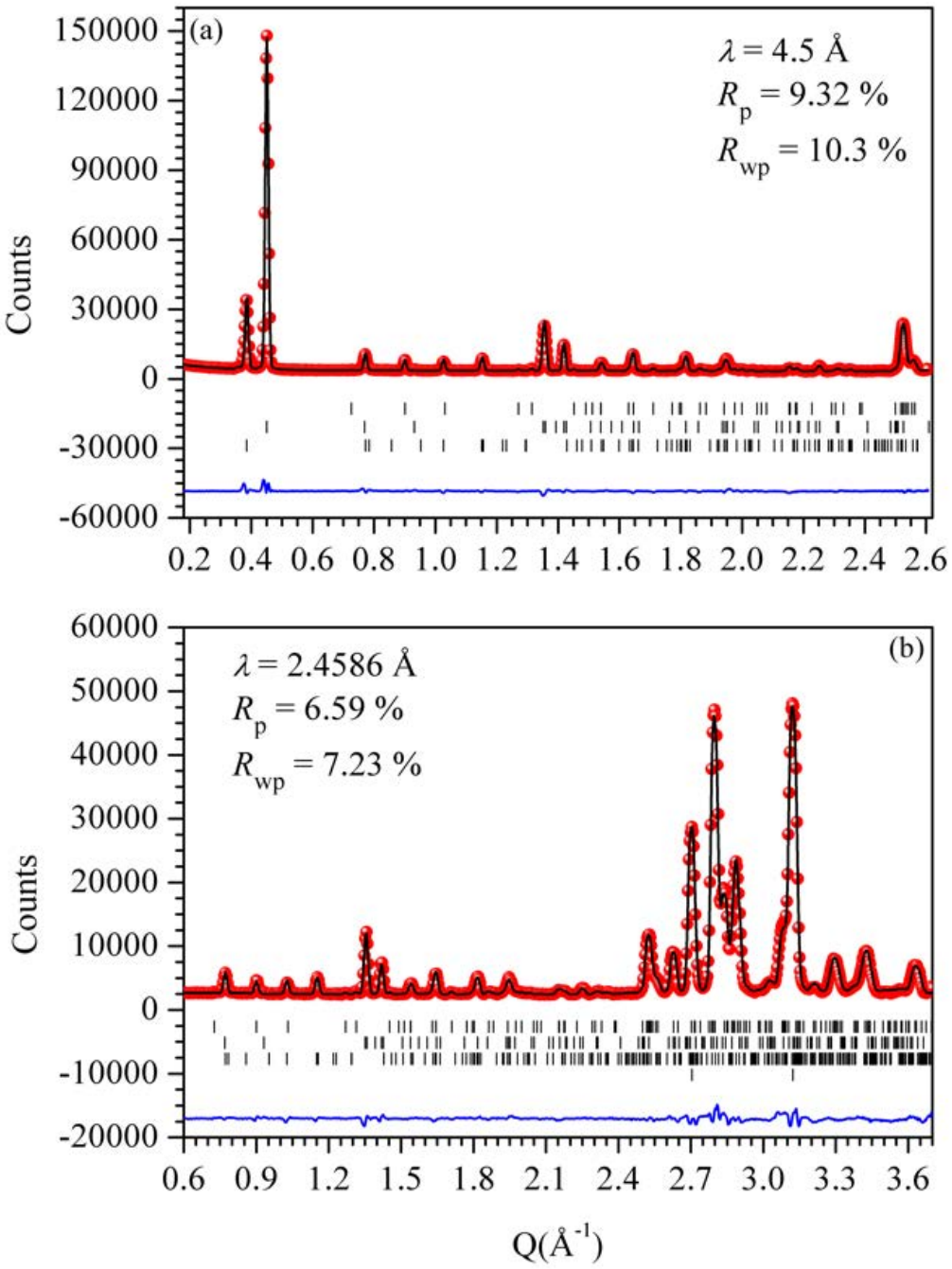

Figure 3.10: Powder diffraction patterns obtained at $T = 1.5\,\mathrm{K}$. The calculated pattern (black solid lines) correspond to the first step described in the context. The vertical bars, from top to bottom, label the reflections of nuclear, k_1, k_2 and Aluminium (sample holder), respectively. The Rietveld factors (Appendix A) are also displayed.

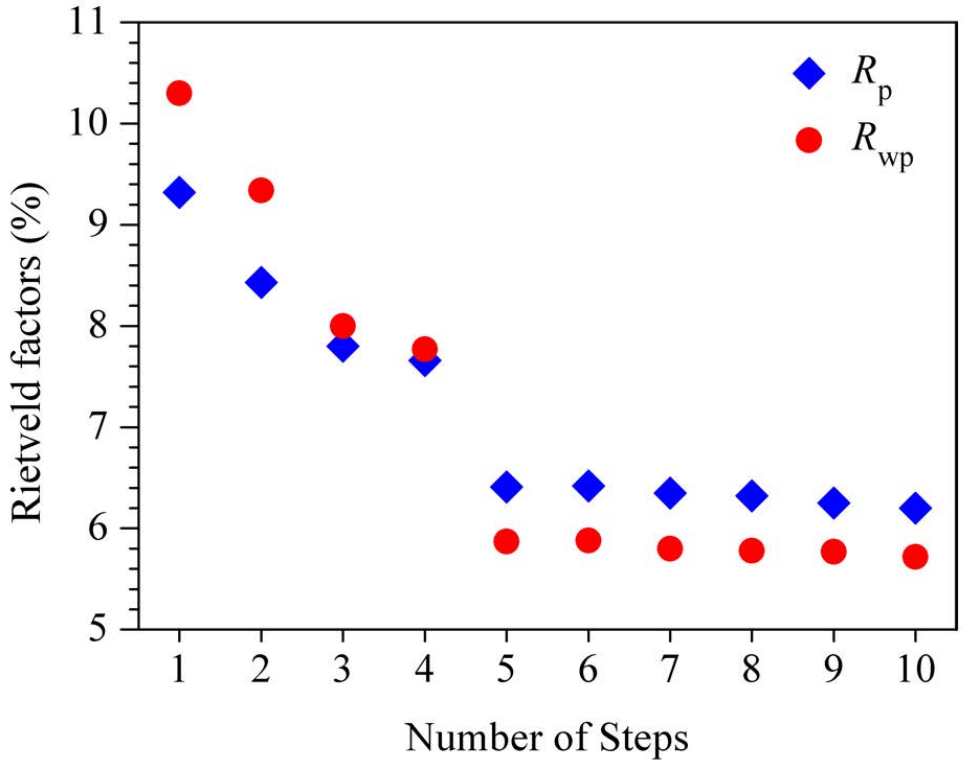

Figure 3.11: Evolution of the Rietveld factors of the neutron diffraction pattern at $\lambda = 4.5$ Å in the refinement process.

Since the low temperature crystallographic structure of γCVO has been analyzed in the past, we have used the atomic positions, lattice parameters, and isotropic displacement parameters (B_{iso}) listed in Table 3.2 ([98]) as our starting parameters. For the magnetic structure, we have followed the bulk susceptibility measurements which suggest an Ising anisotropy along the b-axis and a magnetic moment of $3\,\mu_B$/Co for both Co(1)- and Co(2)- sites [9, 97, 99, 100, 98]. We have used a tripled pseudo-Voigt function to fit the peak shape [106], the starting parameters of which can be found in Ref. [107]. In the first step, we have only refined the scale factors, lattice parameters and zero shifts of the detector. As shown in Fig. 3.10, the calculated patterns are already very close to the experimental observations. In the following, we have freed other parameters in the following sequence:

1. Atomic positions and the amplitudes of the magnetic moments on Co(1)- and Co(2)- sites.

2. Peak shape parameters and asymmetry parameters.

3. Background.

4. Spin orientation of Co(1) in the k_1 phase.

5. Spin orientation of Co(2) in the k_1 phase.

6. Spin orientation of Co(1) in the k_2 phase.

7. Spin orientation of Co(2) in the k_2 phase.

For the k_1 modulation, several initial trials have ruled out Γ_2^1 on Co(2)-sites. This produces a zigzag ferromagnetic Co chain along the b-axis. For the k_2 modulation, several constraints have been applied during the fitting process. This will be discussed in the next subsection. By ending this subsection, we note that the refinement converges in each step and the fitting quality is also greatly improved over this process (Fig. 3.11).

3.2.3 Magnetic phase separation in γ-CoV_2O_6

Magnetic frustration occurs when a system's total free energy cannot be minimized by optimizing the interaction energy between every pair of spins. This can be caused by competing interactions [96] or by geometry e.g. antiferromagnetic interactions on a triangular or tetrahedral unit [15]. As a result, the ground state of a frustrated magnet is often highly degenerate [1]. The degeneracy can be lifted by perturbations such as additional interaction terms [15], quantum fluctuations [108], and so forth. Various exotic spin states may also result, as found by numerical simulations [109, 110]. Evidently, experiments are essential to verify the nature of the interactions, determine their parameters and to confirm the presence of any emergent states.

Another consequence of competing interactions may be phase separation, a common phenomenon among colossal magneto-resistance (CMR) manganites and high-T_c superconductors [10, 111]. There are no constraints on the type of these interactions, though so far most phase separation phenomena require non-magnetic Hamiltonian terms (e.g. Coulomb interaction, electron-phonon coupling). Recently, phase separation possibly of purely magnetic origin was studied in $SrCo_6O_{11}$ where a 'devil's staircase' is realised [112], though the volume fractions of the competing phases were not determined. Dynamic phase separation has also been observed in the quasi-one-dimensional (Q1D) $Ca_3Co_2O_6$ [40] and possible microphases have also been reported here [43, 42]. To our knowledge, static or dynamic phase separation exclusively caused by competing spin exchange interactions, e.g. exchange frustration, on a non-geometrically frustrated lattice has not presently been reported.

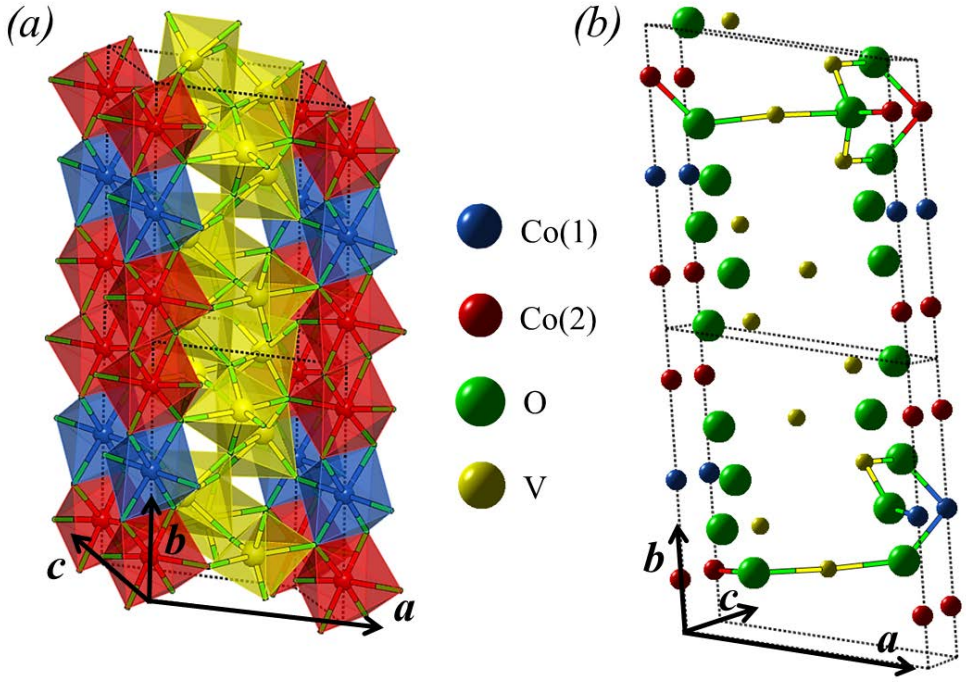

Figure 3.12: (a) Crystal structure of triclinic γCVO. Oxygen anions (omitted for clarity) occupy the corner of the shaded polyhedra. (b) Possible interchain spin exchange paths displayed in two unit cells for Co(1) and Co(2), respectively.

We report magnetic phase separation in the triclinic cobaltate compound γ-CoV_2O_6 (γCVO). γCVO has space group $P\bar{1}$ with edge-sharing CoO_6-octahedra arranged in zigzag chains along the crystallographic b-axis. These chains are well separated by a VO_4-VO_6 polyhedral-network between them (Fig. 3.12a) [82]. Unlike its polymorph α-CoV_2O_6 (αCVO), the transverse nearest neighbour (NN) exchange in γCVO must involve V^{5+} [86]. This significantly weakens the interchain exchange interaction strength as evidenced by a lower ordering temperature in γCVO [86, 97, 98]. As shown in Fig. 3.12a, there are two inequivalent cobalt sites, Co(1) and Co(2). For the Co(2)-Co(2) exchange, there is only one Co^{2+}-O^{2-}-V^{5+}-O^{2-}-Co^{2+} (COVOC) path along the a-axis (Fig. 3.12b). In contrast, two very similar COVOC paths are found along the c-axis, affording the possibility of the so-called 'random frustration' caused by competing interactions [15]. For the Co(1)-Co(1) exchange, no NN COVOC path is found along the a-axis and only one such path is located along the c-axis. Surprisingly, a skew path between interchain Co(1) and Co(2) sites is also found. Its length is close to those of the transverse ones, meaning these skew paths are just as important for the magnetic structure. First of all, they can set up correlations between Co(1) spins along the a-axis. Second, since the

intrachain exchange is mainly ferromagnetic, an antiferromagnetic skew exchange would complicate the final magnetic structure or even lead to further frustration.

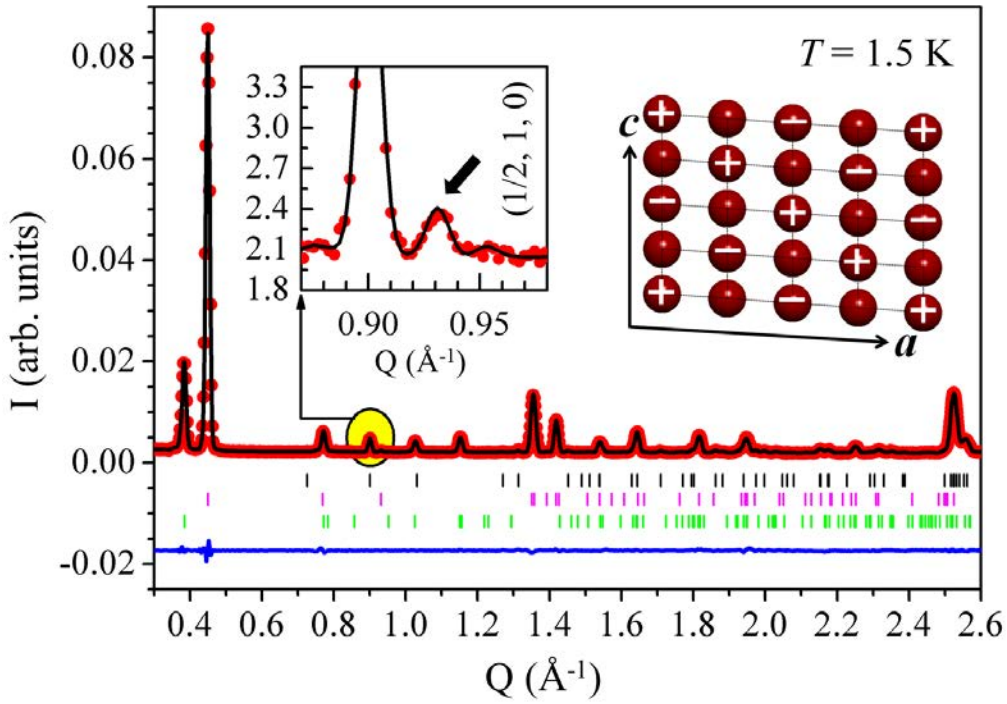

Figure 3.13: Neutron powder diffraction pattern measured at $\lambda = 4.5$ Å, $T = 1.5$ K. The red solid dots are experimental observations. The black and blue lines are the calculated pattern and the difference using the *2*-phase model. Black, pink and green vertical bars mark the nuclear, k_1- and k_2- modulated Bragg positions, respectively. Right inset: Sketch of the *ac*-plane magnetic structure modulated by k_2 in a 5x5 unit cell. Left inset: A weak reflection indexed as $(0.5, 1, 0)$ around 0.931 Å.

On cooling the system down to 1.5 K from the paramagnetic state, magnetic Bragg peaks are observed in the low-Q region (Fig. 3.13). The refined lattice parameters (Table 3.4) are consistent with previous works [98, 99]. In addition to the $k_1 = (0.5, 0, 0)$ wavevector proposed by Kimber *et al.* [98], corresponding to ferromagnetic *bc*-planes antiferromagnetically coupled along the *a*-axis, we find that a second propagation vector $k_2 = (-0.25, 0, 0.25)$ is required to index the rest of the peaks. The in-plane spin modulation of k_2 is shown schematically in the right inset of Fig. 3.13. We also find short range correlations down to the lowest temperature probed (1.5 K). Their contributions below the incommensurate-commensurate lock-in transition $T^* = 5.6$ K are treated in two self-consistent ways: (a) Gaussian functions are used to fit the diffuse profiles on the tails of the main peaks at $Q_1 = (-0.25,\ 0,\ 0.25)$ at ~ 0.39 Å^{-1} and $Q_2 = (0.5, 0, 0)$

at $\sim 0.45\,\text{Å}^{-1}$, respectively (Fig. 3.15b). The background is fixed during the refinement after subtraction of such profiles. (b) Alternatively, they are regarded as a part of the background so that the background is also refined. These two methods produce essentially identical magnetic structures within our fitting resolution.

Although rare, multi-k structures have been predicted and experimentally confirmed in some frustrated systems [113, 114, 109, 110, 115, 116]. We therefore propose two possible magnetic structures for γCVO: (I) a single phase with 2-k-modulation, or (II) two 1-k phases (phase separation). As shown by the Rietveld factors in Table 3.4, both scenarios turn out to fit the data reasonably well, although with some caveats. Possible phase differences between the two inequivalent Co-sites and between the two modulations have been fixed to zero, since we found that these parameters either resulted in unphysically large magnetic moments or did not converge within the fitting resolution. We could not solve exactly the spin orientations modulated by k_2 in either scenario, since the relevant free parameters were highly correlated, resulting in unphysically large standard deviations in the Rietveld refinements.

We have also tested a 'minimal model' for each scenario where all spins modulated by k_2 lie along the b-direction; this is based on the assumption of Ising-like anisotropy along the crystallographic b-axis [97, 99, 100]. This minimal model was then relaxed by allowing spin canting in the ab-, or bc- plane on each Co-site. For the 2-k single phase scenario, this canting does not improve the original refinement produced by the minimal model, and so the corresponding spin orientations are fixed to the b-axis. In a triclinic lattice, we note the spins will still have components in the ac-plane even if the b-axis Ising anisotropy is strictly followed (Table 3.4). The refinement is not sensitive to additional spin canting on Co(1)-sites in the phase separation scenario (fixed along the b-axis for these sites in Table 3.4), but it is considerably improved by including canting in the bc-plane on Co(2)-sites (see below).

Both scenario I and II fit the data reasonably well. However, the global average of the magnetic moment along the b-axis ($\overline{M}_b$) obtained by the 2-k solution is 4.3(3) μ_B. This is close to the value in αCVO where there is large spin-orbit coupling (SOC) [86, 92, 84, 9]. Crystallographic structure analysis shows that the distortion of the CoO_6-octahedron is much weaker in γCVO than in αCVO [87]. This leads to a very small orbital contribution to the total moment in γCVO, as revealed by X-ray magnetic circular dichroism (XMCD) spectroscopy and theoretical calculations [9, 88]. The result is a global average spin moment of $\sim 3.2\,\mu_B$/Co, mainly pointing along the b-axis, in agreement with magnetization measurements [98, 100, 99, 97]. We point out that the 2-$\vec{k}$ solution is *inconsistent* with this value. On the other hand, the phase separation model produces $\overline{M}_b = 3.04(9)\ \mu_B$/Co, in excellent agreement with magnetization, XMCD data, as well as theoretical predictions [9, 88, 98, 100, 99, 97].

Scenario I		2-k	
a, b, c (Å)	7.1515(4)	8.8555(3)	4.7951(2)
α, β, γ (°)	90.144(5)	93.948(2)	102.110(6)
Moments	M_a (μ_B)	M_b (μ_B)	M_c (μ_B)
Co(1) : k_1	-0.5(2)	2.5(1)	0.3(3)
Co(2) : k_1	0.2(1)	2.44(7)	-0.5(2)
$\overline{\text{Co(2)}}$: k_1	0.2(1)	2.44(7)	-0.5(2)
Co(1) : k_2	-0.4(1)	2.0(6)	-0.01(1)
Co(2) : k_2	-0.21(4)	1.0(2)	-0.003(4)
$\overline{\text{Co(2)}}$: k_2	-0.5(1)	2.5(5)	-0.01(1)
Scenario II†		2-phase	
a, b, c (Å)	7.1524(4)	8.8560(3)	4.7954(2)
α, β, γ (°)	90.137(6)	93.949(2)	102.122(7)
Moments	M_a (μ_B)	M_b (μ_B)	M_c (μ_B)
Co(1) : k_1 [65(1) %]	-1.7(3)	2.9(3)	1.1(3)
Co(2) : k_1[65(1) %]	-1.1(2)	3.1(1)	-0.2(2)
$\overline{\text{Co(2)}}$: k_1[65(1) %]	-1.1(2)	3.1(1)	-0.2(2)
Co(1) : k_2[35(1) %]	-0.69(4)	3.3(2)	0.008(4)
Co(2) : k_2[35(1) %]	-0.57(5)	2.8(2)	1.5(4)
$\overline{\text{Co(2)}}$: k_2[35(1) %]	-0.65(2)	3.1(1)	-0.008(2)
Rietveld factors	R_p (%)	R_{wp}(%)	χ^2
2-k	6.29	5.78	4.796
2-phase$^{\bullet}$	6.25	5.77	4.749
2-phase†	6.20	5.72	4.657
2-phase‡	6.20	5.77	4.728

Table 3.4: Magnetic and lattice parameters of γCVO at $T = 1.5$ K. Constraints on the spin orientations for the k_2 modulation have been applied; see main text for details. $\overline{\text{Co(2)}}$ is the central inversion replica of Co(2). The isotropic displacement parameters (B_{iso}) and V atomic positions were fixed to the values reported in Ref. [98]. Lattice parameters, O and Co positions were refined using data at $\lambda = 2.4586$ Å. Three sets of Rietveld factors, corresponding to the minimal model ($^{\bullet}$), inequivalent (†) and equivalent (‡) spin canting on Co(2)- and $\overline{\text{Co(2)}}$- sites, are listed for the 2-phase scenario.

We will now discuss the magnetic structure of this phase separation scenario in detail. Previous susceptibility measurements on γCVO single crystals [97] show that the Co ions still possess Ising-anisotropy along the crystallographic b-axis. Recently, this anisotropy has been challenged by a time-of-flight inelastic neutron scattering study which suggests that one-dimensional magnetism along the b-axis is *not* sufficient to address all of their observations [87]. According to our refinement, the global average moment ($\overline{M}$) is 3.17(8) μ_B/Co. When we compare this to $\overline{M}_b$ we see that bulk Ising-anisotropy is mostly maintained in γCVO. On the other hand, we find that canting in the ac-plane for spins in the k_1 phase is necessary to match some very weak reflections [Fig. 3.13(left-inset)]. For example, the refined structure of the Co(1)-spins in the k_1 phase shows components along all 3 crystal axes (Table 3.4). Since the projections of M_b on both a- and c- axes are weak, e.g. -0.61 μ_B/Co(1) and -0.01 μ_B/Co(1), respectively, in the k_1 phase, the additional non-negligible *in-plane* magnetic moments obtained in our refinements strongly indicate that the spins in γCVO do not lie solely along the b-axis. This might be related to the complex CoO_6-octahehral distortion seen in this compound [88, 9].

By relaxing from the 'minimal model', we can estimate the strength of spin canting in the k_2 phase. By allowing canting in the bc-plane on the Co(2)-sites, i.e. 29(8)° towards the c-axis, the refinement quality characterized by the three Rietveld factors is considerably improved (Table 3.4). This canting angle changes to 19(9)° and the Rietveld factors are increased if we keep the inversion symmetry between Co(2)- and $\overline{\text{Co(2)}}$-sites. These results support the breakdown of inversion symmetry on Co(2)-sites in the spin lattice. This breakdown is only allowed in the k_2 phase based on the representation analysis.

We have also investigated the temperature dependences of the two phases. The magnetic reflections generated by $k_2 = (\text{-}0.25, 0, 0.25)$ are greatly suppressed on heating from 5.6 K ($= T^*$) to 5.8 K. For example, the $Q_3 = (0.75, 0, 0.25)$ reflection at ~ 0.77 Å^{-1} can barely be resolved above T^*, and the remnant intensity is mainly composed of the (0.5, -1, 0) reflection arising from the k_1 phase (Fig. 3.13). Concomitantly, emergent reflections which cannot be indexed using either $k_1 = (0.5, 0, 0)$ or $k_2 = (\text{-}0.25, 0, 0.25)$ appear in a broad Q-range (Fig. 3.14a). As the temperature increases further beyond T^*, the emergent reflection on the left of $(0.75, 0, 0.25)$ continuously shifts towards the low-Q region until it falls under the strong diffuse scattering background at 6.6 K (Fig. 3.14a). By fitting 5 clearly observable emergent reflections, we can rule out the possibility of a commensurate modulation above T^* for these reflections. Unfortunately, an extensive search in incommensurate space produces sets of solutions that cannot be distinguished within our resolution. The peak between 1.33 Å^{-1} and 1.38 Å^{-1} consists exclusively of $Q_4 = (1.5, 0, 0)$ and $Q_5 = (\text{-}0.5, 0, 1)$ reflections of the k_1 phase. Although its intensity starts to drop around T^* (Fig. 3.15a), no additional peaks are observed around

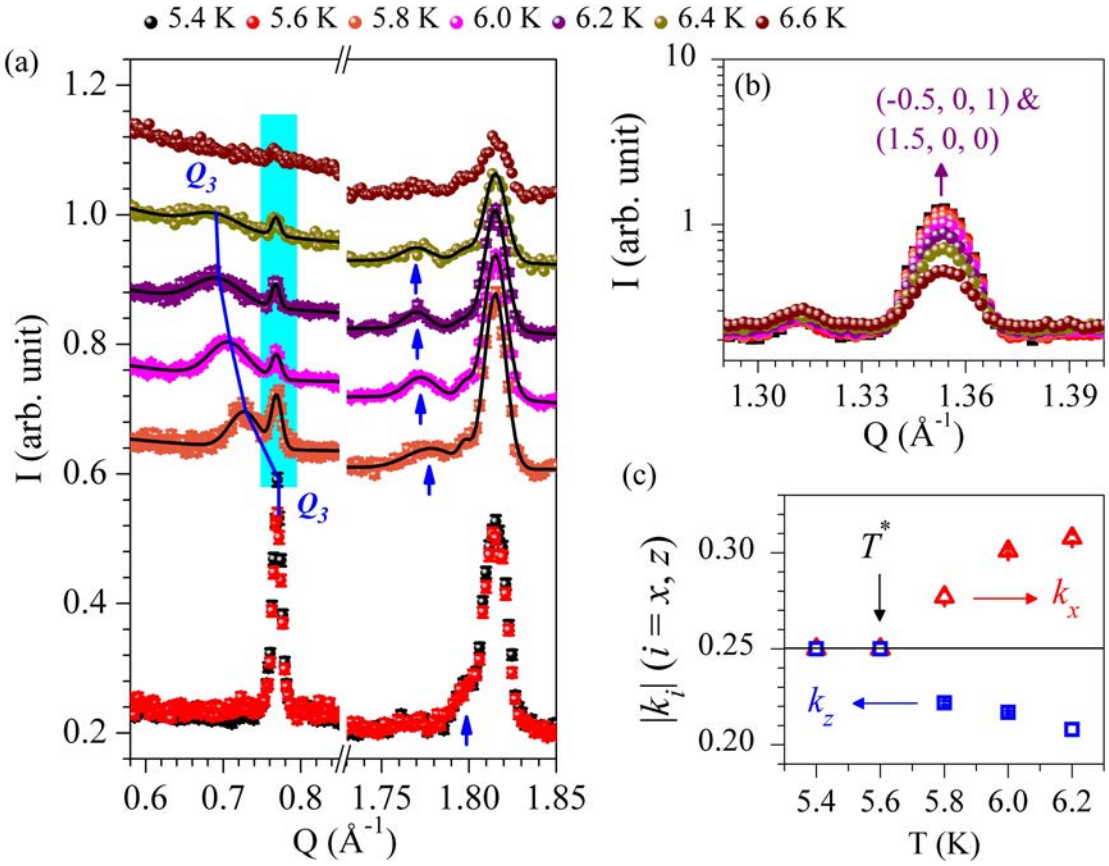

Figure 3.14: (a) Selected regions of the powder diffraction patterns between 5.4 K and 6.6 K, showing the shifting reflections. The peak positions in the intermediate region are fitted with Gaussian functions (solid lines). A constant vertical shift has been applied to patterns measured above T^*. The remnant peak above T^* is indexed as $(0.5, -1, 0)$. (b) Temperature dependence of the $(1.5, 0, 0)$ and $(-0.5, 0, 1)$ reflections generated by k_1, which in contrast do not shift. (c) Temperature dependences of the x and z components of k_2 around T^*.

it (Fig. 3.14b). This suggests that the appearance of the incommensurate peaks above T^* is not related to the k_1 phase. Since previous heat capacity measurements did not reveal any phase transition at T^* [97, 98, 101], these features are consistent with a commensurate-incommensurate lock-in transition of the k_2 phase. We find that only two of the three components of the general incommensurate wavevector, $k_2 = (k_x, k_y, k_z)$, can be uniquely determined at each temperature from the 5 clearly observable incommensurate peaks. Setting $k_y = 0$, we may plot the temperature dependence of $k_2 = (k_x, 0, k_z)$ in Fig. 3.14c. The temperature dependence of the normalized integrated intensity of the Q_3 reflection is also plotted in Fig. 3.15a. T_N for the k_1 phase has been determined to be 6.6 K (the corresponding normalized intensity versus temperature plot has the steepest slope at this point). Since no reflection indexed by k_2 can be observed above T_N, we expect that both phases share the same transition temperature. It is also worth noting that both solutions only give one reflection between 0.6 $\mathrm{Å}^{-1}$ and 0.74 $\mathrm{Å}^{-1}$. Correspondingly, the Q_3 reflection is not resolution limited (Fig. 3.14a), meaning that the k_2 phase becomes short range ordered between T^* and T_N.

Strong diffuse scattering profiles appear above T^* (Fig. 3.15c), and are detectable up to 25 K (Fig. 3.15d). When $T \geqslant T_\mathrm{N}$, the magnetic incoherent scattering background is stabilized, making it possible to study the pure magnetic diffuse scattering signals by subtracting the nuclear contributions taken at 35 K. As shown in Fig. 3.15b, these profiles still center around Q_1 at T_N. Fitting them with a Lorentzian function produces a correlation length (ξ) of 94(4) Å. This is much smaller than $\xi \sim 230$ Å at 1.5 K by fitting the diffuse tails of Q_1 and Q_2 reflections (Fig. 3.15b). Although spin fluctuations set in well above T_N in γCVO, it is very hard to extract their positions at high temperatures due to the extra scattering signals from small angles as well as the weak intensities. However, these spin fluctuations are more related to the k_2 modulation, as revealed by our analysis at temperatures close to T_N. Given that the k_1 phase populates the majority ($\sim 65\,\%$) of the sample, the dominant spin fluctuations related to k_2 above T_N are very surprising.

Incommensurate magnetic microphases with a metastable propagation vector have been studied theoretically on a geometrically frustrated lattice with Ising anisotropy [43]. At very low temperatures, the magnetic structure is commensurate, while metastable incommensurate microphases exist in the intermediate region. It is also suggested that additional subtle coupling terms may stabilize the incommensurate state, as realized in $Ca_3Co_2O_6$ [39]. On the other hand, both single-ion anisotropy and exchange frustration are present in both αCVO and γCVO [87, 88]. As suggested in Refs. [93, 94, 95, 96], the system will form a collinear spin structure if the single-ion anisotropy is stronger compared with the spin exchange interactions, whereas an incommensurate noncollinear spin structure is favoured oppositely. The collinear spin arrangement of αCVO, which possesses a very strong SOC, is consistent with this description [84, 92, 9, 87]. For the γCVO compound

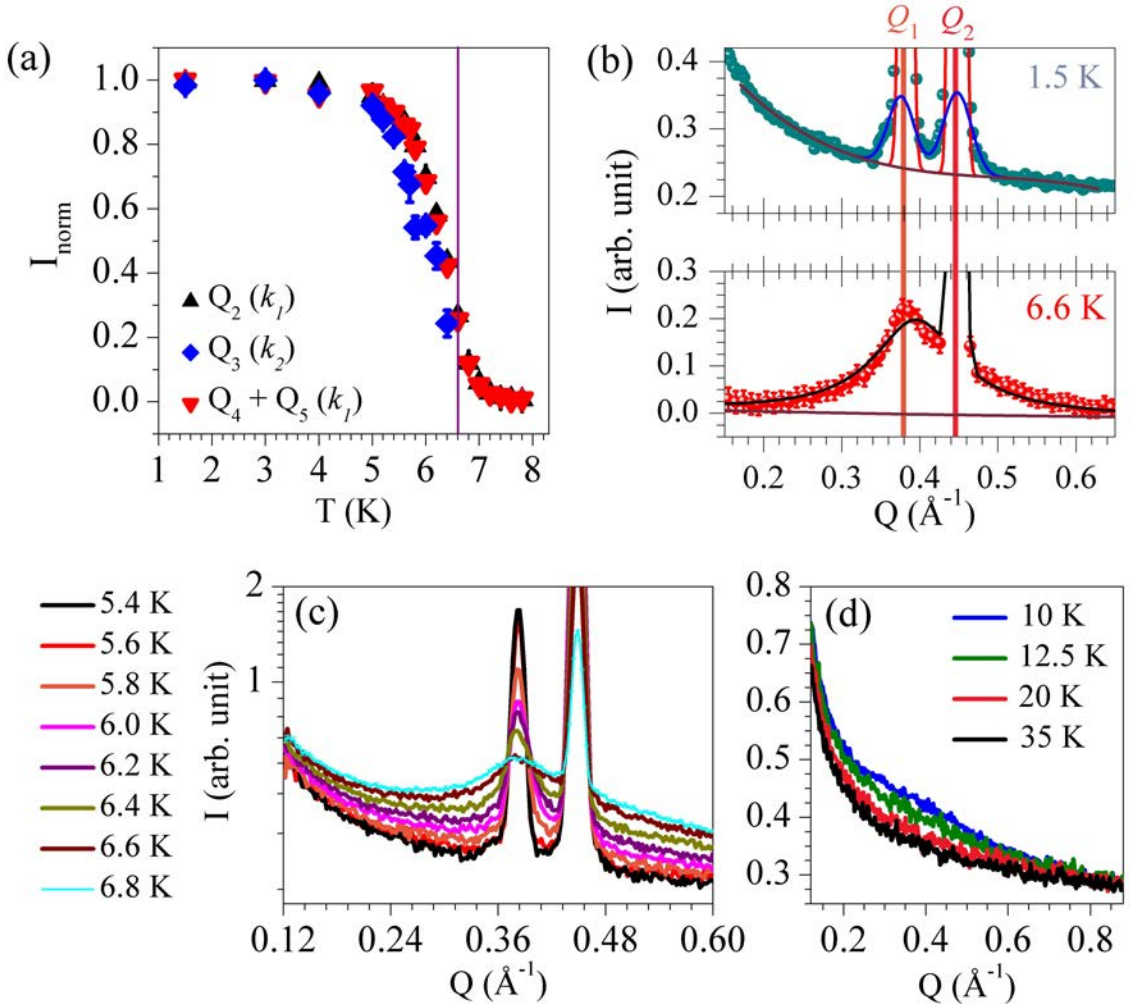

Figure 3.15: (a) Normalized intensity versus temperature plots of reflections at $Q_2 = (0.5, 0, 0)$ and $Q_3 = (1, 0, 0) + k_2$, and the magnetic Bragg peak $\sim 1.35\,\text{Å}^{-1}$ consisting of $Q_4 = (1.5, 0, 0)$ and $Q_5 = (\text{-}0.5, 0, 1)$ reflections. (b) Intensity versus Q curve around the $Q_1 = (\text{-}0.25, 0, 0.25)$ and the Q_2 reflections at (upper) 1.5 K, and (bottom) 6.6 K, respectively. Nuclear scattering background, taken at 35 K, has been subtracted for the 6.6 K pattern. The solid lines are fits described in the text. (c) - (d) Evolution of the diffuse scattering signals in the low-Q region as a function of temperature.

where the SOC is much weaker [9], we propose it is close to the collinear-noncollinear phase boundary. The *2*-phase separation may be caused by local chemical disorder. Alternatively, other types of interactions may be required to further stablize such a state. For example, it has been suggested that the magnetoelectric coupling is responsible for the additional ferrimagnetic microphase in $Ca_3Co_2O_6$ [42]. We note this term is also allowed for the k_2 phase of γCVO due to the broken inversion symmetry of the Co(2) spin lattice [117, 118, 119]. Finally, the complexity of magnetism in γCVO can be further stressed by the reported observation on single crystal samples of magnetic reflections possibly indexed by $k_3 = (\text{-}1/3, 0, 1/3)$ below T^* [100], which are not seen in our study.

3.3 Conclusions and future work

In summary, we have investigated the magnetism of γCVO as a function of temperature using neutron powder diffraction technique. We have established that its low temperature spin structure essentially consists of two single-k phases in a ratio about $65(1):35(1)$. This is the first confirmation of phase separation in a material possessing magnetic 'exchange frustration' but not 'geometric frustration'. For the minority phase, a crossover between long range commensurate and short range incommensurate magnetic order is observed at T^*. Above the magnetic ordering temperature, strong spin fluctuations are observed. Within our experimental resolution, these fluctuations are exclusively modulated k_2.

γCVO can be described by the Hamiltonian writen in Eq. 3.2. Compared with αCVO, the single-ion anisotropy term is weaker in γCVO. This may be responsible for the noncollinear spin structure of the k_2 phase. The onset of the collinear k_1 phase may indicate the anisotropy constant (D) and spin exchange constants ($J^{\perp}$, $J^{\parallel}$) are lying in the critical region where k_1 and k_2 states are degenerate. Alternatively, phase separation indicates Eq. 3.2 may be inadequate to describe γCVO.

Further investigations on this compound are demanded. From a theoretical point of view, it is essential to establish a model which can produce phase separation and incommensurate-commensurate crossover in one of the phases. On the other hand, we shall also perform diffraction measurements on single-crystals to exactly solve its magnetic structure. As discussed in Ref. [118, 117], a magnetoelectric coupling effect is possible in similar systems. Moreover, the polarized neutron diffraction technique is a powerful tool to study the nature of the short range correlation at high temperatures.

CHAPTER 4

MIXED-VALENCE MANGANESE PEROVSKITE, $PR_{0.5}CA_{0.5}MN_{0.97}GA_{0.03}O_3$

4.1 Background

4.1.1 Multiple scale phase separation and colossal magnetoresistance

Colossal magnetoresistance (CMR), which describes a drastic drop in resistance caused by either magnetic field or temperature (Fig. 4.1b), is commonly observed in mixed-valence manganites [2, 10]. Spatial inhomogeneities can spontaneously develop in these materials (phase separation, see Chapter 1.4.2). Phase separation on atomic scales, including polarons (Fig. 4.1c), charge order, orbital order, is often referred as electronic phase separation. This can be related to electron-lattice coupling, electron-electron Coulomb repulsion, and so forth [2, 10]. On the other hand, phase separation on a scale of several hundred nanometres to a few micrometres (Fig. 4.1c) is typically caused by disorder or strains [2, 10, 54].

Currently, it is widely believed that CMR is triggered by the collapse of phase separation on multiple scales [2, 10, 46, 47]. As illustrated in Fig. 4.1, micrometre-scale ferromagnetic metallic domains, which percolate while a large enough magnetic field is applied, have been observed in $La_{1-x}Ca_xMnO_3$ ($x \sim 0.3$) [61]. Correspondingly, CMR in this compound has also been found to correlate with the collapse of polarons (Fig. 4.1c) [120, 56, 57]. These results suggest that both types of phase separation are important to the carrier transport in $La_{1-x}Ca_xMnO_3$ ($x \sim 0.3$). However, the specific role of each phase in the magnetoresistive process is not clear to date. For example, carrier delocalization is often linked to the ferromagnetic Zener double-exchange (DE) [10, 60, 61, 58, 121, 57, 122]. At first sight, this statement may be correct since the ferromagnetic order favors a metal-like state [2]. However, it is questionable in CMR manganites, where the driving mechanism of carrier localization is not DE [2, 10, 46]. Especially for systems showing atomic scale

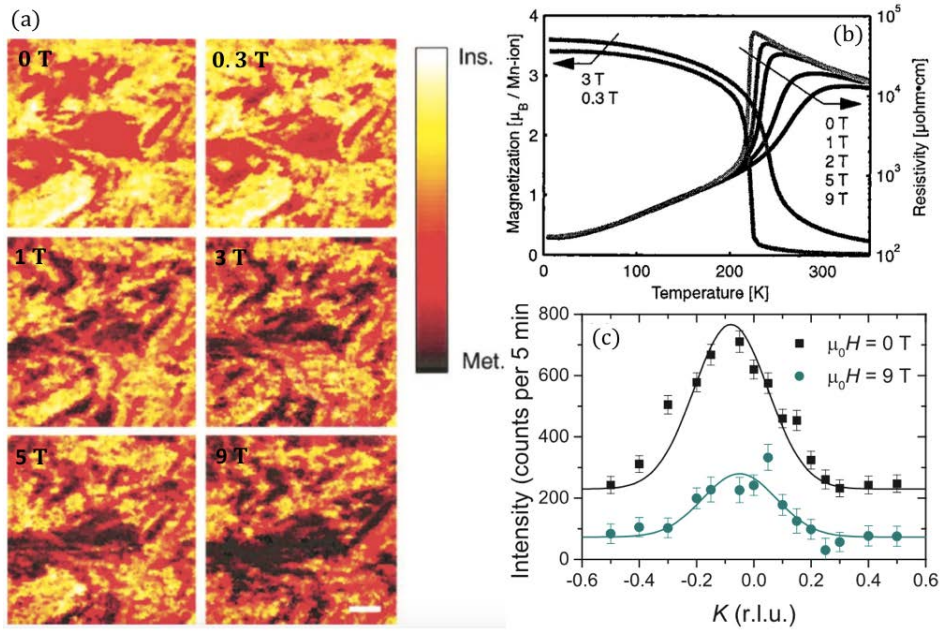

Figure 4.1: (a) Scanning tunneling spectroscopic images ($0.61\,\mu\mathrm{m} \times 0.61\,\mu\mathrm{m}$) of $La_{0.73}Ca_{0.27}MnO_3$ obtained just below T_C [61]. The corresponding magnetic field is labeled in each image. (b) Temperature dependence of Mn magnetic moment and electric resistivity of $La_{0.7}Ca_{0.3}MnO_3$ [61]. (c) Field dependence of the polaron reflection $(1.4, \mathrm{K}, \mathrm{O})$ in $La_{0.7}Ca_{0.3}MnO_3$ when $T = 270\,\mathrm{K}$ ($T_C = 257\,\mathrm{K}$) [120].

inhomogeneities (e.g. polarons, charge/orbital order), i.e. electronic phase separation, DE is less important to the carrier transport than electron-lattice coupling [46]. As a result, it is of particular importance to clarify whether the spin degree of freedom offers an independent force to tune the carrier transport in the carrier delocalization process.

Indeed, the multiple scale phase separation can be reproduced within a unified picture [54]. Ahn *et al* have suggested a model based on the coupling between the electronic and elastic degree of freedom [54], whereas the micrometre phase separation is often linked to the random potential effect caused by quenched disorder in other theories [59, 123]. In other words, by applying additional short-range and long-range strain modulation to the system, both electronic (atomic size) and micrometre phase separation are generated. Since it is feasible to realize strain engineering on thin films, the role of strains on CMR has been investigated. For example, strain-mediated anisotropic electric transport properties have been observed in epitaxially grown $La_{5/8-x}Pr_xCa_{3/8}MnO_3$ films, where the strain is introduced by locking the lattice to an orthorhombic $NdGaO_3$ substrate [124]. The conducting domain percolation process in a strained manganite is also found to correlate with the strains [125]. Microwave impedance images of the $Nd_{0.5}Sr_{0.5}MnO_3$ thin film epitaxially grown on a (110) $SrTiO_3$ substrate are displayed in Fig. 4.2b. At low fields, the system is composed of

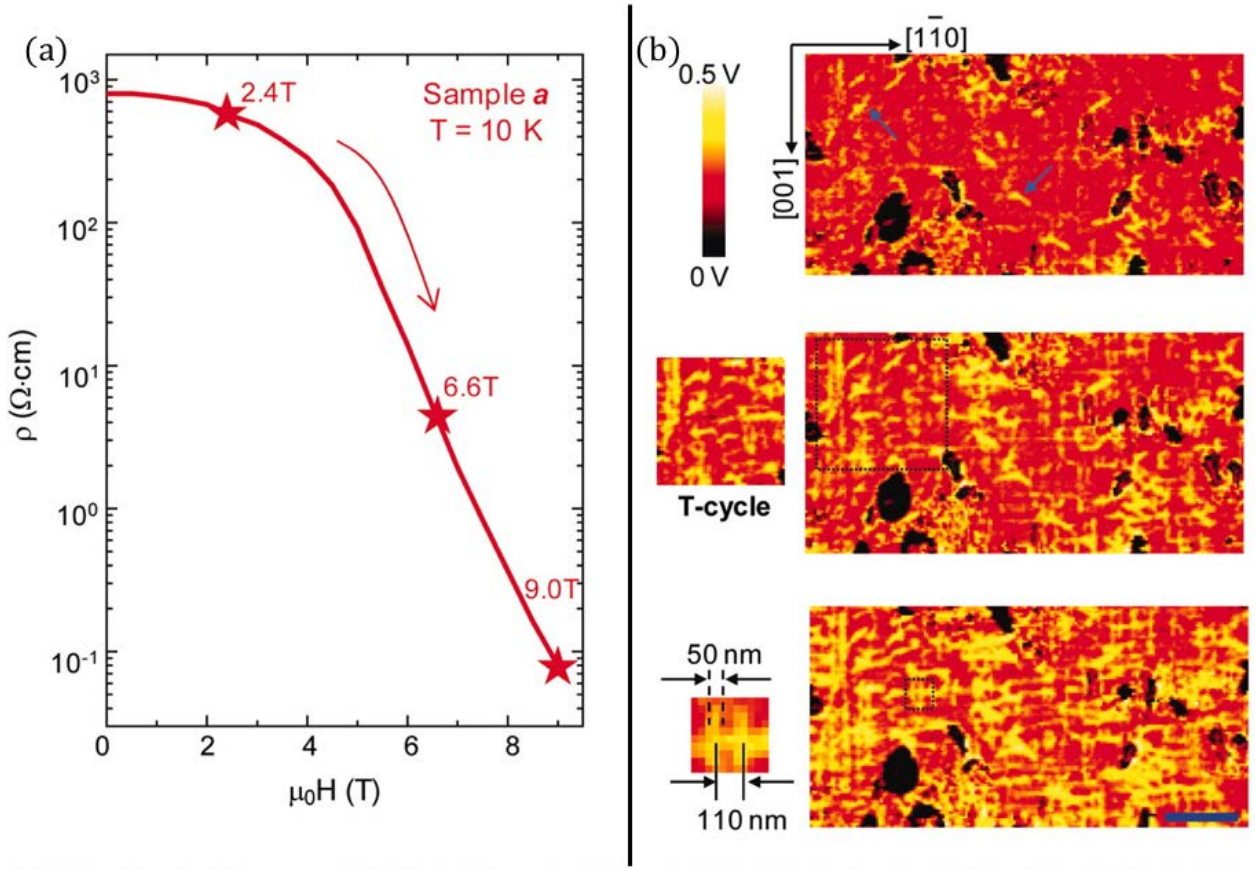

Figure 4.2: (a) Resistance versus magnetic field curve of $Nd_{0.5}Sr_{0.5}MnO_3$ at $T = 10\,K$. (b) Microwave images at different magnetic field. The black regions mark the MnO_x particles [125]. The arrows mark the isolated rodlike ferromagnetic conducting domains which exist at zero field [125]. The strained controlled anisotropic growth regions are highlighted on the left.

randomly distributed rodlike conducting domains (marked by blue arrows). This is a signature of spontaneous micrometre phase separation at zero field [125]. When the percolation is triggered ($\sim 6.6\,T$), these percolative conducting domains (yellow regions) have clear preferential orientations along the (001) and ($1\bar{1}0$) axes of the substrate. These results unambiguously point out that the percolation process, i.e. collapse of micrometre phase separation, in strained thin film manganites is governed by the strains rather than the quenched disorder [124, 125].

Besides the 'substrate locking' in thin films, strains can also nucleate in bulk manganese oxides. For example, $Pr_{0.7}Ca_{0.3}MnO_3$ is a heavily strained system in the charge/orbital order (COO) region as evidenced by the anisotropic broadening of its Bragg reflections (Fig. 4.3) [126]. This is in sharp contrast with the optimal COO compound $Pr_{0.5}Ca_{0.5}MnO_3$ where the strain presence could be barely detected [127]. Since the COO

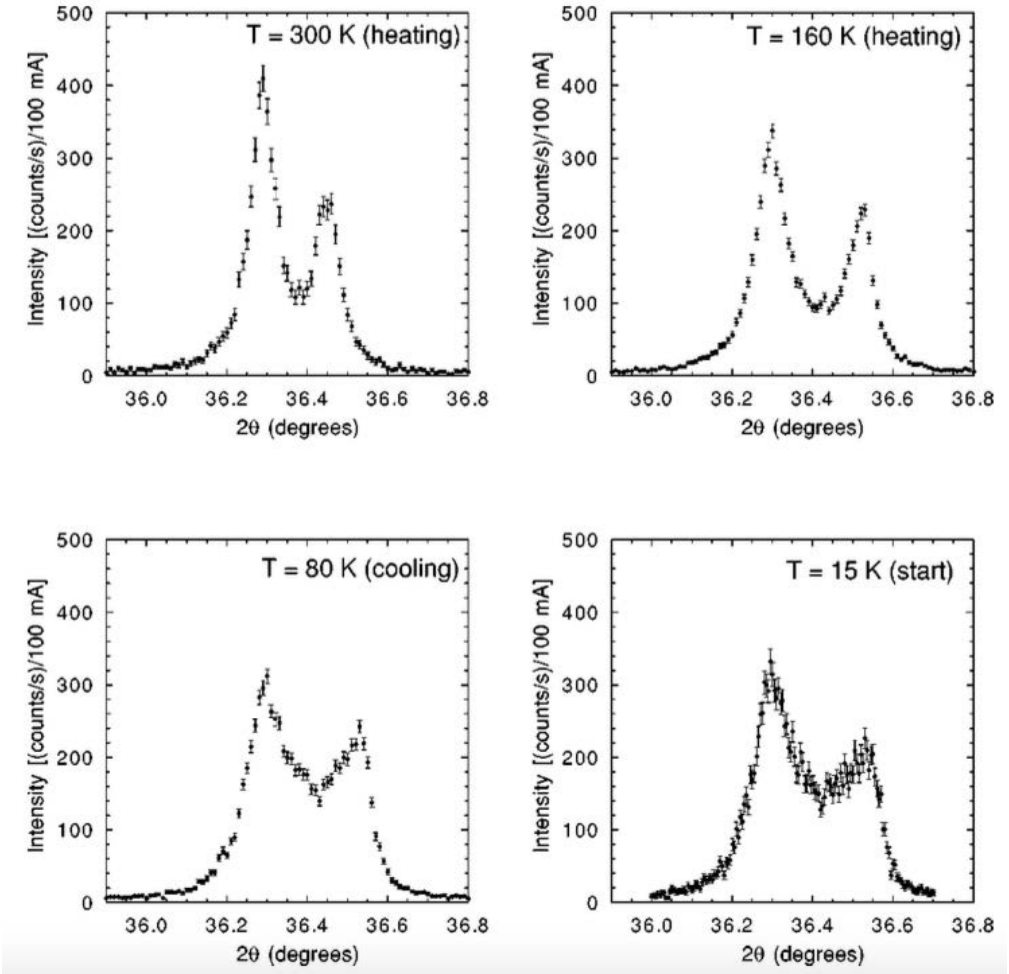

Figure 4.3: Anisotropic strain broadening of the (202)/(040) reflections of $Pr_{0.7}Ca_{0.3}MnO_3$ ($T_{COO} \approx 200\,K$) [126].

of $Pr_{0.7}Ca_{0.3}MnO_3$ is much weaker than that of $Pr_{0.5}Ca_{0.5}MnO_3$ [51, 128], strains may have an effect on the electronic phase separation as well [54]. Unfortunately, the role of anisotropic strains on the electric transport properties in bulk systems has not been investigated so far.

4.1.2 Electronic phase separation and magnetostriction

Due to the strong coupling between elastic and electronic degrees of freedom, the crystallographic structure of CMR compounds is also susceptible to the applied magnetic field. Fig. 4.4b shows the magnetic polaron intensity (I) and the polaron correlation length (ξ) of $La_{0.5}Ca_{0.5}MnO_3$ as a function of magnetic field [58]. This sudden drop of I around 3 T agrees with the onset of magnetoresistance in Fig. 4.4c, as well as the giant volume magnetostriction (ω) in Fig. 4.4c. Based on these observations, the Holstein 'small polarons', which are

localized charge carriers temporarily confined to a single cation site due to the local lattice deformation, have been argued to exist in $La_{0.5}Ca_{0.5}MnO_3$ and the change in ω is the manifestation of its lattice component [58, 129].

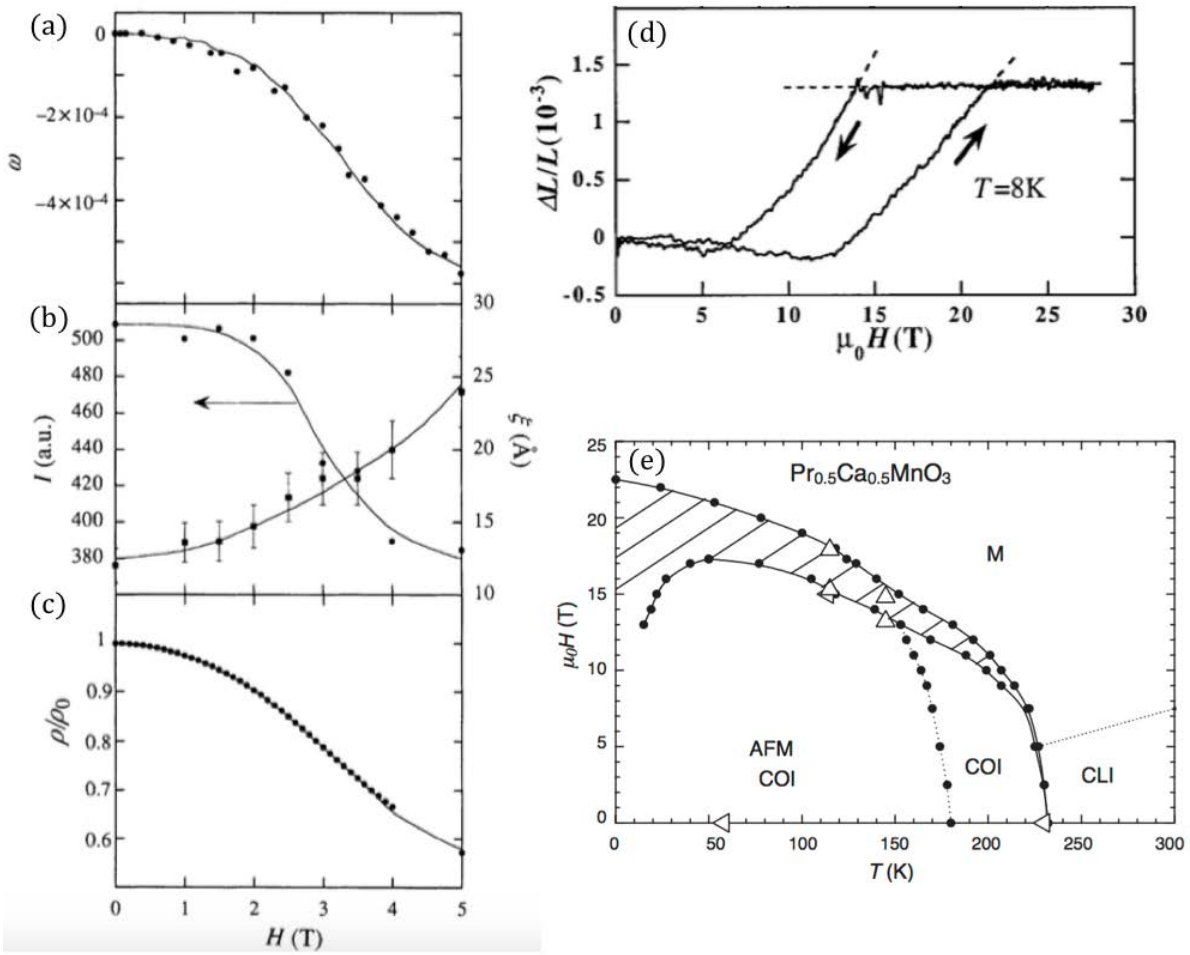

Figure 4.4: (a) Volume magnetostriction, (b) polaron intensity (left) and polaron correlation length (right), (c) resistivity of $La_{0.5}Ca_{0.5}MnO_3$ as a function of magnetic field at $T = 1.1\,T_C$ [58]. (d) Linear magnetostriction of $Pr_{0.5}Ca_{0.5}MnO_3$ at $T = 4\,K$ [128]. (e) Phase diagram of $Pr_{0.5}Ca_{0.5}MnO_3$ determined by the resistivity (solids) and linear magnetostriction (triangles), where AFM = antiferromagnet, COI = charge ordered insulator, M = metal and CLI = charge localized insulator [130].

On the other hand, a giant linear magnetostriction ($\Delta L/L$) effect has been observed in the optimal COO compound $Pr_{0.5}Ca_{0.5}MnO_3$ (Fig. 4.4d). Similarly, the transition of ΔL/L occurs in the region of CMR, as revealed in Fig. 4.4e where the black solid points mark the phase boundary determined by the resistivity

measurements and the open triangles are from the $\Delta L/L$ data [128, 130]. As a result, the giant $\Delta L/L$ has been attributed to the structural transition (elongation of the crystallographic c-axis) caused by the destruction of COO in $Pr_{0.5}Ca_{0.5}MnO_3$ [128].

4.1.3 Electronic phase separation and Jahn-Teller distortion

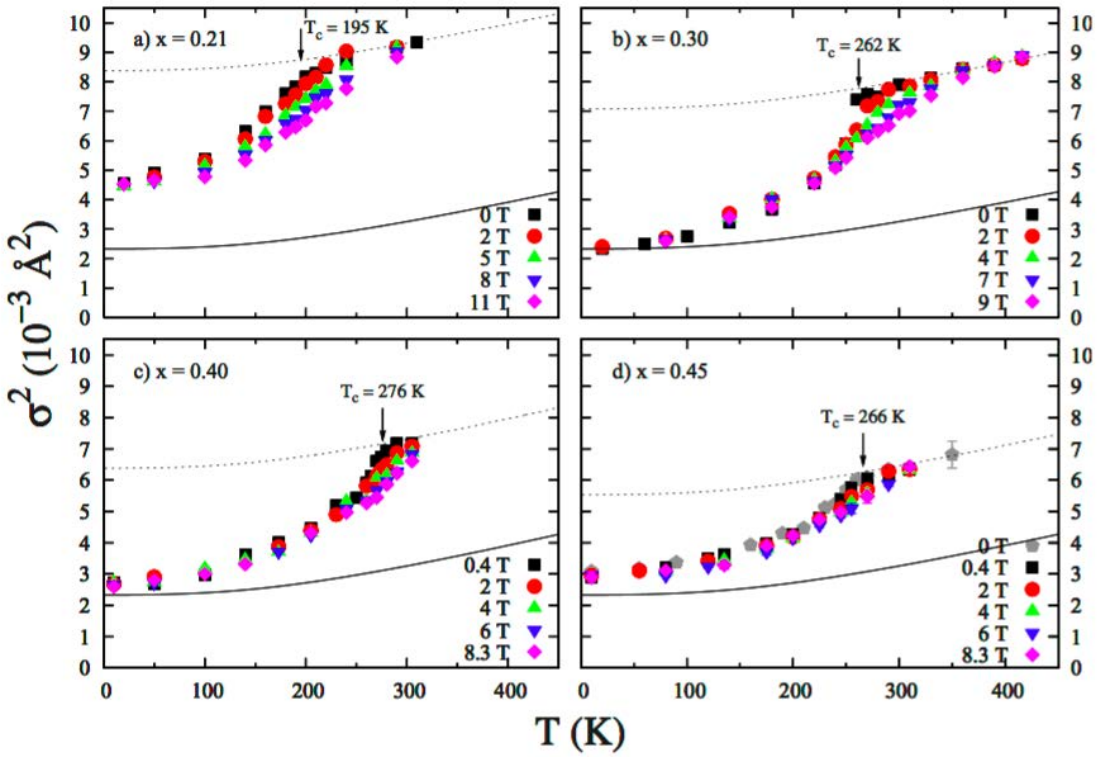

Figure 4.5: σ^2 for the Mn-O pair-distribution function [55], as a function of magnetic field and temperature in $La_{1-x}Ca_xMnO_3$ ($x = 0.21, 0.3, 0.4, 0.45$). The solid line is a fit of σ^2 in the non-Jahn-Teller active lattice $CaMnO_3$.

In this part, we briefly review the relationship between electronic phase separation and Jahn-Teller distortion (Chapter 1.1.6 & 1.2.6) in mixed-valence manganese oxides. Jahn-Teller distortion is an important source of electron-phonon coupling [46]. Therefore it is argued to be one of the driving mechanisms of electronic phase separation [2, 10]. For example, a carrier can be 'self-trapped' in the local potential minimum produced by the strong electron-phonon coupling. The resulting quasiparticle is called a 'Jahn-Teller polaron' [46]. Extended X-ray absorption fine structure (EXAFS) spectroscopy is a powerful tool to probe the local MnO_6-octahedron. The Jahn-Teller distortion level can be characterized by the width (σ) of the Gaussian distribution used to

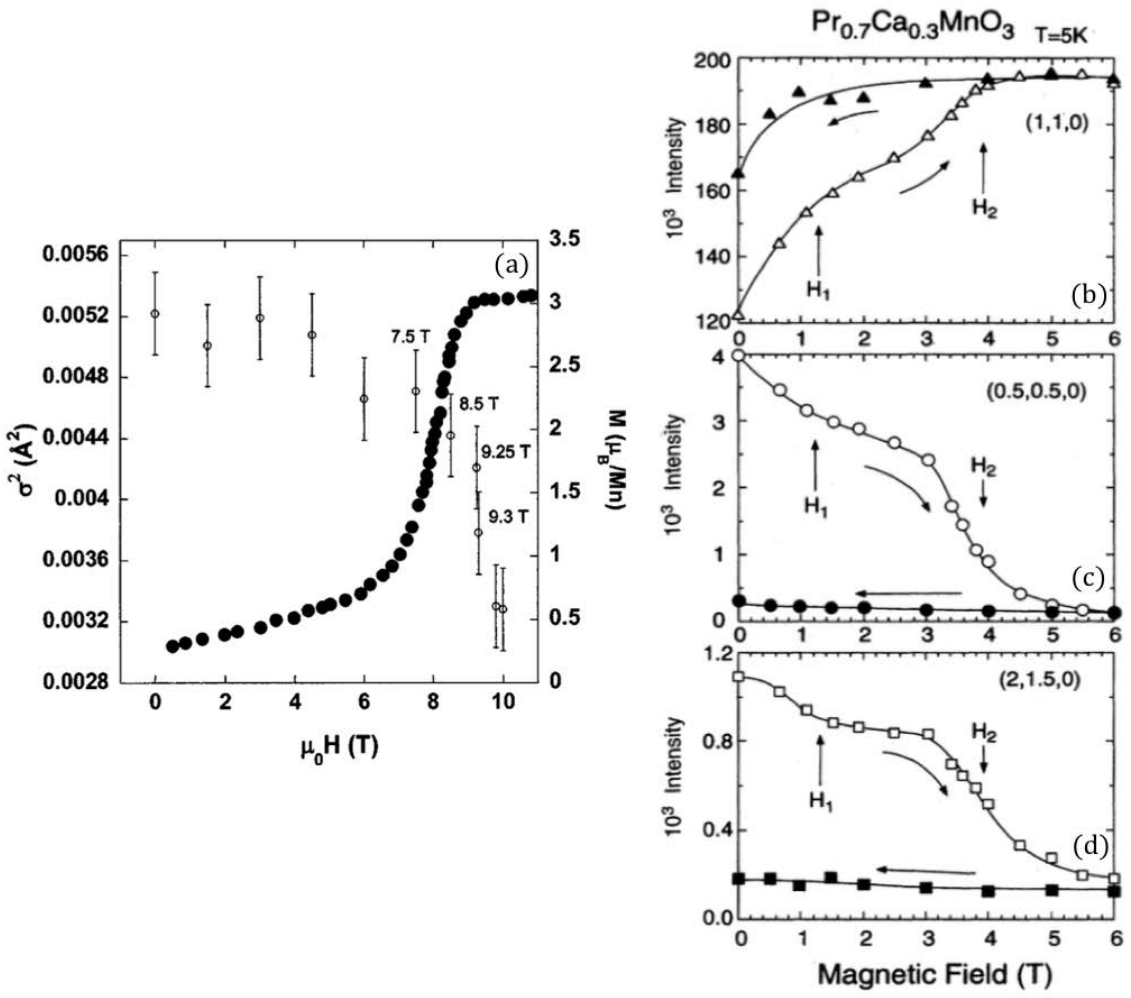

Figure 4.6: (a)The field dependence of σ^2 (open circles) and magnetization (solids) of $La_{0.5}Ca_{0.5}MnO_3$ [132]. (b)-(d) The field dependence of the ferromagnetic, antiferromagnetic and COO Bragg reflections of $Pr_{0.7}Ca_{0.3}MnO_3$, respectively [122].

fit the data [55, 131]. Fig. 4.5 demonstrates the evolution of σ^2 by varying both temperature and magnetic field in the ferromagnetic lanthanide compounds $La_{1-x}Ca_xMnO_3$ ($x = 0.21, 0.3, 0.4, 0.45$) where the CMR occurs around T_C [55, 2]. All samples are significantly distorted in the paramagnetic region. On further cooling, σ^2 is greatly suppressed when ferromagnetism sets in ($T < T_C$). Similarly, applying a magnetic field is also able to suppress the Jahn-Teller distortion. For the other family of CMR compounds with COO, the field dependence of Jahn-Teller distortion has also been investigated. As shown in Fig. 4.6a, the sudden increase in magnetization of $La_{0.5}Ca_{0.5}MnO_3$ is accompanied by the decrease of the distortion parameter $\sigma^2 = < (R - \bar{R})^2 >$, where R is the Mn-O bond length and $\bar{R}$ is the average Mn-O bond length [132]. Since this type of metamagnetic transition is a common signature of COO melting (Fig. 4.6b-d) [122], these results

suggest that the Jahn-Teller distortion is not favoured in the charge/orbital disordered state.

4.1.4 $Pr_{0.5}Ca_{0.5}Mn_{1-x}M_xO_3$, M = Ga, Al, Co, Ti, etc

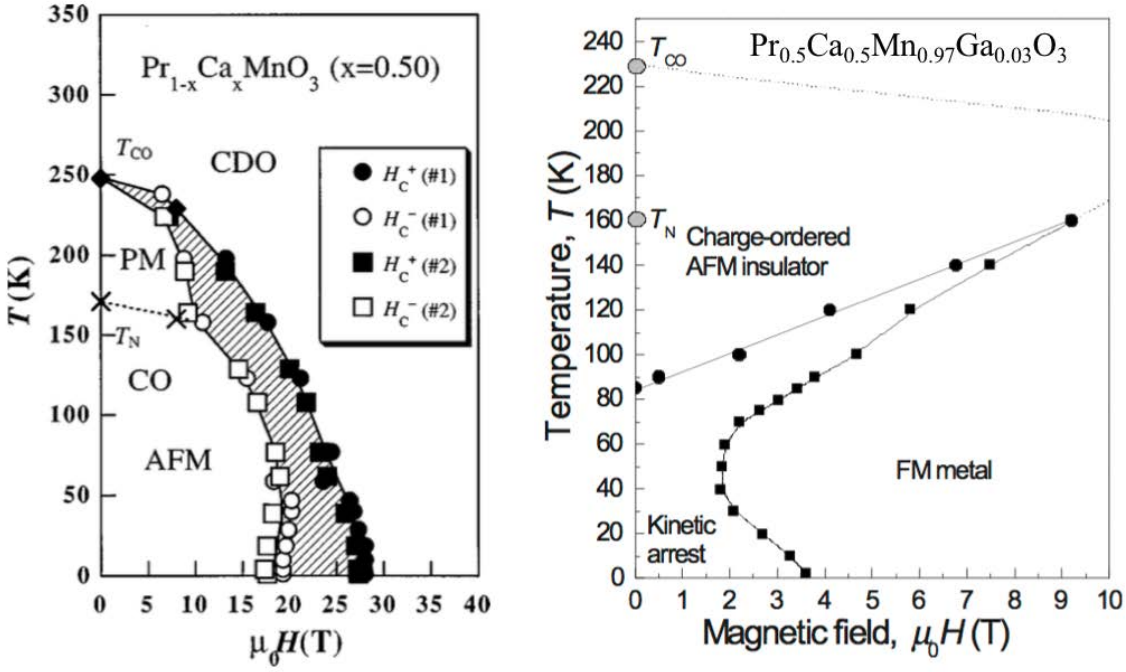

Figure 4.7: Magnetic field - temperature phase diagrams of $Pr_{0.5}Ca_{0.5}MnO_3$ (left) and $Pr_{0.5}Ca_{0.5}Mn_{0.97}Ga_{0.03}O_3$ (right).

Instead of tuning the hole composition on the A-site of a manganese perovskite ($AMnO_3$), substituting Mn with other ions directly affects its spin, charge and orbital ordering. For example, the robust COO in $Pr_{0.5}Ca_{0.5}MnO_3$ can be significantly weakened by a minor Ga^{3+} substitution (3 %) (Fig. 4.7) [128, 133]. This gives the first hint that the electronic phase separation in relevant systems is coupled to these point defects.

Ultrasharp magnetic field induced magnetization steps

Many investigations have been focused on the low temperature multi-step ultrasharp metamagnetic transitions, sometimes also described as magnetic avalanches, in these systems [134, 135, 136, 137]. As shown in Fig. 4.8, ultrasharp metamagnetic transition (width less than 0.2 mT based on the inset of Fig. 4.8d) in $Pr_{0.5}Ca_{0.5}Mn_{0.95}Co_{0.05}O_3$ abruptly sets in between 4.6 K and 4.7 K. When the temperature is further lowered down to 3 K, additional steps appear in the high field region (Fig. 4.8d). In an extreme case, Hardy *et*

al have shown that hundreds of magnetization steps can be realized by cooling $Pr_{0.5}Ca_{0.5}Mn_{0.97}Ga_{0.03}O_3$ to 1.5 K [138]. Each step in magnetization corresponds to a sudden growth of ferromagnetism while the CE (or pseudo-CE) type antiferromagnetic order in the sample is partially suppressed [139, 127]. Since the CE (or pseudo-CE) type antiferromagnetic order in manganites couples tightly with the orbital degree of freedom [2, 122, 52], this antiferro-ferromagnetic transition is also accompanied by a cooperative change of the local lattice distortion, as discussed in the previous section. This sort of diffusionless structure change in manganites is the analogue of the martensite-austenite transformation in alloys [138, 140]. As a result, a martensitic scenario, in which the spin related energy (e.g. exchange interactions, Zeeman energy) is competing with the elastic energy associated with the strains at the antiferromagnetic/ferromagnetic interfaces, has been proposed to quantitatively understand these magnetic avalanches. In this scenario, the spins are locked by these strains at low fields so that the bulk magnetization is not sensitive to magnetic field. However, a sudden growth of ferromagnetism will be promoted once these spins are unlocked by magnetic field.

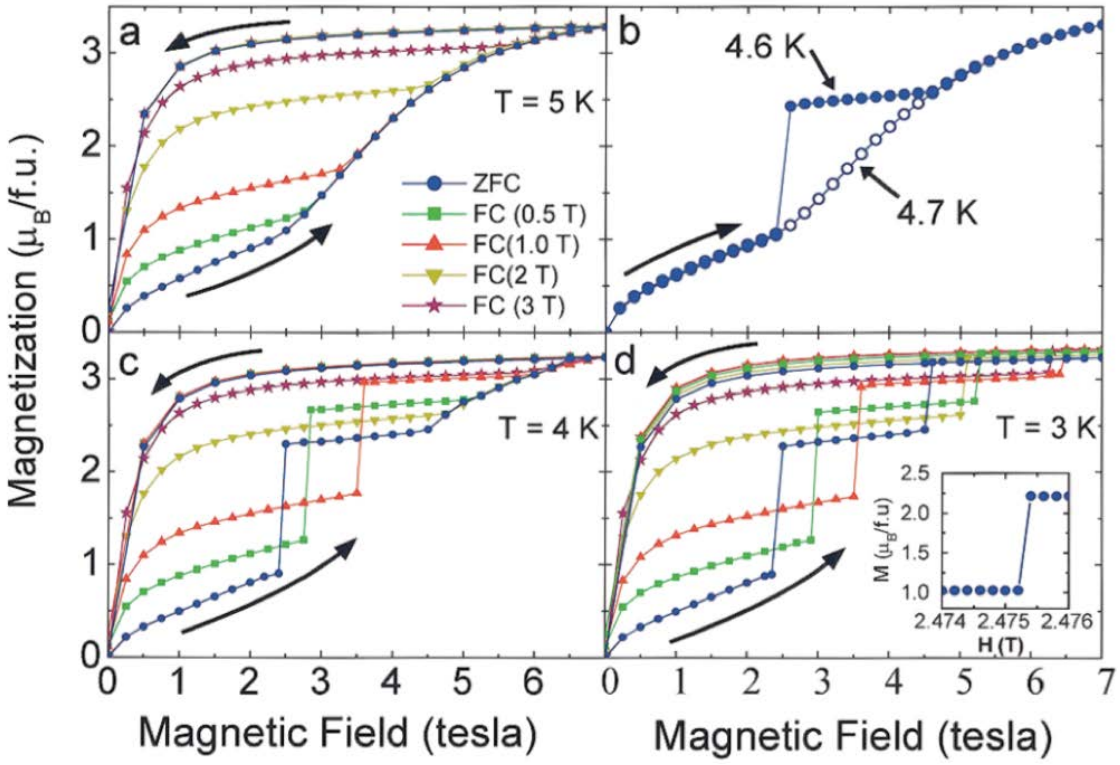

Figure 4.8: a-d, Magnetic field versus magnetization curves of $Pr_{0.5}Ca_{0.5}Mn_{0.95}Co_{0.05}O_3$ under various conditions. FC = field cool, ZFC = zero field cool.

Anisotropic strains and crystallographic phase separation

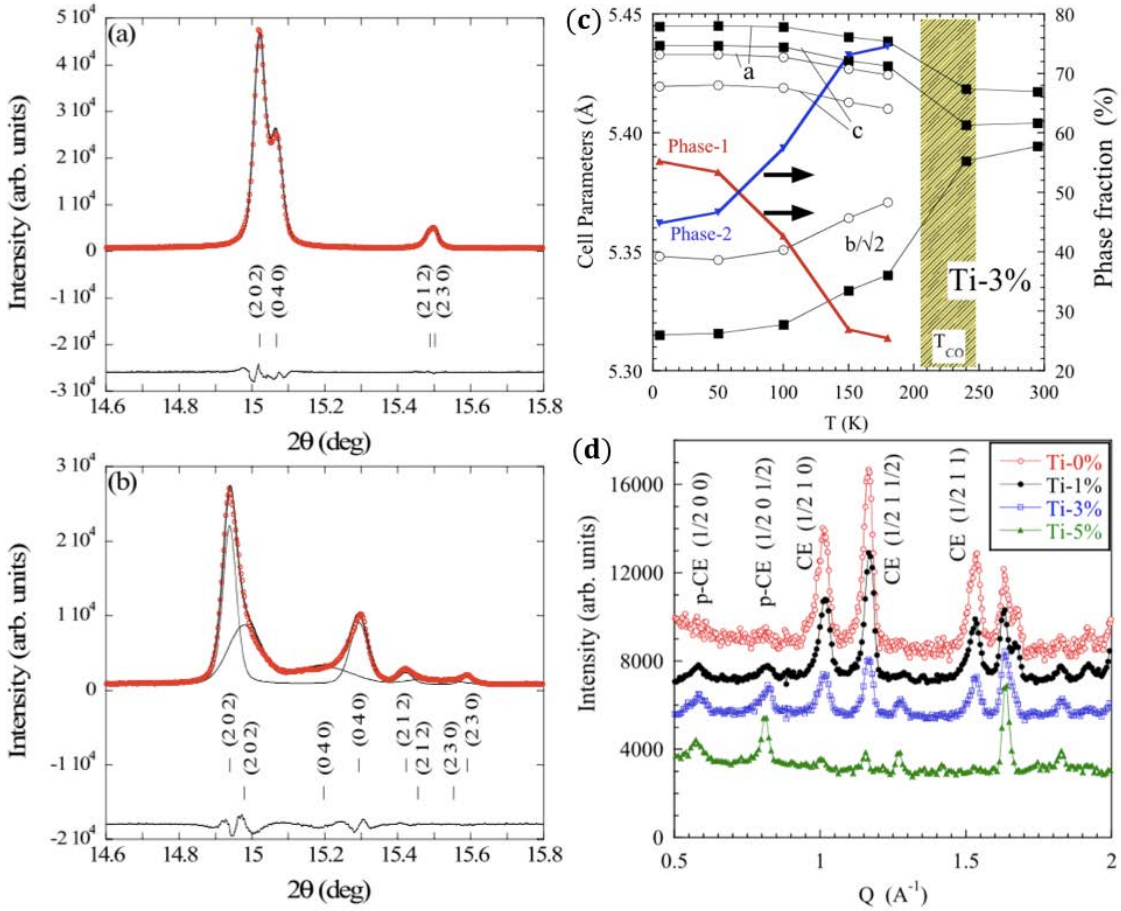

Figure 4.9: Selected region of the synchrotron X-ray powder diffraction ($\lambda = 0.500111(12)$ Å) patterns of $Pr_{0.5}Ca_{0.5}Mn_{0.97}Ti_{0.03}O_3$ [127] at (a) room temperature and (b) 5 K. Two crystallographic phases are needed to fit all the Bragg reflections at 5 K. (c) Temperature dependence of the lattice parameters (left) and the volume fraction of each phase (space group *Pnma*). Phase-1: CE phase. Phase-2: pseudo-CE phase. (d) Neutron powder diffraction patterns of $Pr_{0.5}Ca_{0.5}Mn_{1-x}Ti_xO_3$.

The crystallographic structures of some $Pr_{0.5}Ca_{0.5}Mn_{1-x}M_xO_3$ systems have been studied by the high-resolution synchrotron X-ray diffraction technique [127, 141, 142]. In the charge/orbital ordered region, these systems are found to be strongly strained. The presence of anisotropic strains will broaden the corresponding

Bragg reflections (Fig. 4.9b), which can be described by the Stephens formalism [143]:

$$\sigma^2_{hkl} = \sum_{H,K,L}^{H+K+L=4} S_{HKL} h^H k^K l^L, \tag{4.1}$$

where σ^2_{hkl} is the broadening of the (h, k, l) reflection and S_{HKL} are the parameters refined from the peak shape [102, 106]. For the $Pr_{0.5}Ca_{0.5}Mn_{1-x}M_xO_3$ compounds with an orthorhombic unit cell, this equation reduces to six non-zero terms:

$$\sigma^2_{hkl} = S_{400}h^4 + S_{040}k^4 + S_{004}l^4 + S_{220}h^2k^2 + S_{202}h^2l^2 + S_{022}k^2l^2. \tag{4.2}$$

As an example, the X-ray diffraction patterns of $Pr_{0.5}Ca_{0.5}Mn_{0.97}Ti_{0.03}O_3$ above and below the COO temperature (~ 240 K), measured by García-Muñoz *et al* [127], have been displayed in Fig. 4.9a-b. At room temperature, the pattern can be refined within a single phase approach and the strain broadening parameters are negligible (Table. 4.1). In sharp contrast, these Bragg peaks are significantly broadened at 5 K. Moreover, there are more than *four* peaks in this region, meaning the single phase approach is not enough to match all these peaks. Alternatively, a two phase approach is able to capture all these features (Fig. 4.9b). Indeed, the crystallographic phase separation picture is required to explain the coexistence of CE and pseudo-CE antiferromagnetic phases in this compound revealed by the neutron powder diffraction measurements (Fig. 4.9d).

Table 4.1: Volume fractions, unit cell distortions (D) and strain parameters of $Pr_{0.5}Ca_{0.5}Mn_{0.97}Ti_{0.03}O_3$ [127].

	Fraction	D	S_{400}	S_{040}	S_{004}	S_{220}	S_{202}	S_{022}
Room temperature	100 %	0.997	0.178(3)	0.087(1)	0.160(6)	-0.134(5)	0.89(1)	-0.165(7)
5 K (CE)	55 %	0.9764	0.175(9)	0.239(4)	0.33(1)	-0.02(2)	1.32(3)	-0.02(2)
5 K (pseudo-CE)	45 %	0.9855	2.17(6)	3.02(6)	4.3(1)	-2.9(1)	7.8(2)	-4.5(2)

Besides the Jahn-Teller distortion which is related to the MnO_6-octahedron, the distortion of the unit cell can be charaterized by a parameter $D = \frac{\sqrt{2}b}{a + c}$ (with space group *Pnma*). An undistorted lattice would have $D = 1$, where $D \neq 1$ in distorted cases [127, 141, 142]. As shown in Table. 4.1, the unit cell of $Pr_{0.5}Ca_{0.5}Mn_{0.97}Ti_{0.03}O_3$ is almost undistorted at room temperature, whereas both CE and pseudo-CE phases are highly distorted at 5 K. It is worth noting that the CE phase in all $Pr_{0.5}Ca_{0.5}Mn_{1-x}M_xO_3$ compounds has a more distorted unit cell than the pseudo-CE phase. This is also consistent with the $Pr_{1-x}Ca_xMnO_3$ family [50]. Most of all, COO in both families seems to correlate with D, i.e. the unit

cell distortion tends to stabilize COO [51, 128, 127, 139]. As a result, the COO in the CE phase is more robust than that of the pseudo-CE phases, which is responsible for the two-step metamagnetic transition phenomenon observed in these systems [133, 135]. Specifically, the low field transition is due to the COO melting in the pseudo-CE phase, while higher magnetic field is needed to suppress the COO in the CE phase.

We also emphasize that the less distorted pseudo-CE phase is transforming into the CE phase as temperature is lowered (Fig. 4.9c). On the other hand, the pseudo-CE nuclear lattice is much more strained compared with the CE nuclear lattice (Table. 4.1). This may be caused by the inhomogeneous distribution of M ions in the sample, as stated in Ref. [127].

4.2 Results

4.2.1 Research motivations

In general, by equipping small angle neutron scattering (SANS) and time-of-flight neutron powder diffraction (TOF-NPD) techniques with state-of-the-art sample environments, we want to monitor the evolution of the multiple scale phase separation by varying the magnetic field; as well as check their coupling to the crystallographic lattice. Based on the previous studies, the spin degree of freedom seems to be indispensable to the carrier delocalization [10, 60, 61, 58, 121, 57, 122], whereas DE is not the driving force of the carrier localization in CMR manganites [2, 10, 46]. On the other hand, spins can be locked by strains through magnetoelastic coupling [138]. To our knowledge, the correlation between DE and carrier delocalization in a strained manganite has not been studied to date.

On the other hand, the giant volume (linear) magnetostriction observed in manganese perovskites has been associated with the collapse of electronic phases such as polarons and COO (Fig. 4.4). This scenario has never been verified using the diffraction technique, which directly probes the lattice parameters of the unit cell. Instead, most of the microscopic structure investigations performed in the past have focused on the local Jahn-Teller distortion. All these measurements suggest that the Jahn-Teller distortion in manganese perovskites is weakened by magnetic field across the melting of polarons (COO) (Fig. 4.5 & 4.6).

Besides the magnetism and electric transport properties, the orbital physics is another key concept in transition-metal oxides [52]. For the CMR compounds, an orbital order populates when the system is an insulator [2, 10]. However, the orbital arrangement in the metallic region remains an open question so far. Even in the metallic region, a large fraction of localized carriers should still survive due to the low electric conductivity of the 'bad metal' [2, 144, 145]. These localized carriers are expected to promote some sort of

orbital arrangement such as orbital order or orbital liquid [52]. For example, Cépas *et al* have suggested a $d_{x^2-y^2}$ type orbital order may be stabilised by magnetic field in the half-doped manganites where the zero field orbital order is $d_{3x^2-r^2}/d_{3y^2-r^2}$ type [146]. However, magnetic field induced orbital order has never been observed in these systems. Among all the factors, Jahn-Teller distortion is the key to understand the nature of orbital order. First of all, the crystal field splitting, which correlates with the electron-phonon coupling strength λ (Chapter 1.2.6), is determined by the amplitude of Jahn-Teller distortion. This means a larger Jahn-Teller distortion corresponds to more localized charge carriers [2, 47]. Secondly, the Jahn-Teller distortion mode is responsible for the symmetry of the active e_g orbital [10].

In summary, we are trying to answer the following three questions by carrying out this research project:

1. Does DE couple to the carrier delocalization in a strained manganite?

2. Is the collapse of electronic phase separation responsible for the giant magnetostriction effect in a strained manganite?

3. What is the magnetic field dependences of the Jahn-Teller distortion in a strained manganite?

4.2.2 Data analysis

Time-of-flight neutron powder diffraction

The patterns obtained from TOF-NPD measurements have been analyzed using the Rietveld method described in Appendix A. In this part, we will use the patterns taken at $T = 150\,\mathrm{K}/B = 0\,\mathrm{T}$ and $T = 150\,\mathrm{K}/B = 10\,\mathrm{T}$ as an example to show the general refinement procedure. We have chosen the space group *Pnma* to describe the crystallographic structure of $Pr_{0.5}Ca_{0.5}Mn_{0.97}Ga_{0.03}O_3$ (PCMGO) [139]. For the TOF-NPD pattern, the convolution pseudo-Voigt with back-to-back exponential functions are required to fit the profiles of the Bragg reflections [106, 147]. The instrumental resolution parameters were obtained by measuring the standard $Na_2Ca_3Al_2F_{14}$ sample. For the pseudo-CE phase, these parameters have been fixed and only the *6* strain parameters (Stephens formalism [143]) were allowed to vary during the refinement. For the CE phase, it is much less strained and only occupy a minor fraction at high temperatures [127, 141, 142, 139]. As a result, only the Gaussian component Sig-2 was refined to fit the peak profiles [106, 147]. A third phase, coming from the Al-holder has been treated properly using the LeBail method [148].

In this paragraph, only the sloping background at small d-spacings has been fitted. As discussed in Ref. [127, 141, 142, 139], $Pr_{0.5}Ca_{0.5}Mn_{0.97}Ga_{0.03}O_3$ demonstrate crystallographic phase separation in the COO region ($T < \sim 240\,\mathrm{K}$). However, the more distorted CE phase has a very low volume fraction at high temperatures (Fig. 4.9c). Since the TOF-NPD technique does not have as high resolution as the synchrotron X-ray diffraction, it is reasonable to check whether this minority CE phase can be resolved at 150 K. The refined pattern using a 1-phase model is shown in Fig. 4.10a. Although the overall fitting quality is satisfactory, it is clear that the peak intensities around 2.70 Å (3.82 Å) have been under- (over-) estimated. On the other hand, the 2-phase refinement produces much better profiles to match these peaks (Fig. 4.10b). The refined lattice parameters, atomic positions, strain parameters and phase fractions are listed in Table 4.2.

Table 4.2: Refined structural parameters of PCMGO under the *Pnma* space group. The isotropic displacement parameters have been fixed to the values in Ref. [141]. The pattern at 250 K was refined using the 1-phase model.

	$T = 250\,\mathrm{K}$	$T = 150\,\mathrm{K}$, pseudo-CE phase	$T = 150\,\mathrm{K}$, CE phase
Volume fraction (%)	100	92(3)	7.5(5)
a (Å)	5.4109(6)	5.4142(5)	5.497(3)
b (Å)	7.6176(7)	7.5939(4)	7.508(3)
c (Å)	5.4024(6)	5.4047(6)	5.398(1)
D	0.9963(1)	0.9926(1)	0.9747(5)
(Pr, Ca) site $(x, 0, z)$			
x	0.031(2)	0.039(1)	0.127(9)
z	-0.006(3)	-0.000(2)	-0.24(1)
O(1) site $(x, 0, z)$			
x	0.486(2)	0.490(2)	0.47(1)
z	0.071(2)	0.070(1)	0.18(1)
O(2) site $(x, y\, z)$			
x	0.285(1)	0.282(1)	0.261(8)
y	0.0358(5)	0.0359(5)	0.051(4)
z	-0.283(1)	-0.282(1)	-0.289(9)
S_{400}	1.9(3)	2.6(3)	0
S_{040}	0.29(3)	1.68(7)	0
S_{004}	0.4(1)	2.5(3)	0
S_{220}	-1.3(2)	-2.9(3)	0
S_{202}	1.0(3)	4.8(4)	0
S_{022}	0.1(2)	-2.9(3)	0

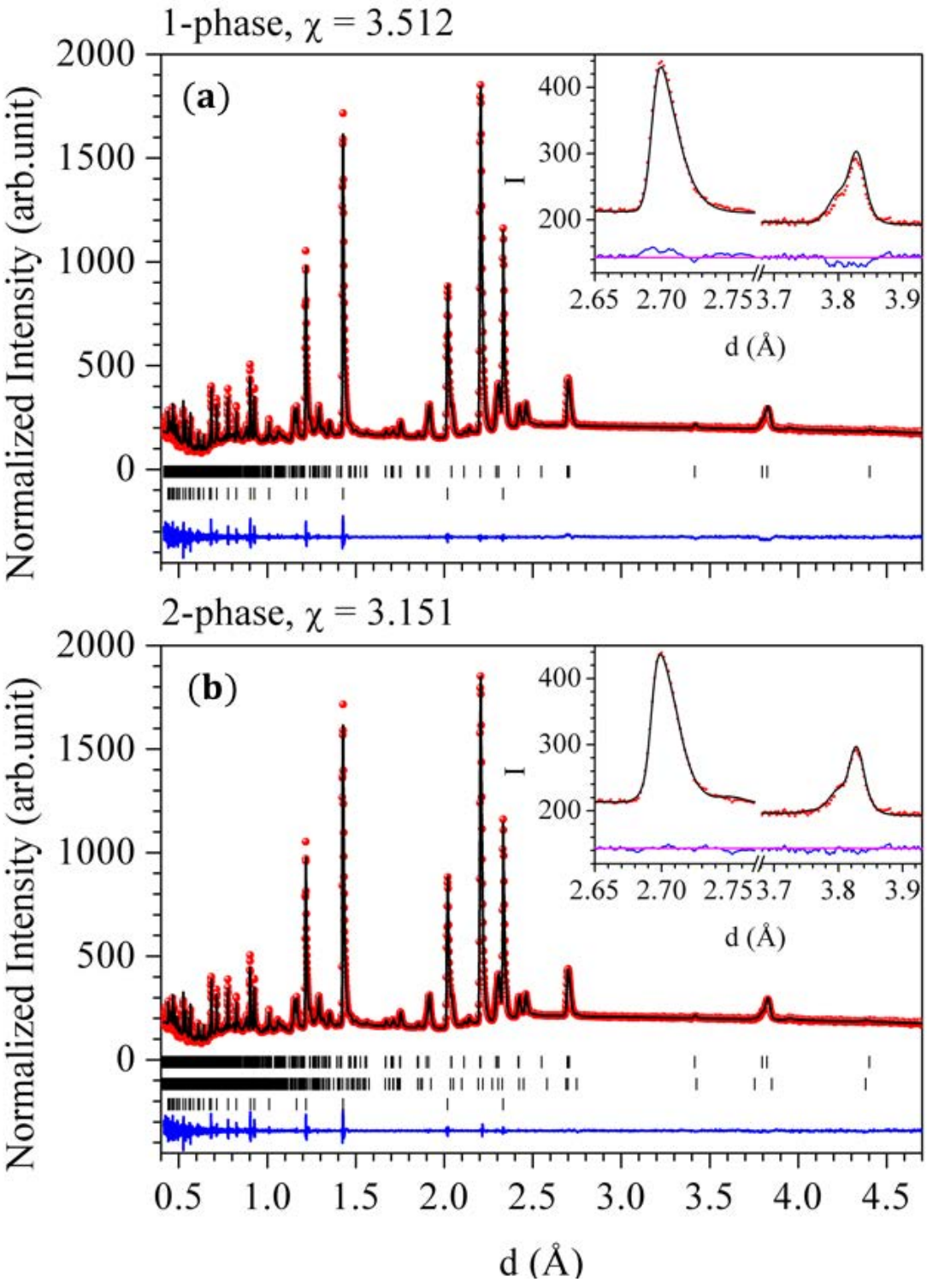

Figure 4.10: Rietveld refinements on the pattern collected at 150 K/0 T using the (a) 1-phase and (b) 2-phase models. From top to bottom, the vertical bars label the Bragg position of the pseudo-CE phase, Al in (a) and pseudo-CE phase, CE phase, Al in (b).

In order to provide further evidence of the presence of a minor CE phase, we have adopted an alternative approach: we go back to the 1-phase model, whereas we also refine the background below the Bragg reflections at large-d spacings. Then we compared the profiles of this 'background' with the profiles of the CE phase obtained from the 2-phase refinement. As shown in Fig. 4.11, the fitting quality is significantly improved comparing with the other 1-phase fitting in Fig. 4.10a.

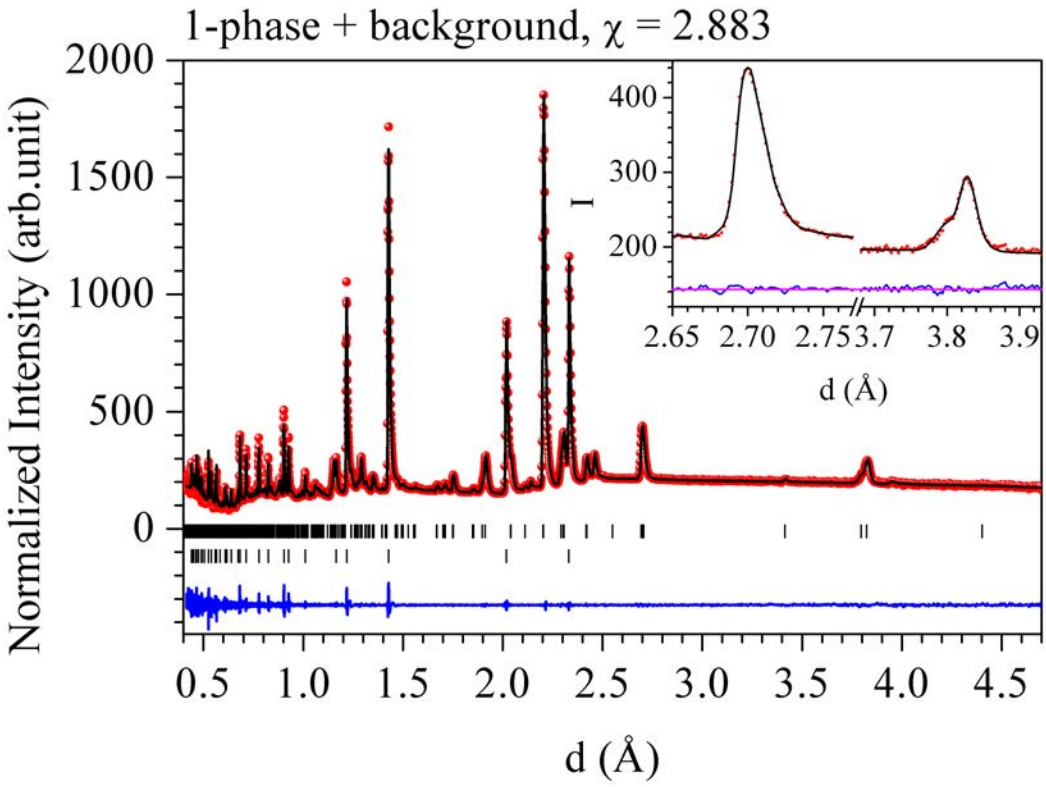

Figure 4.11: Rietveld refinement on the pattern collected at 150 K/0 T. Only one crystallographic phase was refined, while the other minor phase was treated as the background (see main context).

Most of all, the profiles of the CE phase are also captured in the background refinement (Fig. 4.12b). The refined structural parameters are also consistent with those in Table 4.2 within the errors, which further proves the validity of this 1-phase+background method (Fig. 4.12a &c). In sharp contrast, the structural parameters obtained from both 1-phase+background and 2-phase methods do not match with those obtained from the simple 1-phase method, as revealed in Fig. 4.12a &c.

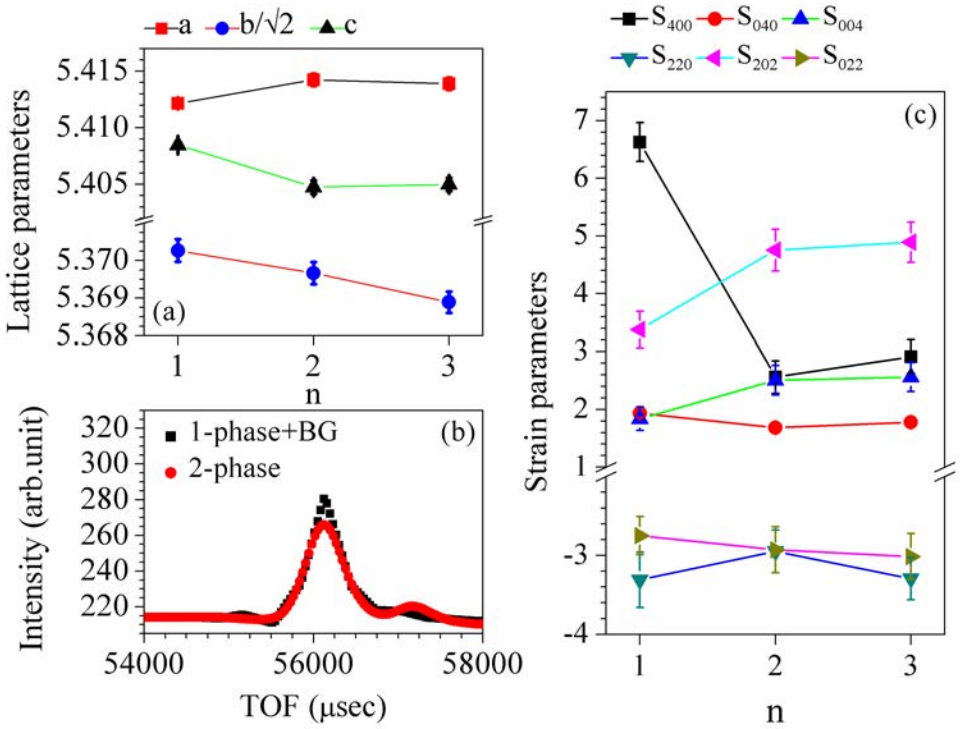

Figure 4.12: (a) and (c) Comparisom of the structural parameters obtained from the 3 different methods discussed in the main context. (b) The CE-phase profiles, corresponding to $d \simeq 2.7\,\text{Å}$, extracted from the 2-phase (red) and 1-phase+background (black) methods.

The 1-phase+background method used at zero magnetic field can be extended to the high field refinements. Since the nuclear Bragg reflections at large d-spacings will be superimposed by the strong ferromagnetic signals in the ferromagnetic region, it would be very hard to refine the minor CE phase. Moreover, the CE COO has been proven to be more robust against the magnetic field than the pseudo-CE COO [51, 128, 139, 127]. This leads to a two-step metamagnetic transition in the $Pr_{0.5}Ca_{0.5}Mn_{1-x}M_xO_3$ family [133, 135]. Based on our estimation, we should still be able to resolve the ferromagnetic transition caused by the minor CE COO melting as long as we can reach the corresponding critical field. However, the second metamagnetic transition, which is associated with the collapse of CE COO, is much smoother compared with the one in the low field region [133, 135]. This continuous feature may further prohibit us from observing the CE COO melting. Since we shall mainly focus on the majority pseudo-CE phase here, the 1-phase+background treatment is a more suitable choice. If the critical field of CE COO melting is beyond our reach in experiments, such 'CE background' would not change with the varying field. On the other hand, any continuous or discontinuous

intensity increase due to the CE COO melting will be captured by this method as well. We note this will not affect the pseudo-CE phase refinement since we can experimentally resolve enough peaks.

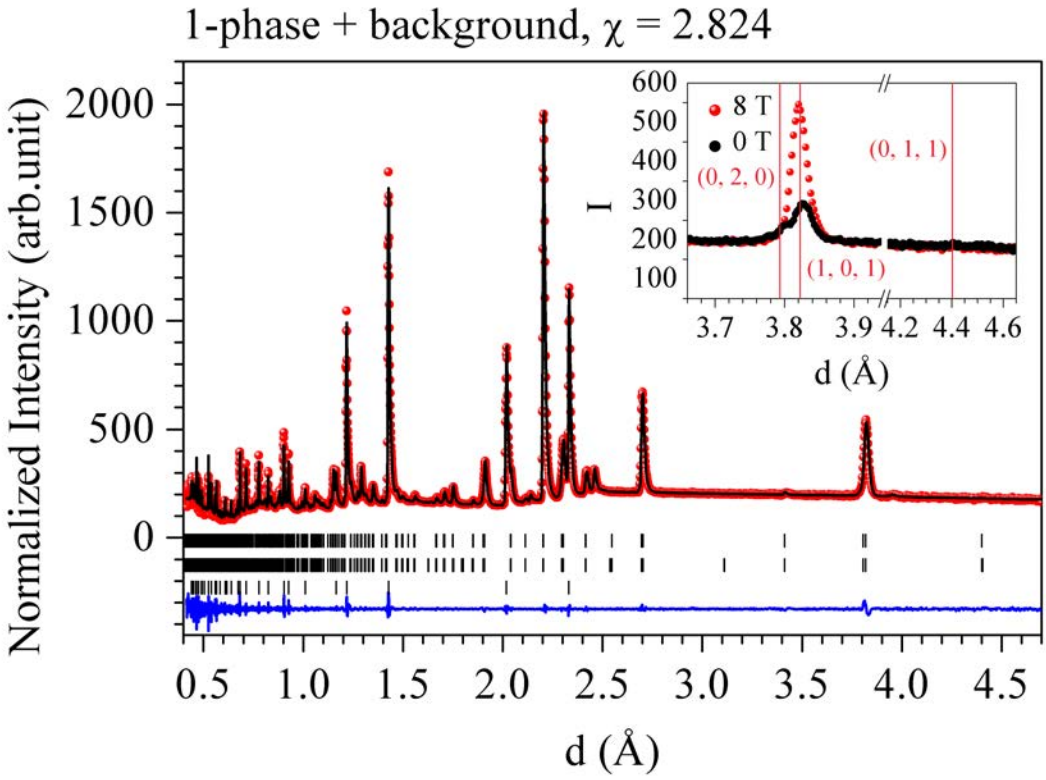

Figure 4.13: Main panel, Rietveld refinement of the pattern collected at 150 K/8 T. Inset: A comparison between the 150 K/8 T and 150 K/0 T patterns. The absence of $(0, 1, 1)$ peak clearly indicates the preferential orientation of the spins with respect to the crystallographic structure.

Since the field-induced ferromagnetism is well established in relevant systems [139], we can escape the representation analysis and start from the lowest symmetry where spins are parallel with each other. The spin orientation, on the other hand, can be obtained by analyzing the intensities of the ferromagnetic Bragg reflections in the high-d region. For example, we cannot probe any intensity at first Bragg point $(0, 1, 1)$ (Fig. 4.13inset), which immediately indicates the spins are not alighed along the magnetic field; and they do not have a major component along the a-axis. Based on the discussion in Chapter 2.44, the spin orientation can be further pinned down by checking the $(0, 2, 0)$ and $(1, 0, 1)$ reflections. The strongest intensity is observed at $(1, 0, 1)$. The $(0, 2, 0)$ reflection does not have an obvious change at 8 T. As a result, the spins should be perpendicular to $(1, 0, 1)$, i.e. the b-axis in an orthorhombic lattice. This hypothesis has been confirmed by the Rietveld

refinement on the pattern (Fig. 4.13). The refined magnetic moment is $\sim 1.6\,\mu_B$/Mn. We note this should be an underestimated value due to the presence of 90° type domains.

Impurity phase: We have also detected three weak peaks which belong to neither of the phases discussed above. Their intensities are not temperature dependent. The strongest peak is located at ~ 2.46 Å in Fig. 4.10, 4.11 and 4.13. We have identified this impurity phase as Mn_3O_4 [149], which has also been discovered in the relevant system $Pr_{0.5}Ca_{0.5}Mn_{1-x}Co_xO_3$ [141].

Small angle neutron scattering

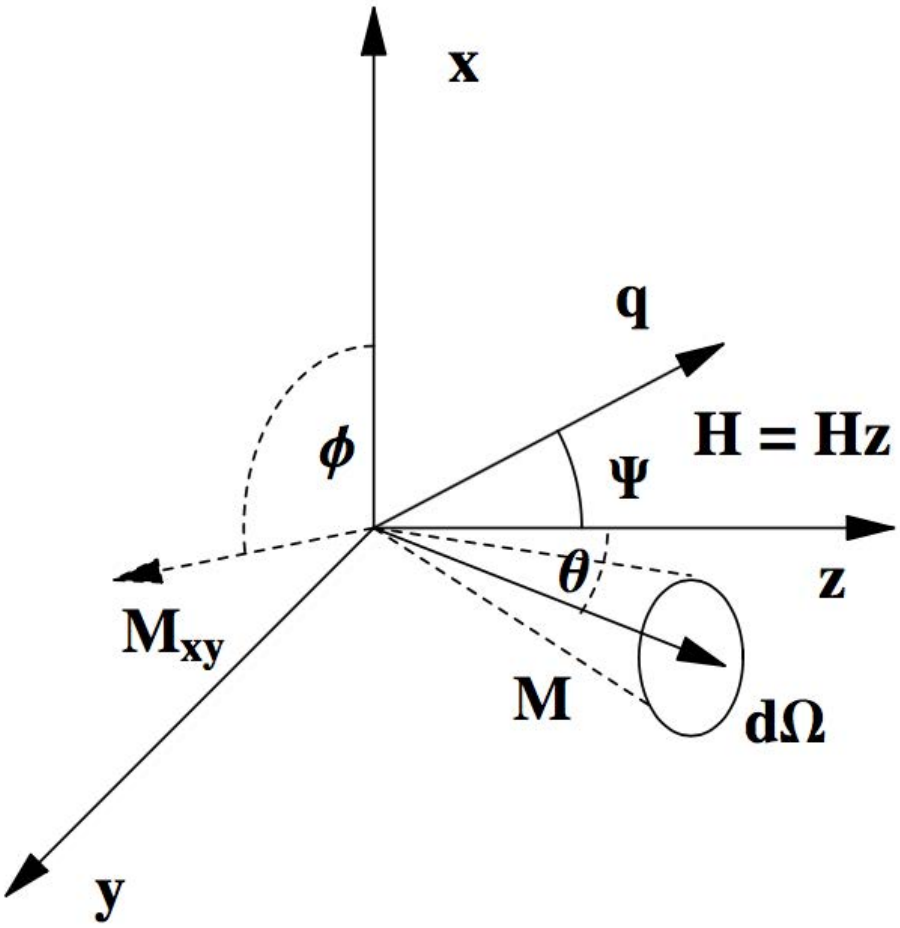

Figure 4.14: The scattering geometry in a SANS experiment. The magnetic field is along the z-axis. The scattering vector is denoted as q.

Now we consider an isotropic polycrystalline magnetic material which does not possess net magnetization at zero field. When the magnetic field is turned on, the magnetic moment will be aligned along the magnetic

field. Provided that the 2-dimensional detector is always perpendicular to the direct beam (Fig. 2.6) and the neutrons are only sensitive to the magnetic moment perpendicular to q, the intensity detected at a wavevector transfer q can be writen as

$$I(q, \Psi) = I_A(q) + I_B(q) \sin^2\Psi, \tag{4.3}$$

where Ψ is the angle between the magnetic field and q (Fig. 4.14), $I_A(q)$ contains the isotropic nuclear scattering signal as well as the magnetic scattering signal from the spins not aligned by the magnetic field, $I_B(q)\, sin^2\Psi$ is the pure magnetic signal from the spins aligned by the magnetic field [150, 151, 152].

We have covered a wide q range from 2.2×10^{-3} Å^{-1} to 0.23 Å^{-1} in our experiments. This enables us to monitor the magnetic field dependence of micrometre and electronic phase separation simultaneously. For the micrometre phases, they can be described by the modified Porod's equation:

$$I_m(q) = 2\pi(\Delta\rho_m)^2(\frac{S}{V})_m q^{-4} exp(-q^2\sigma_m^2), \tag{4.4}$$

where $(\Delta\rho_m)^2$ is the magnetic contrast, $(\frac{S}{V})_m$ is the magnetic specific nonferromagnetic/ferromagnetic interface parameter which is related to the domain dynamics, σ_m is the half width of the magnetic interface profile [153]. On the other hand, the magnetic polarons can be treated as atomic scale inhomogeneities using a Lorentzian function

$$I_p(q) = I_0 \frac{\xi^2}{1 + q^2\xi^2}, \tag{4.5}$$

where ξ is the characteristic size of these polarons [58]. We have also observed the incommensurate orbital order at zero field [154]. As a result, an additional Gaussian term is required

$$I_{OO} = A\, exp(\frac{-(q - q_c)^2}{2W^2})/W\sqrt{2\pi}, \tag{4.6}$$

where q_c is the center of the peak, A is the area, W is the width. Finally, another Porod's equation is used to describe the nuclear scattering [152]

$$I_{nuc}(q) = 2\pi(\Delta\rho_{nuc})^2(\frac{S}{V})_{nuc} q^{-4} exp(-q^2\sigma_{nuc}^2). \tag{4.7}$$

Most of the data discussed in this thesis were collected using a 17-Tesla horizontal magnet [155]. This means the magnetic field is always perpendicular to q so that the scattering pattern should be isotropic based

on eq. 4.3. As a result, the total intensity I(q) was obtained by summing all the intensities at the same q point in the 2D detector. We used three different instrumental configurations to cover the wide q range (2.2×10^{-3} Å to 0.23 Å). As discussed in Chapter 2.5, q is a function of the scattering angle θ and the wavlength λ. In practice, θ can be tuned by changing the distance between the sample and detector (L) (Fig. 2.6). In order to cover the required q range, both L and λ can be modified. Experimentally, we are only counting the number of neutrons instead of directly measuring the scattering cross-section. This means the intensities need to be normalized into absolute units (cm^{-1}) in order to merge the three patterns (Fig. 4.15) [156].

$$I_{abs}(q) = \frac{I(q)}{\Phi_0 \, Tr \, \Omega(q) \, t \, d}, \tag{4.8}$$

where Φ_0 is the incident neutron flux, Tr is the transmission, $\Omega(q)$ is the solid angle at q, t is the measuring time and d is the thickness of the sample [156].

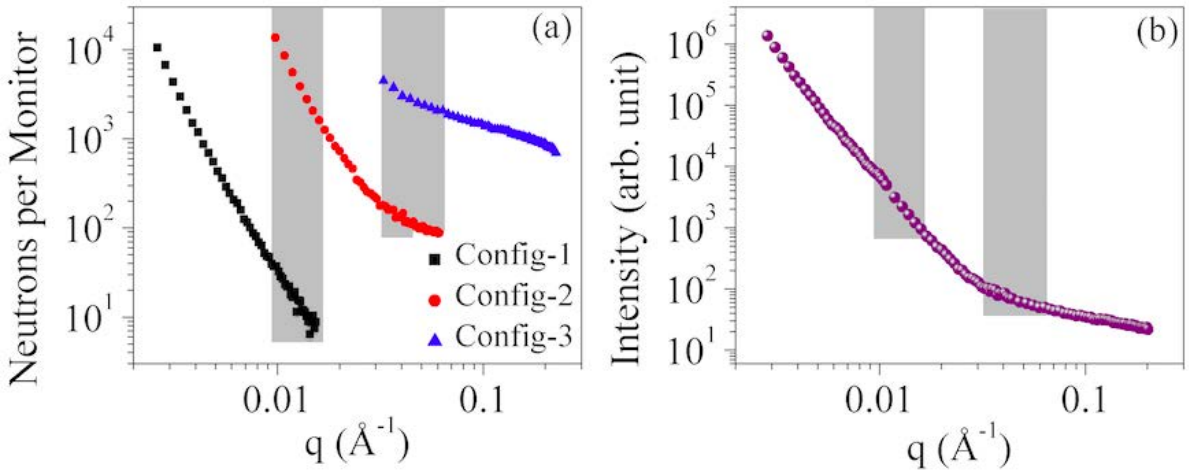

Figure 4.15: $T = 150$ K, $B = 2$ T. (a) I(q)-q curves under different instrumental configurations. (b) The merged curve. The shaded areas mark the overlapping regions.

Unfortunately, we did not measure the transmission parameters properly during the experiment. A slight rescaling has been applied to the data after treatment using eq. 4.8 (Fig. 4.15b). We note this additional treatment does not affect the absolute values of the parameters in the exponential brackets in eq. 4.4 - eq. 4.7. Although the values of other parameters, e.g. the magnetic specific interface $(\frac{S}{V})_m$, will not have any physical meaning, their field dependence still reflects the physics of the sample.

We will use the I(q) versus q curve collected at 150 K/2 T to demonstrate the data analysis process.

Under the horizontal field setup, we fit the experimental curve by

$$I(q) = I_m + I_p + I_{OO} + I_{nuc}. \tag{4.9}$$

As shown in Fig. 4.16a, this model is able to fit the experimental data quite well. More importantly, it is clear each term has its own active region. For example, the intensity in the very low-q region is dominated by the nuclear scattering. This is expected since the object size is proportional to q^{-1} and the crystalline grains are normally on micrometre scales. For the incommensurate orbital order and polarons, we will discuss them in the next subsection.

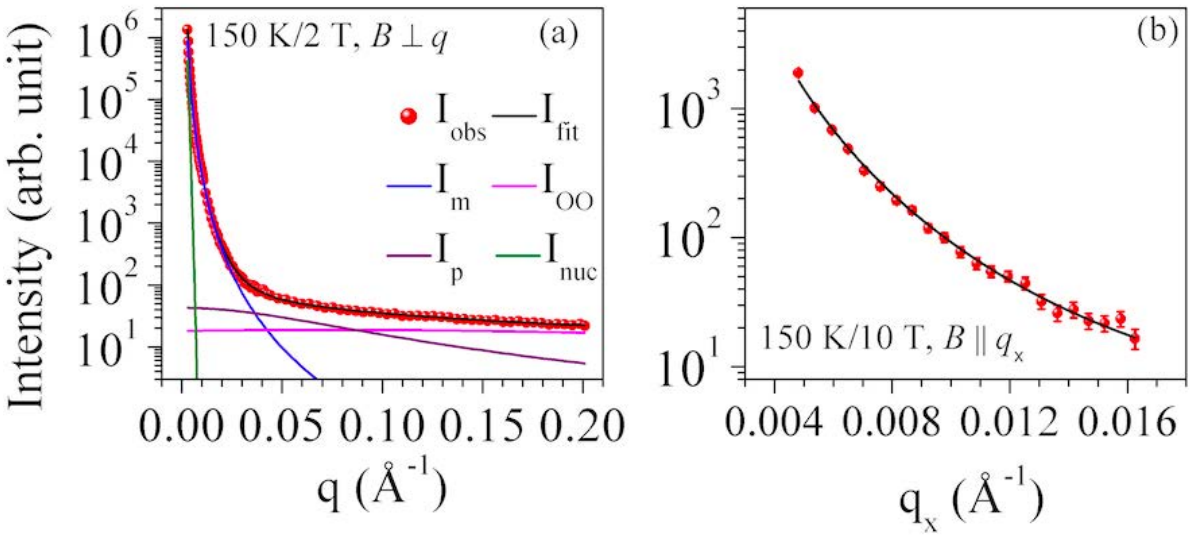

Figure 4.16: (a) I(q) versus q curve at 150 K/2 T under the horizontal field setup and the simulated contributions using eq. 4.9. (b) I(q) versus q curve at 150 K/10 T under the vertical field setup and the simulated contributions using eq. 4.7.

We have also used a vertical field setup (11-Tesla magnet) to double check the validity of the I_{nuc} term. In this case, the magnetic field is parallel to q_x, i.e. horizontal direction in the 2D detector. According to eq. 4.3, the intensity along q_x ($\Psi = 0$) should exclusively contain the nuclear scattering signal when the spins are aligned. As depicted in Fig. 4.16b, the Porod's term I_{nuc} is able to fully reproduce the experimental observations.

In conclusion, we have demonstrated that eq. 4.9 is a very good model to fit the experimental data under the horizontal field setup.

4.2.3 Zero field magnetism at $T = 150\,\mathrm{K}$

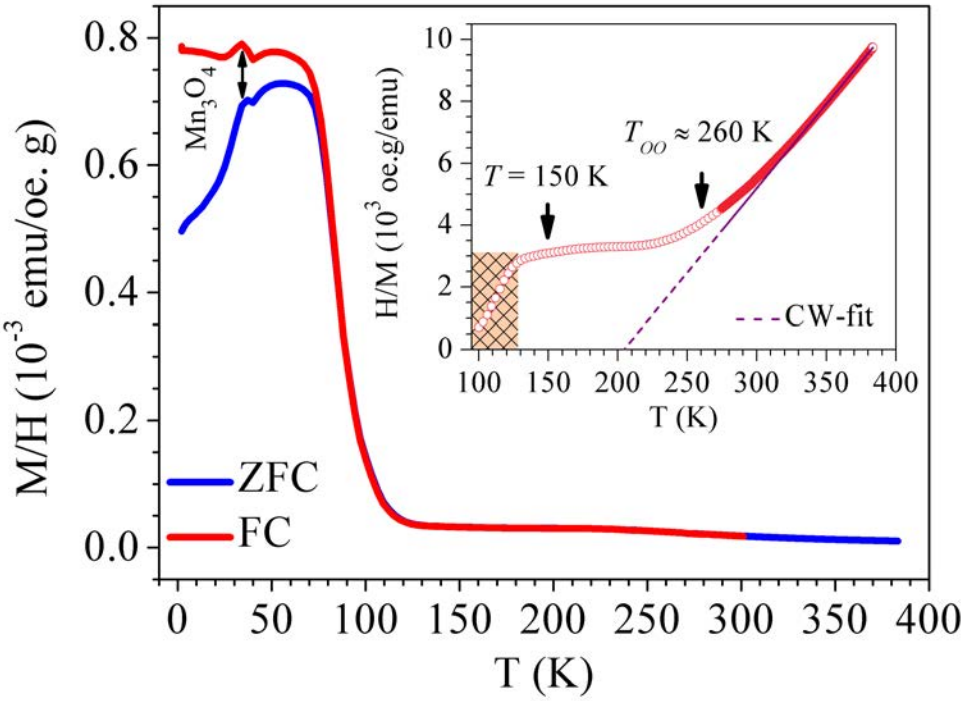

Figure 4.17: Main panel: ZFC and FC curves of PCMGO recorded on warming under $B = 0.05\,\mathrm{T}$. The bump marked by the double arrow is caused by a minor impurity phase identified as Mn_3O_4 (see main text). Inset: Inverse ZFC susceptibility versus temperature curve (open circles). Its linear part above $\sim 350\,\mathrm{K}$ has been fitted by the CW law (dotted line). The hatched area marks the onset of ferromagnetism.

Fig. 4.17 (main panel) shows the low field ($B = 0.05\,\mathrm{T}$) susceptibility (M/H) data of PCMGO as a function of temperature. At high temperatures, both curves overlap. A sudden upturn is observed below $T_\mathrm{C} = 100\,\mathrm{K}$ in both curves, corresponding to the onset of a ferromagnetic order. On further cooling, zero-field-cooled (ZFC) and field-cooled (FC) curves begin to diverge below $T_\mathrm{B} = 80\,\mathrm{K}$, which is associated with the cooperative freezing of the first-order antiferromagnetic to ferromagnetic transition in the literature [157]. Moreover, a weak bump appears around 34 K in both ZFC and FC curves. This coincides with the appearance of an additional peak around 4.93 Å in our TOF-NPD pattern (Fig. 4.18). Since it is a ferromagnetic Bragg position of the impurity phase Mn_3O_4, we interpret this bump to be the onset of ferromagnetism of Mn_3O_4 [149].

The inverse ZFC susceptibility versus temperature curve is plotted in the inset of Fig. 4.17. At very

high temperatures, we have applied a Curie-Weiss fit (purple dotted line). The CW model is only valid at the 'free spin' limit, i.e. spins are not 'talking' to each other [4]. Obviously, additional spin correlations occur in PCMGO below $\sim 350\,\mathrm{K}$. This is often linked to the precursor of electronic phase separation such as orbital order and polarons [141, 58, 59]. The onset temperature of electronic phase separation in PCMGO is determined to be $T_{\mathrm{OO}} \approx 260\,\mathrm{K}$, where the M/H versus temperature curve has the steepest slope. We adopted the OO term in the subscript since we have observed OO in PCMGO, as to be discussed below.

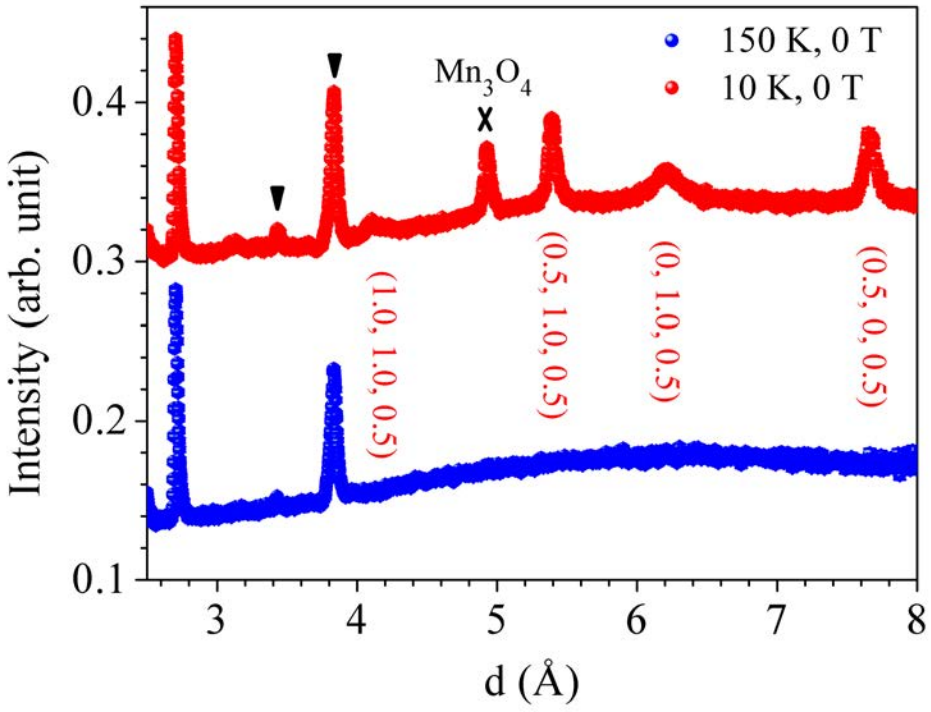

Figure 4.18: Zero field TOF-NPD pattern of PCMGO collected at 10 K (red) and 150 K (blue), respectively. The antiferromagnetic Bragg reflections at large d-spacings have been indexed. The black arrows mark the ferromagnetic Bragg positions. The additional peak around 4.93 Å is the magnetic Bragg reflection of Mn_3O_4 (see main text).

We have also used the TOF-NPD technique to explore the magnetism in PCMGO. As shown in Fig. 4.18, magnetic Bragg reflections belonging to both CE (odd index along b^*) and pseudo-CE (even index along b^*) antiferromagnetic order can be observed at $T = 10\,\mathrm{K}$, further supporting the presence of crystallographic phase separation in PCMGO. The low temperature ferromagnetism revealed by the susceptibility measure-

ments has also been confirmed: additional intensity has been established on top of the ferromagnetic Bragg point (black arrows). A peak around 4.93 Å is corresponds to the ferromagnetic reflection of the impurity phase Mn_3O_4 [149]. At $T = 150\,K$, no magnetic reflections can be resolved, which is consistent with the bulk susceptibility measurements. *As a result, we conclude PCMGO is a heavily strained paramagnet with electronic phase separation at $T = 150\,K$ and $B = 0\,T$.*

4.2.4 Magnetoresistance and magnetic field dependence of magnetization at $T = 150\,K$

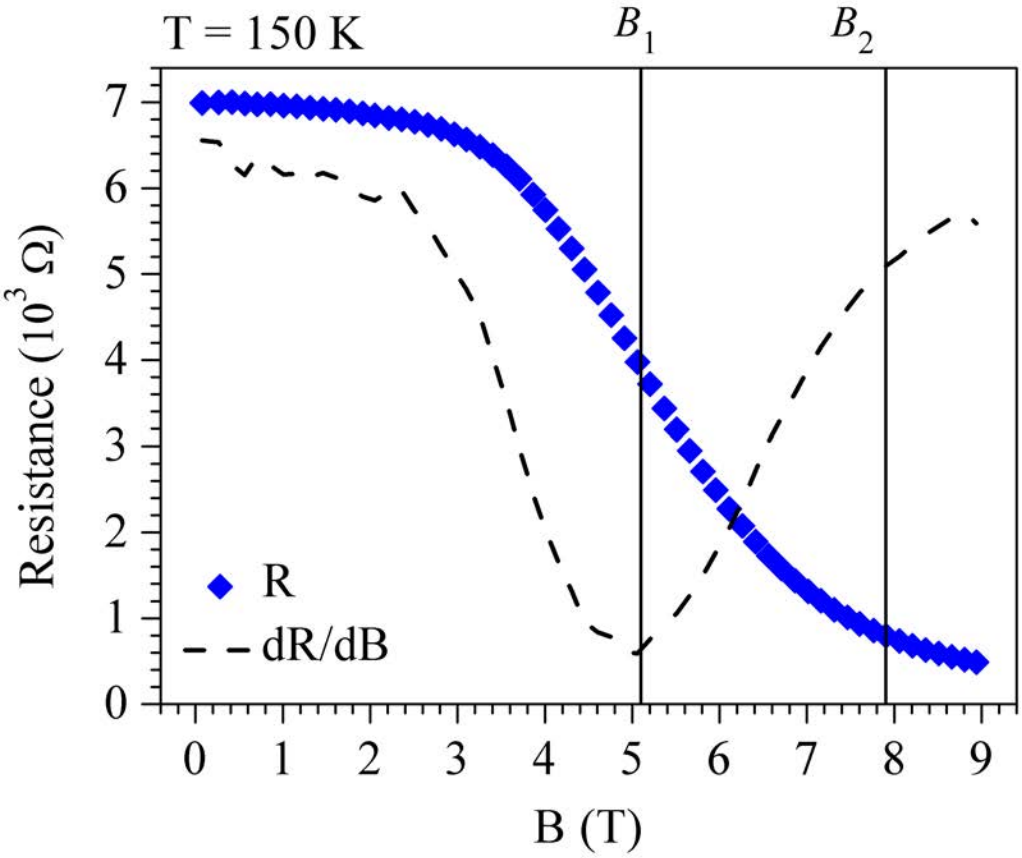

Figure 4.19: Resistance (R) versus magnetic field curve and the derivatives ($\frac{dR}{dB}$) of PCMGO at 150 K. The critical fields B_1 and B_2 are labeled by vertical lines (see main context).

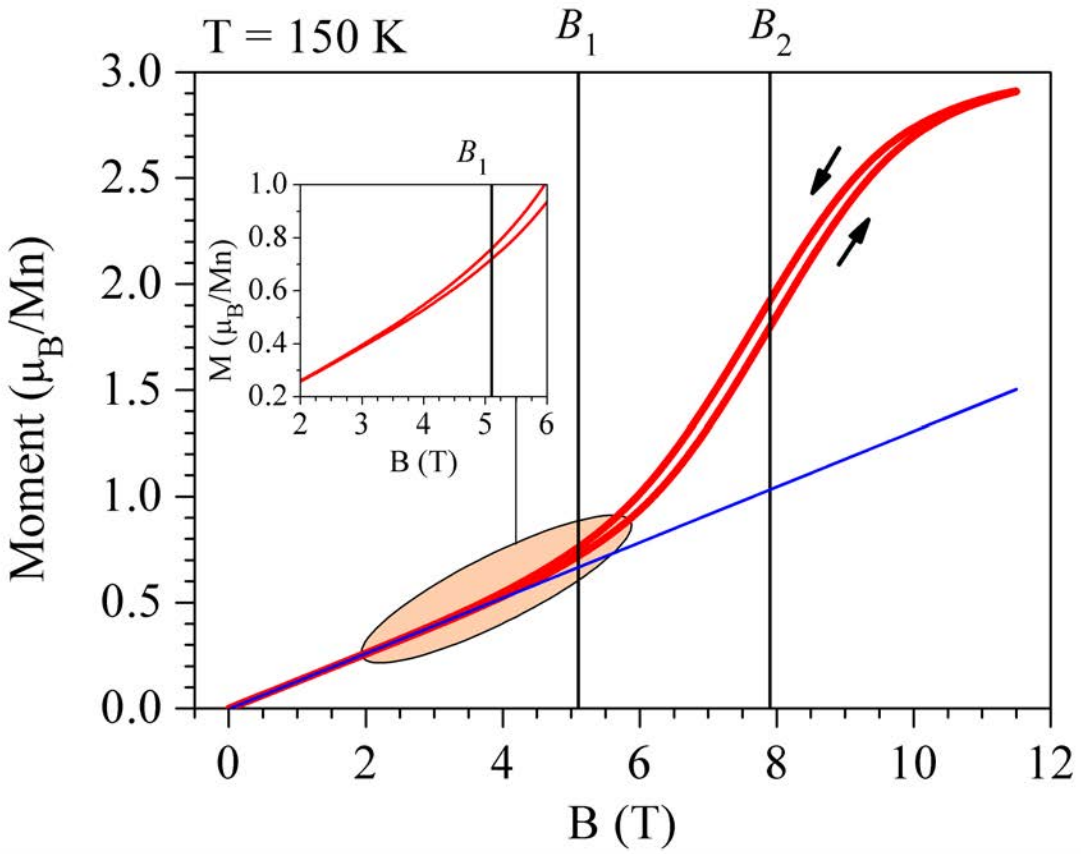

Figure 4.20: Main panel: Magnetization versus magnetic field curve (red line) of PCMGO at 150 K. The black arrows mark the field sweeping direction. The blue line is a linear fit to the low field part where the system is paramagnetic. The critical fields B_1 and B_2 are labeled by vertical lines (see main context). Inset: Enlarged version of the shaded area in the main panel.

After determining the zero field state of PCMGO at $T = 150$ K, the next step is to switch on the magnetic field. As shown in Fig. 4.19, the resistance (R) undergoes a large drop in the high magnetic field (B) region. This magnetoresistance curve has the steepest slope at $B_1 = 5.1$ T. The transition at B_1 is often linked to the melting of electronic phase separation in literatures [58, 51, 122]. For the PCMGO case, the microscopic nature of the transition at B_1 will be discussed in the next subsection. Since the melting of electronic phase separation (e.g. orbital order) is also accompanied by the onset of ferromagnetism in other relevant compounds [122], we have explored the bulk magnetization (M) as a function of B in Fig. 4.20. The M-B curve is linear at low fields, indicating that PCMGO is still paramagnetic. Further increasing B results in a

clear hysteresis effect as well as a sudden increase of magnetic moment. The latter is regarded as a signature of ferromagnetism. The critical field of this paramagnetic-ferromagnetic order transition is $B_2 = 7.9\,\mathrm{T}$, where the M-B curve has the steepest slope. Between B_2 and 11.5 T, we cannot probe any new transition based on the magnetization measurements. In the R-B curve, no transition is observed at B_2 (Fig. 4.19). We are able to resolve magnetic hysteresis from $\sim 3.2\,\mathrm{T}$ up to the highest field meausured (11.5 T). There is no hysteresis at zero field (paramagnetism). As a result, the magnetic hysteresis effect of PCMGO at 150 K is more likely caused by some sort of crystallographic structure transition rather than magnetic domain dynamics.

To conclude this subsection, we have found two critical magnetic fields, $B_1 = 5.1\,\mathrm{T}$ and $B_2 = 7.9\,\mathrm{T}$, using the same criterion (steepest slope) on the same sample batch. As discussed above, two successive electronic phase melting transitions of are expected due to the crystallographic phase separation in PCMGO. Since the pseudo-CE phase is less distorted, it is more susceptible to the magnetic field [50, 51, 128, 139]. However, the transition at B_1 and B_2 cannot be explained by this scenario. The pseudo-CE phase occupies the majority volume of the sample (92(3) %), which is not consistent with the very weak change of magnetization at B_1. On the other hand, the magnetization change at B_2 is too large to be atrributed to the minority CE phase (7.5(5) %). At this point, it seems the transition at B_2 is more likely to be related to the onset of ferromagnetism in the pseudo-CE phase. In this case, the percolation of conducting domains in this phase sets in (at B_1) well ahead of the bulk population of ferromagnetism (at B_2). The ferromagnetic conducting phase fraction (ϕ) can be estimated by the following equation

$$M = \phi\, M_s + (1 - \phi)\, \chi\, B, \tag{4.10}$$

where M_s is the saturation moment and χ is the susceptibility of the paramagnetic insulating phase [153]. Taking the magnetization ($2.9\,\mu_B$/Mn) at 11.5 T as M_s, the ferromagnetic phase fraction in the pseudo-CE phase of PCMGO is estimated to be 2.5 %, which is much lower than $\phi_c = 15\,\%$ in a standard isotropic 3D percolation model [158]. The uncertainties of our estimation have two major sources: (I) PCMGO is not fully saturated at 11.5 T, (II) the minor CE phase may also contribute to M_s in the high field region.

Similar phenomena (Fig. 4.19 and Fig. 4.20) have been reported in the strained compound $Pr_{0.7}Ca_{0.3}MnO_3$ [126, 153]. Although there is no direct evidence, the lower ϕ_c (7 %) in $Pr_{0.7}Ca_{0.3}MnO_3$ has been attributed to the filamentary percolation which has been observed in $Pr_{0.67}Ca_{0.33}MnO_3$ [121]. In other words, the system may form some ferromagnetic conducting filaments of nanometric diameter while keeping the majority portion insulating. As long as the percolation is triggered by magnetic field, the CMR effect will occur. On the other hand, since the majority of the sample is still insulating (paramagnetic or antiferromagnetic), the

magnetization is not supposed to exhibit any large change across such percolation.

4.2.5 Collapse of electronic phase separation induced by magnetic field at $T = 150\,\mathrm{K}$

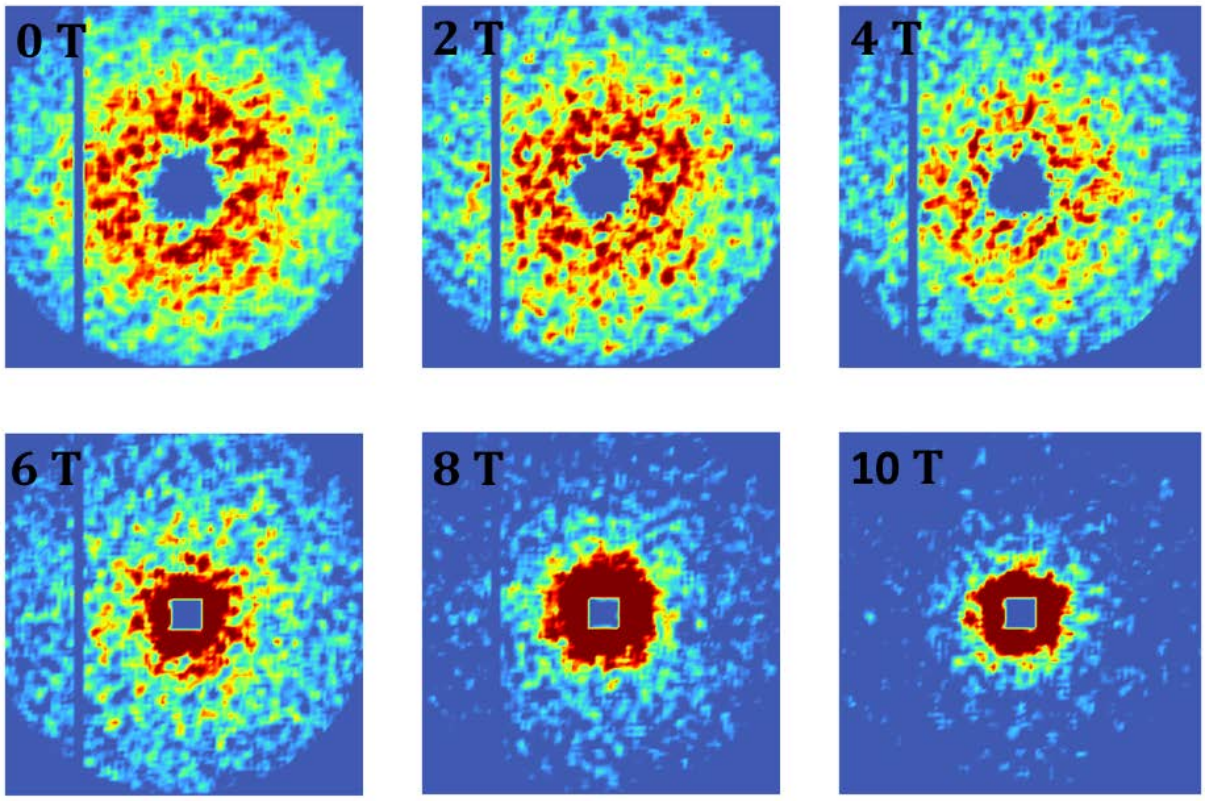

Figure 4.21: The magnetic field dependences of SANS patterns of PCMGO under the same scale (100 – 900 neutron counts per standard monitor). Each patterm covers a q-range from -0.2 $\mathrm{Å}^{-1}$ to 0.2 $\mathrm{Å}^{-1}$ in both directions. The narrow vertical slit on the left of each pattern is coming from a dead detector tube.

Assuming the magnetoresistance of PCMGO is caused by the formation of conducting filaments in magnetic field and the electronic phase separation (e.g. orbital order, polarons) is a bulk behaviour, the majority of the sample will still be insulating, i.e. possessing electronic phase separation, between B_1 and B_2. The second assumption should hold in all relevant CMR manganites since there is no evidence showing the electronic phase separation is not a bulk behaviour to the best of our knowledge. For the specific PCMGO case, the electron diffraction techique has been employed to search for the structure modulation caused by the electronic

phase separation [142, 159]. In most of the crystallites studied, they have observed extra diffraction spots which are the characteristic signatures of charge/orbital order [142, 159].

As discussed above, PCMGO is paramagnetic at 150 K. In all the relevant compounds, e.g. PCMGO and $Pr_{1-x}Ca_xMnO_3$, the orbital order is reported to be incommensurate in the paramagnetic region [142, 154, 159]. We have observed this incommensurate orbital order of PCMGO in our SANS measurements. Fig. 4.21 shows the field dependences of the SANS patterns after subtraction of the background data measured at B = 16 T where the electronic phase separation is almost fully suppressed based on our qualitative analyses (see the next paragraph). In the low field region, a ring-like pattern is observed. These corresponds to a broad peak centered at $\sim 0.075\,\text{Å}^{-1}$. The ring intensity is relatively stable against magnetic field when $B \leqslant 4$ T. However, it is drastically suppressed between 4 T and 6 T. When $B \geqslant 6$ T, additional intensities start to accumulate around the center of these patterns. These intensities are also field dependent. They represent the scattering signals from the micrometre phases (eq. 4.4) rather than the electronic phases based on our qualitative analyses (see the next paragraph).

We note that this type of background subtraction is only for quantitative demonstration. As shown in eq. 4.4-eq. 4.7, there are additional contributions to the neutron scattering signals in the high-q region, meaning the 'background' refered to above may also be field dependent! The best way to extract different contributions out from the total scattering intensity is to fit the I-Q curves using eq. 4.9, as displayed in Fig. 4.16. Fig. 4.22a shows the field dependence of the integrated intensity (I_{OO}) of the incommensurate orbital order peak. I_{OO} is greatly suppressed between 4 T and 6 T, indicating the transition at $B_1 = 5.1$ T is caused by the melting of orbital order. Interestingly, a very weak peak centered at $0.04(1)\,\text{Å}^{-1}$ is required to fit the curves above 4 T. The intensity of this peak is temporarily enhanced between 6 T and 10 T (B_3) followed by a gradual decrease at higher fields up to 16 T. We attribute this peak to the incommensurate orbital order in the minority CE phase. We have also detected the presence of atomic size clusters in PCMGO. They are often linked to the size of magnetic polarons (carrier hopping range) [58]. The correlation length (ξ) of these polarons as a function of magnetic field is plotted in Fig. 4.22b. Similar with the orbital order, ξ also gives a big drop between 4 T and 6 T. While a weak enhancement is observed between 6 T and 8 T, ξ is gradually suppressed above B_3 as well. Fig. 4.22d plots the evolution of the magnetic specific interface parameter (S/V) in magnetic field (eq. 4.4). This parameter reflects the magnetic domain dynamics on much larger scales than that of the electronic phase separation. It peaks exactly around B_2, meaning it is coupled to the bulk magnetization.

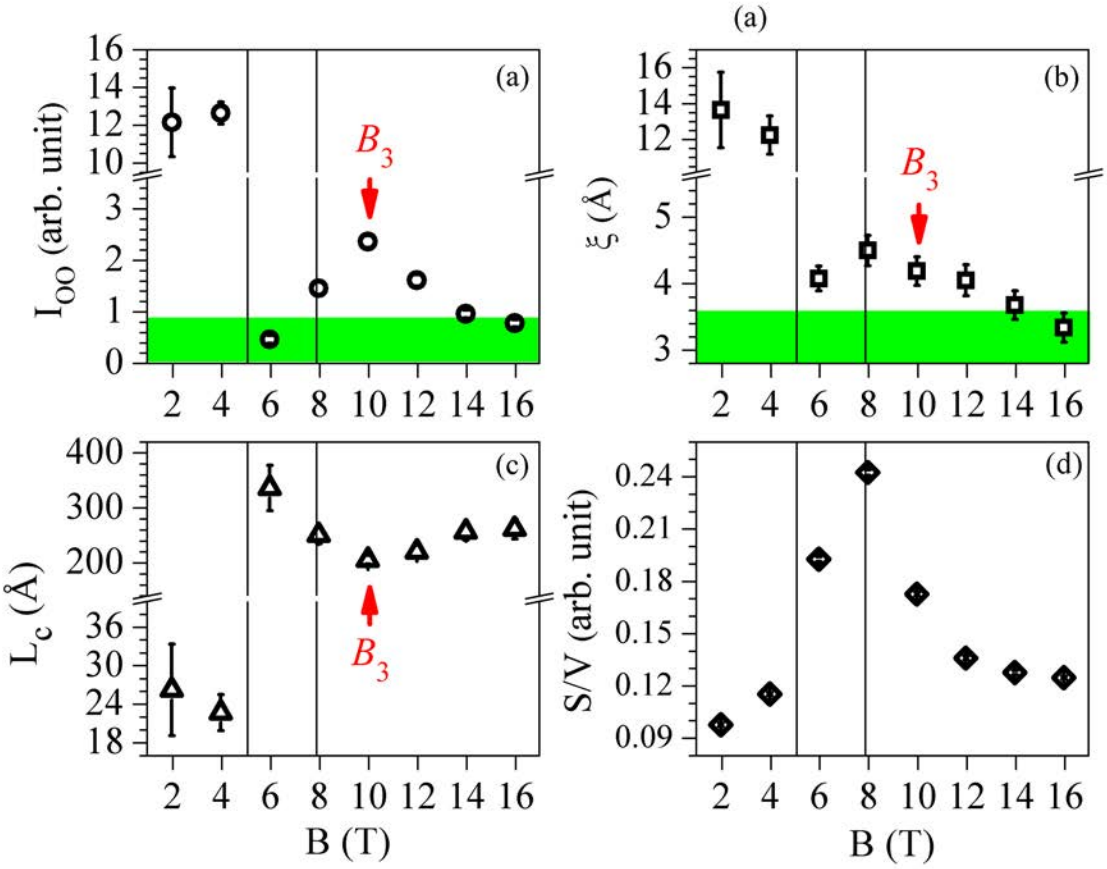

Figure 4.22: Magnetic field dependences of (a) integrated intensity (I_{OO}) of the orbital order peak, (b) polaronic correlation length (ξ), (c) coherence length (L_c) of orbital order and (d) magnetic specific interface (S/V). The vertical lines mark the positions of B_1 and B_2.

Now we discuss the field dependences of I_{OO} and ξ in detail. The orbital order is short range ordered in the entire field region probed. As shown in Fig. 4.22c, its coherence length (L_c) is 18 - 34 Å below B_1. In the high field region, L_c increases to 200 - 400 Å. This agrees with our scenario that the weak peak above B_1 is from the orbital order in the minority CE phase. As proposed in Ref. [127], the distribution of Ga ions is not homogeneous in PCMGO: Ga richer in the pseudo-CE region and Ga poorer in the CE region. Due to the direct substitution of Mn with Ga, the orbital order of Mn ions are very sensitive to the substitution level. It is expected that the orbital order will be more disturbed (weakened) in the Ga richer region (pseudo-CE phase). On the other hand, the orbital order is less affected in the Ga poorer region (CE phase) so

that it is more robust and long range ordered. We note that this type of short range orbital order peak may also be regarded as the signature of the correlations between polarons [56, 57]. Under this scenario, although the integrated intensity drops to zero when the bulk ferromagnetic order is triggered, it will be temporarily enhanced in close proximity to the ferromagnetism, as observed in Refs. [56, 57]. For ξ, which probes the carrier hopping range within one polaron, larger ξ below 6 T may indicate the weaker electron phonon coupling strength in the pseudo-CE phase. As a result, the carriers are less localized [46, 47]. The drop of ξ between 4 T and 6 T can be explained as the delocalization of carriers in the pseudo-CE region. As a result, the corresponding ξ diverges and exceeds the probing region of our SANS measurements. When $B \geqslant B_1$, the collapse of electronic phase separation in the minority CE phase is very smooth (Fig. 4.22a & b). Due to the presence of the nonmagnetic Ga ions which exist as point defects in PCMGO, ξ is expected to drop to the ionic size of Ga^{3+} when the electronic phase separation is completely suppressed.

To conclude this subsection, we have proved that the percolation at B_1 is caused by the collapse of electronic phase separation in the majority pseudo-CE phase, while the transition at B_2 revealed by the bulk magnetization measurements is related to the domain dynamics on micrometre (or even larger) scales. As stated above, electronic phase separation should populate in the whole sample to the best our knowledge. This means our observation rules out the filamentary percolation scenario proposed in Ref [121]. In other words, I_{OO} is not supposed to change a lot across B_1 if the corresponding percolation is due to the conducting filaments formation. For some reason, the spins are 'locked' across the conducting paths percolation in PCMGO. An important message revealed by these observations is that the carrier delocalization (magnetoresistance) in mixed-valence manganese oxides is essentially driven by the electronic phase separation on atomic scales rather than the long range spin order.

4.2.6 Discussion

A possible candidate for the spin locking in mixed-valence manganese oxides is the strains. As discussed in Chapter 4.1.4, the martensitic scenario is commonly used to interpret the field induced magnetic avalanches at very low temperatures. Besides the carrier delocalization which prevails the double exchange interactions, the elastic energy is also important to realize the ferromagnetic spin alignment. As a result, additional energy is required to flip the spins which are 'locked' by the strains. The strains in PCMGO can be phenomenologically characterized by the 6 anisotropic strain parameters using the Stephens formalism (see chapter 4.1.4 & 4.2.2). The field dependences of these anisotropic strains parameters are plotted in Fig. 4.23. At B_2, an obvious anomaly can be seen in all parameters. Except S_{400} which has relatively larger errors, other strain param-

eters are robust in the low field region; but are significantly weakened across B_2, indicating the suppressed anistropic strains at high fields. These results support that the spins in PCMGO have been locked by the strong anisotropic strains. This explains the observation that no more than 2.5 % of PCMGO is ferromagnetic at B_1 (see chapter 4.2.4).

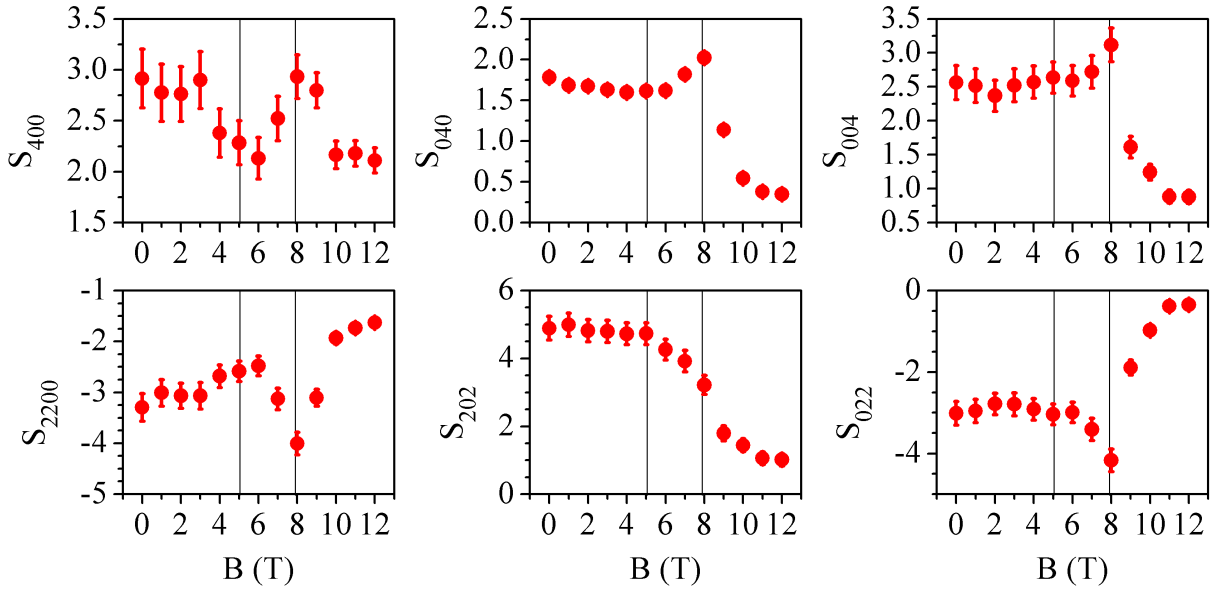

Figure 4.23: Magnetic field dependences of the anisotropic strain parameters of PCMGO at 150 K. The vertical lines mark the positions of $B_1 = 5.1$ T and $B_2 = 7.9$ T.

We have also investigated the field dependences of the lattice parameters and the unit cell volume (Fig. 4.24). In the low field region, our measurements cannot resolve any transition across B_1 for all those parameters. In contrast, the lattice parameters are strongly coupled to the bulk magnetization curve (see Fig. 4.20) around B_2, resulting in a giant negative volume magnetostriction in the high field region (Fig. 4.24b). Both linear and volume magnetostriction effects have been reported in CMR manganites previously [58, 128]. These phenomena were interpreted as the consequence of the melting of the electronic phase separation (polarons, orbital order) [58, 128]. However, our results unambiguously suggest the onset of ferromagnetism is the real trigger. Since the onset of ferromagnetism often overlaps with the melting of electronic phase separation in systems where the spins are not effectively locked by the strains (e.g. $Pr_{0.5}Ca_{0.5}MnO_3$) [128, 127], we emphasize that it is very difficult to distinguish the roles of electronic phase separation and ferromagnetism

in the magnetostrictive process of these materials.

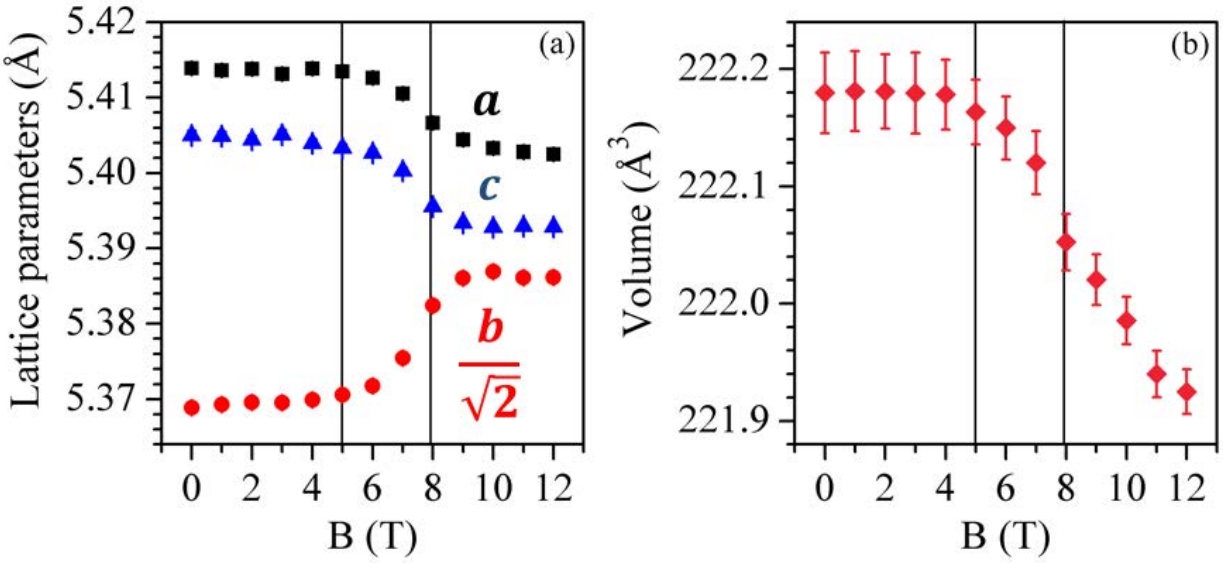

Figure 4.24: Magnetic field dependences of (a) the lattice parameters and (b) unit cell volume of PCMGO at 150 K. The vertical lines mark the positions of B_1 and B_2.

Electron-phonon coupling (EPC) is very important to the formation of electronic phase separation in CMR manganites [46, 2, 10, 47]. Besides the 'tolerance factor' which involves stresses on the Mn-O-Mn bonds from the ionic size mismatch on the rare-earth (Re) sites ($Re_{1-x}A_xMnO_3$), the Jahn-Teller (JT) distortion of the MnO_6-octahedron is another type of EPC [46, 44]. Previous investigations have revealed strong evidence of the coupling between the JT distortion and the electronic phase separation [55, 131, 160]. For example, the JT distortion is significantly softened when carrier delocalization occurs [55, 131, 132]. Due to the presence of the JT distortion, the carriers can be 'self-trapped' on atomic scales, causing an insulating state to the bulk sample [46]. Therefore it is not surprising to observe such softening since a weaker JT state favours carrier delocalization. However, the JT distortion does not necessarily need to be softened in order to realize the carrier delocalization from the theoretical point of view [2, 47]. As discussed in Chapter 1.2.6, the JT distortion can be parameterized by a EPC constant λ. It has been demonstrated by Millis *et al* that CMR can be triggered by simply switching on the magnetic field while keeping the value of λ fixed [47].

On the other hand, the JT distortion sometimes leads to orbital order since it breaks the 2-fold degeneracy of the e_g crystal-electric-field (CEF) level [52]. As shown in Fig. 1.6 of Chapter 1.2.6, there are two types of JT modes which are e_g-active. The Q_3 mode corresponds a elongation of the Mn-O bond along the b-

axis (*Pnma* space group configuration) and compression of the two Mn-O bonds in the *ac*-plane. The Q_2 mode only involves two opposite motions of the two Mn-O bonds in the *ac*-plane. If we label the two e_g orbitals as $d_{x^2-y^2}$ and d_{z^2}, the Q_3 mode tends to completely split these two orbitals, whereas the split orbitals are a mixture of $d_{x^2-y^2}$ and d_{z^2} in the Q_2 mode [161]. In systems with both CE and pseudo-CE types of antiferromagnetic order (e.g. $Pr_{1-x}Ca_xMnO_3$), the Q_2 mode has been argued to be responsible for the $d_{3x^2-r^2}/d_{3y^2-r^2}$ orbital order [2, 52, 162]. As mentioned above, the melting of orbital order in relevant systems is often accompanied by the softening of the JT distortion [132]. A plausible interpretation to this effect is the weakened e_g CEF spliting. Moreover, as pointed out in Ref. [163], the orbital order can also be melted by the enhancement of of the JT distortion in layered manganites, although such behaviour has not been reported in manganites with perovskite structure so far.

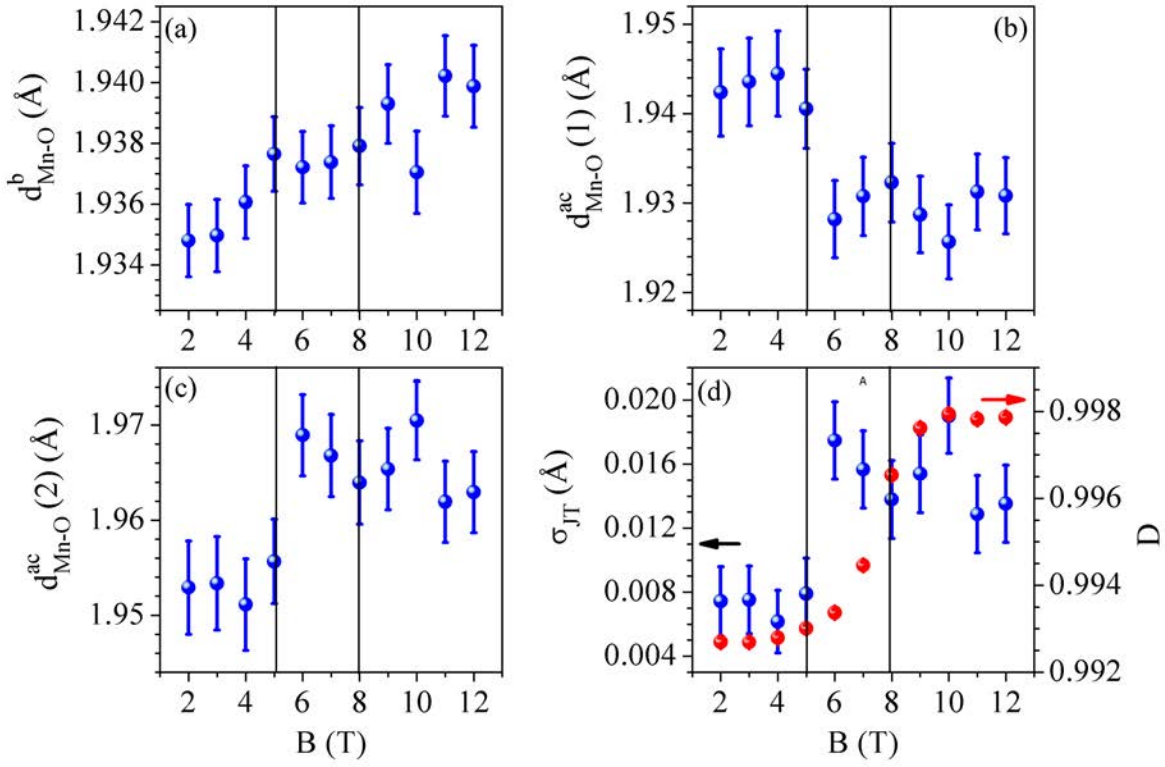

Figure 4.25: (a) - (c) Magnetic field dependences of the Mn-O bond lengths in a MnO_6-octahedron. (d) Magnetic field dependences of the local (left axis, blue solids) and global (right axis, red solids) lattice distortion parameters. The vertical lines mark the positions of B_1 and B_2.

We have explored the field dependences of the Mn-O bonds of PCMGO (Fig. 4.25a-c). When $B \leqslant B_1$, the Mn-O bond along the b-axis (d^b_{Mn-O}) is shorter than the other two Mn-O bonds in the ac-plane [$d^{ac}_{Mn-O}(1)$, $d^{ac}_{Mn-O}(2)$]. Since $d^{ac}_{Mn-O}(1)$ is slightly different from $d^{ac}_{Mn-O}(2)$, both Q_2 and Q_3 modes should exist in this region. When the magnetic field increases from 5 T to 6 T, we cannot resolve any change in the d^b_{Mn-O} channel, whereas two opposite motions have been observed in the $d^{ac}_{Mn-O}(1)$ and $d^{ac}_{Mn-O}(2)$ channels. This corresponds to a enhancement of the Q_3 mode. This transition can be further addressed by using the JT distortion constant (σ_{JT})

$$\sigma_{JT} = \sqrt{\frac{1}{3}\sum_{i=1,2,3}(d^i_{Mn-O} - \bar{d}_{Mn-O})^2}, \tag{4.11}$$

where d^i_{Mn-O} is the individual Mn-O bond length and $\bar{d}_{Mn-O}$ is the mean Mn-O bond length [132]. As shown in Fig. 4.25d, σ_{JT} is clearly enhanced across B_1. In contrast, no change can be resolve across B_2 in all these parameters. We have also plotted out the global unit cell distortion parameter $D = \frac{\sqrt{b}}{a+c}$ in Fig. 4.25d. Apparently, the unit cell remains robust across B_1 and becomes significantly less distorted above B_2, indicating a strong coupling to the spin order.

To finish this subsection, we have proved that the carrier delocalization at B_1 is not related to the filamentary percolation proposed in Ref. [121]. It is caused by the collapse of electronic phase separation in the whole sample. Contradicting previous experimental investigations [132], the carrier delocalization in PCMGO is an exceptional case where the JT distortion is enhanced. This is realised by further mixing the two e_g orbitals, $d_{x^2-y^2}$ and d_{z^2} , to suppress the $d_{3x^2-r^2}/d_{3y^2-r^2}$ orbital order, rather than recovering the 2-fold degeneracy of the e_g level. The spins are 'locked' in place by the strong anisotropic strains in PCMGO. While these spins are not coupled to the electronic phase separation, our results unambiguously reveal a strong spin-lattice coupling on the unit cell level, which is the real cause of the giant magnetostriction effect commonly observed in these systems.

4.3 Conclusions and future work

In this project, we have investigated the magnetic field dependences of electronic phase separation, spin and crystallographic structure in the paramagnetic region of the strained manganese perovskite PCMGO. We have found that the carrier delocalization is caused by the collapse of electronic phase separation in the whole sample. Surprisingly, this process is assisted by the enhancement of JT distortion (Q_2 mode) rather than the opposite way which has been commonly observed in other perovskite manganites. On the other hand, the long range ferromagnetic order is insignificant to the carrier delocalization process in this strained

compound. We clarify that the giant volume magnetostriction effect does not come from the melting of electronic phase separation (polarons, orbital order), as proposed in Ref [58, 128]. It is more related to the strong spin-lattice coupling. Most of all, we emphasize spins are still very important to the magnetoresistance. As depicted in Fig. 4.19, the R-B curve does not start to flatten until B_2. ***Based on these results, we propose that the CMR effect is essentially governed by two independent mechanisms: (I) carrier delocalization caused by the collapse of electronic phase separation (II) ferromagnetic double-exchange interaction.*** *We stress it is very difficult to distinguish the roles of these two processes across the magnetoresistive transition in systems where the anisotropic strains are weak.*

In the future, it would be very interesting to investigate the magnetic field dependences of electronic phase separation, spin and crystallographic structure in the magnetic ordered region of PCMGO. Moreover, it is also worth revisiting the other strained compound $Pr_{0.7}Ca_{0.3}MnO_3$ where bulk ferromagnetism and carrier delocalization are also separated in the magnetic field [153].

CHAPTER 5

DILUTED PYROCHLORE, $Y_2(CR_{1-X}GA_{X-0.5}SB_{0.5})_2O_7$

5.1 Background

5.1.1 Magnetic 3d transition-metal pyrochlores

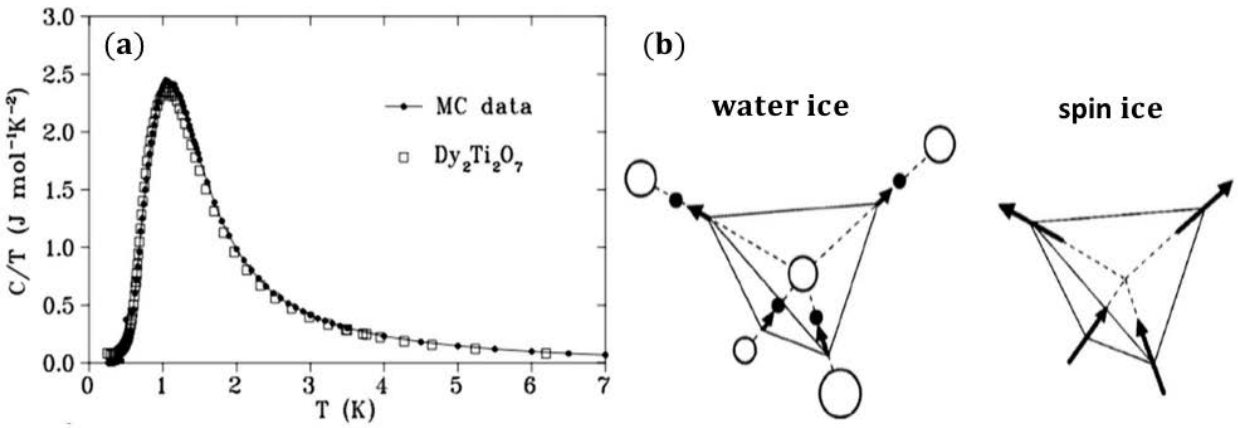

Figure 5.1: (a) Heat capacity versus temperature curves (open squares) of $Dy_2Ti_2O_7$. The black solids are the Monte-Carlo simulations for the dipolar-spin-ice model [15]. (b) Illustration of the water ice and spin ice configurations.

As discussed in Chapter 1.3, the pyrochlore structure has a chemical formula $A_2B_2O_7$ [15]. Due to the predominant magnetic dipolar interactions, rare-earth (RE) pyrochlores with nonmagnetic B-sites usually do not develop long range spin order until very low temperatures, e.g. $\sim 1\,K$ in $Gd_2Ti_2O_7$ [4, 15]. In most cases, the magnetic ground state is highly degenerate. For example, the ground state spin configuration in

$RE_2Ti_2O_7$ (RE = Dy, Ho) can be described by two spins pointing towards the center of the RE-tetrahedron and the other two pointing outwards (Fig. 5.1). This two-in/two-out structure is reminiscent of the arrangement of protons in water ice, so it is named as 'spin ice' (Fig. 5.1b). Due to the cubic structure of these pyrochlores (space group $Fd\bar{3}m$), there are six energetically equivalent two-in/two-out spin configurations on each RE-tetrahedron, and therefore the number of ground states in a bulk sample is infinite, making the system highly degenerate at low temperatures [15].

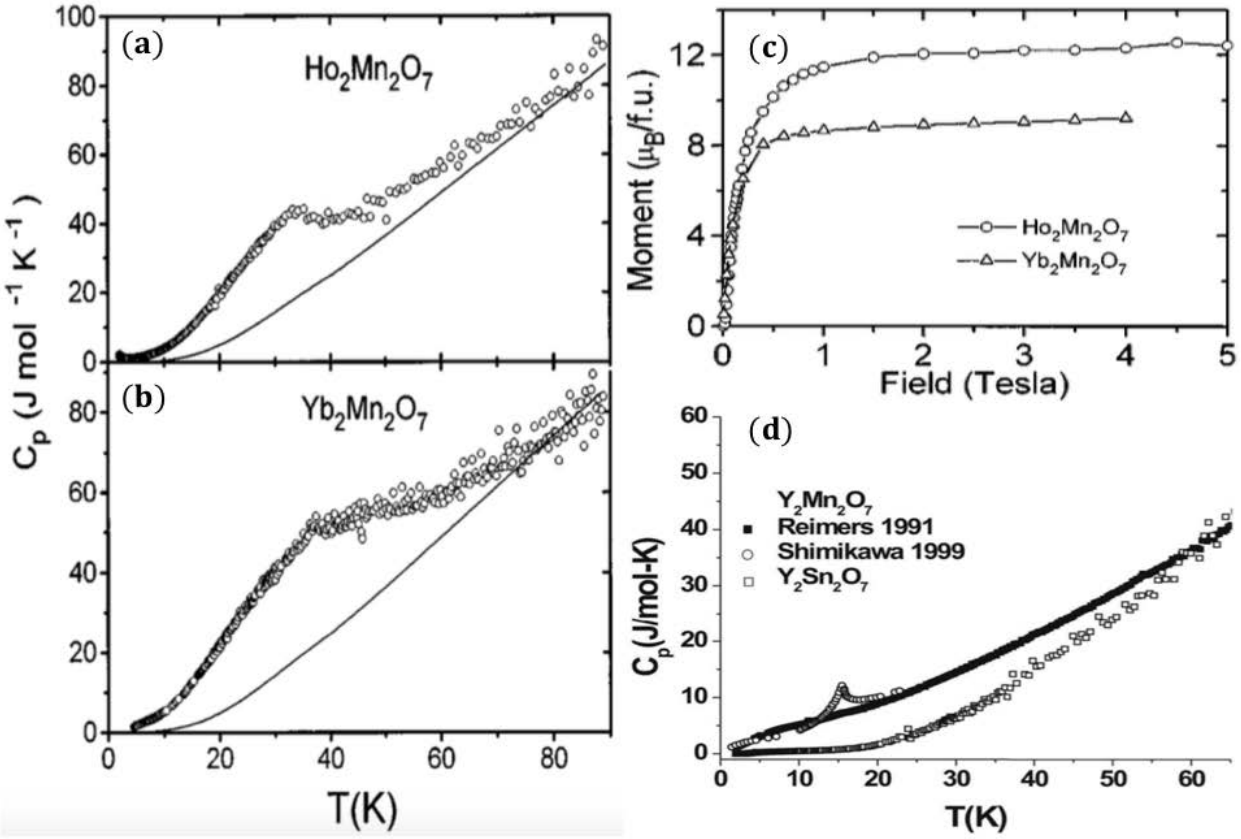

Figure 5.2: Heat capacity versus temperature curves of (a) $Ho_2Mn_2O_7$ and (b) $Yb_2Mn_2O_7$. The solid lines are lattice contributions. (c) Field dependences of magnetization of $Ho_2Mn_2O_7$ and $Yb_2Mn_2O_7$ collected at 5.0 K. (d) Heat capacity data on $Y_2Mn_2O_7$ measured by different groups [15].

In sharp contrast, long range ferromagnetic order with very high Curie temperature has been realized in RE pyrochlores with magnetic transition-metal (TM) ions on B-sites (Fig. 5.2a - c) [35]. As shown in Fig. 5.2a & b, T_C is found to be around 38 K in $Ho_2Mn_2O_7$ and $Yb_2Mn_2O_7$. Compared with the very low

transition temperature ($\sim$ 1 K) in RE pyrochlores with nonmagnetic B-sites, the high T_C in $RE_2TM_2O_7$ indicates the important role of TM ions to the acutual spin ordering.

Although these RE manganese pyrochlores show ferromagnetic behaviour at low temperatures (Fig. 5.2c). The paramagnetic-to-ferromagnetic order transition window revealed by the heat capacity measurements is very broad (Fig. 5.2a & b). This may indicate the presence of disorder in those systems. Since these compounds are not stable at ambient pressure at any temperatures, they must be prepared using high pressure methods in order to secure the Mn^{4+} oxidation state [164]. However, a careful check on the valence of the Mn ions as well as the chemical stoichiometry has not been performed to date. As shown in Fig. 5.2d, heat capacity data of $Y_2Mn_2O_7$ reported by different groups show very clear discrepancies [15]. These observations suggest that the magnetic properties in manganese pyrochlores are very sensitive to the disorder. We also note that an additional Lorentzian-squared term is required to produce satisfactory fits to the small angle neutron scattering data collected in these system [35]. This Lorentzian-squared term is commonly found in materials with site-disorder.

5.1.2 Structural disorder and magnetism

The disorder in manganese pyrochlores is related to the quality of the samples. It has been suggested that structural disorder could well be intrinsic in other pyrochlore compounds, and more importantly, be responsible for the lack of long range spin order in corresponding systems [15, 24, 25, 26, 29, 30, 165, 166, 167]. For example, a dipolar spin ice model, which contains the nearest neighbour exchange and long range dipolar interactions [168], has been argued to be appropriate to describe $Tb_2Ti_2O_7$. Using the estimated values of the coupling constants, a long range antiferromagnetic order should develop below $\sim$ 1 K. However, neutron scattering measurements on both single crystals and powder of $Tb_2Ti_2O_7$ have revealed no static magnetic order but short range correlations between Tb^{3+} spins on the nearest neighbour scales down to 50 mK [169, 170]. Moreover, muon spin relaxation measurements have only observed paramagnetic fluctuations down to 60 mK [171]. As a result, the magnetic ground state of $Tb_2Ti_2O_7$ has been established to be a spin liquid (or cooperative paramagnet) [15]. On the other hand, the crystal field degeneracy of the non-Kramer Tb^{3+} ion is susceptible to Jahn-Teller distortions [172]. Since the magnetoelastic coupling usually suppresses frustration [173, 174], the spin liquid state of $Tb_2Ti_2O_7$ may suggest frustration in lattice degrees of freedom as well [175]. In other words, intrinsic lattice disorder plays a key role in the spin liquid physics of $Tb_2Ti_2O_7$ through the magnetoelastic coupling, as revealed by multiple experiments [165, 166, 167].

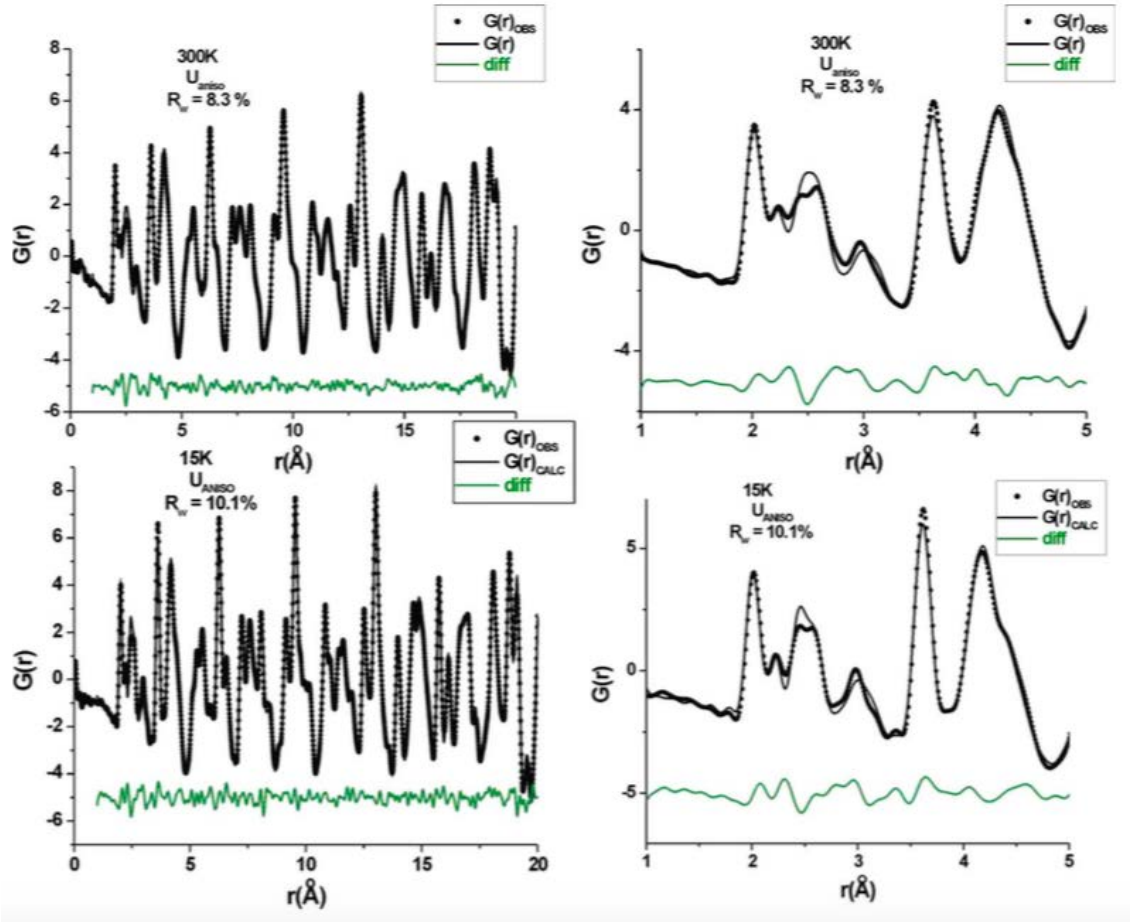

Figure 5.3: PDF as a function of distance r of $Y_2Mo_2O_7$ at various temperatures. The fits are based on a fully ordered model with anisotropic atomic displacement factors for all atoms [25]

As discussed in Chapter 1.3.2, the spin glass state in $Y_2Mo_2O_7$ has been ascribed to the local structure disorder. It is also demonstrated in Ref. [25] that the fits to the neutron pair-distribution-function (PDF) always become worse on cooling, indicating the development of local disorder (Fig. 5.3). However, this does not necessarily suggest any magnetoelastic coupling, as has been revealed in the $Tb_2Ti_2O_7$, due to the presence of disorder in both local and average structures at 300 K (Fig. 5.3). Recently, a new model, in which the four Mo^{4+} ions on each Mo-tetrahedron obey a two-in/two-out displacement rule, has been proposed by Thygesen *et al* based on their analyses of both X-ray and neutron PDF data [32]. They have highlighted the key role of orbital frustration. The disorder of the spin exchange interaction comes from the resulting cooperative O^{2-} ion displacements. Nonetheless, the bond disorder level in $Y_2Mo_2O_7$ is too weak to generate any spin glass state according to the conventional mean field theory predictions [27]. This

puzzle has been solved by Saunders *et al* who have successfully introduced a spin glass state at the weak bond disorder limit [29]. However, the spin freezing temperature ($T_{\rm f}$) would scale with the disorder strength (Δ) in this model. This leads to an estimated $T_{\rm f}$ which is 20-30 times smaller than that determined by the experiments [30]. In order to fully reproduce the spin glass transition as well as the high $T_{\rm f}$ in $Y_2Mo_2O_7$, the spin-lattice coupling term is required (Fig. 5.4), as demonstrated by Ref. [30].

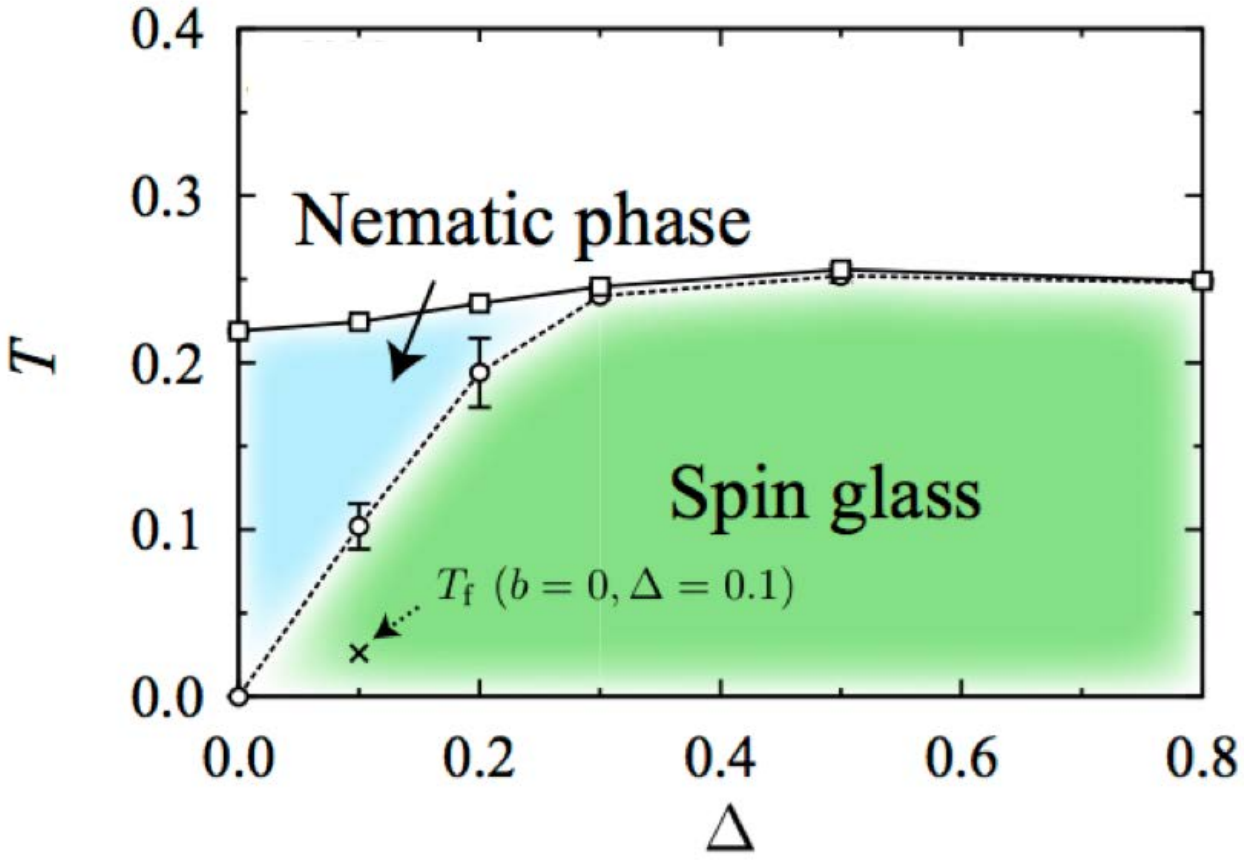

Figure 5.4: Bond disorder strength (Δ) - temperature (T) phase diagram obtained at $b = 0.2$, where b is the spin-lattice coupling constant [30]. The nematic and spin glass transition temperatures are denoted by squares and circles.

5.1.3 $RE_2(Cr_{0.5}Sb_{0.5})_2O_7$, RE = Ho, Y, Dy, Tb, Er, etc

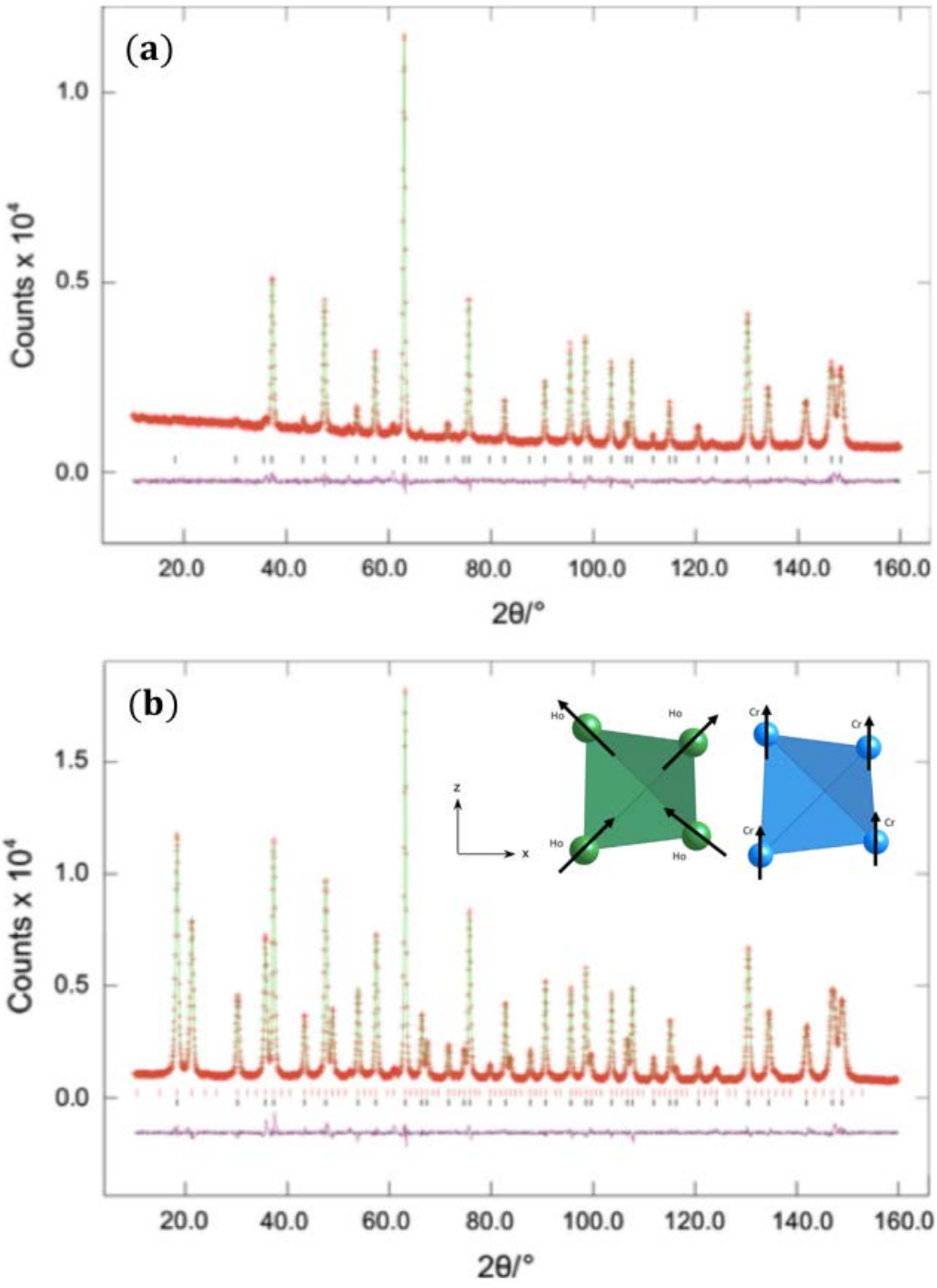

Figure 5.5: Neutron powder diffraction patterns ($\lambda = 1.8857$Å) of $Ho_2(Cr_{0.5}Sb_{0.5})_2O_7$ at (a) 298 K and (b) 1.5 K. Inset of (b): The refined magnetic structure at 1.5 K.

Nonmagnetic ion dilution in pyrochlores can be traced back to 1960s, when Bongers *et al* investigated the bulk magnetism of $RE_2(Cr_{0.5}Sb_{0.5})_2O_7$ (RE = Ho, Y, Dy, Tb, Er, etc) [176]. For the $Ho_2(Cr_{0.5}Sb_{0.5})_2O_7$ compound, it enters into a ferromagnetic-like state below $T_C \sim 10\,K$ [176]. This value is considerably larger when the B-site is completely nonmagnetic ($\sim 1\,K$ in $Ho_2Ti_2O_7$), indicating the important role of the magnetic TM ions on B-site. Neutron powder diffraction experiments have been carried out on $Ho_2(Cr_{0.5}Sb_{0.5})_2O_7$ by Whitaker *et al* [177]. Sharp magnetic reflections are clearly observed at low temperatures (Fig. 5.5). By assuming the four Ho^{3+} spins on each tetraheron obey the two-in/two-out configuration and Cr^{3+} spins ferromagnetically align along the *c*-axis [Fig. 5.5b(inset)], they have successfully refined the diffraction pattern at 1.5 K. Unlike the highly frustrated two-in/two-out spin ice state in $Ho_2Ti_2O_7$ [15], Whitaker *et al* have also suggested the two-in/two-out structure of Ho^{3+} spins in $Ho_2(Cr_{0.5}Sb_{0.5})_2O_7$ is actually ordered due to the presence of Ho^{3+}-Cr^{3+} coupling [177].

5.2 Results

5.2.1 Research motivations

As reported in Ref. [177], $Ho_2(Cr_{0.5}Sb_{0.5})_2O_7$ develops long range magnetic order below 13 K. Ho^{3+}-Cr^{3+} coupling plays a key role on the ordering of Ho^{3+} ions. However, it is not clear how this Ho^{3+}-Cr^{3+} coupling will affect the Cr^{3+} ordering. According to Bongers *et al*, the effective Cr^{3+}-Cr^{3+} spin exchange is ferromagnetic with Curie-Weiss temperature $\theta_{CW} \sim 15\,K$ [176]. At the first sight, one would expect an ordered (or partially ordered) magnetic ground state in $Y_2(Cr_{0.5}Sb_{0.5})_2O_7$ since the Sb fraction (0.5) is still well below the nonmagnetic ion percolation threshold on a pyrochlore lattice $x_c = 0.61$ [178]. Moreover, Cr^{3+} is stable at ambient pressure. This means the valence disorder which hinders the long range magnetic order in $Y_2Mn_2O_7$ should not be important in $Y_2(Cr_{0.5}Sb_{0.5})_2O_7$.

It has been theoretically proposed that very weak bond disorder can introduce a spin glass state [29, 30]. In this model, the spin freezing temperature T_f does not depend on the disorder level Δ if there is spin-lattice coupling in the system [30], as experimentally verified in $Y_2Mo_2O_7$ [23]. However, T_f will scale with Δ in the absence of spin-lattice coupling, and therefore be significantly lowered at the weak bond disorder limit (Fig. 5.4) [29, 30]. As pointed out recently, the spin-lattice coupling in $Y_2Mo_2O_7$ is essentially mediated by the orbital degrees of freedom [32]. In magnetic 3d TM pyrochlores, the orbital moment is usually quenched [4], which indicates the spin-lattice coupling is probably not dominant in these systems. As a result, the TM pyrochlore family with very weak bond disorder is an ideal candidate to test the spin glass theory proposed

in Ref. [29, 30] at zero spin-lattice coupling limit.

The spinel compound $ZnCr_2O_4$, in which the Cr^{3+} ions form a pyrochlore sublattice with corner-sharing tetrahedra, is also worth mentioning. It enters into a co-planar antiferromagnetic state below $T_N = 12.5\,K$ [179]. Since the cubic pyrochlore lattice with Heisenberg-type antiferromagnetic interactions cannot order [15], the onset of antiferromagnetism has been attributed to the spin-driven lattice symmetry breaking at T_N [179, 180, 174, 181]. As a result, a cooperative spin-lattice coupling exists in this special case, as included in the spin-glass model by Shinaoka *et al* to account for the spin freezing transition in $Zn_{1-x}Cd_xCr_2O_4$ ($x \geqslant 0.01$) [182].

More importantly, we highlight the magnetic ground state switches from antiferromagnetic to spin glass by nonmagnetic ion dilution in $Zn(Cr_{1-x}Ga_x)_2O_4$ when x is between 0.2 and 0.25 [183, 184]. This critical value is much lower than the nonmagnetic ion percolation threshold on a pyrochlore lattice: $x_c = 0.61$ [178]. Nonmagnetic ion dilution can cause random distortion to the spin exchange network formed by TMO_6-octahedra due to the size mismatch between nonmagnetic and magnetic ions, and therefore leads to bond disorder. The ionic radii of Ga^{3+} and Cr^{3+} are 0.62 Å and 0.615 Å, respectively. This places $Zn(Cr_{1-x}Ga_x)_2O_4$ to the weak bond disorder limit. However, T_f is not sensitive to Δ in this compound due to the presence of spin-lattice coupling [30].

Based on the discussions above, we have demonstrated that bond disorder is essential to understand the spin glass state on a pyrochlore lattice. The spin freezing temperature T_f is controlled by the bond disorder strength Δ and spin-lattice coupling. While the theories proposed by Saunders *et al* [29] and Shinaoka *et al* [30] have been tested in the presence of both spin-lattice coupling and weak bond disorder, they have not been verified in systems without spin-lattice coupling yet. In the following, we have proposed a potential TM pyrochlore candidate $Y_2(Cr_{0.5}Sb_{0.5})_2O_7$ to test the relevant theories.

5.2.2 Data analysis

The neutron powder patterns have been refined using the Rietveld method described in Appendix A. We have adopted the general crystallographic structure for a pyrochlore with space group $Fd\bar{3}m$ in our refinement [15]. The lattice parameters, atomic positions and isotropic atomic displacement parameters (B_{iso}) in Ref. [177] by refining the room temperature X-ray diffraction pattern of $Y_2(Cr_{0.5}Sb_{0.5})_2O_7$ have been used as the starting parameters in our refinements. A Thompson-Cox-Hastings pseudo-Voigt convoluted with axial divergence asymmetry function has been used to fit the peak shape of the nuclear reflections [106]. The magnetic Bragg peaks which can be observed at high magnetic fields were fitted by a Gaussian function [106].

5.2.3 Absence of magnetic order in $Y_2(Cr_{0.5}Sb_{0.5})_2O_7$: a spin glass candidate

Introduction

Magnetic frustration refers to systems where the total free energy cannot be minimized by optimizing the interaction energy between each pair of spins [1]. It is responsible for the abundant spin structures in pyrochlore compounds where 'geometric frustration', i.e. corner-sharing tetrahedral network consisting of magnetic cations, coexist with competing spin interactions [15]. The consequential magnetic ground state can be highly degenerate (spin liquid) in a Heisenberg magnet with antiferromagnetic spin exchange interactions [185, 186]. This degeneracy can be partially lifted in rare-earth compounds $R_2Ti_2O_7$ ($R = Dy, Ho$) to form a exotic state called 'spin ice' [15, 187, 188]. Strikingly, the quasiparticles excitations of a spin ice state are found to resemble the behaviour of magnetic monopoles [189, 190]. Moreover, peculiar long range order can also result in relevant systems. The low temperature spin modulation in $Gd_2Ti_2O_7$ was initially proposed to be 4-k with propagation vector $\mathbf{k} = [\frac{1}{2}\frac{1}{2}\frac{1}{2}]^*$ [113]. Recently, this solution has been theoretically reproduced by taking into account the thermal fluctuations which were not accessible within mean-field approaches [114], but this model was challenged by Paddison *et al* recently [191]. Strong evidence using neutron diffraction measurements has been provided to show it is essentially 1-k modulation in $Gd_2Ti_2O_7$ [191].

Another interesting state which may rise in pyrochlores is spin glass (SG). In general, a SG state prevails in systems dominated by randomness and frustration. For example, the sign of Ruderman-Kittel-Kasuya-Yosida (RKKY) interaction in lightly doped $Au_{1-x}Fe_x$ ($x \sim 0.05$) is very sensitive to the distance between Fe-sites [192, 193]. SG in this class of materials is induced by zero-point spin exchange fluctuations, i.e competing antiferromagnetic and ferromagnetic spin interactions. SG is also commonly observed in diluted magnets around the nonmagnetic site percolation threshold [194]. Compared with these classic systems, the appearance of SG on a 'clean' pyrochlore lattice is nontrivial to understand. Clear signatures of SG have been observed in $Y_2Mo_2O_7$ [23, 195, 21]. Recent advancement in theory strongly point to the key role of weak bond disorder on the spin freezing in geometically frustrated antiferromagnets [29, 196]. Moreover, an additional spin-lattice coupling term is required to correctly reproduce the spin freezing temperature (T_f) of $Y_2Mo_2O_7$ [30]. These theories can also be applied to other SG compounds such as $Zn_{1-x}Cd_xCr_2O_4$ and $Zn(Cr_{1-x}Ga_x)_2O_4$ [30, 182, 183, 184]. On the other hand, T_f is expected to be controlled by the disorder strength (Δ) in the absence of spin-lattice coupling [29]. This will significantly reduce the onset temperature of SG in relevant systems [30]. In Mo-pyrochlores, the spin-lattice coupling is essentially mediated by the orbital degrees of freedom [32, 197]. However, this contribution is often insignificant in 3d transition-metal (TM) pyrochlores due to the orbital quenching effect, making them ideal systems to validate the theory in

the zero spin-lattice coupling limit. We note the cooperative spin-lattice coupling in the other 3d TM family, $Zn_{1-x}Cd_xCr_2O_4$ and $Zn(Cr_{1-x}Ga_x)_2O_4$, is related to a novel spin-Peierls-like phase transition, rather than the conventional orbital physics [179, 180, 174, 181].

Following this idea, we have synthesized $Y_2(Cr_{1-x}Ga_{x-0.5}Sb_{0.5})_2O_7$ $(0.5 \leqslant x \leqslant 0.9)$ for investigation. By randomly substituting the magnetic TM ions (Cr) with nonmagnetic ions (Sb/Ga), we have created site disorder which is a conventional way of approaching SG [194]. Most of all, bond disorder is also introduced into our samples due to the size mismatch between magnetic and nonmagnetic ions. This feature has been proven to be responsible for the SG state in geometrically frustrated magnets. For the Y_2CrSbO_7 $(x = 0.5)$ sample which is well below the nonmagnetic site percolation threshold $(x_c \simeq 0.61)$ [178], our high-resolution neutron powder diffraction (HRNPD) measurements cannot detect any long range spin order down to 2 K. This is in sharp contrast with the prevailing ferromagnetic spin exchange interactions as revealed by $\theta_{CW} = 20.1(6)$ K. Compared with nonmagnetic site percolation, our simulations concerning disordered bond percolation predicts a much lower threshold $(x_c' \simeq 0.23)$. x_c' is in excellent agreement with the onset of SG in $Zn(Cr_{1-x}Ga_x)_2O_4$ where x is between 0.2 and 0.25 [183, 184]. Our Rietveld refinement confirms the average Cr-O-Cr bond angle [130.19(2)°] is in the critical region where the corresponding spin exchange constant changes its sign. The resulting zero-point spin exchange fluctuations may further assist the formation of SG in Y_2CrSbO_7 $(x = 0.5)$.

Experiments

Polycrystalline samples of $Y_2(Cr_{1-x}Ga_{x-0.5}Sb_{0.5})_2O_7$ $(0.5 \leqslant x \leqslant 0.9)$ were synthesized by the traditional solid reaction method. A homogeneously ground mixture of $GaSbO_4$ ($CrSbO_4$) and Y_2O_3 (4N) were heated in air for 6 days at 1200 °C with several intermediate regrindings to prepare Y_2GaSbO_7 (Y_2CrSbO_7). $GaSbO_4$ ($CrSbO_4$) raw materials were preprared by sintering Ga_2O_3 (Cr_2O_3) (3N) and Sb_2O_3 (3N, 5 % excess to compensate the volatilization) for 3 days at 640 °C, and then 5 days at 1200 °C with several intermediate regrindings as well. The intermediate temperature (640 °C) is to transform Sb_2O_3 into Sb_2O_4. Finally, $Y_2Cr_{1-x}Ga_xSbO_7$ were obtained by heating the stoichiometrically mixed Y_2GaSbO_7 and Y_2CrSbO_7 powders for 5 days at 1200 °C.

The room temperature crystallographic structure of each sample was checked by the X-ray powder diffraction technique using a Bruker D8 diffractometer (Cu Kα1, $\lambda = 1.5406$ Å). Magnetic susceptibility data were collected using a Magnetic Property Measurement System (MPMS, Quantum Design).

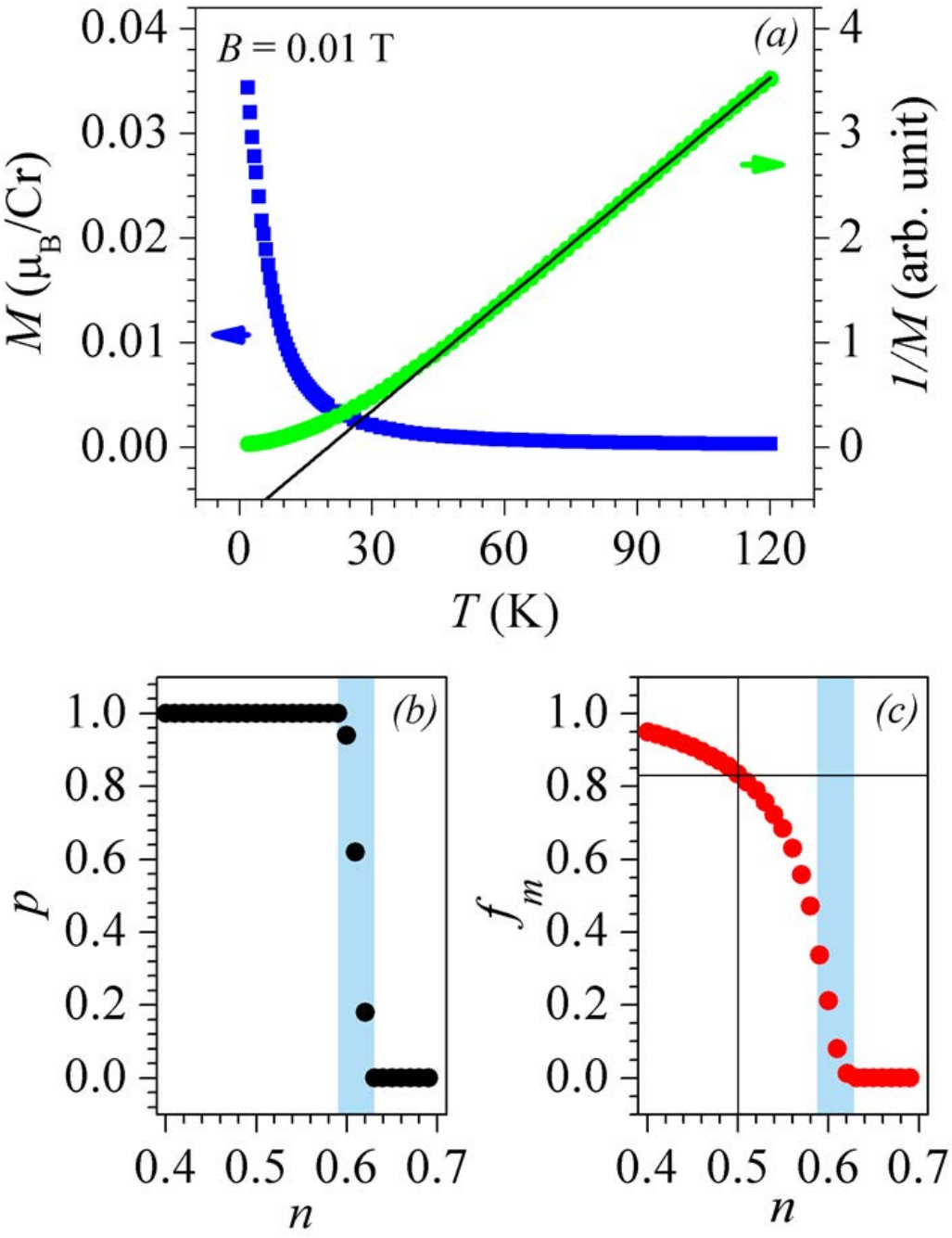

Figure 5.6: (a) χ-T (left axis) and $1/\chi$-T (right axis) curves of Y_2CrSbO_7 measured at $B = 0.01$ T. The black solid curve is a Curie-Weiss fit to the linear part of the χ-T curve at high temperatures. (b) Nonmagnetic ion substitution level (n) dependence of site percolation probability (p). (c) Fraction of percolative magnetic clusters (f_m) as a function of the nonmagnetic ion fraction (n). The results were obtained by a 50-times sampling simulation on a $N \times N \times N$ ($N = 64$) lattice.

HRNPD patterns were collected at the D2B powder diffractometer ($\lambda = 1.594$ Å) equipped with a 5-Tesla vertical cryomagnet at the Institute Laue-Langevin (ILL) in Grenoble, France. About 8 g of powder was hydraulically pressed into a cylinder (height = 11 mm, diameter = 13 mm) to avoid any field-induced texture and then loaded into a vanadium container. Rietveld refinements were performed using the FullProf package [102, 106].

A minor impurity phase $YCrO_3$, with volume fraction 3.4(2) %, is necessary to match some very weak peaks in our HRNPD patterns [Fig. 5.7(inset)]. The onset of antiferromagnetism in $YCrO_3$ is responsible for the kink around 142 K in our susceptibility curves (data not shown here) [177]. As a result, we will only show susceptibility data measured below 120 K in the following.

Main results and discussion

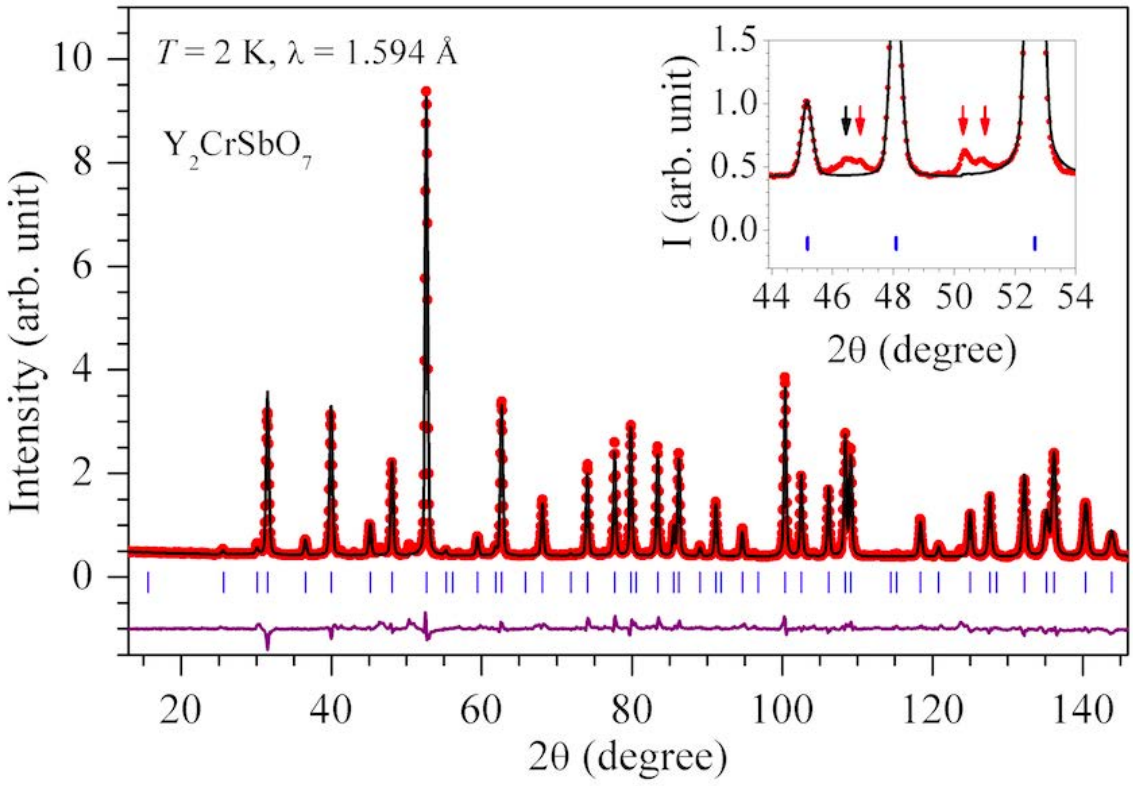

Figure 5.7: (main panel) HRNPD pattern (red solids) of Y_2CrSbO_7 at $T = 2.0$ K, $B = 0$ T. Calculated pattern (black line), nuclear Bragg positions (blue vertical line) and difference (purple line) are also displayed. (inset) Enlarged version of a selected angle region. Additional peaks from $YCrO_3$ (red arrows) and V (black arrow) can be visualized.

The low field ($B = 0.01\,\mathrm{T}$) susceptibility (χ) data of Y_2CrSbO_7 is shown in Fig. 5.6a. Although distinct deviation from standard paramagnetic behaviour sets in below $\sim 40\,\mathrm{K}$, no magnetic transition can be observed down to the lowest temperature probed (1.8 K). By fitting the linear part of the inverse susceptibility ($1/\chi$) versus temperature curve between 40 K and 120 K, we obtained $T_{\mathrm{CW}} = 20.1(6)\,\mathrm{K}$, meaning Y_2CrSbO_7 is a highly frusrated system dominated by ferromagnetic spin exchange interactions. This is in sharp contrast with the fully occupied compound $Y_2Mn_2O_7$ (same electronic configuration $3d^3$) which has a ferromagnetic-like state below 15 K [33, 34]. The absence of ferromagnetism in Y_2CrSbO_7 is confirmed by the HRNPD pattern measured at 2.0 K (Fig. 5.7). Only nuclear reflections can be resolved in our refinement. The refined crystallographic parameters of Y_2CrSbO_7 ($x = 0.5$) and $Y_2Cr_{0.4}Ga_{0.6}SbO_7$ (n = 0.8) at 2.0 K are listed in Table 5.1.

Table 5.1: Structural parameters of Y_2CrSbO_7 and $Y_2Cr_{0.4}Ga_{0.6}SbO_7$. The corresponding HRNPD patterns were refined under space group $Fd\bar{3}m$ ($a = b = c,\ \alpha = \beta = \gamma = 90°$). The only atomic position needs to be refined is O2 (x, 0.125, 0.125) [177].

	Y_2CrSbO_7 $T = 300\,\mathrm{K}, B = 0\,\mathrm{T}$	Y_2CrSbO_7 $T = 2\,\mathrm{K}, B = 0\,\mathrm{T}$	Y_2CrSbO_7 $T = 2\,\mathrm{K}, B = 5\,\mathrm{T}$	$Y_2Cr_{0.4}Ga_{0.6}SbO_7$ $T = 2\,\mathrm{K}, B = 0\,\mathrm{T}$
a (Å)	10.1620(1)	10.15235(7)	10.15143(5)	10.15081(8)
x (O2)	0.4178(1)	0.41793(8)	0.41792(9)	0.4182(1)
B_{iso} (Y) (Å^2)	0.72(2)	0.69(1)	0.65(1)	0.58(1)
B_{iso} (Cr) (Å^2)	0.44(2)	0.34(1)	0.31(1)	0.51(2)
B_{iso} (O1) (Å^2)	0.15(3)	0.17(2)	0.08(2)	0.17(3)
B_{iso} (O2) (Å^2)	0.45(1)	0.439(8)	0.399(9)	0.37(1)
Cr - O2 (Å)	1.9810(6)	1.9787(3)	1.9785(4)	1.9774(5)
Cr - Cr (Å)	3.59282(3)	3.58940(2)	3.58907(1)	3.58885(2)
Cr - O2 - Cr (°)	130.14(2)	130.19(1)	130.19(2)	130.31(2)

As mentioned above, a SG state often emerges in systems close to the nonmagnetic site percolation threshold. To check the influence of site disorder in Y_2CrSbO_7, we have simulated the fraction of percolative magnetic ions (f_m) as well as percolation probability (p) at various nonmagnetic ion substitution levels (x). Our model predicts a site percolation threshold $x_c \simeq 0.61$ which is consistent with previous studies (Fig. 5.6b) [178]. More importantly, 83 % of the sample ($x = 0.5$) is populated by the percolative magnetic sites as shown in Fig. 5.6c. This suggests that site disorder is not strong enough to affect the magnetic

properties of Y_2CrSbO_7 yet.

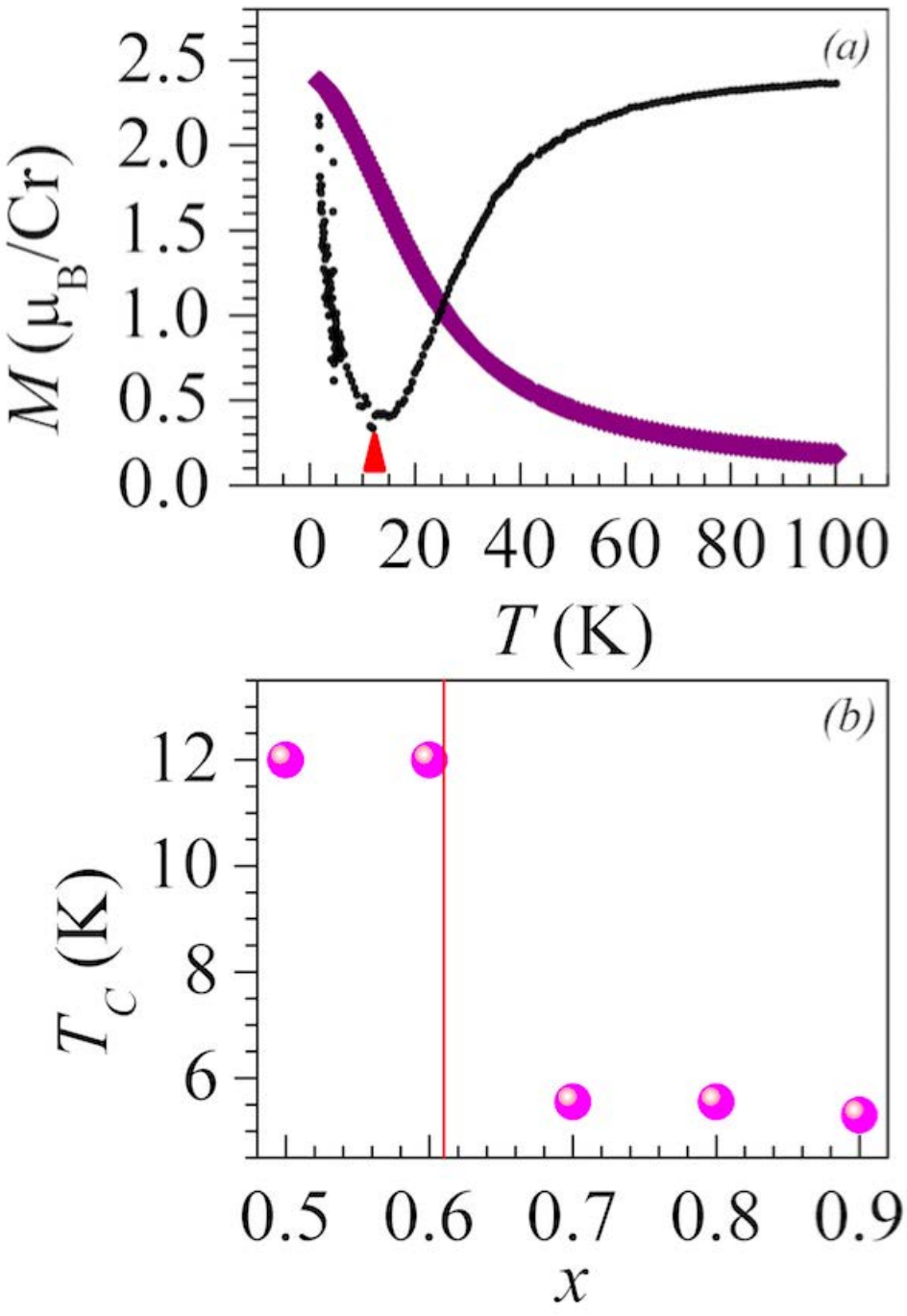

Figure 5.8: (a) Magnetization (M) - temperature (T) curve (purple) of Y_2CrSbO_7 at 5 T. The black solids is the derivative of the M-T curve. The red arrow marks the position of T_C. (b) T_C - x plot (pink). x_c is labeled by the red line.

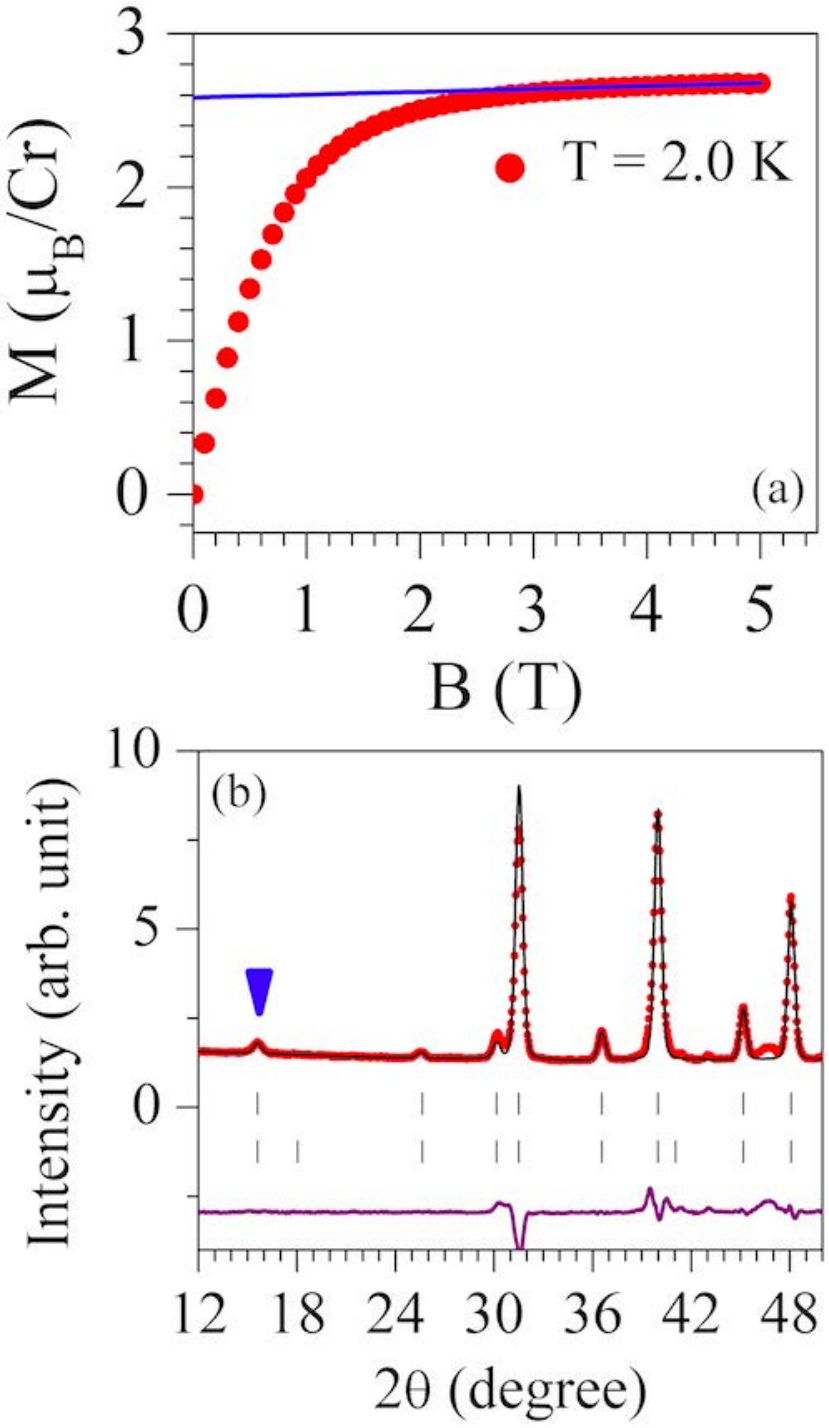

Figure 5.9: (a) Magnetization (M) versus magnetic field (T) curve (red solids) of Y_2CrSbO_7 at 2 K. The blue line is a linear fit to the data above 3.5 T. (b) HRNPD pattern and the Rietveld refinement of Y_2CrSbO_7 at 2 K/5 T. The blue arrow marks the ferromagnetic reflection at the reciprocal position $(1, 1, 1)$.

f_{m} is very sensitive to x in the critical region of nonmagnetic site percolation (Fig. 5.6c). Thus another possible explanation for the absence of magnetic order in the synthesized Y_2CrSbO_7 is off-stoichiometry towards the $x > 0.5$ side. In order to rule out this scenario, we have studied the temperature dependence of magnetization in $Y_2(Cr_{1-x}Ga_{x-0.5}Sb_{0.5})_2O_7$ ($0.5 \leqslant x \leqslant 0.9$) in the high field region where the magnetic frustration is suppressed. As shown in Fig. 5.8a, ferromagnetic-like behaviour is recovered under $B = 5\,\mathrm{T}$ evidenced by a weak plateau at low temperatures. The Curie temperature (T_{C}) is determined by the minimum in the corresponding derivative curve. T_{C} as a function of x is displayed in Fig. 5.8b. A sudden decrease of T_{C} is observed between $x = 0.6$ and $x = 0.8$. This is consistent with the nonmagnetic site percolation at $x_c \simeq 0.61$ (Fig. 5.6b). Moreover, the magnetization (M) of Y_2CrSbO_7 shows linear dependence on magnetic field above $B = 3.5\,\mathrm{T}$ (Fig. 5.9a). Extrapolating the high field M-B curve produces a saturation moment (M_{sat}) around $2.585\,\mu_B$/Cr. On the other hand, the total magnetic moment ($M_{tot} = gJ$, where g is the Landé g-factor and J is the total angular momentum) of the Cr^{3+} ion can be obtained by fitting the linear part of the low field $1/\chi$-T curve in Fig. 5.6a. By assuming the g is 2, we get $M_{tot} = 3.12\,\mu_B$/Cr. The difference between M_{sat} and M_{tot} can be explained by the presence of non-percolative spin clusters in Y_2CrSbO_7 (Fig. 5.6c). As a result, f_{m} is around 83 % in Y_2CrSbO_7. This generates an effective nonmagnetic ion fraction x_{eff} exactly around 0.5. This confirms off-stoichiometry is not present in Y_2CrSbO_7. We have also refined the magnetic structure at $B = 5\,\mathrm{T}$ (Fig. 5.9b). This corresponds to a simple collinear ferromagnetic alignment along the c-axis with a propagation vector $k = (0, 0, 0)$ and an effective moment $2.4(1)\,\mu_B$/Cr. We note the spins can also point along are axes due to the cubic symmetry ($Fd\bar{3}m$) of a pyrochlore structure.

Besides the site disorder induced by random nonmagnetic ion substitution, bond disorder also exists in such systems due to the inevitable size mismatch between magnetic and nonmagnetic ions. The ionic radii of Cr^{3+}, Sb^{5+} and Ga^{3+} are 0.615 Å, 0.60 Å and 0.62 Å, respectively. The small variations of ionic radii on B-site puts Y_2CrSbO_7 to the weak bond disorder limit. The effect of nonmagnetic ion substitution can be readily demonstrated by the x-dependences of Cr-O2-Cr bond angle, the Cr-O2 bond length and the isotropic atomic displacement parameter of O2 in Table 5.1. Due to the random substitution of B-sites with Sb^{5+} ions, there are five Cr/Sb-tetrahedral configurations randomly distributed in the sample, corresponding to empty, single, double, triple and full occupation by Cr ions (Fig. 5.10a - e). The bond disorder could apply random strains to the BO_6-octahedron, leading to random deviations of the Cr-O2-Cr bond angle from the average value (Fig. 5.10f). We have calculated the substituting region where percolative magnetic clusters exclusively consisting of fully Cr-occupied tetrahedral can be found (Fig. 5.10a). In this case, there will be no bond disorder in the corresponding percolative magnetic region. As shown in Fig. 5.11a, the new percolation

threshold ($x_c' \simeq 0.23$) is signicantly reduced compared with $x_c \simeq 0.61$ for site disorder. Most of all, this model is consistent with the observations in $Zn(Cr_{1-x}Ga_x)_2O_4$ where the Cr/Ga sublattice also has a pyrochlore structure [183, 184]. While $ZnCr_2O_4$ has a antiferromagnetic ground state, substitution Cr^{3+} with Ga^{3+} switches this system to SG between $x = 0.2$ and $x = 0.25$ [183, 184]. Moreover, the effective ordered moment is reduced by a factor of 20 % even at $x = 0.05$, which is close to 26 % predicted by our model. As a result, our model should capture the essential physics in Y_2CrSbO_7. Y_2CrSbO_7 ($x = 0.5$) is in a region dominated by bond disorder. We also note the fast drop of f_m even below x_c' (Fig. 5.11b). This indicates the fraction of long range order in relevant systems is extremely sensitive to the bond disorder strength even at the weak limit.

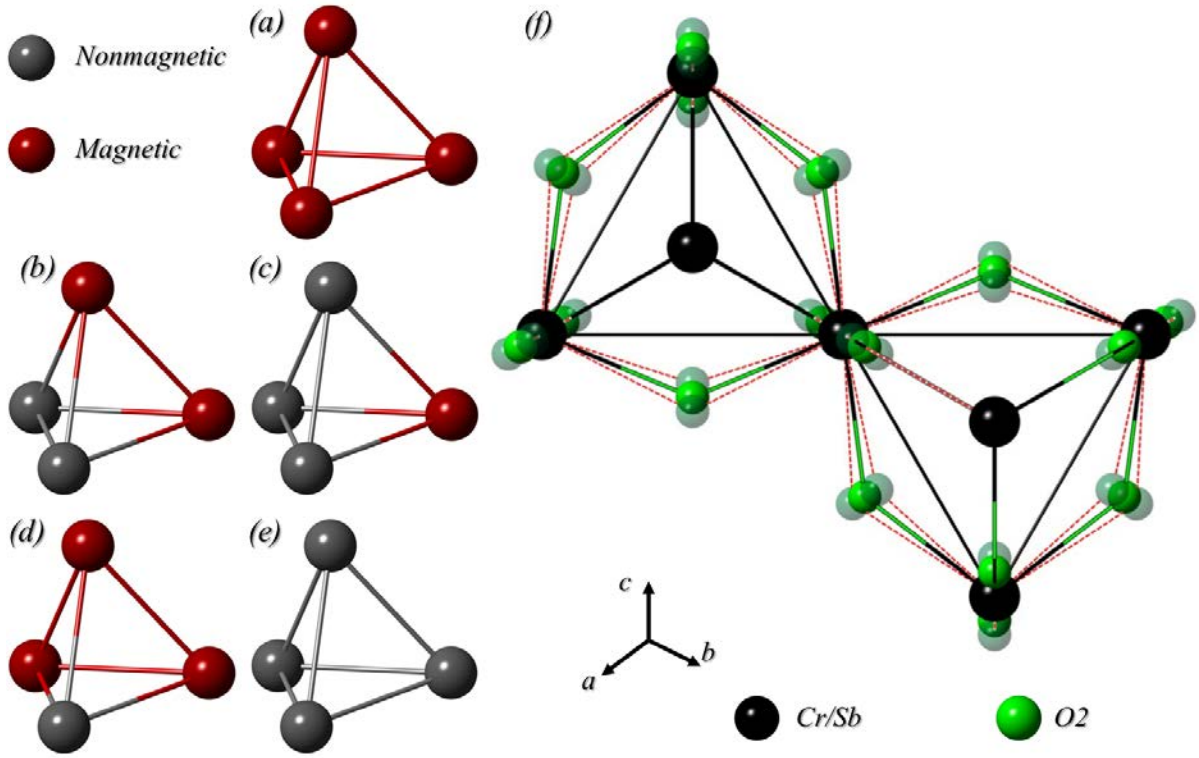

Figure 5.10: (a) - (e) Five possible configurations of a single Cr/Sb-tetrahedron. The bonds are displayed by dual-band cylinders. (f) Possible influence of bond disorder to the local structure in a unit cell. O2 oxygens (green spheres) will deviate from their average position (translucent green spheres), producing a random distribution of Cr/Sb-O2-Cr/Sb bond angles in the sample (red dotted lines). The Cr/Sb-tetrahedral network is linked by black lines.

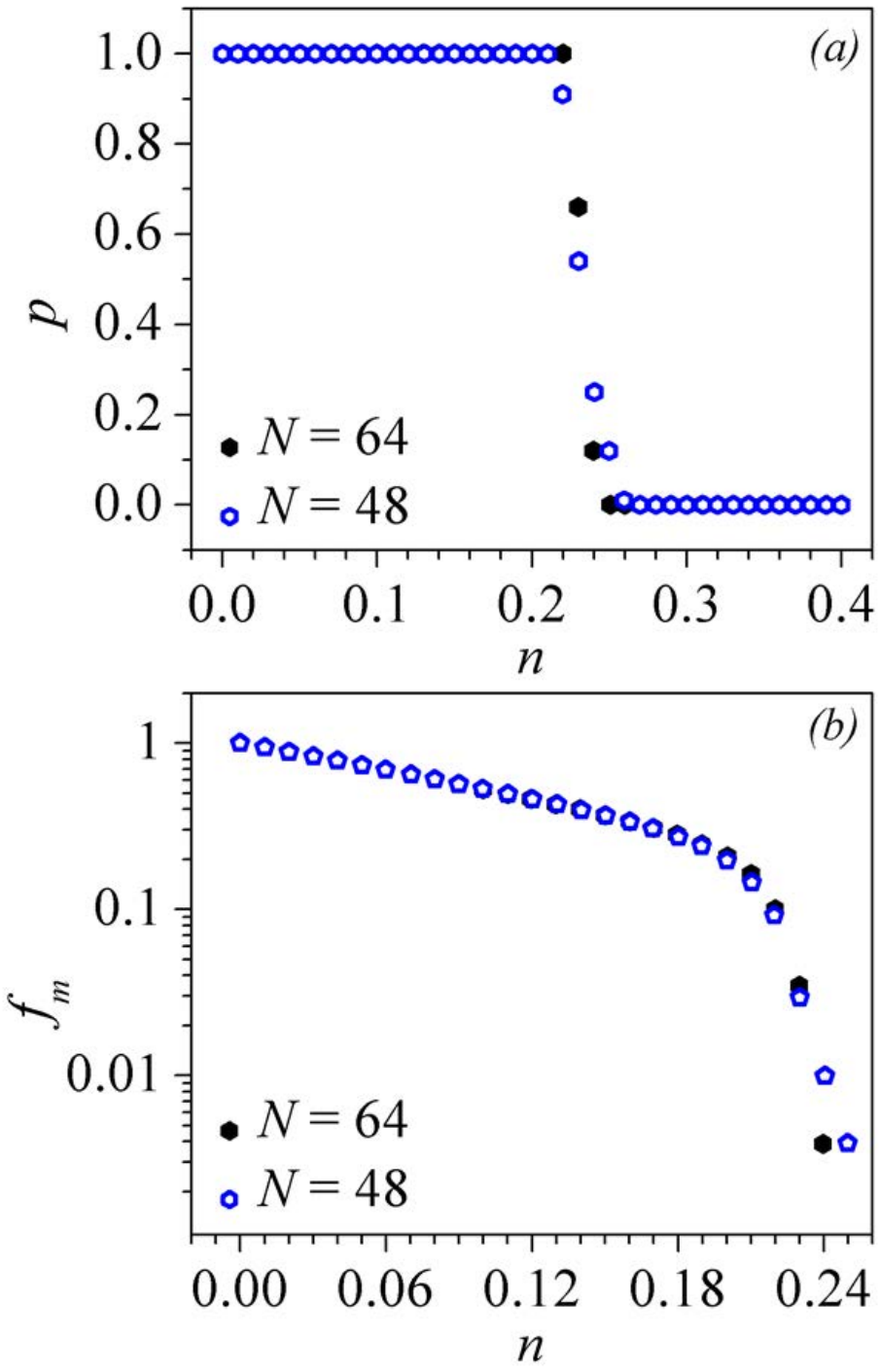

Figure 5.11: (a) Pecolation probability (p) of bond disorder as a function of the nonmagnetic ion fraction (n). (b) f_m - n curve after taking bond disorder into account. The results were obtained by a 100-times sampling simulation on 64×64×64 (black) and 48×48×48 (blue) lattices, respectively.

Based on the prevailing bond disorder and the lack of long range order down to 1.8 K of Y_2CrSbO_7, we propose SG as its possible magnetic ground state. The SG in Y_2CrSbO_7 may be further assisted by the zero-point spin exchange fluctuations. The refined average Cr/Sb-O2-Cr/Sb bond angle and Cr/Sb-O2 distance are 130.19(1)° and 1.9783(3) Å, respectively (Table 5.1). According to the Goodenough-Kanamori rules [12, 198], the nature of TM-O-TM spin exchange is mostly determined by the exchange bond angle and the bond lengths. While both bond distance and the type of ion are fixed, the bond angle becomes the only dominant parameter. Y_2CrSbO_7 belongs to a series of Cr^{3+} oxides with almost identical values of Cr-O bond length [199]. As investigated in Ref [199], 130.19(1)° is in a critical region where the effective spin exchange constant changes its sign. The zero-point spin fluctuations could be triggered by the bond disorder, as shown in Fig. 5.10f.

The appearance of such SG states in weakly disordered pyrochlore lattices has been studied, e.g. $Y_2Mo_2O_7$ [29, 196, 30]. It is shown that a SG can appear at very low bond disorder level. The corresponding T_f will be very low (scale with Δ) unless the spin-lattice coupling term is included. For Y_2CrSbO_7, the spin-lattice coupling effect is expected to be insignificant due to the orbital quenching effect. On the other hand, the disorder strengh is also weak evidenced by the small ionic size mismatch on B-sites. This makes Y_2CrSbO_7 a candidate to study purely weak bond disorder induced SG state in the absence of spin-lattice coupling.

5.3 Conclusions and future work

In summary, we have carried out susceptibility and HRNPD measurements on $Y_2(Cr_{1-x}Ga_{x-0.5}Sb_{0.5})_2O_7$ ($0.5 \leqslant x \leqslant 0.9$). While Y_2CrSbO_7 is not sensitive to nonmagnetic site disorder based on multiple evidence, we cannot observe any long range order down to the lowest temperature probed (1.8 K). We propose the bond disorder caused by the ionic size mismatch between Cr^{3+} and Sb^{5+} is the origin of this phenemenon. Further assisted by the zero-point spin exchange fluctuations, Y_2CrSbO_7 may be another SG candidate among pyrochlores. Unlike $Y_2Mo_2O_7$, the SG state in Y_2CrSbO_7 is exclusively caused by weak disorder effect.

Our results also provide important motivations to future studies. For example, lower temperature ($T < 1.8$ K) characterizations are neccesary to confirm the real state of Y_2CrSbO_7 above $T = 0$ K. Moreover, new materials are demanded to test n'_c predicted by our geometry model.

CHAPTER 6

SUMMARY

6.1 γ-CoV_2O_6

We have performed neutron diffraction studies on the quasi-one-dimensional magnet γ-CoV_2O_6, which possesses competing magnetic interactions but not geometric frustration. We have found that the low temperature magnetic reflections can be indexed by two propagation vectors, $k_1 = (0.5, 0, 0)$ and $k_2 = (-0.25, 0, 0.25)$. More importantly, we propose that this compound develops two single-k phases in a volume ratio of $65(1) : 35(1)$ below $T_N = 6.6\,K$. By further decreasing the temperature, the minority phase modulated by k_2 undergoes an incommesurate-commensurate lock-in transition at $T^* = 5.6\,K$.

6.2 $Pr_{0.5}Ca_{0.5}Mn_{0.97}Ga_{0.03}O_3$

We have studied the strained manganese perovskite $Pr_{0.5}Ca_{0.5}Mn_{0.97}Ga_{0.03}O_3$ (PCMGO). By varying the magnetic field at $T = 150\,K$, where PCMGO has a paramagnetic ground state, the carrier delocalization driven by the collapse of electronic phase separation (orbital order, polarons) occurs at $B_{c1} = 5.1\,T$. Surprisingly, the Jahn-Teller distortion is enhanced above B_{c1}, contradicting the softening picture reported previously. On the other hand, the spins remain mostly paramagnetic across B_{c1} and do not become ferromagnetic at a much higher field $B_{c2} = 7.9\,T$, where a giant magnetostriction effect is observed. This decoupling between carrier delocalization and ferromagnetism is related to the prevailing anisotropic strains in PCMGO. Most of all, the magnetoresistance in PCMGO can be detected up to B_{c2}, rather than B_{c1}. These results strongly suggest that colossal magnetoresistance is driven by two independent forces: (I) carrier delocalization, and (II) ferromagnetic double-exchange.

6.3 $Y_2(Cr_{1-x}Ga_{x-0.5}Sb_{0.5})_2O_7$, $0.5 \leqslant x \leqslant 0.9$

We have studied the magnetism of the diluted transition metal pyrochlores $Y_2(Cr_{1-x}Ga_{x-0.5}Sb_{0.5})_2O_7$ ($0.5 \leqslant x \leqslant 0.9$). Although Y_2CrSbO_7 ($x = 0.5$) is well below the nonmagnetic site percolation threshold $x_c \simeq 0.61$, both susceptibility and neutron powder diffraction measurements cannot detect any magnetic long range order down to 2 K. We propose that the magnetic long range order in Y_2CrSbO_7 is suppressed by the bond disorder, which has a much lower percolation threshold $x_c' \simeq 0.23$ based on our simulations, caused by the weak ionic size mismatch between Cr^{3+} and Sb^{5+}. Bond disorder in pyrochlores can lead to a spin glass at low temperatures. In the absence of spin-lattice coupling, the spin freezing temperature scales with the bond disorder strength based on the recent spin glass theories [30, 29]. As a result, Y_2CrSbO_7 is a potential spin glass candidate with a very low spin freezing temperature due to its very weak bond disorder and zero spin-lattice coupling.

APPENDIX A

RIETVELD REFINEMENT

Experimentally, the i^{th} intensity ($I_{\mathrm{obs,\,i}}$), together with the corresponding standard deviations (σ_i), of a diffraction pattern is always recorded as a function of some variable (x_i), e.g. scattering angle, time-of-flight or energy. On the other hand, the calculated profile I_{calc} can be expressed as

$$I_{\mathrm{calc,\,i}} = \sum_n S_n \sum_Q I_{n,\,Q}\Omega(x_i - x_{n,\,Q}) + b_n, \tag{A.1}$$

where n labels the phase number, S_n is the scale factor, Q labels the Bragg reflection position, $I_{n,\,Q}$ is the calculated intensity, Ω is the reflection profile function which models both instrumental and sample effects, b_n is the background. Some of these parameters, e.g. L ad F have already been discussed in Chapter. 2.2. In FullProf, the general expression of $I_{n,\,Q}$ can be writen as

$$I_{n,\,Q} = \Big\{L,\, A,\, P,\, C,\, F^2\Big\}_{n,\,Q}, \tag{A.2}$$

where L contains the *Lorentz*, polarization and mutiplicity factors, F is structure factor, A is the absorption correction, P is the preferred orientation function and C includes the spherical corrections [102]. In the Rietveld refinement process, I_{calc} is being optimised by minimizing the chi-square parameter

$$\chi^2 = \sum_i w_i \Big\{I_{\mathrm{obs,\,i}} - I_{\mathrm{calc,\,i}}(\alpha)\Big\}^2, \tag{A.3}$$

where w_i is the weigting factor, $\alpha = \{\alpha_1, \alpha_2, \alpha_3 ...\}$ stands for the parameter space to be determined. From mathematical point of view, $\left\{\dfrac{\partial\chi^2}{\partial\alpha}\right\}_{\alpha_{opt}} = 0$ once the optimum parameters are (α_{opt}) found [106].

By providing some initial guessing paramters α_{ini}, a *Taylor* expansion can be applied to $I_{\mathrm{calc}}(\alpha)$ around

α_{ini} to start the iterative process. Until a convergence criterion is satisfied, the shifts of the parameters δ_α by solving the normal equations in the m^{th} cycle will be added to the starting parameters of the $(m+1)^{th}$ cycle: $(\alpha_{ini})_{m+1} = (\alpha_{ini})_m + \delta_{\alpha,\,m}$. After finishing the simulation, an individual set of parameters are used to judge the quality of this refinement. They include the profile factor R_p, the weighted profile factor R_{wp} which can be expressed by [106]

$$R_p = 100 \times \frac{\sum_i |I_{\mathrm{obs,\,i}} - I_{\mathrm{calc,\,i}}|}{\sum_i I_{\mathrm{obs,\,i}}}, \tag{A.4}$$

$$R_{wp} = 100 \times \left\{ \frac{\sum_i w_i |I_{\mathrm{obs,\,i}} - I_{\mathrm{calc,\,i}}|^2}{w_i \sum_i I^2_{\mathrm{obs,\,i}}} \right\}^{1/2}. \tag{A.5}$$

In practice, a Rieveld refinement can easily get stuck due to various reasons such as a bad choice of starting parameters, correlation between paramters and the large number of paramters to be fitted. As a result, some expertise are required. For example, background, zero shift of the detector and lattice parameters can be obtained first by an alternative *Lebail* profile matching approach [148]. Moreover, it is sensible to refine the parameters step-by-step in the early stage. Although the detailed refinement procedure is sample specific, a recommended sequence is summarized below [102]:

1, Scale factor.

2, The sloppy part of the background.

3, Atomic positions and Debye-Wallter factors.

4, Peak shape function and asymmetry parameters.

5, Microstructural parameters if required.

...

LIST OF REFERENCES

[1] H. T. Diep. *Frustrated Spin Systems*. World Scientific, *2nd* edition, 2013.

[2] Elbio Dagotto. *Nanoscale Phase Separation and Colossal Magnetoresistance*. Springer, 2003.

[3] `https://www.khanacademy.org/science/chemistry/electronic-structure-of-atoms/orbitals-and-electrons/a/the-quantum-mechanical-model-of-the-atom`.

[4] Stephen Blundell. *Magnetism in Condensed Matter*. Oxford University Press, 2011.

[5] I. M. Rae, Alastair. *Quantum Mechanics*. Adam Hilger, *2nd* edition, 1986.

[6] P. A. M. Dirac. *The principles of quantum mechanics*. Oxford University Press, 4th edition, 1958.

[7] M. Gerloch and R. C. Slade. *Ligand-Field Parameters*. Cambridge University Press, 1973.

[8] Zu-Fei Huang, Fei Du, Chun-Zhong Wang, Deng-Pan Wang, and Gang Chen. Low-spin Mn^{3+} ion in rhombohedral $LiMnO_2$ predicted by first-principles calculations. *Phys. Rev. B*, 75:054411, Feb 2007.

[9] N. Hollmann, S. Agrestini, Z. Hu, Z. He, M. Schmidt, C.-Y. Kuo, M. Rotter, A. A. Nugroho, V. Sessi, A. Tanaka, N. B. Brookes, and L. H. Tjeng. Spectroscopic evidence for exceptionally high orbital moment induced by local distortions in α-CoV_2O_6. *Phys. Rev. B*, 89:201101, May 2014.

[10] Elbio Dagotto, Takashi Hotta, and Adriana Moreo. Colossal magnetoresistant materials: the key role of phase separation. *Physics Reports*, 344(13):1 – 153, 2001.

[11] Gregory H. Wannier. The structure of electronic excitation levels in insulating crystals. *Phys. Rev.*, 52:191–197, Aug 1937.

[12] John B. Goodenough. *Magnetism And The Chemical Bond*. Wiley, 1963.

[13] Joaqun Garca and Gloria Subas. The verwey transitiona new perspective. *Journal of Physics: Condensed Matter*, 16(7):R145, 2004.

[14] Tôru Moriya. Anisotropic superexchange interaction and weak ferromagnetism. *Phys. Rev.*, 120:91–98, Oct 1960.

[15] Jason S. Gardner, Michel J. P. Gingras, and John E. Greedan. Magnetic pyrochlore oxides. *Rev. Mod. Phys.*, 82:53–107, Jan 2010.

[16] M. A. Ruderman and C. Kittel. Indirect exchange coupling of nuclear magnetic moments by conduction electrons. *Phys. Rev.*, 96:99–102, Oct 1954.

[17] Tadao Kasuya. A theory of metallic ferro- and antiferromagnetism on zener's model. *Progress of Theoretical Physics*, 16(1):45–57, 1956.

[18] Kei Yosida. Magnetic Properties of Cu-Mn Alloys. *Phys. Rev.*, 106:893–898, Jun 1957.

[19] Mariana J. Whitaker. Synthesis and characterisation of chemically modified schafarzikite and pyrochlore minerals. *PhD Thesis, University of Birmingham*, December 2013.

[20] K. Binder and A. P. Young. Spin glasses: Experimental facts, theoretical concepts, and open questions. *Rev. Mod. Phys.*, 58:801–976, Oct 1986.

[21] J.E. Greedan, M. Sato, Xu Yan, and F.S. Razavi. Spin-glass-like behavior in Y2Mo2O7, a concentrated, crystalline system with negligible apparent disorder. *Solid State Communications*, 59(12):895 – 897, 1986.

[22] J. S. Gardner, B. D. Gaulin, S.-H. Lee, C. Broholm, N. P. Raju, and J. E. Greedan. Glassy Statics and Dynamics in the Chemically Ordered Pyrochlore Antiferromagnet $Y_2Mo_2O_7$. *Phys. Rev. Lett.*, 83:211–214, Jul 1999.

[23] M. J. P. Gingras, C. V. Stager, N. P. Raju, B. D. Gaulin, and J. E. Greedan. Static Critical Behavior of the Spin-Freezing Transition in the Geometrically Frustrated Pyrochlore Antiferromagnet $Y_2Mo_2O_7$. *Phys. Rev. Lett.*, 78:947–950, Feb 1997.

[24] C. H. Booth, J. S. Gardner, G. H. Kwei, R. H. Heffner, F. Bridges, and M. A. Subramanian. Local lattice disorder in the geometrically frustrated spin-glass pyrochlore $Y_2Mo_2O_7$. *Phys. Rev. B*, 62:R755–R758, Jul 2000.

[25] J. E. Greedan, Delphine Gout, A. D. Lozano-Gorrin, Shahab Derahkshan, Th. Proffen, H.-J. Kim, E. Božin, and S. J. L. Billinge. Local and average structures of the spin-glass pyrochlore $Y_2Mo_2O_7$ from neutron diffraction and neutron pair distribution function analysis. *Phys. Rev. B*, 79:014427, Jan 2009.

[26] Amit Keren and Jason S. Gardner. Frustration Driven Lattice Distortion: An NMR Investigation of $Y_2Mo_2O_7$. *Phys. Rev. Lett.*, 87:177201, Oct 2001.

[27] D Sherrington and W Southernl. Spin glass versus ferromagnet. *Journal of Physics F: Metal Physics*, 5(5):L49, 1975.

[28] Jacques Villain. Insulating spin glasses. *Zeitschrift für Physik B Condensed Matter*, 33(1):31–42, 1979.

[29] T. E. Saunders and J. T. Chalker. Spin freezing in geometrically frustrated antiferromagnets with weak disorder. *Phys. Rev. Lett.*, 98:157201, Apr 2007.

[30] Hiroshi Shinaoka, Yusuke Tomita, and Yukitoshi Motome. Spin-glass transition in bond-disordered heisenberg antiferromagnets coupled with local lattice distortions on a pyrochlore lattice. *Phys. Rev. Lett.*, 107:047204, Jul 2011.

[31] H. J. Silverstein, K. Fritsch, F. Flicker, A. M. Hallas, J. S. Gardner, Y. Qiu, G. Ehlers, A. T. Savici, Z. Yamani, K. A. Ross, B. D. Gaulin, M. J. P. Gingras, J. A. M. Paddison, K. Foyevtsova, R. Valenti, F. Hawthorne, C. R. Wiebe, and H. D. Zhou. Liquidlike correlations in single-crystalline $Y_2Mo_2O_7$: An unconventional spin glass. *Phys. Rev. B*, 89:054433, Feb 2014.

[32] Peter M. M. Thygesen, Joseph A. M. Paddison, and et al. Orbital Dimer Model for Spin-Glass State in $Y_2Mo_2O_7$. 2016. arXiv, 1603.03087 (2016).

[33] J. N. Reimers, J. E. Greedan, R. K. Kremer, E. Gmelin, and M. A. Subramanian. Short-range magnetic ordering in the highly frustrated pyrochlore $Y_2Mn_2O_7$. *Phys. Rev. B*, 43:3387–3394, Feb 1991.

[34] Y. Shimakawa, Y. Kubo, N. Hamada, J. D. Jorgensen, Z. Hu, S. Short, M. Nohara, and H. Takagi. Crystal structure, magnetic and transport properties, and electronic band structure of $A_2Mn_2O_7$ pyrochlores ($A = \mathrm{Y}, \mathrm{In}, \mathrm{Lu}$, and Tl). *Phys. Rev. B*, 59:1249–1254, Jan 1999.

[35] J. E. Greedan, N. P. Raju, A. Maignan, Ch. Simon, J. S. Pedersen, A. M. Niraimathi, E. Gmelin, and M. A. Subramanian. Frustrated pyrochlore oxides, $Y_2Mn_2O_7$, $Ho_2Mn_2O_7$, and $Yb_2Mn_2O_7$: Bulk magnetism and magnetic microstructure. *Phys. Rev. B*, 54:7189–7200, Sep 1996.

[36] J.-G. Cheng, J.-S. Zhou, and J. B. Goodenough. Thermal conductivity, electron transport, and magnetic properties of single-crystal $Ca_3Co_2O_6$. *Phys. Rev. B*, 79:184414, May 2009.

[37] S. Aasland, H. Fjellvg, and B. Hauback. Magnetic properties of the one-dimensional $Ca_3Co_2O_6$. *Solid State Communications*, 101(3):187 – 192, 1997.

[38] T. Burnus, Z. Hu, M. W. Haverkort, J. C. Cezar, D. Flahaut, V. Hardy, A. Maignan, N. B. Brookes, A. Tanaka, H. H. Hsieh, H.-J. Lin, C. T. Chen, and L. H. Tjeng. Valence, spin, and orbital state of Co ions in one-dimensional $Ca_3Co_2O_6$: An x-ray absorption and magnetic circular dichroism study. *Phys. Rev. B*, 74:245111, Dec 2006.

[39] S. Agrestini, L. C. Chapon, A. Daoud-Aladine, J. Schefer, A. Gukasov, C. Mazzoli, M. R. Lees, and O. A. Petrenko. Nature of the Magnetic Order in $Ca_3Co_2O_6$. *Phys. Rev. Lett.*, 101:097207, Aug 2008.

[40] S. Agrestini, C. L. Fleck, L. C. Chapon, C. Mazzoli, A. Bombardi, M. R. Lees, and O. A. Petrenko. Slow Magnetic Order-Order Transition in the Spin Chain Antiferromagnet $Ca_3Co_2O_6$. *Phys. Rev. Lett.*, 106:197204, May 2011.

[41] Taketo Moyoshi and Kiyoichiro Motoya. Incommensurate Magnetic Structure and Its Long-Time Variation in a Geometrically Frustrated Magnet $Ca_3Co_2O_6$. *Journal of the Physical Society of Japan*, 80(3):034701, 2011.

[42] K. Prsa, M. Laver, M Mansson, and et al. Magnetic nano-fluctuations in a frustrated magnet. 2014. arXiv, 1404.7398 (2016).

[43] Y. Kamiya and C. D. Batista. Formation of Magnetic Microphases in $Ca_3Co_2O_6$. *Phys. Rev. Lett.*, 109:067204, Aug 2012.

[44] H. Y. Hwang, S-W. Cheong, P. G. Radaelli, M. Marezio, and B. Batlogg. Lattice Effects on the Magnetoresistance in Doped $LaMnO_3$. *Phys. Rev. Lett.*, 75:914–917, Jul 1995.

[45] P. G. Radaelli, G. Iannone, M. Marezio, H. Y. Hwang, S-W. Cheong, J. D. Jorgensen, and D. N. Argyriou. Structural effects on the magnetic and transport properties of perovskite $A_{1-x}A'_xMnO_3$ ($x = 0.25$, 0.30). *Phys. Rev. B*, 56:8265–8276, Oct 1997.

[46] A. J. Millis. Lattice effects in magnetoresistive manganese perovskites. *Nature*, 392(6672):147–150, 03 1998.

[47] A. J. Millis, Boris I. Shraiman, and R. Mueller. Dynamic Jahn-Teller Effect and Colossal Magnetoresistance in $La_{1-x}Sr_xMnO_3$. *Phys. Rev. Lett.*, 77:175–178, Jul 1996.

[48] S. Jin, T. H. Tiefel, M. McCormack, R. A. Fastnacht, R. Ramesh, and L. H. Chen. Thousandfold Change in Resistivity in Magnetoresistive La-Ca-Mn-O Films. *Science*, 264(5157):413–415, 1994.

[49] C. Martin, A. Maignan, M. Hervieu, and B. Raveau. Magnetic phase diagrams of $L_{1-x}A_xMnO_3$ manganites ($L = \mathrm{Pr}, \mathrm{Sm}$; $A = \mathrm{Ca}, \mathrm{Sr}$). *Phys. Rev. B*, 60:12191–12199, Nov 1999.

[50] Z. Jirk, S. Krupika, Z. ima, M. Dlouh, and S. Vratislav. Neutron diffraction study of $Pr_{1-x}Ca_xMnO_3$ perovskites. *Journal of Magnetism and Magnetic Materials*, 53(1):153 – 166, 1985.

[51] Y. Tomioka, A. Asamitsu, H. Kuwahara, Y. Moritomo, and Y. Tokura. Magnetic-field-induced metal-insulator phenomena in $Pr_{1-x}Ca_xMnO_3$ with controlled charge-ordering instability. *Phys. Rev. B*, 53:R1689–R1692, Jan 1996.

[52] Y. Tokura and N. Nagaosa. Orbital physics in transition-metal oxides. *Science*, 288(5465):462–468, 2000.

[53] C. H. Booth, F. Bridges, G. H. Kwei, J. M. Lawrence, A. L. Cornelius, and J. J. Neumeier. Direct Relationship between Magnetism and MnO_6 Distortions in $La_{1-x}Ca_xMnO_3$. *Phys. Rev. Lett.*, 80:853–856, Jan 1998.

[54] K. H. Ahn, T. Lookman, and A. R. Bishop. Strain-induced metal-insulator phase coexistence in perovskite manganites. *Nature*, 428(6981):401–404, 03 2004.

[55] F. Bridges, L. Downward, J. J. Neumeier, and T. A. Tyson. Detailed relationship between local structure, polarons, and magnetization for $La_{1-x}Ca_xMnO_3$ ($0.21 \leq x \leq 0.45$). *Phys. Rev. B*, 81:184401, May 2010.

[56] Pengcheng Dai, J. A. Fernandez-Baca, N. Wakabayashi, E. W. Plummer, Y. Tomioka, and Y. Tokura. Short-Range Polaron Correlations in the Ferromagnetic $La_{1-x}Ca_xMnO_3$. *Phys. Rev. Lett.*, 85:2553–2556, Sep 2000.

[57] C. P. Adams, J. W. Lynn, Y. M. Mukovskii, A. A. Arsenov, and D. A. Shulyatev. Charge Ordering and Polaron Formation in the Magnetoresistive Oxide $La_{0.7}Ca_{0.3}MnO_3$. *Phys. Rev. Lett.*, 85:3954–3957, Oct 2000.

[58] J. M. De Teresa, M. R. Ibarra, P. A. Algarabel, C. Ritter, C. Marquina, J. Blasco, J. Garcia, A. del Moral, and Z. Arnold. Evidence for magnetic polarons in the magnetoresistive perovskites. *Nature*, 386(6622):256–259, 03 1997.

[59] D. Akahoshi, M. Uchida, Y. Tomioka, T. Arima, Y. Matsui, and Y. Tokura. Random potential effect near the bicritical region in perovskite manganites as revealed by comparison with the ordered perovskite analogs. *Phys. Rev. Lett.*, 90:177203, May 2003.

[60] M. Uehara, S. Mori, C. H. Chen, and S. W. Cheong. Percolative phase separation underlies colossal magnetoresistance in mixed-valent manganites. *Nature*, 399(6736):560–563, 06 1999.

[61] M. Fäth, S. Freisem, A. A. Menovsky, Y. Tomioka, J. Aarts, and J. A. Mydosh. Spatially inhomogeneous metal-insulator transition in doped manganites. *Science*, 285(5433):1540–1542, 1999.

[62] A. K. Cheetham and P. Day. *Solid state chemistry: Techniques*. Oxford: Clarendon, 1988.

[63] G. L. Squires. *Introduction to the theory of thermal neutron scattering*. Cambridge University Press, 3rd edition, 2012.

[64] D. S. Sivia. *Elementary Scattering Theory: for X-ray and neutron users*. Oxford University Press, 2011.

[65] A. Guinier. *X-Ray Diffraction in Crystals, Imperfect Crystals, and Amorphous Bodies*. Dover Publications, Inc., 1994.

[66] E. Prince. *International Tables for CrystallographyVolume C: Mathematical, physical and chemical tables*. International Union of Crystallography, 2006.

[67] http://www.slideshare.net/rajeshchowdary8686/history-of-atom-bomb.

[68] https://www.psi.ch/media/the-sinq-neutron-source.

[69] J. Baruchel, J. L. Hodeau, M. S. Lehmann, J. R. Regnard, and C. Schlenker. *Neutron and Synchrotron Radiation for Condensed Matter Studies: Volume 1: Theory, Instruments and Methods: Theory, Instruments and Methods*. Springer, 1993.

[70] https://www.ill.eu/instruments-support/instruments-groups/instruments/d20/description/instrument-layout/.

[71] http://isaacs.sourceforge.net/phys/chem.html.

[72] M R Eskildsen, E M Forgan, and H Kawano-Furukawa. Vortex structures, penetration depth and pairing in iron-based superconductors studied by small-angle neutron scattering. *Reports on Progress in Physics*, 74(12):124504, 2011.

[73] O. Glatter and O. Kratky. *Small Angle X-ray Scattering*. Academic Press, 1982.

[74] Ralph Gilles, Andreas Ostermann, Christian Schanzer, Bernhard Krimmer, and Winfried Petry. The concept of the new small-angle scattering instrument sans-1 at the frm-ii. *Physica B: Condensed Matter*, 385-386, Part 2:1174 – 1176, 2006.

[75] http://www.mlz-garching.de/sans-1.

[76] M. McElfresh. *Fundamentals of magnetism and magnetic measurements featuring Quantum Design's Magnetic Property Measuring System*. Quantum Design, 1994.

[77] http://www.geocities.ws/pranab_muduli/squid.html.

[78] M. Tinkham. *Introduction to superconductivity*. Dover Publications, Inc., 2nd edition, 2004.

[79] Simon Foner. Versatile and sensitive vibrating sample magnetometer. *Review of Scientific Instruments*, 30(7), 1959.

[80] M. Tinkham. *Physical Property Measurement System: Hardware Manual*. Quantum Design, 6th edition, 2008.

[81] I Miccoli, F Edler, H Pfnr, and C Tegenkamp. The 100th anniversary of the four-point probe technique: the role of probe geometries in isotropic and anisotropic systems. *Journal of Physics: Condensed Matter*, 27(22):223201, 2015.

[82] Hk. Muller-Buschbaum and M. Kobel. Ein neuer Strukturtyp der Oxovanadate MV_2O_6: NiV_2O_6. *Zeitschrift fr anorganische und allgemeine Chemie*, 596(1):23–28, 1991.

[83] B. Jasper-Tonnies and Hk. Muller-Buschbaum. Synthese und Strukturuntersuchung von CoV_2O_6. *Zeitschrift fr anorganische und allgemeine Chemie*, 508(1):7–11, 1984.

[84] Mikael Markkula, Angel M. Arevalo-Lopez, and J. Paul Attfield. Neutron diffraction study of monoclinic brannerite-type CoV_2O_6. *Journal of Solid State Chemistry*, 192:390 – 393, 2012.

[85] A. Saúl, D. Vodenicarevic, and G. Radtke. Theoretical study of the magnetic order in α-CoV_2O_6. *Phys. Rev. B*, 87:024403, Jan 2013.

[86] Zhangzhen He, Jun-Ichi Yamaura, Yutaka Ueda, and Wendan Cheng. CoV_2O_6 Single Crystals Grown in a Closed Crucible: Unusual Magnetic Behaviors with Large Anisotropy and 1/3 Magnetization Plateau. *Journal of the American Chemical Society*, 131(22):7554–7555, 2009.

[87] F. Wallington, A. M. Arevalo-Lopez, J. W. Taylor, J. R. Stewart, V. Garcia-Sakai, J. P. Attfield, and C. Stock. Spin-orbit transitions in α- and $\gamma - CoV_2O_6$. *Phys. Rev. B*, 92:125116, Sep 2015.

[88] Bongjae Kim, Beom Hyun Kim, Kyoo Kim, Hong Chul Choi, Sang-Yeon Park, Y. H. Jeong, and B. I. Min. Unusual magnetic properties induced by local structure in a quasi-one-dimensional Ising chain system: α-CoV_2O_6. *Phys. Rev. B*, 85:220407, Jun 2012.

[89] Hiroshi Kageyama, Kazuyoshi Yoshimura, Koji Kosuge, Hiroyuki Mitamura, and Tsuneaki Goto. Field-Induced Magnetic Transitions in the One-Dimensional Compound $Ca_3Co_2O_6$. *Journal of the Physical Society of Japan*, 66(6):1607–1610, 1997.

[90] Shintaro Ishiwata, Dan Wang, Takashi Saito, , and Mikio Takano. High-Pressure Synthesis and Structure of $SrCo_6O_{11}$: Pillared Kagome Lattice System with a 1/3 Magnetization Plateau. *Chemistry of Materials*, 17(11):2789–2791, 2005.

[91] Mikael Markkula, Angel M. Arévalo-López, and J. Paul Attfield. Field-induced spin orders in monoclinic CoV_2O_6. *Phys. Rev. B*, 86:134401, Oct 2012.

[92] M. Lenertz, J. Alaria, D. Stoeffler, S. Colis, A. Dinia, O. Mentré, G. André, F. Porcher, and E. Suard. Magnetic structure of ground and field-induced ordered states of low-dimensional α-CoV_2O_6: Experiment and theory. *Phys. Rev. B*, 86:214428, Dec 2012.

[93] Randy S. Fishman. Phase diagram of a geometrically frustrated triangular-lattice antiferromagnet in a magnetic field. *Phys. Rev. Lett.*, 106:037206, Jan 2011.

[94] G. Chen, S. Choi, and L. Radzihovsky. Magnetic orders, excitations, and phase transitions in $Fe_{1+y}Te$. *Phys. Rev. B*, 88:165117, Oct 2013.

[95] D. Parshall, G. Chen, L. Pintschovius, D. Lamago, Th. Wolf, L. Radzihovsky, and D. Reznik. Competition between commensurate and incommensurate magnetic ordering in $Fe_{1+y}Te$. *Phys. Rev. B*, 85:140515, Apr 2012.

[96] Luis Seabra, Philippe Sindzingre, Tsutomu Momoi, and Nic Shannon. Novel phases in a square-lattice frustrated ferromagnet : $\frac{1}{3}$-magnetization plateau, helicoidal spin liquid, and vortex crystal. *Phys. Rev. B*, 93:085132, Feb 2016.

[97] Zhangzhen He and Mitsuru Itoh. Single crystal flux growth of the Ising spin-chain system γ-CoV_2O_6. *Journal of Crystal Growth*, 388:103 – 106, 2014.

[98] Simon A. J. Kimber, Hannu Mutka, Tapan Chatterji, Tommy Hofmann, Paul. F. Henry, Heloisa N. Bordallo, Dimitri N. Argyriou, and J. Paul Attfield. Metamagnetism and soliton excitations in the modulated ferromagnetic Ising chain CoV_2O_6. *Phys. Rev. B*, 84:104425, Sep 2011.

[99] M. Lenertz, A. Dinia, S. Colis, O. Mentr, G. Andr, F. Porcher, and E. Suard. Magnetic Structure of Ground and Field Induced Ordered States of Low-Dimensional γ-CoV_2O_6. *The Journal of Physical Chemistry C*, 118(25):13981–13987, 2014.

[100] Yvo Drees, Stefano Agrestini, Oksana Zaharko, and Alexander Christoph Komarek. Floating Zone Single Crystal Growth of γ-CoV_2O_6 with Substantially Enhanced Crystal Size and Quality. *Crystal Growth & Design*, 15(3):1168–1172, 2015.

[101] M. Nandi and P. Mandal. Magnetic and magnetocaloric properties of quasi-one-dimensional Ising spin chain CoV_2O_6. *Journal of Applied Physics*, 119(13), 2016.

[102] Juan Rodrguez-Carvajal. Recent advances in magnetic structure determination by neutron powder diffraction. *Physica B: Condensed Matter*, 192(1):55 – 69, 1993.

[103] H. M. Rietveld. A profile refinement method for nuclear and magnetic structures. *Journal of Applied Crystallography*, 2(2):65–71, Jun 1969.

[104] `http://www.ccp14.ac.uk/ccp/web-mirrors/plotr/Tutorials&Documents/basireps.pdf`.

[105] Rodrguez-Carvajal, J. and Boure, F. Symmetry and magnetic structures. *EPJ Web of Conferences*, 22:00010, 2012.

[106] Juan Rodrguez-Carvajal. An introduction to the program: FullProf 2000. 2001. https://www.ill.eu/sites/fullprof/index.html.

[107] `https://www.psi.ch/sinq/dmc/data-analysis`.

[108] Lucile Savary, Kate A. Ross, Bruce D. Gaulin, Jacob P. C. Ruff, and Leon Balents. Order by Quantum Disorder in $Er_2Ti_2O_7$. *Phys. Rev. Lett.*, 109:167201, Oct 2012.

[109] Tsuyoshi Okubo, Trung Hai Nguyen, and Hikaru Kawamura. Cubic and noncubic multiple-q states in the heisenberg antiferromagnet on the pyrochlore lattice. *Phys. Rev. B*, 84:144432, Oct 2011.

[110] Tsuyoshi Okubo, Sungki Chung, and Hikaru Kawamura. Multiple-q states and the skyrmion lattice of the triangular-lattice heisenberg antiferromagnet under magnetic fields. *Phys. Rev. Lett.*, 108:017206, Jan 2012.

[111] V.J. Emery and S.A. Kivelson. Frustrated electronic phase separation and high-temperature superconductors. *Physica C: Superconductivity*, 209(4):597 – 621, 1993.

[112] T. Matsuda, S. Partzsch, T. Tsuyama, E. Schierle, E. Weschke, J. Geck, T. Saito, S. Ishiwata, Y. Tokura, and H. Wadati. Observation of a Devil's Staircase in the Novel Spin-Valve System $SrCo_6O_{11}$. *Phys. Rev. Lett.*, 114:236403, Jun 2015.

[113] J R Stewart, G Ehlers, A S Wills, S T Bramwell, and J S Gardner. Phase transitions, partial disorder and multi- k structures in $Gd_2Ti_2O_7$. *Journal of Physics: Condensed Matter*, 16(28):L321, 2004.

[114] Behnam Javanparast, Zhihao Hao, Matthew Enjalran, and Michel J. P. Gingras. Fluctuation-driven selection at criticality in a frustrated magnetic system: The case of multiple-k partial order on the pyrochlore lattice. *Phys. Rev. Lett.*, 114:130601, Apr 2015.

[115] J. Bourgeois, G. André, S. Petit, J. Robert, M. Poienar, J. Rouquette, E. Elkaïm, M. Hervieu, A. Maignan, C. Martin, and F. Damay. Evidence of magnetic phase separation in $LuFe_2O_4$. *Phys. Rev. B*, 86:024413, Jul 2012.

[116] M. Pregelj, A. Zorko, O. Zaharko, H. Nojiri, H. Berger, L. C. Chapon, and D. Aron. Spin-stripe phase in a frustrated zigzag spin-1/2 chain. *Nat. Commun.*, 6:7255, 2015.

[117] Sang-Wook Cheong and Maxim Mostovoy. Multiferroics: a magnetic twist for ferroelectricity. *Nat. Mat.*, 6:13, 2007.

[118] Y. J. Choi, H. T. Yi, S. Lee, Q. Huang, V. Kiryukhin, and S.-W. Cheong. Ferroelectricity in an ising chain magnet. *Phys. Rev. Lett.*, 100:047601, Jan 2008.

[119] K. Singh, A. Maignan, D. Pelloquin, O. Perez, and Ch. Simon. Magnetodielectric coupling and magnetization plateaus in α-CoV_2O_6 crystals. *J. Mater. Chem.*, 22:6436–6440, 2012.

[120] Joel S. Helton, Daniel M. Pajerowski, Yiming Qiu, Yang Zhao, Dmitry A. Shulyatev, Yakov M. Mukovskii, Georgii L. Bychkov, Sergei N. Barilo, and Jeffrey W. Lynn. Polaron-mediated spin correlations in metallic and insulating $La_{1-x}A_xMnO_3$ ($A = \mathrm{Ca, Sr, or Ba}$). *Phys. Rev. B*, 90:214411, Dec 2014.

[121] M. Viret, F. Ott, J. P. Renard, H. Glättli, L. Pinsard-Gaudart, and A. Revcolevschi. Magnetic filaments in resistive manganites. *Phys. Rev. Lett.*, 93:217402, Nov 2004.

[122] H. Yoshizawa, H. Kawano, Y. Tomioka, and Y. Tokura. Neutron-diffraction study of the magnetic-field-induced metal-insulator transition in $Pr_{0.7}Ca_{0.3}MnO_3$. *Phys. Rev. B*, 52:R13145–R13148, Nov 1995.

[123] Jan Burgy, Adriana Moreo, and Elbio Dagotto. Relevance of cooperative lattice effects and stress fields in phase-separation theories for cmr manganites. *Phys. Rev. Lett.*, 92:097202, Mar 2004.

[124] T. Z. Ward, J. D. Budai, Z. Gai, J. Z. Tischler, Lifeng Yin, and J. Shen. Elastically driven anisotropic percolation in electronic phase-separated manganites. *Nat Phys*, 5(12):885–888, 12 2009.

[125] Keji Lai, Masao Nakamura, Worasom Kundhikanjana, Masashi Kawasaki, Yoshinori Tokura, Michael A. Kelly, and Zhi-Xun Shen. Mesoscopic percolating resistance network in a strained manganite thin film. *Science*, 329(5988):190–193, 2010.

[126] D. E. Cox, P. G. Radaelli, M. Marezio, and S-W. Cheong. Structural changes, clustering, and photoinduced phase segregation in $Pr_{0.7}Ca_{0.3}MnO_3$. *Phys. Rev. B*, 57:3305–3314, Feb 1998.

[127] J. L. García-Muñoz, C. Frontera, P. Beran, N. Bellido, J. Hernández-Velasco, and C. Ritter. Consequences of embedding Ti^{4+} $3d^0$ centers in $Pr_{0.50}Ca_{0.50}MnO_3$: Phase competition in $Pr_{0.50}Ca_{0.50}Mn_{1-x}Ti_xO_3$. *Phys. Rev. B*, 81:014409, Jan 2010.

[128] M. Tokunaga, N. Miura, Y. Tomioka, and Y. Tokura. High-magnetic-field study of the phase transitions of $R_{1-x}Ca_xMnO_3$ (R = Pr, Nd). *Phys. Rev. B*, 57:5259–5264, Mar 1998.

[129] T. Holstein. Studies of polaron motion. *Annals of Physics*, 8(3):343 – 389, 1959.

[130] M. Doerr, G. Remnyi, M. Rotter, S. Sahling, M. Saint-Paul, and M. Loewenhaupt. Magnetoelastic investigations at prcamno manganites. *Journal of Magnetism and Magnetic Materials*, 290291, Part 2:906 – 909, 2005. Proceedings of the Joint European Magnetic Symposia (JEMS' 04).

[131] L. Downward, F. Bridges, S. Bushart, J. J. Neumeier, N. Dilley, and L. Zhou. Universal Relationship between Magnetization and Changes in the Local Structure of $La_{1-x}Ca_xMnO_3$: Evidence for Magnetic Dimers. *Phys. Rev. Lett.*, 95:106401, Sep 2005.

[132] T. A. Tyson, M. Deleon, M. Croft, V. G. Harris, C.-C. Kao, J. Kirkland, and S-W. Cheong. Magnetic field melting of the charge-ordered state of $La_{1?2}Ca_{1?2}MnO_3$: A local structure perspective. *Phys. Rev. B*, 70:024410, Jul 2004.

[133] Z. W. Ouyang, H. Nojiri, and S. Yoshii. Unusual metamagnetic transitions in $Pr_{0.5}Ca_{0.5}Mn_{0.97}Ga_{0.03}O_3$ studied by pulsed magnetic fields. *Phys. Rev. B*, 78:104404, Sep 2008.

[134] R. Mahendiran, A. Maignan, S. Hébert, C. Martin, M. Hervieu, B. Raveau, J. F. Mitchell, and P. Schiffer. Ultrasharp magnetization steps in perovskite manganites. *Phys. Rev. Lett.*, 89:286602, Dec 2002.

[135] Y. Y. Wu, H. N. Li, Z. C. Xia, Y. Huang, Z. W. Ouyang, L. Li, L. X. Xiao, L. P. Peng, J. W. Huang, and H. K. Zuo. Magnetic field-induced metamagnetic transitions of $Pr_{0.5}Ca_{0.5}Mn_{0.97}Ga_{0.03}O_3$. *Journal of Applied Physics*, 110(1), 2011.

[136] S. Hébert, A. Maignan, V. Hardy, C. Martin, M. Hervieu, and B. Raveau. Avalanche like field dependent magnetization of mn-site doped charge-ordered manganites. *Solid State Communications*, 122(6):335 – 340, 2002.

[137] S. Hébert, V. Hardy, A. Maignan, R. Mahendiran, M. Hervieu, C. Martin, and B. Raveau. Magnetic-field-induced step-like transitions in mn-site doped manganites. *Journal of Solid State Chemistry*, 165(1):6 – 11, 2002.

[138] V. Hardy, S. Majumdar, M. R. Lees, D. McK. Paul, C. Yaicle, and M. Hervieu. Power-law distribution of avalanche sizes in the field-driven transformation of a phase-separated oxide. *Phys. Rev. B*, 70:104423, Sep 2004.

[139] C. Yaicle, C. Martin, Z. Jirak, F. Fauth, G. André, E. Suard, A. Maignan, V. Hardy, R. Retoux, M. Hervieu, S. Hébert, B. Raveau, Ch. Simon, D. Saurel, A. Brûlet, and F. Bourée. Neutron scattering evidence for magnetic-field-driven abrupt magnetic and structural transitions in a phase-separated manganite. *Phys. Rev. B*, 68:224412, Dec 2003.

[140] Eduard Vives, Jordi Ortín, Lluís Mañosa, Ismael Ràfols, Ramon Pérez-Magrané, and Antoni Planes. Distributions of avalanches in martensitic transformations. *Phys. Rev. Lett.*, 72:1694–1697, Mar 1994.

[141] C. Yaicle, C. Frontera, J. L. García-Muñoz, C. Martin, A. Maignan, G. André, F. Bourée, C. Ritter, and I. Margiolaki. Avalanches, irreversibility, and phase separation in Co-substituted $Pr_{0.50}Ca_{0.50}Mn_{1-x}Co_xO_3$. *Phys. Rev. B*, 74:144406, Oct 2006.

[142] C. Yaicle, F. Fauth, C. Martin, R. Retoux, Z. Jirak, M. Hervieu, B. Raveau, and A. Maignan. $Pr_{0.5}Ca_{0.5}Mn_{0.97}Ga_{0.03}O_3$, a strongly strained system due to the coexistence of two orbital ordered phases at low temperature. *Journal of Solid State Chemistry*, 178(5):1652 – 1660, 2005.

[143] Peter W. Stephens. Phenomenological model of anisotropic peak broadening in powder diffraction. *Journal of Applied Crystallography*, 32(2):281–289, Apr 1999.

[144] M. Roy, J. F. Mitchell, A. P. Ramirez, and P. Schiffer. Doping-induced transition from double exchange to charge order in $La_{1-x}Ca_xMnO_3$ near $x = 0.50$. *Phys. Rev. B*, 58:5185–5188, Sep 1998.

[145] T. V. Ramakrishnan, H. R. Krishnamurthy, S. R. Hassan, and G. Venketeswara Pai. Theory of insulator metal transition and colossal magnetoresistance in doped manganites. *Phys. Rev. Lett.*, 92:157203, Apr 2004.

[146] O. Cépas, H. R. Krishnamurthy, and T. V. Ramakrishnan. Instabilities and insulator-metal transitions in half-doped manganites induced by magnetic-field and doping. *Phys. Rev. B*, 73:035218, Jan 2006.

[147] `http://docs.mantidproject.org/v3.7.1/fitfunctions/NeutronBk2BkExpConvPVoigt.html`.

[148] A. Le Bail, H. Duroy, and J.L. Fourquet. Ab-initio structure determination of $LiSbWO_6$ by X-ray powder diffraction. *Materials Research Bulletin*, 23(3):447 – 452, 1988.

[149] S. Hirai, A. M. dos Santos, M. C. Shapiro, J. J. Molaison, N. Pradhan, M. Guthrie, C. A. Tulk, I. R. Fisher, and W. L. Mao. Giant atomic displacement at a magnetic phase transition in metastable Mn_3O_4. *Phys. Rev. B*, 87:014417, Jan 2013.

[150] André Heinemann and Albrecht Wiedenmann. Benefits of polarized small-angle neutron scattering on magnetic nanometer scale structure modeling. *Journal of Applied Crystallography*, 36(3 Part 1):845–849, Jun 2003.

[151] D. Saurel, Ch. Simon, A. Brûlet, A. Heinemann, and C. Martin. Small-angle neutron scattering study of the steplike magnetic transformation in $Pr_{0.70}Ca_{0.30}MnO_3$. *Phys. Rev. B*, 75:184442, May 2007.

[152] Damien Saurel, Annie Brûlet, André Heinemann, Christine Martin, Silvana Mercone, and Charles Simon. Magnetic field dependence of the magnetic phase separation in $Pr_{1-x}Ca_xMnO_3$ manganites studied by small-angle neutron scattering. *Phys. Rev. B*, 73:094438, Mar 2006.

[153] Damien Saurel, Charles Simon, Alain Pautrat, Christine Martin, Charles Dewhurst, and Annie Brûlet. Evolution of the conducting phase topology at the percolation threshold in colossal magnetoresistance manganites: A magnetic small-angle neutron scattering study. *Phys. Rev. B*, 82:054427, Aug 2010.

[154] R. Kajimoto, H. Yoshizawa, Y. Tomioka, and Y. Tokura. Commensurate-incommensurate transition in the melting process of orbital ordering in $Pr_{0.5}Ca_{0.5}MnO_3$: A neutron diffraction study. *Phys. Rev. B*, 63:212407, May 2001.

[155] Alexander T. Holmes, Gary R. Walsh, Elizabeth Blackburn, Edward M. Forgan, and Marc Savey-Bennett. A 17 t horizontal field cryomagnet with rapid sample change designed for beamline use. *Review of Scientific Instruments*, 83(2), 2012.

[156] I. Grillo. *Small-Angle Neutron Scattering and Applications in Soft Condensed Matter*, pages 723–782. Springer Netherlands, Dordrecht, 2008.

[157] Weida Wu, Casey Israel, Namjung Hur, Soonyong Park, Sang-Wook Cheong, and Alex de Lozanne. Magnetic imaging of a supercooling glass transition in a weakly disordered ferromagnet. *Nat Mater*, 5(11):881–886, 11 2006.

[158] Scott Kirkpatrick. Percolation and conduction. *Rev. Mod. Phys.*, 45:574–588, Oct 1973.

[159] S. Mori, T. Katsufuji, N. Yamamoto, C. H. Chen, and S-W. Cheong. Microstructure related to charge and orbital ordering in $Pr_{0.5}Ca_{0.5}MnO_3$. *Phys. Rev. B*, 59:13573–13576, Jun 1999.

[160] V. Dediu, C. Ferdeghini, F. C. Matacotta, P. Nozar, and G. Ruani. Jahn-teller dynamics in charge-ordered manganites from raman spectroscopy. *Phys. Rev. Lett.*, 84:4489–4492, May 2000.

[161] J. B. Goodenough, A. Wold, R. J. Arnott, and N. Menyuk. Relationship Between Crystal Symmetry and Magnetic Properties of Ionic Compounds Containing Mn^{3+}. *Phys. Rev.*, 124:373–384, Oct 1961.

[162] F. Rivadulla, M. A. López-Quintela, J. Mira, and J. Rivas. Jahn-teller vibrational anisotropy determines the magnetic structure in orthomanganites. *Phys. Rev. B*, 64:052403, Jul 2001.

[163] T. Kimura, Y. Tomioka, A. Asamitsu, and Y. Tokura. Anisotropic magnetoelastic phenomena in layered manganite crystals: Implication of change in orbital state. *Phys. Rev. Lett.*, 81:5920–5923, Dec 1998.

[164] M.A. Subramanian, C.C. Torardi, D.C. Johnson, J. Pannetier, and A.W. Sleight. Ferromagnetic $R_2Mn_2O_7$ pyrochlores (R = Dy, Lu, Y). *Journal of Solid State Chemistry*, 72(1):24 – 30, 1988.

[165] J. P. C. Ruff, B. D. Gaulin, J. P. Castellan, K. C. Rule, J. P. Clancy, J. Rodriguez, and H. A. Dabkowska. Structural Fluctuations in the Spin-Liquid State of $Tb_2Ti_2O_7$. *Phys. Rev. Lett.*, 99:237202, Dec 2007.

[166] J. P. C. Ruff, Z. Islam, J. P. Clancy, K. A. Ross, H. Nojiri, Y. H. Matsuda, H. A. Dabkowska, A. D. Dabkowski, and B. D. Gaulin. Magnetoelastics of a Spin Liquid: X-Ray Diffraction Studies of $Tb_2Ti_2O_7$ in Pulsed Magnetic Fields. *Phys. Rev. Lett.*, 105:077203, Aug 2010.

[167] T. Fennell, M. Kenzelmann, B. Roessli, H. Mutka, J. Ollivier, M. Ruminy, U. Stuhr, O. Zaharko, L. Bovo, A. Cervellino, M. K. Haas, and R. J. Cava. Magnetoelastic Excitations in the Pyrochlore Spin Liquid $Tb_2Ti_2O_7$. *Phys. Rev. Lett.*, 112:017203, Jan 2014.

[168] Byron C. den Hertog and Michel J. P. Gingras. Dipolar interactions and origin of spin ice in ising pyrochlore magnets. *Phys. Rev. Lett.*, 84:3430–3433, Apr 2000.

[169] J. S. Gardner, A. Keren, G. Ehlers, C. Stock, Eva Segal, J. M. Roper, B. Fåk, M. B. Stone, P. R. Hammar, D. H. Reich, and B. D. Gaulin. Dynamic frustrated magnetism in $Tb_2Ti_2O_7$ at 50 mK. *Phys. Rev. B*, 68:180401, Nov 2003.

[170] J. S. Gardner, B. D. Gaulin, A. J. Berlinsky, P. Waldron, S. R. Dunsiger, N. P. Raju, and J. E. Greedan. Neutron scattering studies of the cooperative paramagnet pyrochlore $Tb_2Ti_2O_7$. *Phys. Rev. B*, 64:224416, Nov 2001.

[171] A. Keren, J. S. Gardner, G. Ehlers, A. Fukaya, E. Segal, and Y. J. Uemura. Dynamic Properties of a Diluted Pyrochlore Cooperative Paramagnet $(Tb_pY_{1-p})_2Ti_2O_7$. *Phys. Rev. Lett.*, 92:107204, Mar 2004.

[172] G A Gehring and K A Gehring. Co-operative jahn-teller effects. *Reports on Progress in Physics*, 38(1):1, 1975.

[173] Oleg Tchernyshyov, R. Moessner, and S. L. Sondhi. Order by distortion and string modes in pyrochlore antiferromagnets. *Phys. Rev. Lett.*, 88:067203, Jan 2002.

[174] Gia-Wei Chern, C. J. Fennie, and O. Tchernyshyov. Broken parity and a chiral ground state in the frustrated magnet $CdCr_2O_4$. *Phys. Rev. B*, 74:060405, Aug 2006.

[175] T. Taniguchi, H. Kadowaki, H. Takatsu, B. Fåk, J. Ollivier, T. Yamazaki, T. J. Sato, H. Yoshizawa, Y. Shimura, T. Sakakibara, T. Hong, K. Goto, L. R. Yaraskavitch, and J. B. Kycia. Long-range order and spin-liquid states of polycrystalline $Tb_{2+x}Ti_{2-x}O_{7+y}$. *Phys. Rev. B*, 87:060408, Feb 2013.

[176] P. F. Bongers and E. R. Van Meurs. Ferromagnetism in compounds with pyrochlore structure. *Journal of Applied Physics*, 38(3), 1967.

[177] Mariana J. Whitaker and Colin Greaves. Magnetic ordering in the pyrochlore Ho_2CrSbO_7 determined from neutron diffraction, and the magnetic properties of other RE_2CrSbO_7 phases (RE=Y, Tb, Dy, Er). *Journal of Solid State Chemistry*, 215:171 – 175, 2014.

[178] C L Henley. Effective hamiltonians and dilution effects in kagome and related anti-ferromagnets. *Canadian Journal of Physics*, 79(11-12):1307–1321, 2001.

[179] S.-H. Lee, C. Broholm, T. H. Kim, W. Ratcliff, and S-W. Cheong. Local spin resonance and spin-peierls-like phase transition in a geometrically frustrated antiferromagnet. *Phys. Rev. Lett.*, 84:3718–3721, Apr 2000.

[180] A. B. Sushkov, O. Tchernyshyov, W. Ratcliff II, S. W. Cheong, and H. D. Drew. Probing Spin Correlations with Phonons in the Strongly Frustrated Magnet $ZnCr_2O_4$. *Phys. Rev. Lett.*, 94:137202, Apr 2005.

[181] Ch. Kant, J. Deisenhofer, T. Rudolf, F. Mayr, F. Schrettle, A. Loidl, V. Gnezdilov, D. Wulferding, P. Lemmens, and V. Tsurkan. Optical phonons, spin correlations, and spin-phonon coupling in the frustrated pyrochlore magnets $CdCr_2O_4$ and $ZnCr_2O_4$. *Phys. Rev. B*, 80:214417, Dec 2009.

[182] W. Ratcliff, S.-H. Lee, C. Broholm, S.-W. Cheong, and Q. Huang. Freezing of spin correlated nanoclusters in a geometrically frustrated magnet. *Phys. Rev. B*, 65:220406, Jun 2002.

[183] D. Fiorani, S. Viticoli, J. L. Dormann, J. L. Tholence, and A. P. Murani. Spin-glass behavior in an antiferromagnetic frustrated spinel: $ZnCr_{1.6}Ga_{0.4}O_4$. *Phys. Rev. B*, 30:2776–2786, Sep 1984.

[184] S.-H. Lee, W. Ratcliff, Q. Huang, T. H. Kim, and S-W. Cheong. Néel to spin-glass-like phase transition versus dilution in geometrically frustrated $ZnCr_{2-2x}Ga_{2x}O_4$. *Phys. Rev. B*, 77:014405, Jan 2008.

[185] R. Moessner and J. T. Chalker. Properties of a classical spin liquid: The heisenberg pyrochlore antiferromagnet. *Phys. Rev. Lett.*, 80:2929–2932, Mar 1998.

[186] R. Moessner and J. T. Chalker. Low-temperature properties of classical geometrically frustrated antiferromagnets. *Phys. Rev. B*, 58:12049–12062, Nov 1998.

[187] M. J. Harris, S. T. Bramwell, D. F. McMorrow, T. Zeiske, and K. W. Godfrey. Geometrical Frustration in the Ferromagnetic Pyrochlore $Ho_2Ti_2O_7$. *Phys. Rev. Lett.*, 79:2554–2557, Sep 1997.

[188] Steven T. Bramwell and Michel J. P. Gingras. Spin ice state in frustrated magnetic pyrochlore materials. *Science*, 294(5546):1495–1501, 2001.

[189] D. J. P. Morris, D. A. Tennant, S. A. Grigera, B. Klemke, C. Castelnovo, R. Moessner, C. Czternasty, M. Meissner, K. C. Rule, J.-U. Hoffmann, K. Kiefer, S. Gerischer, D. Slobinsky, and R. S. Perry. Dirac Strings and Magnetic Monopoles in the Spin Ice $Dy_2Ti_2O_7$. *Science*, 326(5951):411–414, 2009.

[190] C. Castelnovo, R. Moessner, and S. L. Sondhi. Magnetic monopoles in spin ice. *Nature*, 451(7174):42–45, 01 2008.

[191] Joseph A.M. Paddison and et al. Nature of Partial Magnetic Order in the Frustrated Antiferromagnet $Gd_2Ti_2O_7$. arXiv, 1506.05045 (2016), 2015.

[192] G. J. Nieuwenhuys, B. H. Verbeek, and J. A. Mydosh. Towards a uniform magnetic phase diagram for magnetic alloys with mixed types of order. *Journal of Applied Physics*, 50(B3), 1979.

[193] Marc Gabay and Gérard Toulouse. Coexistence of spin-glass and ferromagnetic orderings. *Phys. Rev. Lett.*, 47:201–204, Jul 1981.

[194] D. H. Reich, B. Ellman, J. Yang, T. F. Rosenbaum, G. Aeppli, and D. P. Belanger. Dipolar magnets and glasses: Neutron-scattering, dynamical, and calorimetric studies of randomly distributed ising spins. *Phys. Rev. B*, 42:4631–4644, Sep 1990.

[195] Kiyotaka Miyoshi, Yoshinori Nishimura, Kenji Honda, Kenji Fujiwara, and Jun Takeuchi. Successive Spin Freezing Behavior in a Pyrochlore Antiferromagnet $Y_2Mo_2O_7$ under Magnetic Fields. *Journal of the Physical Society of Japan*, 69(11):3517–3520, 2000.

[196] A. Andreanov, J. T. Chalker, T. E. Saunders, and D. Sherrington. Spin-glass transition in geometrically frustrated antiferromagnets with weak disorder. *Phys. Rev. B*, 81:014406, Jan 2010.

[197] U. Walter. Treating crystal field parameters in lower than cubic symmetries. *Journal of Physics and Chemistry of Solids*, 45(4):401 – 408, 1984.

[198] Junjiro Kanamori. Superexchange interaction and symmetry properties of electron orbitals. *Journal of Physics and Chemistry of Solids*, 10(2):87 – 98, 1959.

[199] Kiyosi Motida and Syhei Miyahara. On the 90° Exchange Interaction between Cations (Cr^{3+}, Mn^{2+}, Fe^{3+} and Ni^{2+}) in Oxides. *Journal of the Physical Society of Japan*, 28(5):1188–1196, 1970.